APPLIED COMPUTATIONAL ELECTROMAGNETICS SOCIETY JOURNAL

Special Issue on ACES-China 2018

Guest Editors:

Xiaomin Pan, Beijing Institute of Technology
Qi Wu, Beihang University
Maokun Li, Tsinghua University

June 2019
Vol. 34 No. 6
ISSN 1054-4887

The ACES Journal is abstracted in INSPEC, in Engineering Index, DTIC, Science Citation Index Expanded, the Research Alert, and to Current Contents/Engineering, Computing & Technology.

The illustrations on the front cover have been obtained from the research groups at the Department of Electrical Engineering, The University of Mississippi.

THE APPLIED COMPUTATIONAL ELECTROMAGNETICS SOCIETY JOURNAL

Vol. 34 No. 6 June 2019

SPECIAL ISSUE ON ACES-CHINA 2018

Parallel Integral Equation Based Non-overlapping DDM for Fast Solving Electromagnetic Scattering Problems with Changeable Parts

Zongjing Gu [1], Xunwang Zhao [1], Chang Zhai [1], Zhongchao Lin [1], Yu Zhang [1], and Qi Zhang [2]

[1] Shaanxi Key Laboratory of Large Scale Electromagnetic Computing
Xidian University, Xi'an, Shaanxi 710071, China
xdguzongjing@163.com, xwzhao@mail.xidian.edu.cn, jione92@163.com

[2] Science and Technology on Electromagnetic Compatibility Laboratory
China Ship Development and Design Center, Wuhan 430064, China

Abstract ─ In this paper, a parallel non-overlapping domain decomposition method (DDM) using electric field integral equation (EFIE) is proposed for fast and accurate analysis of electrically large PEC objects with changeable parts in the condition of limited resources. The approach has considered that there are null fields as well as electric current inside a metal object in the original problem, then a novel transmission condition similar to an absorbing boundary is adopted, hence the continuity of electric currents is enhanced and the convergence is further improved in the outer iterative procedure. Moreover, the coupling between different subdomains is calculated in the manner of near field to avoid the storage of the mutual impedance. Some numerical examples are given to demonstrate the efficiency and stability of the proposed method.

Index Terms ─ Domain decomposition method, electrically large, integral equation, transmission condition.

I. INTRODUCTION

In the research field of electromagnetic (EM) scattering, the situation that the local elements located in the overall target rotate or translate while most of the elements remain unchanged is often encountered, for example the gun barrel of a tank rotating or a certain aircraft changing flight posture during formation flying. Generally, in order to study the EM scattering characteristics of the changed model, we have to re-compute the overall target, even though only a small element of the overall target has changed. Obviously, it is extremely time-consumed and wasteful of computing resources for the recalculation of the unchanged parts. It is desirable for computational electromagnetic to provide efficient algorithms for such demands of practical engineering.

Nowadays, Method of Moment (MoM) based on integral equation (IE) is the most accurate numerical methods in the field of computational electromagnetics, which is a numerical method based on Maxwell equation and the boundary conditions of a given problem [1]. However, a huge complex dense matrix will be generated when solving electrically large EM problems, causing that the time taken to solve the matrix equation by using lower/upper (LU) decomposition solver accounts for more than 90% of the total calculation process. More important is that the memory requirement and the computing complexity of the LU solver are in proportion to $O(N^2)$ and $O(N^3)$, respectively, where N is the number of unknowns. Hence, its expensive demands for memory and computing time to solve the matrix equation limit the application of MoM [2]. In order to reduce the memory requirement and computation complexity, the traditional high frequency methods [3, 4] or fast algorithms such as the fast multiple methods [5, 6] are proposed. However, the high frequency methods are at the expense of accuracy, and fast algorithms may confront with slow convergence or even divergence issues in applications involving complex structures [2].

The domain decomposition method (DDM) based on electric field integral equation (EFIE) paves a new way to break through these bottlenecks and has become an effective method to solve electrically large problems [7-10]. In view of this, combining the EFIE with DDM (IE-DDM) makes it possible to solve some problems that we faced. Further, this method provides unprecedented flexibility and convenience for simulating the object with changeable parts, since it stores the unchanged portion matrix after LU factorization in random access memory (RAM) and just needs to re-compute the changed portion of the model during the design process. Finally, the accurate results of each case are obtained through iterative solution and hence the memory requirements and CPU time are reduced greatly. It is should be pointed out that the coupling between different subdomains is obtained using the near field produced by the current to avoid the storage of the mutual impedance [2].

To further improve the ability and efficiency of

Submitted On: October 15, 2018
Accepted On: December 21, 2018

the DDM for simulating scattering performances of electrically large EM objects, one of frequently used and effective ways is to adopt parallel EM algorithm on distributed-memory computers [11-14]. In this case, this paper uses Message Passing Interface (MPI) parallel programming model to accelerate the solution of the EM problems with changeable parts.

This paper is organized as follows. In Section II, the algorithm of the non-overlapping DDM is presented. Section III provides numerical examples to demonstrate the correctness and robustness of the proposed method. Finally, some conclusions are given in Section IV.

II. FORMULATION

A. Domain decomposition strategy

An arbitrarily shaped three-dimensional PEC problem can be modeled with surface integral equations. The scattered electric filed $\boldsymbol{E}^s$ generated by the equivalent electric current $\boldsymbol{J}$ residing on the PEC surface S shown in Fig. 1 can be established firstly [1]:

$$\boldsymbol{E}^s(\boldsymbol{J}(\boldsymbol{r}'))=\eta L(\boldsymbol{J}(\boldsymbol{r}')), \tag{1}$$

where $\eta=\sqrt{\mu/\varepsilon}$ is the wave impedance in free-space, and $L(\boldsymbol{J}(\boldsymbol{r}))$ is linear operator, which given by:

$$L(\boldsymbol{X})=-jk\int_S\left[\boldsymbol{X}(\boldsymbol{r}')+\frac{1}{k^2}(\nabla'\cdot\boldsymbol{X}(\boldsymbol{r}'))\nabla\right]G(R)ds', \tag{2}$$

where G(R) is the Green's function, $R=|\boldsymbol{r}-\boldsymbol{r}'|$ is the distance between the source and the field point. $\boldsymbol{J}(\boldsymbol{r}')$ is the equivalent surface electric current on the PEC surface S and can be expanded in a set of known functions with unknown coefficients $a_n{}^S$, which can be expressed as [1, 2]:

$$\boldsymbol{J}(\boldsymbol{r}')=\sum_{n=1}^{N}a_n{}^S\,\boldsymbol{f}_n(\boldsymbol{r}'), \tag{3}$$

where N is the number of RWG basis functions $\boldsymbol{f}_n(\boldsymbol{r}')$ on surface S [1].

Compared with overlapped DDM [7, 8], the integral equation based non-overlapping domain decomposition method (IE-NDDM) proposed in this paper only adds artificial touching-faces between adjacent subdomains to make each of them closed. In the following, a novel domain decomposition strategy will be introduced. For the sake of clarity, it is considered that a PEC object Ω is divided into three non-overlapping closed subdomains Ω_1, Ω_2 and Ω_3, which is illuminated by incident plane wave $\{E^{inc},H^{inc}\}$ as shown in Fig. 1. S_m is the exterior boundary except the artificial touching-face $S_{t,m}$ of the subdomains Ω_m. $S_{t,m}$ denotes the artificial touching-face between the subdomain Ω_m and Ω_n except the curve Γ_{mn}. Γ_{mn} is defined as the boundary curve of the artificial touching-face $S_{t,m}$. $\hat{\boldsymbol{n}}_m$ is the outward unit vector of the subdomain Ω_m.

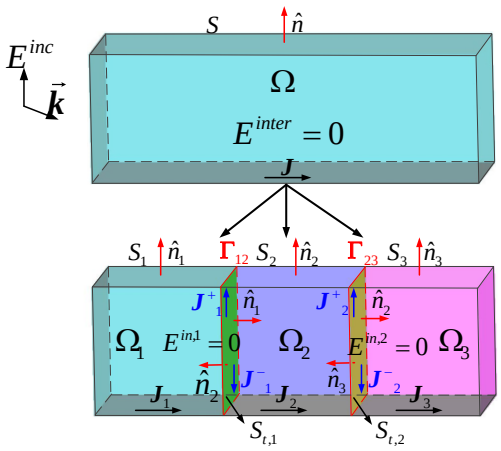

Fig. 1. Decomposition of Ω into three non-overlapping subdomains Ω_1, Ω_2 and Ω_3.

Then, the equation (3) can be rewritten as:

$$\begin{aligned}\boldsymbol{J}(\boldsymbol{r}')=&\sum_{n=1}^{N_1}a_{1,n}{}^{S_1}\,\boldsymbol{f}_{1,n}(\boldsymbol{r}')+\sum_{n=1}^{N_2}a_{2,n}{}^{S_2}\,\boldsymbol{f}_{2,n}(\boldsymbol{r}')\\&+\sum_{n=1}^{N_3}a_{3,n}{}^{S_3}\,\boldsymbol{f}_{3,n}(\boldsymbol{r}'),\end{aligned} \tag{4}$$

where N_m is the number of RWG basis functions on surface S_m. Due to the introduction of artificial touching-face, the current $\boldsymbol{J}_m$ residing on the subdomain m (m=1, 2, 3) can be expressed as:

$$\begin{cases}\boldsymbol{J}_1(\boldsymbol{r}')=\sum_{n=1}^{N_1}a_{1,n}{}^{S_1}\,\boldsymbol{f}_{1,n}(\boldsymbol{r}')+\sum_{m\in S_{t,1}}a_{1,m}{}^{S_{t,1}}\,\boldsymbol{f}_{1,m}{}^{S_{t,1}}(\boldsymbol{r}')\\ \boldsymbol{J}_2(\boldsymbol{r}')=\sum_{n=1}^{N_2}a_{2,n}{}^{S_2}\,\boldsymbol{f}_{2,n}(\boldsymbol{r}')+\sum_{m\in S_{t,1}}a_{2,m}{}^{S_{t,1}}\,\boldsymbol{f}_{2,m}{}^{S_{t,1}}(\boldsymbol{r}')\\ \qquad\qquad+\sum_{m\in S_{t,2}}a_{2,m}{}^{S_{t,2}}\,\boldsymbol{f}_{2,m}{}^{S_{t,2}}(\boldsymbol{r}')\\ \boldsymbol{J}_3(\boldsymbol{r}')=\sum_{n=1}^{N_3}a_{3,n}{}^{S_3}\,\boldsymbol{f}_{3,n}(\boldsymbol{r}')+\sum_{m\in S_{t,2}}a_{3,m}{}^{S_{t,2}}\,\boldsymbol{f}_{3,m}{}^{S_{t,2}}(\boldsymbol{r}')\end{cases}. \tag{5}$$

Generally, the first order transmission condition is widely used on the artificial touching-faces to ensure the continuity of electric currents, expressed as:

$$\boldsymbol{J}^+{}_m(\boldsymbol{r}')=-\boldsymbol{J}^-{}_m(\boldsymbol{r}'),\ \ \boldsymbol{r}'\in S_{t,m}. \tag{6}$$

In addition, it is well known that there are null electric fields as well as electric currents inside the PEC object as shown in Fig. 1 [1, 2]. With this taken into account, a novel explicit boundary condition is given:

$$a_{1,m}{}^{S_{t,1}}=a_{2,m}{}^{S_{t,1}}=a_{2,m}{}^{S_{t,2}}=a_{3,m}{}^{S_{t,2}},\quad m\in S_{t,1},S_{t,2}, \tag{7}$$

which combines equation (5) and (6) to efficiently solve the PEC problem. In fact, this novel explicit boundary condition can be regarded as an absorbing boundary, which not only enhances the continuity of electric currents across adjacent subdomains, but also ensures the IE-NDDM being equivalent to the original problem (see

Section III.A).

B. Fast solving scattering problems with changeable parts

For explanation purposes, the Galerkin test is adopted to weight linear equation (1) and the following matrix equations is obtained [1, 2]:

$$\begin{bmatrix} \mathbf{Z}_{11} & \mathbf{Z}_{12} & \mathbf{Z}_{13} \\ \mathbf{Z}_{21} & \mathbf{Z}_{22} & \mathbf{Z}_{23} \\ \mathbf{Z}_{31} & \mathbf{Z}_{32} & \mathbf{Z}_{33} \end{bmatrix} \begin{bmatrix} \mathbf{I}_1 \\ \mathbf{I}_2 \\ \mathbf{I}_3 \end{bmatrix} = \begin{bmatrix} \mathbf{V}_1 \\ \mathbf{V}_2 \\ \mathbf{V}_3 \end{bmatrix}, \quad (8)$$

where $\mathbf{Z}_{ij}$ (i=j) is the self-impedance matrix in subdomain Ω_i, $\mathbf{Z}_{ij}$ (i≠j) is the mutual impedance matrix between subdomain Ω_j and Ω_i, $\mathbf{I}_i$ is the unknown current coefficient to be determined and $\mathbf{V}_i$ denotes the given source vector in subdomain Ω_i.

The unknown coefficients will be persistently updated by solving the local model equation until convergence. The number of iteration is initialized being zero (k=0), and the currents in all subdomains are zero ($\mathbf{I}_i(0)$=0 (i=1,2,3)). The user-specified convergence parameter is δ. Setting k=1, 2 …, at k+1th step, the unknown current coefficients can be expressed as:

$$\mathbf{I}_i^{(k+1)} = -\mathbf{Z}_{ii}^{-1} \sum_{j<i} \mathbf{Z}_{ij} \mathbf{I}_j^{(k+1)} - \mathbf{Z}_{ii}^{-1} \sum_{j>i} \mathbf{Z}_{ij} \mathbf{I}_j^{(k)} + \mathbf{Z}_{ii}^{-1} \mathbf{V}_i. \quad (9)$$

The residual error δ_k at kth iteration is used to express the convergence behavior of the iterative method, which is defined as:

$$\delta_k = \frac{\left\| \mathbf{I}_i^{(k)} - \mathbf{I}_i^{(k-1)} \right\|}{\left\| \mathbf{I}_i^{(k)} \right\|}, \quad (i = 1, 2, 3,). \quad (10)$$

When max (δ_k) ≤ δ at the kth step, the iterative process stops. It is should be pointed out that the mutual impedance in equation (9) is actually unnecessary to be stored and the product $\Delta \mathrm{V}_i^{(k+1)}$ of $\mathbf{Z}_{ij}$ and $\mathbf{I}_j^{(k+1)}$ (j<i) or $\Delta \mathrm{V}_i^{(k)}$ of $\mathbf{Z}_{ij}$ and $\mathbf{I}_j^{(k)}$ (j>i) can be obtained using the near field produced by the current,

$$\Delta \mathbf{V}_i^{(k)} = \mathbf{Z}_{ij} \mathbf{I}_j^{(k)} = \int_{S^i} \boldsymbol{f}_n(\boldsymbol{r}') \mathbf{E}_i^{(k)}(\boldsymbol{J}) \mathrm{d}s, \quad (i \neq j), \quad (11)$$

where S^i is the exterior boundary of subdomain Ω_i, and $\mathbf{E}_i^{(k)}$ denotes the nearfield of subdomain Ω_i produced by the rest subdomains at kth step. Hence the memory requirement and CPU time are reduced greatly [16].

In order to describe the process of solving scattering problems with changeable parts using IE-NDDM proposed in this paper, we take the decomposed PEC object with three subdomains shown in Fig. 2 as an example. In this case, compared with Fig. 1, only the posture of subdomain Ω_1 has changed and is named changeable parts. Thus, the self-impedance matrix $\mathbf{Z}_{11}$ in subdomain Ω_1 has changed also [2]. Especially, we have stored the self-impedance matrix of subdomain Ω_2 and Ω_3 after LU factorization in RAM, namely, unchanged portion matrix, when simulating the case shown in Fig. 1. At this time, the computation and factorization of the self-impedance matrix Z_{ii} (i=2, 3) can be avoided to save computing time. Finally, the accurate results can be obtained through iterative solution expressed by equation (9).

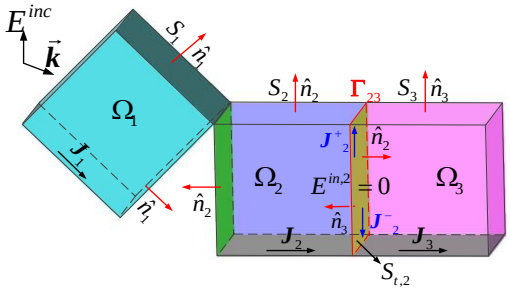

Fig. 2. Notations for domain decomposition with changeable parts.

C. Parallelization implementation on IE-NDDM

In this paper, the parallel IE-NDDM code is implemented through MPI. The flowchart of parallel IE-NDDM solving EM problems with changeable parts is shown in Fig. 3. In order to facilitate the implementation of the algorithm, the changeable parts are divided into one or more subdomains numbered 1, 2…m, during the modeling process.

First step, all parallel processes are used to set up and solve the matrix equation of a single self-domain in turn, until the calculation of all self-domains is finished. The parallel implementation in self-domain mainly involves parallel matrix filling followed by a parallel solution of the dense matrix equation. It is necessary to divide self-domain matrix into matrix blocks and distribute those blocks to different processes for the purpose of load balance. Specifically, a block-cyclic matrix distribution is adopted among processes [2]. In addition, the parallel LU decomposition is utilized as the parallel matrix equation solver for the sake of accuracy [15]. Figure 3 shows this process under the labels computing self-domain matrix.

Second step, the coupling between subdomains is calculated by looping over geometric elements between subdomains, and in consequent, the parallelization of this process could be implemented directly through distributing those geometric elements into different processes uniformly. Figure 3 shows this process under the labels with iterative process.

Third step, once the outer iterative procedure is convergent, the accurate results are obtained through superposition of far-field generated by all subdomains. Figure 3 shows this process under the labels calculating far-field.

If there are one or more changeable subdomains, the changed subdomains need to re-compute according to step 1, this process is shown in Fig. 3 under the labels re-computing changed subdomains, and then, the accurate results of new case are obtained after executing step 2 and step 3.

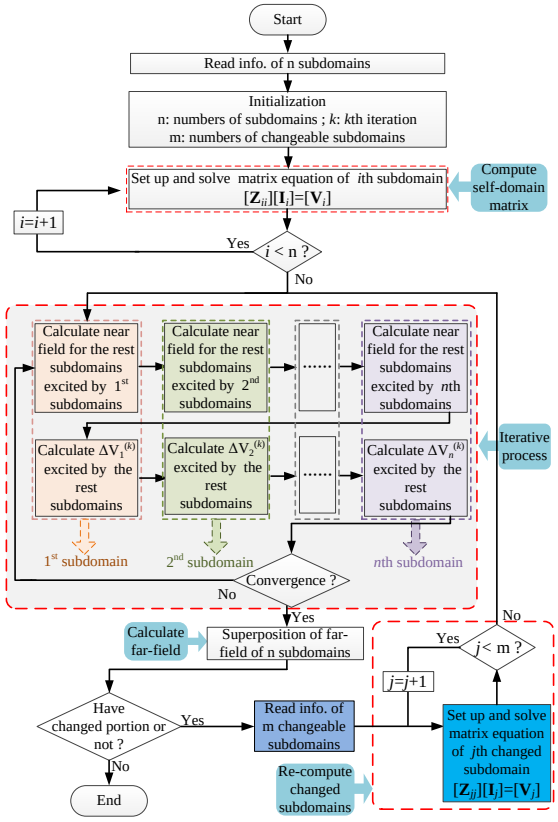

Fig. 3. Parallel framework of IE-NDDM for solving EM problems with m changeable subdomains.

III. NUMERICAL RESULTS

Three EM examples are presented to demonstrate the efficiency and accuracy of the proposed method. The residual error for outer iterative convergence is set to 1.0e–3. The two-dimensional (2D) bistatic radar cross section (RCS) of these classical cases is obtained to present the correctness and robustness of the proposed method. Two computational platforms are used in this paper [16]:

Platform I: A workstation with two six-core 64 bit Intel Xeon E5-2620 2.0 GHz CPUs, 64GB RAM and 6TB disk.

Platform II: High-Performance Computing (HPC) cluster from Xidian University (XD-HPC), which is equipped with 140 compute nodes connected by 56Gbps InfiniBand network, and each node has two 12-core Intel Xeon 2690-v2 2.2GHz CPUs and 64 GB memory.

A. Validation

The first simulation consists of the analysis of a PEC cylinder. The length of the cylinder is 10 m and the diameter is 2m. A *z*-axis polarized plane wave operating at 600MHz impinges along the *x*-axis direction is considered. In this simulation, the model is decomposed into ten subdomains as shown in Fig. 4, where each color represents one subdomain. The bistatic RCS results obtained using in-home MoM code (RWG), FEKO commercial software and IE-NDDM are given, respectively, which are used to validate the accuracy of the method proposed. The simulations are performed using the Platform I aforementioned (24 processes).

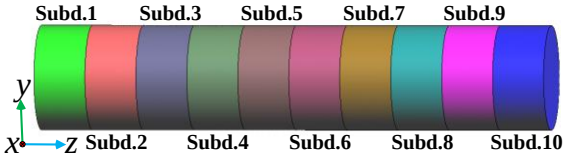

Fig. 4. Model of a cylinder divided into ten subdomains.

Figure 5 shows smooth current distributions, without noticeable discontinuities across subdomain boundaries. Figure 6 shows the RCS comparison for the proposed IE-NDDM, the in-house MoM code and FEKO. It is observed in Fig. 6 that the RCS curves agree well with each other, and the proposed IE-NDDM in this paper is verified and validated. It is observed in Fig. 7 that fast convergence rate has been achieved, which reaches 0.006 at the seventh step in outer-iterative procedure.

The computational resources for solving each subdomain and overall solution are recorded in Table 1. We can observe that the parallel IE-NDDM algorithm leads to almost 68% memory reduction, and the CPU time is greatly reduced.

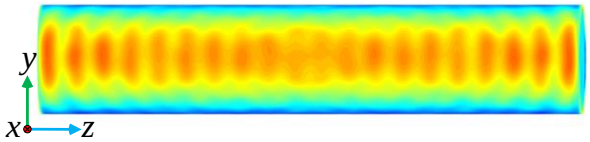

Fig. 5. Surface electric current distribution on the cylinder.

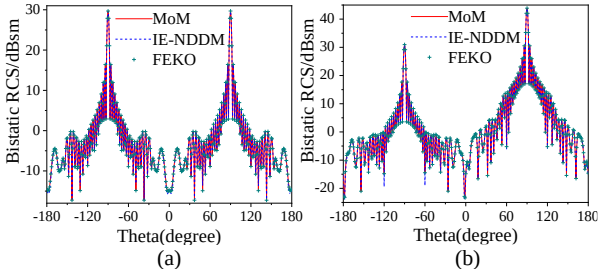

Fig. 6. Bistatic RCS curve of the cylinder: (a) *xoz* plane and (b) *yoz* plane.

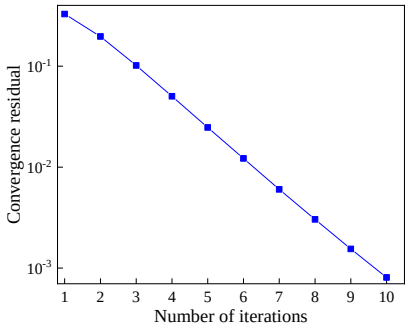

Fig. 7. Convergence curve of IE-NDDM.

Table 1: Computational resources of the cylinder

Method	Unknowns	Storage (GB)	CPU Time (h)
DDM	Subd.1 20112 Subd.2 20052 Subd.3 20055 Subd.4 20130 Subd.5 20109 Sudb.6 20106 Subd.7 20124 Subd.8 20118 Subd.9 20097 Subd.10 20097	60.20	8.886
MoM (RWG)	111636	187.71	12.731
MoM (FEKO)			14.515

B. Scattering from a tank with gun barrel rotating

In this part, the scattering characteristics of a tank with gun barrel rotating are solved to show the advantages of this method in solving local changeable parts problems. The incident plane wave propagates towards head (–*x* axis), and the polarization direction is +*z* axis. The frequency of the plane wave is 1 GHz. Dimension of the tank is 9.5m×3.2m×2.3m, and it is divided into four subdomains, as shown in Fig. 8 with each color representing one subdomain.

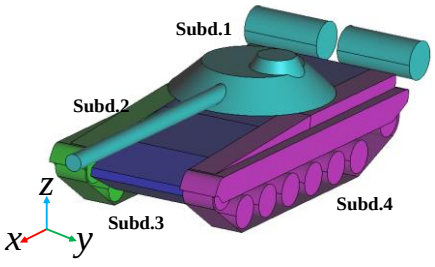

Fig. 8. Model of the tank divided into four subdomains.

The gun barrel rotates along the *z* axis, and the included angle θ_e with x-axis is 0˚, 10˚, 15˚, respectively, as shown in Fig. 9. The simulation is performed on Platform II using 30 compute nodes with each employing 24 processes (720 processes).

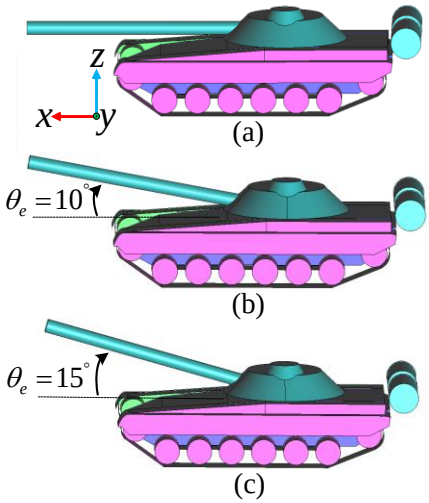

Fig. 9. Model of the tank with gun barrel at different elevation angles: (a) θ_e =0˚, (b) θ_e =10˚, and (c) θ_e =15˚, respectively.

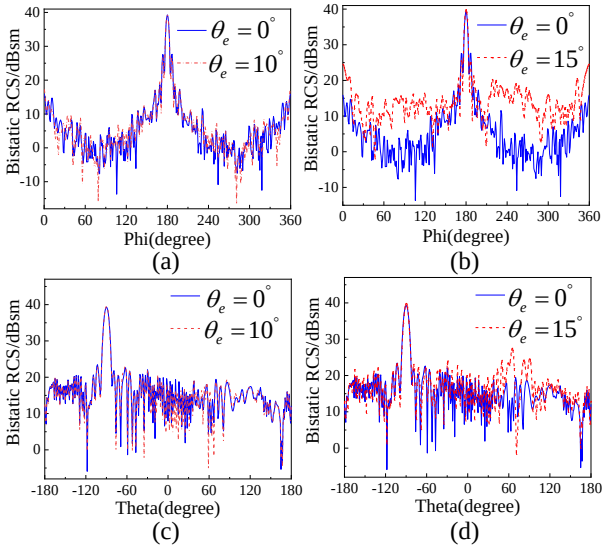

Fig. 10. 2D bistatic RCS curves of the tank with changeable parts: (a) and (b) are *xoy* plane, (c) and (d) are *xoz* plane.

The bistatic RCS results obtained by IE-NDDM are shown in Fig. 10. One can see that the maximum value of RCS remains unchanged basically, when the included angle θ_e with *x* axis is 0˚, 10˚ and 15˚, respectively. Further, RCS values shown in Fig. 10 (a) with $0^\circ \le \varphi \le 150^\circ$ and $210^\circ \le \varphi \le 360^\circ$, and shown in Fig. 10 (b) with $210^\circ \le \theta \le 360^\circ$ has changed greatly when the included angle θ_e is 15˚. The computational resources for solving each subdomain

are recorded in Table 2. It can be observed that the method proposed in this paper shows great advantage in solving scattering problems with changeable parts.

Table 2: Computational resources of the tank with gun barrel rotating

Unknowns	Storage (GB)	Posture	CPU Time (h)
Subd.1 108375 Subd.2 120397 Subd.3 150750 Subd.4 120295	945.29	Unchanged parts	2.47
		θ_e=0°	2.26
		θ_e=10°	2.26
		θ_e=15°	2.26
Overall solution 499818	3722.58	--	--

C. Scattering from an aircraft formation

In this example, the scattering characteristics of an aircraft formation with changing flying posture, an electrically large problem, has been solved by parallel IE-NDDM algorithm to further highlight the advantage of the proposed method. The model consists of five aircrafts (one bomber and four fighters), and among which the aircraft numbered I changes its flying posture. As shown in Fig. 11, the aircraft formation is divided into eleven subdomains with each color representing one subdomain, and the distances between aircrafts are given.

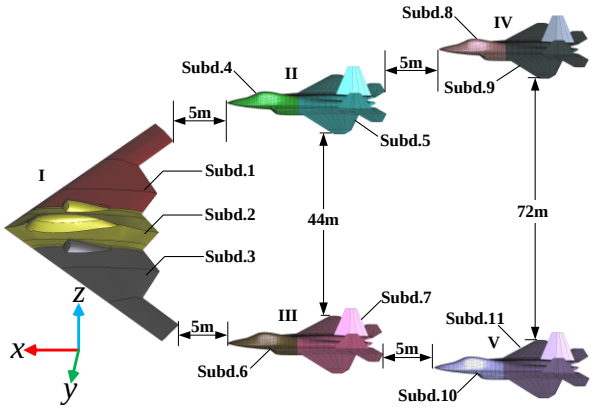

Fig. 11. Model of an aircraft formation.

Particularly, in this simulation, both connected subdomains (e.g., Sub.1 and Sub.2) and unconnected subdomains (e.g., Sub.3 and Sub.4) are included. Due to the fact that the current is discontinuous inherently between unconnected subdomains, hence, there is no need for any transmission conditions between unconnected subdomains, and only the coupling needs to be calculated in the manner of near field.

The included angle θ_e between the flying direction of the aircraft numbered I and x axis is 0°, 15°, 30°, respectively, as shown in Fig. 12. The incident plane wave is toward the nose (-x axis), and is polarized along +z axis, and the operation frequency is 300 MHz.

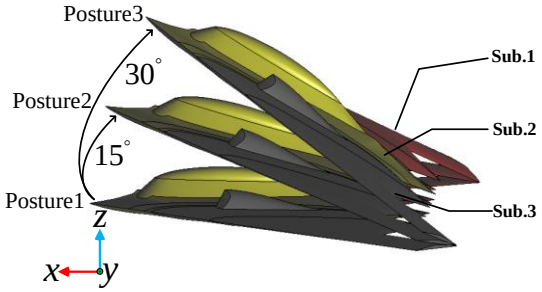

Fig. 12. Model of an aircraft I changing flying posture.

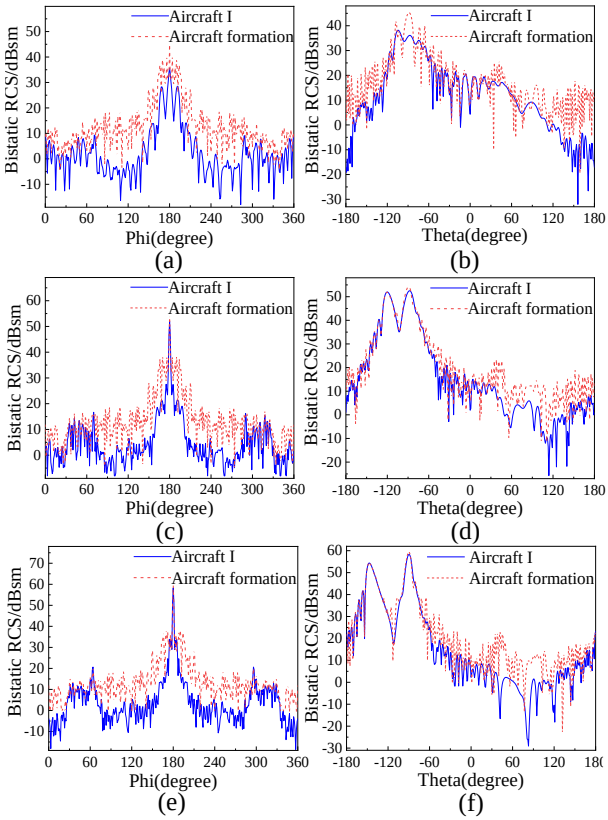

Fig. 13. 2D bistatic RCS curves of the aircraft formation with changeable parts: (a) *xoy* plane with θ_e =0° (posture1), (b) *xoz* plane with θ_e =0° (posture1), (c) *xoy* plane with θ_e =15° (posture2), (d) *xoz* plane with θ_e =15° (posture2), (e) *xoy* plane with θ_e =30° (posture3), and (f) *xoz* plane with θ_e =30° (posture3), respectively.

The simulation is performed on Platform II using 50 compute nodes with each employing 24 processes (1200 processes). The 2D bistatic RCS curves of the aircraft formation obtained by IE-NDDM are shown in Fig. 13. The computational resources for solving each subdomain

are accorded in Table 3. As shown in Fig. 13, with the elevation angle θ_e increasing, the contribution of the aircraft I to the bistatic RCS of the entire aircraft formation decreases. And the parallel IE-NDDM saves over 86.8% memory compared with MoM (overall solution).

Table 3: Computational resources of the aircraft formation

Unknowns	Storage (TB)	Posture	CPU Time (h)
Subd.1 100464 Subd.2 125853 Subd.3 100134	1.21	Unchanged parts	2.33
Subd.4 52152 Subd.5 95379		Posture1	2.9
Subd.6 52116 Subd.7 95382		Posture2	2.9
Subd.8 52122 Subd.9 95370 Subd.10 52128 Subd.11 95310		Posture3	2.9
Overall solution 793182	9.16	--	--

IV. CONCLUSION

An integral equation based on non-overlapping domain decomposition method (IE-NDDM) for the scattering analysis of PEC targets with changeable parts is proposed. A novel explicit transmission condition is applied to enforce the current continuity across adjacent subdomains, which allows the IE-NDDM keep the same level of accuracy than pure techniques such as MoM. Particularly, the coupling between different subdomains is calculated in the manner of near field, which significantly reduces the memory and CPU time. These techniques extend the capability of MoM to solve electrically large problems.

ACKNOWLEDGMENT

This work was supported in part by the National Key Research and Development Program of China under Grant 2017YFB0202102, in part by the National Science Foundation of China under Grant 61301069, in part by the China Postdoctoral Science Foundation funded project under Grant 2017M613068, in part by the National Key Research and Development Program of China under Grant 2016YFE0121600.

REFERENCES

[1] R. F. Harrington, *Field Computations by Moment Methods*. Macmillan, New York, 1968.

[2] Y. Zhang and T. K. Sarkar, *Parallel Solution of Integral Equation Based EM Problems in the Frequency Domain*. Hoboken, NJ: Wiley, 2009.

[3] J. Chen, M. Zhu, M. Wang, S. Li, and X. Li, "A hybrid MoM-PO method combining ACA technique for electromagnetic scattering from target above a rough surface," *ACES Journal*, vol. 29, no. 4, pp. 301-306, 2014.

[4] Y. Kim, H. Kim, K. Bae, J. Park, and N. Myung, "A hybrid UTD-ACGF technique for DOA finding of receiving antenna array on complex environment," *IEEE Trans. Antennas Propag*., vol. 63, no. 11, pp. 5045-5055, 2015.

[5] J. M. Song, C. C. Lu, and W. C. Chew, "Multilevel fast multipole algorithm for electromagnetic scattering by large complex object," *IEEE Trans. Antennas Propag*., vol. 45, no. 10, pp. 1488-1493, 1997.

[6] F. Hu, Z. Nie, and J. Hu, "An efficient parallel multilevel fast multipole algorithm for large-scale scattering problems," *ACES Journal*, vol. 25, no. 4, pp. 381-387, 2010.

[7] K. Han, Z. Nie, and Y. Wang, "A simply constructed overlapped domain decomposition method for solving large scattering problems," *Electromagnetics*, vol. 36, no. 7, pp. 470-484, 2016. DOI: 10.1080/02726343.2016.1220908.

[8] W. Li, W. Hong, and H. Zhou, "Integral equation-based overlapped domain decomposition method for the analysis of electromagnetic scattering of 3D conducting objects," *Microwave & Optical Technology Letters*, vol. 49, no. 5, pp. 1225-1230, 2007. DOI: 10.1002/mop.22479.

[9] W. Li, H. Zhou, J. Hu, et al., "An ODDM-based solution to CFIE with impedance boundary condition," *IEEE Antennas & Wireless Propagation Letters*, vol. 10, no. 9, pp. 1197-1200, 2011. DOI: 10.1109/LAWP.2011.2172969.

[10] Z. Peng, R. Hiptmair, Y. Shao, et al., "Domain decomposition preconditioning for surface integral equations in solving challenging electromagnetic scattering problems," *IEEE Transactions on Antennas & Propagation*, vol. 64, no. 1, pp. 210-223, 2015. DOI: 10.1109/TAP.2015.2500908.

[11] L. Gurel and O. Ergul, "Hierarchical parallelization of the multilevel fast multipole algorithm (MLFMA)," *Proc. IEEE*, vol. 101, no. 2, pp. 332-341, Feb. 2013.

[12] B. Michiels, J. Fostier, I. Bogaert, and D. De Zutter, "Full-wave simulations of electromagnetic scattering problems with billions of unknowns," *IEEE Trans. Antennas Propag*., vol. 63, no. 2, pp. 796-799, 2015.

[13] X. M. Pan, and X. Q. Sheng, "A sophisticated parallel MLFMA for scattering by extremely large targets," *IEEE Antennas Propag. Mag*., vol. 50, no. 3, pp. 129-138, June, 2008.

[14] X. M. Pan, W. C. Pi, M. L. Yang, Z. Peng, and X. Q. Sheng, "Solving problems with over one billion unknowns by the MLFMA," *IEEE Trans. Antennas Propag*., vol. 60, no. 5, pp. 2571-2574, 2012.

[15] X. Zhao, Y. Chen, H. Zhang, Y. Zhang, and T. K. Sarkar, "A new decomposition solver for complex electromagnetic problems," *IEEE Antennas Propag*. Mag., vol. 59, no. 3, pp. 131-140, 2017.

[16] A. Tzoulis and T. F. Eibert, "Efficient electromagnetic near-field computation by the multilevel fast multipole method employing mixed near-field/far-field translations," *IEEE Antennas and Wireless Propagation Letters*, vol. 4, pp. 449-452, 2005.

Zongjing Gu received the B.S. degree from ShanDong Normal University, JiNan, China, in 2013, and is currently working toward the Ph.D. degree at Xidian University. His current research interests is computational electromagnetic.

Xunwang Zhao received the B.S., and Ph.D. degrees from Xidian University, Xi'an, China, in 2004, and 2008, respectively. He joined Xidian University as a Faculty Member in 2008. As Principal Investigator, he is doing or has completed some projects including project of NSFC.

A Divergence-free Meshless Method for Transient Vector Wave Equations

Shunchuan Yang [1], Donglin Su [1], and Zhizhang (David) Chen [2]

[1] School of Electronic and Information Engineering
Beihang University, Beijing, 100083, China
scyang@buaa.edu.cn

[2] Department of Electrical and Computer Engineering
Dalhousie University, Halifax, Nova Scotia, B3H 4R2, Canada

Abstract ─ With the implementation of the vector radial basis function (RBF), which is theoretically divergence free, we propose a meshless method for solving the transient vector wave equation. Unlike the conventional radial point interpolation meshless (RPIM) method based on the scalar RBF that solves electric field and magnetic field components separately with scalar wave equations, the proposed method solves the vector wave equation directly. Therefore, the long-existing technical challenge of the source in the traditional RPIM method is resolved due to the direct solution of the vector wave equation. In addition, the stability condition of the proposed method is presented. At last, several numerical experiments are conducted to validate the accuracy of the proposed solver.

Index Terms ─ Divergence free, meshless, RPIM, vector radial basis function (RBF).

I. INTRODUCTION

Compared with the conventional numerical methods such as the finite-difference time-domain (FDTD) method, the method of moment (MOM) and the finite-element (FEM), the meshless methods have various intrinsic merits of conformal modeling, multi-scale adaptation and relatively easy node refinement. With these merits, many efforts have been made to develop various forms of the node-based meshless methods in the recent years. They include the element-free Galerkin method [1], the moving least square reproducing kernel method [2], the smoothed particle electromagnetic method [3], the radial point interpolation meshless (RPIM) method [4], the 3-D RPIM method [5] and its unconditional stable version [6]. In these meshless methods, only spatial node location information is needed to model electromagnetic problems. No connection information among nodes is required, which is the main difference between spatial nodes and discrete mesh. As a result, the re-arrangement of grid lines is no longer required when a structure is modified and refined partially.

Another issue associated with the numerical methods, especially the time-domain based numerical solvers, is the divergence property: in a continuous domain, magnetic fields are always divergence-free and so are electric fields in charge free regions. When we develop numerical methods for solving electromagnetic problems, this divergence property may or may not be preserved. Somehow this issue has been ignored in most literatures. If the divergence property is not preserved, spurious numerical solutions may emerge and lead to incorrect results [7]. Indeed, it has been found that the conventional radial point interpolation meshless (RPIM) method does not always retain this divergence-free property and spurious solutions do show up in the solutions [8].

Towards this end, the divergence-free vector-based RBFs were developed for non-electromagnetic or non-electrical applications. A matrix-valued vector RBF, which is different from the scalar RBF, was developed and proven theoretically divergence free [9]. More work was presented in [9-13]. In particular, the divergence-free vector RBF was successfully developed for Navier-Stokes equation [11,12] and astrophysical magneto-hydrodynamics (MHD) [13]. We successfully applied vector RBFs to solve Maxwell's equations with detailed discussion of the properties of the vector RBFs [14]. However, like the conventional RPIM method where all six field components are solved, the method presented in [14] still requires dual sets of the nodes (E- and H-nodes). This increases computational cost compared with other methods directly solving the wave equations.

In this paper, we propose a meshless method which is incorporated with the vector RBF for solving the full vector wave equations. We have reported our initial results in [15]. In the proposed method, only one set of field quantities (either E- or H-fields) needs to be dealt with. Therefore, it is easier to implement than the method

Submitted On: September 24, 2018
Accepted On: January 26, 2019

proposed in [14]. Since we solve the vector wave equation like the vector FEM, only **E** or **H** fields are available. For most applications, it is enough to extract the interested parameters. However, if we indeed need to another type fields, it could be quite easy to obtain through the Maxwell's equations without any troubles.

The paper is organized in the following manner. In Section II, detailed formulations of the proposed meshless method for the solutions of vector wave equation are described. In Section III, the stability condition of the proposed method is presented. In Section IV, accuracy of the proposed method is verified with numerical examples. Finally, the conclusion is drawn in Section V.

II. THEORY

Without losing the generality, we consider the general second-order vector wave equation for the electrical field in a lossless medium:

$$\nabla\times\frac{1}{\mu_r}\nabla\times\mathbf{E}(\mathbf{r},t)+\frac{\varepsilon_r}{c_0^2}\partial_t^2\mathbf{E}(\mathbf{r},t)=-\mu_0\partial_t\mathbf{J}(\mathbf{r},t), \quad (1)$$

where **E**(**r**,t) is the electric field, **J**(**r**,t) is the current density, ε is permittivity of the medium, μ_0 is the permeability of the free space, μ_r is the relative permeability of the medium.

To obtain the numerical solution of (1), a solution domain is first discretized with spatial nodes pre-defined by users. Then electric field **E**(**r**,t) is approximated in expansion with the following node-based vector shape functions:

$$\mathbf{E}=\sum_i^N\mathbf{\Phi}_i\mathbf{E}_i, \quad (2)$$

where N is the number of the scatting nodes in the local support domain, $\mathbf{\Phi}_i$ is the vector shape function associated with the node i with dimension of 3×3, $\mathbf{E}_i$ is the corresponding expansion coefficient in vector (field vector) with respect to node i and it is of the dimension of 3×1. By using (2) to approximate the electric field, we need to properly define the vector shape functions that embody the divergence-free property mentioned before.

Mathematically, a divergence free field, denoted as **u**, can always be expressed as the curl of another vector field with the definition of Coulomb gauge [11,12]:

$$\begin{aligned}\mathbf{u}&=\nabla\times\nabla\times\sum_{j=1}^N\phi(\mathbf{R}-\mathbf{R_j})\mathbf{A}_j\\&=\left(-\Delta\mathbf{I}+\nabla\nabla^T\right)\sum_{j=1}^N\phi(\mathbf{R}-\mathbf{R_j})\mathbf{A}_j\end{aligned}, \quad (3)$$

where $\nabla=\left[\frac{\partial}{\partial x},\frac{\partial}{\partial y},\frac{\partial}{\partial z}\right]^T$, ϕ is a preselected scalar basis function, $\mathbf{A}_j=\left(A_{xj},A_{yj},A_{zj}\right)^T$ is the unknown vector expansion coefficient to be determined, **I** is 3×3 identity matrix and Δ is the Laplace operator, which can be expressed as:

$$\Delta=\begin{bmatrix}\frac{\partial^2}{\partial x^2}+\frac{\partial^2}{\partial y^2}+\frac{\partial^2}{\partial z^2} & & \\ & \frac{\partial^2}{\partial x^2}+\frac{\partial^2}{\partial y^2}+\frac{\partial^2}{\partial z^2} & \\ & & \frac{\partial^2}{\partial x^2}+\frac{\partial^2}{\partial y^2}+\frac{\partial^2}{\partial z^2}\end{bmatrix}. \quad (4)$$

The scalar Gaussian radial basis function (RBF) is selected as the scalar basis function in this paper which is expressed as $\phi_j=e^{-\alpha|\mathbf{r}-\mathbf{r}_j|^2}=e^{-\alpha r^2}$, $\mathbf{r}=(x,y,z)$ is the position vector of the observation point, $\mathbf{r}_j=(x_j,y_j,z_j)$ is the position vector of node j, $r=|\mathbf{r}-\mathbf{r}_j|$ is the distance between observation node **r** and node $\mathbf{r}_j$, and α is called the shape parameter which controls the decaying rate of the RBF.

By substituting $\phi_j=e^{-\alpha|\mathbf{r}-\mathbf{r}_j|^2}=e^{-\alpha r^2}$ into (3), we can find the vector RBF $\mathbf{\Psi}_j$ related to node j, which is defined on node j, and shape function $\mathbf{\Phi}$ as:

$$\mathbf{\Psi}_j=\left(-\Delta\mathbf{I}+\nabla\nabla^T\right)\phi_j, \quad (5a)$$

$$\mathbf{\Phi}_j=\mathbf{B}_v\mathbf{A}_v^{-1}\mathbf{u}_s, \quad (5b)$$

and

$$\mathbf{u}=\sum_{j=1}^N\mathbf{\Phi}_j\mathbf{u}_j, \quad (5c)$$

where

$\mathbf{u}_s=\begin{bmatrix}....&u_{jx}&u_{jy}&u_{jz}&\cdots\end{bmatrix}^T$, $\mathbf{u}_j=\begin{bmatrix}u_{jx}&u_{jy}&u_{jz}\end{bmatrix}^T$, $\mathbf{B}_v$ includes the vector RBFs, which could be expressed as:

$$\mathbf{B}_v=\begin{bmatrix}\mathbf{\Psi}(\|\mathbf{R}_1-\mathbf{R}\|)&\mathbf{\Psi}(\|\mathbf{R}_1-\mathbf{R}\|)&\cdots&\mathbf{\Psi}(\|\mathbf{R}_1-\mathbf{R}\|)\end{bmatrix},$$

and

$$\mathbf{A}_v=\begin{bmatrix}\mathbf{\Psi}(\|\mathbf{R}_1-\mathbf{R}_1\|)&\mathbf{\Psi}(\|\mathbf{R}_1-\mathbf{R}_2\|)&\cdots&\mathbf{\Psi}(\|\mathbf{R}_1-\mathbf{R}_n\|)\\ \mathbf{\Psi}(\|\mathbf{R}_2-\mathbf{R}_1\|)&\mathbf{\Psi}(\|\mathbf{R}_2-\mathbf{R}_2\|)&\cdots&\mathbf{\Psi}(\|\mathbf{R}_2-\mathbf{R}_n\|)\\ \vdots&\vdots&&\vdots\\ \mathbf{\Psi}(\|\mathbf{R}_n-\mathbf{R}_1\|)&\mathbf{\Psi}(\|\mathbf{R}_n-\mathbf{R}_2\|)&\cdots&\mathbf{\Psi}(\|\mathbf{R}_n-\mathbf{R}_n\|)\end{bmatrix}.$$

The dimension of $\mathbf{A}_v$ is 3N×3N and $\mathbf{B}_v$ 3×3N. The dimension of the interpolation matrix for the conventional RPIM method is N×N. Therefore, the time- and memory-consumption for the construction of the vector shape function are larger than that with the conventional RPIM method for a single node. Since local RBF is usually selected so that N is relatively small. Therefore, the computational cost to construct the shape function from (5b) is relatively small compared with that of overall simulation time. In addition, only one set of electric

nodes needs to be solved and the computational efficiency of the proposed method remains reasonably high.

After expanding the (5a), we obtain the vector RBFs in terms of the scalar RBFs in reference to node *j*:

$$\boldsymbol{\Psi}_j = \begin{bmatrix} -\partial_y^2 - \partial_z^2 & \partial_x\partial_y & \partial_x\partial_z \\ \partial_y\partial_x & -\partial_x^2 - \partial_z^2 & \partial_y\partial_z \\ \partial_z\partial_x & \partial_z\partial_y & -\partial_x^2 - \partial_y^2 \end{bmatrix} \phi_j . \tag{6}$$

The detailed properties of the vector RBF and theoretical proof of their divergence properties can be found in [11]. To better understand the vector RBFs, a two dimensional vector RBF at $\boldsymbol{r}_j = [0\ 0]^T$ with $\alpha = 5$ [13] is plotted in two dimension in Fig. 1. It is easy to find that the first two rows of the vector RBF present two mutually orthogonal dipole modes: Fig. 1 (a) is the horizontal dipole mode and Fig. 1 (b) is the vertical dipole mode; rotation of one dipole leads to another. Obviously, both dipole modes are divergence free. Therefore, the field expanded by them is divergence free.

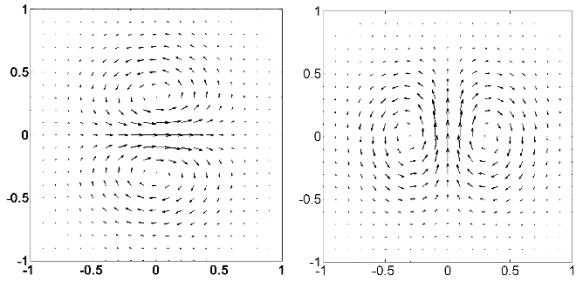

(a) The first vector (b) The second vector

Fig. 1. Vector RBF visualization with $\alpha = 5$.

Because of the vector nature of the proposed shape function, the curl operation upon the expanded fields can easily be obtained after applying the curl operator to the vector shape function. Then, we have the following results:

$$\nabla\times\boldsymbol{\Psi}_j = \begin{bmatrix} 0 & -\partial_x^2\partial_z - \partial_z^3 - \partial_y^2\partial_z & \partial_x^2\partial_y + \partial_y^3 + \partial_z^2\partial_y \\ \partial_x^2\partial_z + \partial_z^3 + \partial_y^2\partial_z & 0 & -\partial_z^2\partial_x - \partial_x^3 - \partial_y^2\partial_x \\ -\partial_x^2\partial_y - \partial_y^3 - \partial_z^2\partial_y & \partial_z^2\partial_x + \partial_x^3 + \partial_y^2\partial_x & 0 \end{bmatrix} \phi_j , \tag{7a}$$

$$\nabla\times\nabla\times\boldsymbol{\Psi}_j = \left(\partial_x^2 + \partial_z^2 + \partial_y^2\right) \begin{bmatrix} \partial_y^2 + \partial_z^2 & -\partial_x\partial_y & -\partial_x\partial_z \\ -\partial_x\partial_y & \partial_x^2 + \partial_z^2 & -\partial_z\partial_y \\ -\partial_x\partial_z & -\partial_z\partial_y & \partial_x^2 + \partial_y^2 \end{bmatrix} \phi_j . \tag{7b}$$

When the variables in the *z* direction remain constant, (7) reduce to the two-dimensional cases and it is significantly simplified. We obtain the following formulations:

$$\nabla\times\boldsymbol{\Psi}_j = \begin{bmatrix} 0 & 0 & \partial_x^2\partial_y + \partial_y^3 \\ 0 & 0 & -\partial_x^3 - \partial_y^2\partial_x \\ -\partial_x^2\partial_y - \partial_y^3 & \partial_x^3 + \partial_y^2\partial_x & 0 \end{bmatrix} \phi_j , \tag{8a}$$

$$\nabla\times\nabla\times\boldsymbol{\Psi}_j = \left(\partial_x^2 + \partial_y^2\right) \begin{bmatrix} \partial_y^2 & -\partial_x\partial_y & 0 \\ -\partial_x\partial_y & \partial_x^2 & 0 \\ 0 & 0 & \partial_x^2 + \partial_y^2 \end{bmatrix} \phi_j . \tag{8b}$$

With the well-defined vector shape function and spatial placement of the nodes in the solution domain, we can solve the vector wave equation (1) with the proposed vector-based meshless method. By substituting (2) into (1), we get the semi-discretized vector wave equation:

$$\nabla\times\frac{1}{\mu_r}\nabla\times\sum_i^N \boldsymbol{\Phi}_i\mathbf{E}_i + \frac{\varepsilon_r}{c_0^2}\partial_t^2\sum_i^N \boldsymbol{\Phi}_i\mathbf{E}_i = -\mu_0\partial_t\mathbf{J} . \tag{9}$$

To make (9) practical for computation, the collocation approach is applied to (9), which means that we test (9) with Dirac Delta function associated centered at node *i*. Due to the Kroneckor's delta property of the shape function [14], we obtain the semi-discretized formulation:

$$\left(\nabla\times\frac{1}{\mu_r}\nabla\times\sum_j^N \boldsymbol{\Phi}_j\mathbf{E}_j\right)\Bigg|_{node_i} + \frac{\varepsilon_r}{c_0^2}\partial_t^2\mathbf{E}_i = -\mu_0\partial_t\mathbf{J}\Big|_{node_i} . \tag{10}$$

By applying the central finite difference in the time domain to (9), we reach the final time-marching formulation:

$$\mathbf{E}_i^{n+1} = 2\mathbf{E}_i^n - \mathbf{E}_i^{n-1} - \frac{c_0^2\Delta t^2}{\varepsilon_r}\left(\nabla\times\frac{1}{\mu_r}\nabla\times\sum_j^N \boldsymbol{\Phi}_j\mathbf{E}_j^n\right)\Bigg|_{node_i} - \frac{\Delta t^2}{\varepsilon}\partial_t\mathbf{J}\Big|_{node_i}^n . \tag{11}$$

To make (11) more compact, we split and compute (11) in two steps:

$$\mathbf{Q}_i^{n+1} = \mathbf{Q}_i^n - \frac{\Delta t^2}{\mu_0\varepsilon}\left(\nabla\times\frac{1}{\mu_r}\nabla\times\sum_j^N \boldsymbol{\Phi}_j\mathbf{E}_j^n\right)\Bigg|_{node_i} - \frac{\Delta t^2}{\varepsilon}\partial_t\mathbf{J}\Big|_{node_i}^n , \tag{12a}$$

$$\mathbf{E}_i^{n+1} = \mathbf{Q}_i^{n+1} + \mathbf{E}_i^n , \tag{12b}$$

where **Q** is the intermediate vector introduced to speed up the computation. (11) is a vector form that can be directly solved without the need to expand the Maxwell's equations into six scalar partial derivative equations for six field components (unlike what is done with the conventional methods).

With the conventional RPIM method and the FDTD method, the vector field equations are expanded into separate scalar wave equations and numerical methods are adopted and applied to solve each of the scalar equations, respectively; this poses a technical challenge when the current source or charges are encountered: field components need to be coupled and computed with nonzero divergence at source points or charge locations. However, now with the proposed meshless method based on the divergence-free vector RBFs, the issue no longer exists since a source term is incorporated into (11) and the wave equations are solved in a coupled vector manner.

When compared with the conventional time-domain

finite-element method, the proposed meshless method is a node-based solver where only the spatial locations of the nodes that discretize the solution domain need to be known; in other words, the node-based property of the meshless methods is preserved including its capability of conforming and multiscale modeling.

III. STABILITY CONDITION

Since the proposed meshless method deploys explicit time-marching scheme, it is conditionally stable. We can obtain its stability condition based on the result presented in [16] for the proposed vector meshless method,

$$\Delta t \le \frac{\sqrt{|\lambda|_{\max}}}{c_0\sqrt{\rho(\mathbf{T})}}, \tag{13}$$

where λ is the eigenvalue of matrix $-\frac{\Delta t^2}{\mu_0\varepsilon}\mathbf{T}$, $\rho(\mathbf{T})$ is the spectral radius of $\mathbf{T}$ whose element is $T_{ij} = \left(\nabla\times\frac{1}{\mu_r}\nabla\times\sum_j^N \mathbf{\Phi}_j\right)\Big|_{node_i}$. We could find that T_{ij} is a function of the vector RBF corresponding to the corresponding node and material parameters, more specific, relative permeability. Therefore, the node location and material information are embodied into $\mathbf{T}$. For homogeneous media, $|\lambda|_{\max}$ = 4 can be obtained. Therefore, all temporal steps in the proposed meshless method should satisfy the following condition:

$$\Delta t \le \frac{2\varepsilon_r}{c_0\sqrt{\rho(\mathbf{T})}}. \tag{14}$$

To determine the maximum time step allowed in the proposed method, we need to evaluate the eigenvalues of $\mathbf{T}$. As stated in [5], those eigenvalues are related to the minimum node space. When a large number of nodes are involved, direct evaluation of (14) is quite time-consuming and another solution is to select an approximated time step through minimum nodal spacing in [5].

IV. NUMERICAL RESULTS

In this section, we choose several numerical experiments to validate the accuracy and convergence properties of the proposed meshless method for the vector wave equations.

A. One dimensional structure

Due to the existence of the analytical solutions of the one-dimensional cavity with perfect electric conductor (PEC), we select it for the initial verification of the proposed method. The length of the cavity is 1 meter. The initial condition of the electric field is given as $E_z = \sin(k\pi x/L)$ and the region is source free. The theoretical field distribution is given as:

$$E_z = \cos(k\pi ct/L)\cdot\sin(k\pi x/L), \tag{15}$$

where k is the mode number and L is the length of the cavity.

The nodes are selected uniformly distributed in the cavity with the distance between two neighboring nodes being 1 mm. The shape parameter is selected as 10 and the average node number in each local support domain is 7. For fair comparison, the cavity was also simulated with the FDTD with the uniform of cell size of 1mm, which implies that two method have the same number of field points. To reduce the effect of the time step on the accuracy, the time steps for the proposed meshless method and the FDTD method are selected small so that CFLN = 0.1, where CFLN is the ratio of the time step to the maximum time step allowable with the FDTD method and similar definition in two and three dimensional cases.

Figure 2 shows the field value obtained with the FDTD method and the proposed solver at 10 ns. Good agreements between the results obtained with the proposed method, the FDTD method and the analytical solution are observed. However, we can find that at the peak the proposed method can achieve more accurate solution than that of the FDTD method. Figure 3 presents the absolute error between the numerical solutions and the analytical results. At the peak the error of the proposed method is three times smaller than that of the FDTD method. It confirms that the proposed solver can obtain more accurate results than those of the FDTD method.

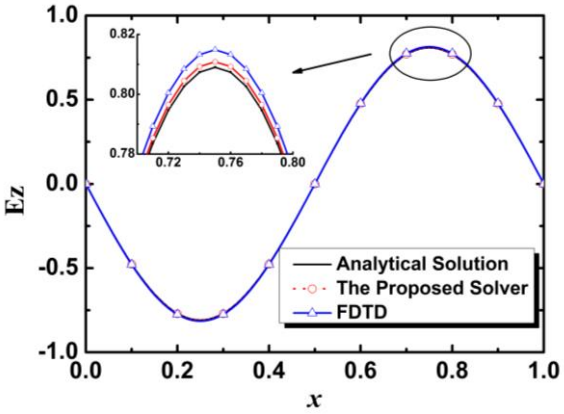

Fig. 2. The Ez field value at 10 ns.

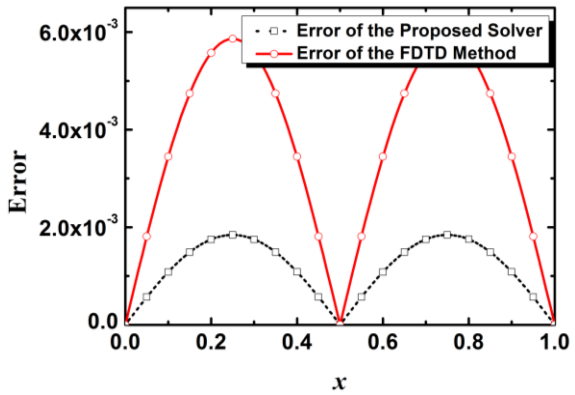

Fig. 3. The absolute solution difference between the proposed method and the FDTD method.

Figure 4 illustrates the relative L_2 error; the L_2 error is computed with the equation below:

$$L_2 = \log_{10}\left(\frac{\left\|\mathbf{E}^N - \mathbf{E}^A\right\|_2}{\left\|\mathbf{E}^A\right\|_2}\right), \tag{16}$$

where $\mathbf{E}^N$ is the numerical electrical field obtained with the FDTD method or the proposed method and $\mathbf{E}^A$ is the analytical field solution. The error of the two methods goes up as k increases. This is because that the dispersion errors increase with the mode number when the spatial discretization remains unchanged. However, the accuracy of the proposed method is about two order higher than that of the FDTD method. The reason is that the meshless method is essentially a high order method and more nodes are involved in the support domain than that of the FDTD method for each time step updating.

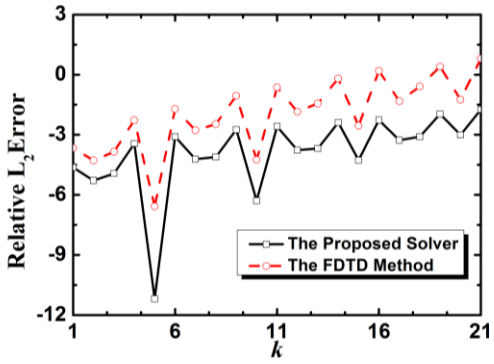

Fig. 4. The relative L2 error of the proposed solver and the FDTD method.

B. Two-dimensional structure

We also considered an air-filled perfect electric conducting (PEC) cavity with PEC boundary conditions. The cavity is a good structure for numerical validation since it embodies multiple incidences and reflections of electromagnetic waves. The dimensions of the cavity under consideration are 1 m × 1 m with uniform discretization of cell size 2 cm. The initial condition is given as:

$$E_z = \sin(m\pi x)\sin(n\pi y), \tag{17}$$

where m and n are the mode numbers in the x and y directions, respectively. The theoretical electric field inside the cavity can be expressed as:

$$E_z = \sin(m\pi x)\sin(n\pi y)\cos(\omega t), \tag{18}$$

where $\omega = c_0\pi\sqrt{m^2+n^2}$.

A small time step, CFLN=0.1, is selected again for the FDTD method and the proposed method to decrease the numerical error. The average number of the nodes considered in the local support domain is 9 and the shape parameter is selected to be 5 for Gaussian radial basis function (RBF). The distance between two nearest nodes is 0.02 m. The cell size is also 0.02m for the FDTD method. Therefore, the spatial resolutions for the proposed method and the FDTD are the same to make fair comparison.

Figure 5 shows E_z field obtained with the proposed method at 10 ns with m = 2, and n = 2 for TM_{22}. Figure 6 presents the absolute error of the results obtained with the two methods at 10 ns. The error pattern distribution of the proposed method is the same as that of the FDTD method. However, the magnitudes are smaller than those of the FDTD method. It means that the proposed method can obtain more accurate results than the FDTD method. Again, this is because the proposed meshless method is essentially a higher-order method.

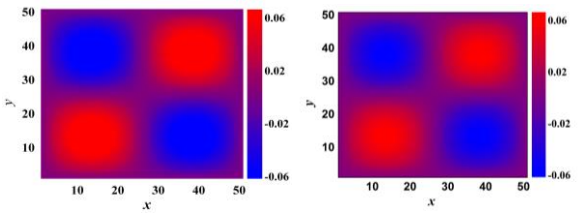

Fig. 5. The analytical field (a) and numerical value obtained from the method (b) at 10 ns.

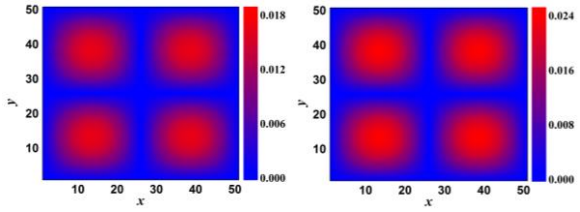

Fig. 6. The absolute error for the proposed method (a) and the FDTD method (b) at 10 ns.

Figure 7 illustrates the relative L_2 error changing with m with fixed n. It can be found that the errors of the proposed method are smaller than those of the FDTD method for all the m modes with n = 1 and n = 3. Another interesting observation is that as m increases, the L_2 errors of the two methods level off to the same value. This is because the spatial sampling density is not sufficient to capture highly-varied field distributions of the higher modes with large m and n.

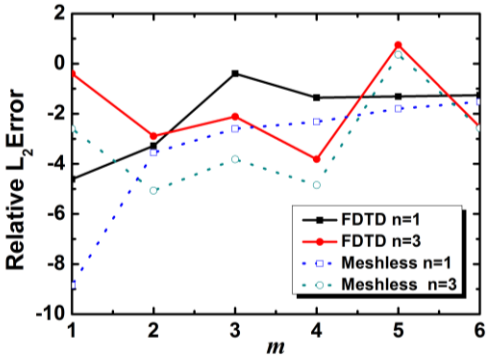

Fig. 7. The L_2 error of the proposed method and the FDTD method verse m with n=1 and n=3 at 10 ns.

C. Three-dimensional structure

In a three-dimensional case, an air-filled PEC cavity with PEC boundary condition and dimensions of 1 m × 1 m × 1 m is considered. Again the cavity is a good structure for numerical validation since it embodies multiple incidences and reflections of electromagnetic waves. The cavity is discretized with uniform discretization of cell size 0.1 m. When the same initial condition for the two-dimensional case is chosen, the exactly same analytical solution is obtained. We choose a quite small time step (CFLN=0.1) for the FDTD method and the proposed method to decrease the numerical error. Average number of the nodes in the local support domain is 16 and the shape parameter is 0.5. The distance between two nearest nodes is 0.1 m. The cell size is also 0.1m for the FDTD method to make fair comparison.

Figure 8 presents E_z field obtained from the proposed solver at 10.5 ns with m = 2, and n = 2. The field distribution is TM_{22} mode. As shown in Fig. 9, the error pattern of the proposed method is exactly the same as that of the FDTD method. However, its magnitudes are smaller than those of the FDTD method, which means that the proposed method can obtain more accurate results than the FDTD method. Again, the reason is that the proposed meshless method is a high order method.

Figure 10 presents the relative L_2 error changing with m. It can be found that the error of the proposed method is smaller than that of the FDTD method for all the m modes with n = 1 and n = 2. The relative L_2 errors of the two methods increase as m goes up. To obtain more accurate results for higher-order modes, denser nodes are required for the two methods. Another interesting observation is that for the FDTD method, the error of TM_{11} is larger than that of TM_{12} at 10. 5 ns; so is for the proposed method.

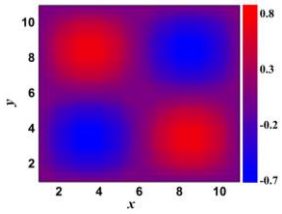

Fig. 8. The field value obtained from the proposed method at 10.5 ns.

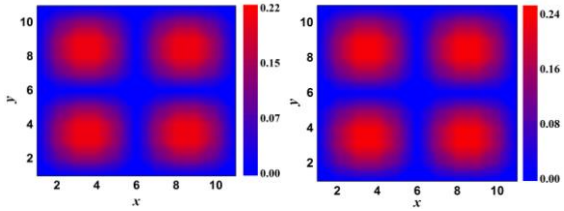

(a) (b)

Fig. 9. The absolute error for the proposed method (a) and the FDTD method (b) at 10.5 ns.

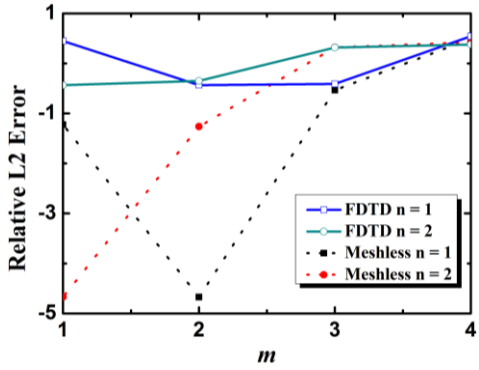

Fig. 10. The L_2 error of the proposed solver and the FDTD method verse m with n=1 and n=2 at 10.5 ns.

Figure 11 shows the charge density in dB, at z = 0.4 m, obtained from the proposed method with m = 2 and n = 2 at 10.5 ns. The charge density level is about -15 dB which is at the level of numerical noise. In other words, we can safely consider no artificial charge accumulation for the proposed method like other divergence-free methods, such as the FDTD method.

The FDTD method takes 0.42 s and 5 Mb memory to complete the simulation, however, the proposed method, takes 1.18 s and 5 Mb memory. This is because

in the proposed method more nodes are involved for field updating. However, it could be mitigated to further explore the conformal modelling and coefficient reuse when regular node distribution is used. We will explore those possibilities in the future.

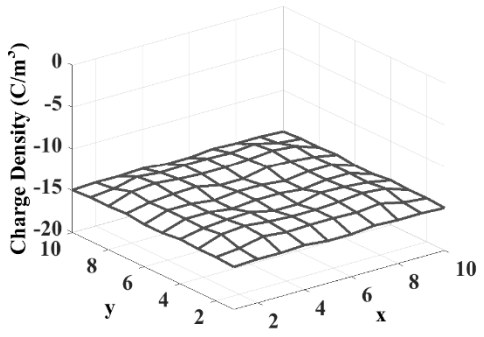

Fig. 11. The charge density at z = 0.4 m plane of the proposed solver with n=2 and m=2 at 10.5 ns. Note: charge density is in dB scale.

Some further remarks upon the proposed vector meshless method are made here: (a) as we have shown in the numerical experiments, the proposed method show the promising potential to serve as a general numerical method, like the FDTD method, but with more accurate results with the same level of discretization. (b) When certain applications, such as electron emission [17], in which the divergence properties are of significant importance are considered, the proposed method could be a better option than the traditional RPIM [5]; since the proposed method is divergence-preserved without introducing any artificial charges. (c) Another issue is how to define a good node distribution in the computational domain. Some early researches have been done in [18]. Interested readers are referred to them for more details.

Currently, we are working on development of the perfectly matched layer so that the proposed method could solve practical complex problems.

V. CONCLUSION

A vector-based meshless method is proposed for the transient electromagnetic analysis. The proposed method is based on the vector RBF and is proven to be divergence free. It solves the vector wave equation directly rather than the corresponding scalar wave equations separately. Therefore, only one set of field quantities (either E- or H-fields) needs to be solved. Its numerical accuracy and convergence properties are investigated through numerical experiments and compared with the analytical solutions. The numerical results reveal that the proposed method offers higher numerical accuracy than the FDTD method with the same level of discretization density.

VI. APPENDIX

The fourth order partial derivative of the Gausses RBF is expressed as:

$$\partial_{xxxx}\phi = \left(12a^2 - 40a^3x^2 + 16a^4x^4\right)\exp\left[-a\left(x^2+y^2+z^2\right)\right], \quad (A1)$$

$$\partial_{xxxy}\phi = -2ay\left(12a^2x - 8a^3x^3\right)\exp\left[-a\left(x^2+y^2+z^2\right)\right], \quad (A2)$$

$$\partial_{xxyy}\phi = \left(4a^2x^2 - 2a\right)\left(4a^2y^2 - 2a\right)\exp\left[-a\left(x^2+y^2+z^2\right)\right], \quad (A3)$$

$$\partial_{xxxz}\phi = -2az\left(12a^2x - 8a^3x^3\right)\exp\left[-a\left(x^2+y^2+z^2\right)\right], \quad (A4)$$

$$\partial_{xxyz}\phi = 4a^2yz\left(4a^2x^2 - 2a\right)\exp\left[-a\left(x^2+y^2+z^2\right)\right], \quad (A5)$$

$$\partial_{xxzz}\phi = \left(4a^2x^2 - 2a\right)\left(4a^2z^2 - 2a\right)\exp\left[-a\left(x^2+y^2+z^2\right)\right], \quad (A6)$$

where $\phi = \exp\left[-a\left(x^2+y^2+z^2\right)\right]$.

Other entities can be achieved by cyclic permutation of *x*,*y*,*z*.

Let $\mathbf{M} = \nabla\times\nabla\times\mathbf{\Psi}_j$, the entities of $\mathbf{M}$ are shown below:

$$\mathbf{M}_{11} = \left(\partial_x^2\partial_y^2 + \partial_x^2\partial_z^2 + \partial_z^2\partial_y^2 + \partial_z^4 + \partial_y^4 + \partial_y^2\partial_z^2\right)\phi_j, \quad (A7)$$

$$\mathbf{M}_{12} = -\left(\partial_x^3\partial_y + \partial_z^2\partial_x\partial_y + \partial_x\partial_y^3\right)\phi_j, \quad (A8)$$

$$\mathbf{M}_{13} = -\left(\partial_x^3\partial_z + \partial_x\partial_z^3 + \partial_x\partial_z\partial_y^2\right)\phi_j, \quad (A9)$$

$$\mathbf{M}_{22} = \left(\partial_y^2\partial_x^2 + \partial_z^2\partial_x^2 + \partial_z^2\partial_y^2 + \partial_x^4 + \partial_z^4 + \partial_y^2\partial_z^2\right)\phi_j, \quad (A10)$$

$$\mathbf{M}_{23} = -\left(\partial_z\partial_y^3 + \partial_z^3\partial_y + \partial_z\partial_y\partial_x^2\right)\phi_j, \quad (A11)$$

$$\mathbf{M}_{31} = \mathbf{M}_{13}, \quad (A12)$$

$$\mathbf{M}_{32} = \mathbf{M}_{32}, \quad (A13)$$

$$\mathbf{M}_{33} = \left(\partial_x^2\partial_y^2 + \partial_y^2\partial_x^2 + \partial_z^2\partial_x^2 + \partial_x^4 + \partial_y^4 + \partial_z^2\partial_y^2\right)\phi_j. \quad (A14)$$

ACKNOWLEDGMENT

The authors would appreciate the financial support from the National Natural Science Foundation of China under Grant 61427803 and Grant 61761017.

REFERENCES

[1] V. Cingoski, N. Miyamoto, and H. Yamashita, "Element-free Galerkin method for electromagnetic field computations," *IEEE Trans. Magnetics*, vol. 34, pp. 3236-3239, 1998.

[2] S. A. Viana and R. C. Mesquita, "Moving least square reproducing kernel method for electromagnetic field computation," *IEEE Trans. Magnetics*, vol. 35, pp. 1372-1375, 1999.

[3] G. Ala, E. Francomano, A. Tortorici, E. Toscano, and F. Viola, "Smoothed particle electromagnetics: A mesh-free solver for transients," *J. Comput. and Applied Math.*, vol. 191, pp. 194-205, 2006.

[4] T. Kaufmann, C. Fumeaux, and R. Vahldieck, "The meshless radial point interpolation method for time-domain electromagnetics," *IEEE MTT-S International Microwave Symposium Digest*, pp.

61-64, 2008.

[5] Y. Yu and Z. Chen, "A 3-D radial point interpolation method for meshless time-domain modeling," *IEEE Trans. Microw. Theory Tech.*, vol. 57, pp. 2015-2020, 2009.

[6] Y. Yu and Z. Chen, "Towards the development of an unconditionally stable time-domain meshless method," *IEEE Trans. Microw. Theory Tech*., vol. 58, pp. 578-586, 2018.

[7] B. Jiang, J. Wu, and L. A. Povinelli, "The origin of spurious solutions in computational electromagnetics," *J. Comput. Physics*, vol. 125, pp. 104-123, 1996.

[8] T. Kaufmann, C. Engstrom, C. Fumeaux, and R. Vahldieck, "Eigenvalue analysis and longtime stability of resonant structures for the meshless radial point interpolation method in time domain," *IEEE Trans. Microw. Theory and Tech*., vol. 58 , pp. 3399-3408, 2010.

[9] S. Lowitzsch, "Matrix-valued radial basis functions: Stability estimates and applications," *Advances Comput. Math*., vol. 23, pp. 299-315, 2005.

[10] S. Lowitzsch, "A density theorem for matrix-valued radial basis functions," *Numerical Algorithms*, vol. 39, pp. 253-256, 2005.

[11] S. Lowitzsch, "Approximation and Interpolation Employing Divergence-free Radial Basis Functions with Applications," *Ph.D. Dissertation*, Texas A&M University, 2002.

[12] H. Wendland, "Divergence-free kernel methods for approximating the Stokes problem," *Society for Industrial and Applied Mathematics Journal on Numerical Analysis*, vol. 47, pp. 3158-3179, 2009.

[13] C. P. McNally, "Divergence-free interpolation of vector fields from point values–exact $\nabla \cdot B=0$ in numerical simulations," *Monthly Notices of the Royal Astronomical Society: Letters*, vol. 413, pp. L76-L80, 2011.

[14] S. Yang, Z. Chen, Y. Yu, and S. Ponomarenko, "A divergence-free meshless method based on the vector basis function for transient electromagnetic analysis," *IEEE Trans. Microw. Theory Tech*., vol. 62, pp. 1409-1416, 2014.

[15] J. Zhang, J. Lu, Y. Liu, and S. Yang, "A vector meshless method for transient vector wave equations," *2018 International Appl. Comp. Electro. Society (ACES) Symp.*, Aug. 2018.

[16] D. Jiao and J. Jin, "A general approach for the stability analysis of the time-domain finite-element method for electromagnetic simulations," *IEEE Trans. Antena. Propag.*, vol. 50, pp. 1624-1632, 2002.

[17] D. Smithe, J. Cary, and J. Carlsson, "Divergence preservation in the ADI algorithms for electromagnetics," *J. Comput. Phys.*, vol. 228, pp. 7289-7299, 2009.

[18] O. Vlasiuk, T. Michaels, N. Flyer, and B. Fornberg, "Fast high-dimensional node generation with variable density," *Computers & Mathematics with Applications*, vol. 76, no. 7, pp. 1739-1757, 2018.

Shunchuan Yang received the B.S., M. S. and Ph.D. degrees from Sichuan University, China, in 2009, Zhejiang University, China, in 2012, and Dalhousie University, Canada, in 2015, respectively. Yang joined Beihang University as an Associate Professor in 2017. His research interests include development of advanced numerical methods for computational electromagnetics (CEM) both in time and frequency domains and their applications in integrated circuits modeling, multiphysics and complex media modeling. Yang was a recipient of Killam Awards of Dalhousie University in 2014 and Chinese Government Award for Outstanding Self-financed Students Abroad in 2013.

Donglin Su received the B.S., M.S., and Ph.D. degrees in Electronic Engineering from Beihang University (BUAA), Beijing, China, in 1983, 1986, and 1999, respectively. In 1986, she joined the Faculty of School of Electronics and Information Engineering, BUAA, where she is currently a Full Professor. Her research interests include the numerical methods for microwave and millimeter-wave integrated circuits and systematic electromagnetic compatibility design of various aircrafts.

She is a senior member of the Chinese Institute of Electronics. She is the General Chair of 2018 International ACES Symposium and the Chair of Beijing Chapter of the IEEE Antennas and Propagation Society and the Deputy Chair of the Antennas Society, Chinese Institute of Electronics.

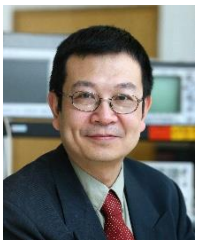

Zhizhang (David) Chen received the Master degree in Radio Engineering from Southeast University, P. R. China, the Ph.D. degree in Electrical Engineering from the University of Ottawa, Canada. He was a NSERC Post-doctoral Fellow with McGill University, Montreal, Canada, in 1993. He is currently a Professor with Dalhousie University, Halifax, Nova Scotia, Canada, where he had also served as the Head of the Department of Electrical and Computer Engineering. He has been

an Adjunct or Visiting Professor with the University of Nottingham of UK, École Nationale Supérieure des Télécommunications de Bretagne of France, Shanghai Jiao Tong University, Beijing University of Aeronautics and Astronautics, Fuzhou University, Hong Kong University of Science and Technology and the University of Electronic Science and Technology of China.

Chen has authored and co-authored over 370 journal and conference papers in computational electromagnetics, RF/microwave electronics, antennas, and wireless technologies. He was one of the originators of the unconditionally stable methods that have been highly cited and used. He and his team also developed a number of nonlinear ultra-wideband receivers and planar wireless power transfer transmitting and receiving structures.

He has been an Associate Editor of the recently founded IEEE Journal on Multiscale and Multiphysics Computational Techniques (2016-2019) and Guest Editors of several professional journals and magazines. He has been invited to give many invited talks and plenary speeches at various international meetings, conferences and forums. He was also involved in organizing in many international workshops and conferences as Chair, Co-Chair, session organizer and committee members. His current research interests are in time-domain electromagnetic modeling techniques, ultra-wideband wireless communication systems and wireless power transfer. He received of the 2005 Nova Scotia Engineering Award, a 2006 Dalhousie graduate teaching award, the 2007 & 2015 Dalhousie Faculty of Engineering Research Award, the 2013 IEEE Canada Fessenden Medal and Dalhousie University Professorship. He is the Fellow of the IEEE, the Canadian Academy of Engineering and the Engineering Institute of Canada.

A Hybrid Approach for Rapid Computation of Monostatic Radar Cross Section Problems with Characteristic Basis Function Method and Singular Value Decomposition

Wenyan Nie [1] and Zhonggen Wang [2*]

[1] School of Mechanical and Electrical Engineering
Huainan Normal University, Huainan, 232001, China
wynie5240@163.com

[2] School of Electrical and Information Engineering
Anhui University of Science and Technology, Huainan, 232001, China
*zgwang@ahu.edu.cn

Abstract ─ Characteristic basis function method (CBFM) is one of the effective methods to analyze wide-angle electromagnetic scattering characteristics of objects. In the general CBFM, a mass of plane waves is required to construct the characteristic basis function (CBFs) for a large-scale target resulting in a large number of CBFs. Furthermore, the accuracy cannot be further enhanced via general method by increasing the number of incident plane waves to obtain adequate CBFs. In order to alleviate these problems, a hybrid approach is proposed for fast computation of monostatic radar cross section of objects. The proposed method applies the singular value decomposition to compress the excitation matrix and introduces a new method to construct the CBFs considering the mutual interaction among blocks. Under such circumstances, the number of matrix equation solutions and the number of CBFs are both significantly reduced. Thus, the time of constructing CBFs and the complexity of reduced matrix both are reduced. Numerical examples verify and demonstrate that the proposed method is credible both in terms of accuracy and efficiency.

Index Terms ─ Characteristic basis function method, characteristic basis functions, radar cross section, singular value decomposition.

I. INTRODUCTION

The method of moments (MoM) [1] is known as an effective method to solve electromagnetic scattering problems. However, it imposes a great burden on the CPU, both in terms of computational time and memory requirement when dealing with large scale scatter problems. Fortunately, a variety of acceleration algorithms have been proposed to relieve these problems, such as the fast multipole method (FMM) [2], the adaptive integral method (AIM) [3], the multilevel fast multipole method (MLFMM) [4], the adaptive cross approximation (ACA) algorithm [5], the domain decomposition method [6, 7] and the fast dipole method (FDM) [8]. These methods have advantages in matrix-vector products (MVPs) and can handle large number of unknowns. However, most of above mentioned approaches are not appropriate for obtaining accurate monostatic radar cross section (RCS) analysis. To over this problem, many efforts have been devoted to the fast solution of monostatic RCS [9-11]. However, these methods need to use iteration method to solve liner equations which can lead to convergence difficulties when dealing with an ill-conditioned matrix.

Recently, the characteristic basis function method (CBFM) [12, 13] has been proposed that the entire scatter is divided into several blocks and each block can be solved as an independent domain. The size of the impedance matrix of the CBFM is much smaller than that of the MoM because the number of characteristic basis functions (CBFs) is smaller than the RWGs. It can be performed using the direct method for the matrix calculation; it is therefore suitable for multiple right hand-sides problem, such as monostatic RCS analysis. However, the construction of the CBFs relies on adequate incident plane waves (PWs) excited. The number of CBFs is increased with increase in the size of analysis target, which will cause more time consumption in singular value decomposition (SVD). Besides, it will be difficult to solve and store the reduced matrix directly. Under this condition, few hybrid methods have been proposed. The multilevel characteristic basis function method (MLCBFM) has been introduced in [14] to reduce the number of unknowns by applying CBFM recursively. In [15], the MLFMM is combined with the CBFM to efficiently calculate the reduced matrix. In

Submitted On: October 7, 2018
Accepted On: February 21, 2019

[16], improved primary CBFs (IPCBFs) are proposed to decrease the number of the CBFs. In [17-19], the high level CBFs are calculated by fully considering the mutual coupling effects among the sub-blocks, but the total number of CBFs is increased. To some extent, these methods save time and reduce the storage requirement. However, the number of incident PWs in these methods is always overestimated and the redundant PWs will increase the calculation time both in terms of the CBFs construction and the reduced matrix calculation. In this paper, a hybrid CBFs construction method is presented. Firstly, the SVD procedure is utilized to remove the redundancy in the excitation PWs before calculating the CBFs. Secondly, the improved CBFs (ICBFs) are obtained by considering the couple effects among the blocks. Since the ICBFs contain the information of the primary CBFs (PCBFs) and the secondary level CBFs (SCBFs), the number of CBFs of each block will be reduced significantly that will further minimize the reduced matrix, hence the calculation time is also cut down. The efficiency of the proposed method is demonstrated using several examples in the paper.

II. CHARACTERISTIC BASIS FUNCTION METHOD

The CBFM divides the target into M blocks and each block is solved as an independent domain by using the CBFs [12, 13]. For each block, the CBFs can be obtained from Eq. (1):

$$\mathbf{Z}_{ii}^{e} \cdot \mathbf{J}_i^{\mathrm{CBFs}} = \mathbf{V}_i^{N_{\mathrm{pws}}} \quad (i = 1, 2, \cdots, M), \tag{1}$$

where $\mathbf{Z}_{ii}^{e}$ denotes the self-impedance of the extended block i, with dimensions of $N_i^{eb} \times N_i^{eb}$. The N_i^{eb} represents the number of unknown belonging to the extended block i and $\mathbf{V}_i^{N_{\mathrm{pws}}}$ is the excitation matrix with dimensions of $N_i^{eb} \times N_{\mathrm{pws}}$, the N_{pws} is the number of incident PWs. To eliminate the redundant information in $\mathbf{J}_i^{\mathrm{CBFs}}$ caused by overestimation, the SVD is used to reduce the redundancy of the initial CBFs. Suppose, the same number B of CBFs is obtained on each block after SVD, where B is smaller than N_{pws}, the surface current of the target can be expressed as a liner combination of these CBFs as:

$$\mathbf{J} = \begin{bmatrix} \mathbf{J}_1 \\ \vdots \\ \mathbf{J}_i \\ \vdots \\ \mathbf{J}_M \end{bmatrix} = \sum_{k=1}^{B} \mathbf{a}_1^k \begin{bmatrix} \left[\mathbf{J}_1^k\right] \\ \vdots \\ [0] \\ \vdots \\ [0] \end{bmatrix} + \cdots\cdots + \sum_{k=1}^{B} \mathbf{a}_M^k \begin{bmatrix} [0] \\ \vdots \\ [0] \\ \vdots \\ \left[\mathbf{J}_M^k\right] \end{bmatrix}, \tag{2}$$

where $\mathbf{a}_i^k$ are the unknown expansion coefficients and $\mathbf{J}_i^k$ is the kth CBFs of block i. The total number of CBFs is BM and the reduced matrix equation $\mathbf{Z}^R \boldsymbol{\alpha} = \mathbf{V}^R$ can be constructed as follows:

$$\begin{bmatrix} \mathbf{Z}_{11}^R & \mathbf{Z}_{12}^R & \cdots & \mathbf{Z}_{1M}^R \\ \mathbf{Z}_{21}^R & \mathbf{Z}_{22}^R & \cdots & \mathbf{Z}_{2M}^R \\ \vdots & \vdots & \ddots & \vdots \\ \mathbf{Z}_{M1}^R & \mathbf{Z}_{M2}^R & \cdots & \mathbf{Z}_{MM}^R \end{bmatrix} \begin{bmatrix} \boldsymbol{\alpha}_1 \\ \boldsymbol{\alpha}_2 \\ \vdots \\ \boldsymbol{\alpha}_M \end{bmatrix} = \begin{bmatrix} \mathbf{V}_1^R \\ \mathbf{V}_2^R \\ \vdots \\ \mathbf{V}_M^R \end{bmatrix}, \tag{3}$$

where the $\boldsymbol{\alpha}_i = (\mathbf{a}_i^1, \mathbf{a}_i^2, \cdots, \mathbf{a}_i^B)^{\mathrm{T}}$ represent the unknown weights of the CBFs on the block i, $\mathbf{Z}_{ij}^R$ represents the interactions between blocks i and j, and $\mathbf{V}_i^R$ is the excitation vector. The $\mathbf{Z}_{ij}^R$, $\boldsymbol{\alpha}_i$ and $\mathbf{V}_i^R$ are the sub-matrices of $\mathbf{Z}^R$, $\boldsymbol{\alpha}$ and $\mathbf{V}^R$, respectively. The $\mathbf{Z}_{ij}^R$ and $\mathbf{V}_i^R$ can be generated by using Eqs. (4) and (5):

$$\mathbf{Z}_{ij}^R = \mathbf{J}_i^{\mathrm{H}} \mathbf{Z}_{ij} \mathbf{J}_j, \tag{4}$$

$$\mathbf{V}_i^R = \mathbf{J}_i^{\mathrm{H}} \mathbf{V}_i, \tag{5}$$

where the H stands for conjugated transpose, $\mathbf{Z}_{ij}$ represents the original mutual impedance matrix between the extended block i and block j, and $\mathbf{V}_i$ is the original excitation vector. After the reduced matrix $\mathbf{Z}^R$ is generated, the unknown coefficients of the CBFs $\boldsymbol{\alpha}_i$ can be obtained by solving Eq. (3). Substituting the $\boldsymbol{\alpha}_i$ into Eq. (2), the total current distribution on the surface of the target can be obtained.

III. HYBRID CBFs CONSTRUCTION METHOD

The CBFM partly realizes the time-saving and memory requirement reduction in the calculation. However, the problem of time-consuming in CBFs construction is still existed when the size of target is increased. More importantly, for large-scale monostatic problem, the accuracy cannot be further enhanced via general method, in which the accuracy is improved by increasing the number of incident PWs to obtain adequate CBFs. Thus, a hybrid approach to solve above mentioned problems is presented.

Firstly, the redundancy information in the incident PWs is fully considered. The CBFs are solved using Eq. (1), where the incident excitation $\mathbf{V}_i^{N_{\mathrm{pws}}}$ can be described as follows:

$$\mathbf{V}_i^{N_{\mathrm{pws}}} = (\mathbf{V}_i^1(\mathbf{r}_1, \mathbf{p}_1) \cdots \mathbf{V}_i^t(\mathbf{r}_t, \mathbf{p}_t) \cdots \mathbf{V}_i^{N_{\mathrm{pws}}}(\mathbf{r}_{N_{\mathrm{pws}}}, \mathbf{p}_{N_{\mathrm{pws}}})), \tag{6}$$

where $\mathbf{r}_t$ and $\mathbf{p}_t$ represent the incident direction and polarization, respectively. $\mathbf{V}_i^t(\mathbf{r}_t, \mathbf{p}_t)$ is a matrix indicating a plane wave from a direction with a polarization. However, because the shape of each block under analysis is different, the incident PWs are usually redundant. In order to reduce the redundant PWs, the SVD is applied to deal with the excitation matrix before calculating CBFs:

$$\mathbf{V}_i^{N_{\text{pws}}} = \mathbf{U}\mathbf{W}\mathbf{V}^{\text{T}}, \tag{7}$$

where $\mathbf{U}$ and $\mathbf{V}$ are orthogonal matrices of dimensions $N_i^{eb} \times N_i^{eb}$ and $N_{\text{pws}} \times N_{\text{pws}}$, respectively. $\mathbf{W}$ is an $N_i^{eb} \times N_{\text{pws}}$ diagonal matrix and the elements of the diagonal matrix are the singular values of $\mathbf{V}_i^{N_{\text{pws}}}$. The superscript T denotes the transpose operation. Setting an appropriate threshold that typically set to be 0.001, a new set of incident excitations will be obtained retaining only those with relative singular values above the threshold. Hence, a new excitation matrix named $\mathbf{V}_i^{\text{New}}$ is obtained and the number of PWs is decreased. For the sake of simplicity, we assume that all of the blocks contain the same number K of PWs. The dimension of $\mathbf{V}_i^{\text{New}}$ is $N_i^{eb} \times K$, and K is always smaller than N_{pws}. Replacing $\mathbf{V}_i^{N_{\text{pws}}}$ in Eq. (1) with $\mathbf{V}_i^{\text{New}}$, a new equation can be constructed as follows:

$$\mathbf{Z}_{ii}^e \mathbf{J}_i^p = \mathbf{V}_i^{\text{New}}. \tag{8}$$

By solving Eq. (8), K PCBFs ($\mathbf{J}_i^p$) can be obtained on each block. The total number of matrix equation solutions is $M \cdot K$, which is smaller than $M \cdot N_{\text{pws}}$ in the CBFM as $K << N_{\text{pws}}$. Compared with the general CBFM, the time required to construct the CBFs in new method is reduced.

Secondly, the couple effects among blocks are fully consider. In [18], the SCBFs are calculated subsequently using the following equations:

$$\mathbf{Z}_{ii}^e \mathbf{J}_i^{s_1} = -\sum_{j=1(j\neq i)}^{M} \mathbf{Z}_{ij} \mathbf{J}_j^p, \tag{9}$$

$$\mathbf{Z}_{ii}^e \mathbf{J}_i^{s_2} = -\sum_{j=1(j\neq i)}^{M} \mathbf{Z}_{ij} \mathbf{J}_j^{s_1}, \tag{10}$$

where $\mathbf{J}_i^{s_1}$ and $\mathbf{J}_i^{s_2}$ represent the first-level SCBFs and the second-level SCBFs, respectively. By removing the influence of the extended part, the SCBFs $\mathbf{J}_i^{s_1}$ and $\mathbf{J}_i^{s_2}$ can be obtained by solving Eq. (9) and (10) separately. Following the above described procedure, *3K* CBFs can be obtained on each block (including K $\mathbf{J}_i^p$, K $\mathbf{J}_i^{s_1}$ and K $\mathbf{J}_i^{s_2}$). In order to further reduce the number of obtained CBFs, the ICBFs is proposed by combing the PCBFs and the SCBFs. For block *i*, the transformation is defined as follows:

$$\begin{aligned}
\mathbf{Z}_{ii}^e \mathbf{J}_i^p + \mathbf{Z}_{ii}^e \mathbf{J}_i^{s_1} + \mathbf{Z}_{ii}^e \mathbf{J}_i^{s_2} &= \mathbf{Z}_{ii}^e \left(\mathbf{J}_i^p + \mathbf{J}_i^{s_1} + \mathbf{J}_i^{s_2} \right) \\
&\equiv \mathbf{Z}_{ii}^e \mathbf{J}_i^I \\
&= \mathbf{V}_i^{\text{New}} + \mathbf{V}_i^{'} + \mathbf{V}_i^{''} \\
&= \mathbf{V}_i^{\text{New}} - \sum_{j=1(j\neq i)}^{M} \mathbf{Z}_{ij} \mathbf{J}_j^p - \sum_{j=1(j\neq i)}^{M} \mathbf{Z}_{ij} \mathbf{J}_j^{s_1},
\end{aligned} \tag{11}$$

where $\mathbf{V}_i^{'}$ and $\mathbf{V}_i^{''}$ represent the multiple scattering by the PCBFs ($\mathbf{J}_i^p$) and the SCBFs ($\mathbf{J}_i^{s_1}$) from other blocks, respectively. By solving Eq. (11), K ICBFs of block i can be obtained, the number of CBFs is further reduced. Furthermore, the $\mathbf{J}_i^I$ contains the information that represents the $\mathbf{J}_i^{s_1}$ and $\mathbf{J}_i^{s_2}$, so $\mathbf{J}_i^I$ can indicates the real current distribution in block *i*.

IV. NUMERICAL RESULTS

In this section, the hybrid method (CBFM-SVD) is applied to three test samples to demonstrate the accuracy and efficiency. All the targets are analyzed by multiple PWs with two modes of polarization, and All examples are carried out on a personal computer with an Inter (R) Core (TM) i5-6500 CPU with 3.2 GHz (only one core is used) and 16 GB RAM. The relative error *Err* is introduced and defined as follows:

$$Err = \left(\left\| \mathbf{I}_{\text{x}} - \mathbf{I}_{\text{MOM}} \right\|_2 / \left\| \mathbf{I}_{\text{MoM}} \right\|_2 \right) \times 100\%, \tag{12}$$

where $\mathbf{I}_{\text{MoM}}$ is the current coefficient vector computed by the FEKO, and $\mathbf{I}_{\text{x}}$ is the current coefficient vector computed by the CBFM or the CBFM-SVD. $\|\bullet\|_2$ represents the vector-2 norm.

First, the monostatic RCS of a perfect electric conduct (PEC) almond with the length of 252.374 mm at a frequency of 7 GHz is computed. There are 11564 triangular patches remained in the surface of almond after mesh subdivision and the number of unknowns is 27579. The entire almond is divided into 8 blocks. In the two methods, the number of incident PWs is set as $N_\theta = N_\phi = 20$, where N_θ and N_ϕ represent the number of incident PWs in the directions of θ and ϕ, respectively. The total numbers of CBFs and the relative error of two methods under different SVD thresholds are shown in Table 1. It can be seen that the relative error of the CBFM-SVD converges faster with reducing the SVD threshold, which proves that the CBFM-SVD has higher accuracy than CBFM because the presence of SCBFs. Taking into account the computational accuracy and computational efficiency of the two methods, the SVD threshold of the CBFM-SVD is selected as 0.005, and the SVD threshold of CBFM is selected as 0.001. The number of CBFs retained on each block and the size of reduced matrix are shown in Table 2. It can be seen that the number of CBFs and the dimensions of the reduced matrix are both decreased when the CBFM-SVD is used. In order to further illustrate the efficiency and accuracy of the proposed method, the comparison of relative error is shown in Fig. 1. It can be seen that the relative error of the CBFM-SVD converges faster with increase in the number of CBFs. The current coefficients of one arbitrary RWG basis with multiple incident angles, computed by the conventional CBFM and the CBFM-SVD are compared in Fig. 2, which are in good agreement. The

monostatic RCS in $\theta\theta$ polarization and $\phi\phi$ polarization calculated by using the CBFM and the CBFM-SVD are presented in Fig. 3 and Fig. 4, respectively. It can be seen from the figures that the results are coincided well with each other.

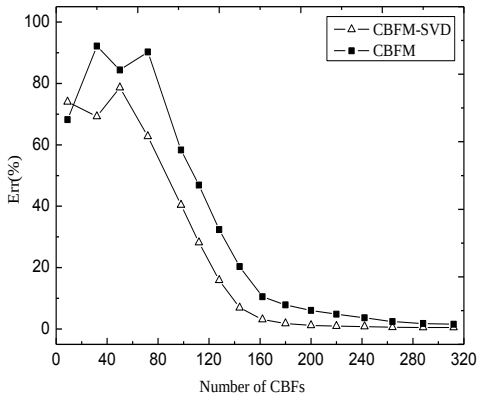

Fig. 1. The current error versus the CBFs number.

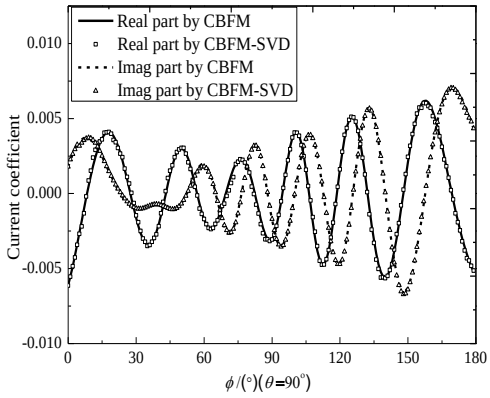

Fig. 2. Current coefficients for PEC almond.

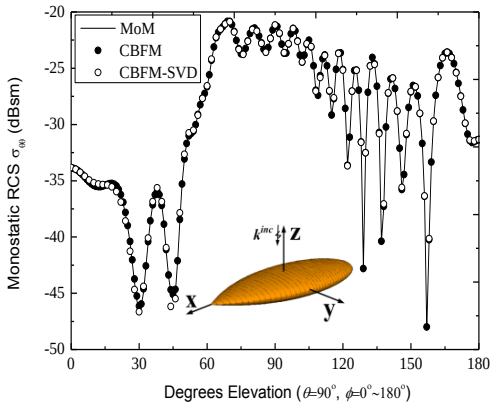

Fig. 3. The monostatic RCS of NASA in $\theta\theta$ polarization.

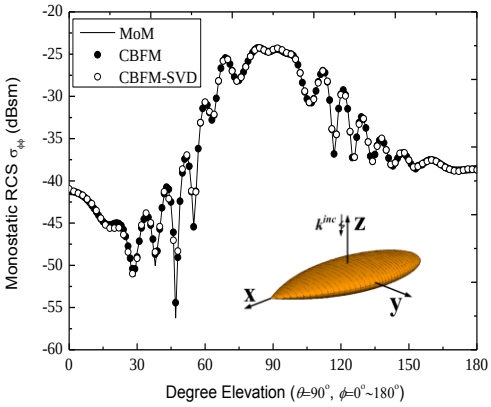

Fig. 4. The monostatic RCS of NASA in $\phi\phi$ polarization.

Then the scattering problem of a PEC cube with length of 1.2 m is presented. The frequency is 500 MHz and the cube is divided into 10 blocks. The surface of cube is discretized in 9660 triangular patches and the total number of unknowns is 24711. In the CBFM, the number of incident PWs is set as $N_\theta = N_\phi = 20$, so 800 CBFs are generated for each block and only 176 CBFs (average value) are remained via SVD. The remained CBFs are applied to construct the reduced matrix with the dimensions of 1763×1763. While in the CBFM-SVD, each block is excited by using 20 PWs in the directions of θ and ϕ. Only 127 PWs (average value) are remained resulting in 127 ICBFs for each block by using the SVD. The dimensions of reduced matrix are 1271×1271. Comparing with the CBFM, the size of matrix is further decreased. The calculation results are shown in Fig. 5 and Fig. 6, respectively. It can be seen that the results are coincided well with each other.

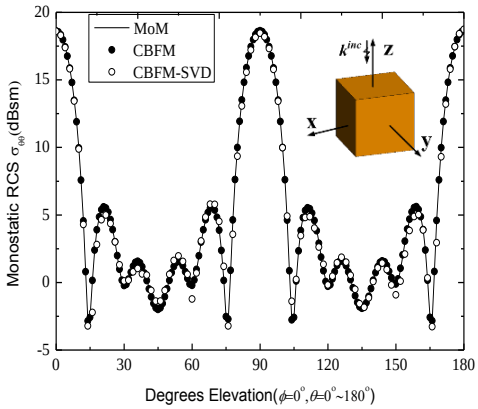

Fig. 5. The monostatic RCS of a PEC cub in $\theta\theta$ polarization.

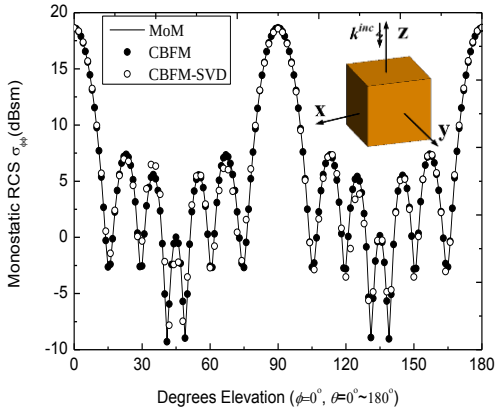

Fig. 6. The monostatic RCS of a PEC cub in $\phi\phi$ polarization.

Finally, the monostatic RCS of sixteen discrete cylinders are computed. Each cylinder has same size with height of 0.5 m and radius of 0.25 m. The frequency of incident PWs is 500 MHz and the target is divided into 16 blocks. After mesh subdivision, the surface of the objective is discretized in 20416 triangular patches and the total number of unknowns is 30624. In the CBFM, the number of incident PWs is set as $N_\theta = N_\phi = 20$. By taking advantage of SVD, the number of CBFs is reduced to 147 and the size of the reduced matrix is 2352×2352. In the CBFM-SVD, the number of incident PWs is defined as $N_\theta = N_\phi = 20$, via SVD only 111 PWs are remained resulting in 111 ICBFs for each block. In terms of the matrix size, the size of reduced matrix in the CBFM-SVD is smaller than that in the CBFM, with the dimensions of 1776×1776. The monostatic RCS in $\theta\theta$ polarization and $\phi\phi$ polarization calculated by using the CBFM and the CBFM-SVD are presented in Fig. 7 and Fig. 8, respectively. The result obtained by the CBFM-SVD agrees very well with that obtained by the CBFM.

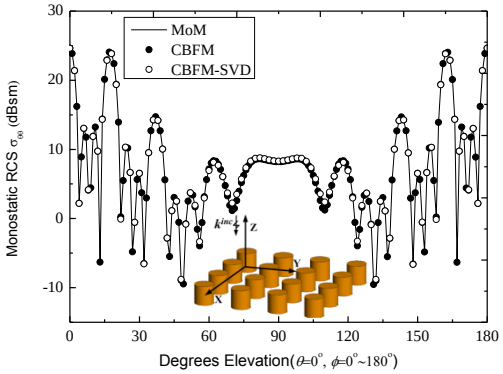

Fig. 7. The monostatic RCS of sixteen discrete cylinders in $\theta\theta$ polarization.

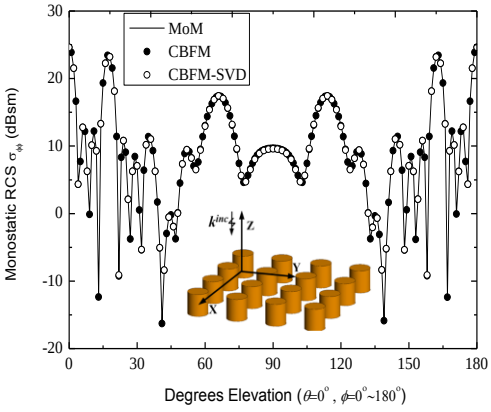

Fig. 8. The monostatic RCS of sixteen discrete cylinders in $\phi\phi$ polarization.

The calculation time of the two methods are summarized in Table 3. It can be seen that the CBFM-SVD outperforms the conventional CBFM, both in CBFs construction and in RCS computational time, the CPU time of the CBFs construction and the RCS computational time are remarkably reduced and the gains are about 38% and 22%, respectively.

VI. CONCLUSION

In this paper, a hybrid method (CBFM-SVD) is presented to efficiently compute the monostatic RCS of objects. In the proposed method, the number of required PWs has been remarkably reduced by further compression using the SVD that results in fewer matrix equation solutions. Furthermore, a novel scheme for CBFs construction is proposed by taking full consideration of the couple effects among the sub-blocks to enhance the computation accuracy. The results have validated and demonstrated that the proposed CBFM-SVD is capable of more efficiently calculating the monostatic RCS compared with the conventional CBFM without compromising the accuracy.

ACKNOWLEDGMENT

This work was supported by the Natural Science Foundation of Anhui Province under Grant No. 1808085MF166, the Anhui Provincial Key Science Foundation for Outstanding Young Talent under No. gxyq2017060, the Postdoctoral Science Foundation of Anhui Province under Grant No. 2017B214, the Overseas Visiting and Training Program for Outstanding Young Talents of Anhui Province under No. gxgwfx2018025, and the Natural Science Foundation of Anhui Provincial Education Department under Grant No. KJ2016A669.

Table 1: The total CBFs number and the relative error of two methods under different SVD threshold

SVD Threshold	CBFM		CBFM-SVD	
	Err (%)	CBFs number	*Err* (%)	ICBFs number
0.08	36.035	442	28.413	427
0.05	22.728	548	19.864	506
0.03	12.918	613	9.474	574
0.01	8.595	798	4.206	769
0.005	5.887	905	2.961	872
0.003	3.353	1073	2.323	1035
0.001	2.986	1219	2.037	1156

Table 2: The CBFs number retained on each block of two methods

Method	Block 1	Block 2	Block 3	Block 4	Block 5	Block 6	Block 7	Block 8	Size of Reduced Matrix
CBFM	124	168	185	190	180	164	130	78	1219×1219
CBFM-SVD	88	125	132	140	130	109	94	54	872×872

Table 3: The consequences of two methods comparing in different samples

Problems	Method	CBFs Construction(s)	Reduced Matrix Calculation(s)	Solving Matrix and RCS(s)	Total Time(s)
Problem 1	CBFM	2573.09	1910.68	24.92	4533.61
	CBFM-SVD	1519.02	1593.64	21.60	3155.86
Problem 2	CBFM	3205.64	2241.91	29.84	5507.23
	CBFM-SVD	1956.62	1797.64	22.84	3798.30
Problem 3	CBFM	3966.63	4299	41.57	8348.85
	CBFM-SVD	2607.51	3524.17	34.20	6200.08

REFERENCES

[1] R. F. Harrington, *Field Computation by Method of Moments*. IEEE Press, New York, NY, USA, 1992.

[2] R. Coifman, V. Rokhlin, and S. Wandzura, "The fast multipole method for the wave equation: A pedestrian prescription," *IEEE Antennas and Propagation Magazine*, vol. 53, no. 3, pp. 7-12, 1993.

[3] E. Bleszynski, M. Bleszynski, and T. Jaroszewicz, "Adaptive integral method for solving large-scale electromagnetic scattering and radiation problems," *Radio Science*, vol. 31, no. 5, pp. 1225-1251, 1996.

[4] J. M Song, C. C. Lu, and W. C. Chew, "Multilevel fast multipole algorithm for electromagnetic scattering by large complex objects," *IEEE Trans. Antennas Propag.*, vol. 45, no. 10, pp. 1488-1493, 1997.

[5] K. Zhao, M. N. Vouvakis, and J.-F. Lee, "The adaptive cross approximation algorithm for accelerated method of moments computations of EMC," *IEEE Transactions on Electromagnetic Compatibility*, vol. 47, no. 4, pp. 763-773, 2005.

[6] A. Freni, P. De Vita, P. Pirinoli, *et al.*, "Fast-factorization acceleration of MoM compressive domain-decomposition," *IEEE Trans. Antennas Propag.*, vol. 59, no. 1 2, pp. 4588-4599, 2011.

[7] J. Hu, R. Zhao, M. Tian, *et al.*, "Domain decomposition method based on integral equation for solution of scattering from very thin conducting cavity," *IEEE Trans. Antennas Propag*., vol. 62, no. 10, pp. 5344-5348, 2014.

[8] X. Chen, C. Gu, Z. Niu, Y. Niu, and Z. Li, "Fast dipole method for electromagnetic scattering from perfect electric conducting targets," *IEEE Trans. Antennas Propag*., vol. 60, no. 2, pp. 1186-1191, 2012.

[9] A. Schroder, H. D. Bruxns, and C. Schuster, "A hybrid approach for rapid computation of two-dimensional monostatic radar cross section problems with the multilevel fast multipole algorithm," *IEEE Trans. Antennas Propag*., vol. 60, no. 12, pp. 6058-6061, 2012.

[10] X. M. Pan and X. Q. Sheng, "Fast solution of linear systems with many right hand sides based on skeletonization," *IEEE Antennas Wireless Propag. Lett.*, vol. 15, no. 1, pp. 301-304, 2016.

[11] X. M. Pan, S. L. Huang, and X. Q. Sheng, "Wide angular sweeping of dynamic electromagnetic responses from large targets by MPI parallel skeletonization," *IEEE Trans. Antennas Propag.*, vol. 66, no. 3, pp. 1619-1623, 2018.

[12] E. Lucente, A. Monorchio, and R. Mittra, "An

iteration free MoM approach based on excitation independent characteristic basis functions for solving large multiscale electromagnetic scattering problems," *IEEE Trans. Antennas Propag*., vol. 56, no. 4, pp. 999-1007, 2008.

[13] V. V. S. Prakash and R. Mittra, "Characteristic basis function method: A new technique for efficient solution of method of moments matrix equations," *Microwave and Optical Technology Letters*, vol. 36, no. 2, pp. 95-100, 2003.

[14] Y. F. Sun, K. Lu, and G. H. Wang, "Analysis of electromagnetic scattering from dielectric objects using multilevel characteristic basis function method," *Chinese Journal of Radio Science*, vol. 28, no. 1, pp. 92-96, 2009.

[15] E. Garcia, C. Delgado, L. Lozano, I. Gonzalez-Diego, and M. F. Catedra, "An efficient hybrid-scheme combining the characteristic basis function method and the multilevel fast multipole algorithm for solving bistatic RCS and radiation problems," *Progress In Electromagnetics Research B*, vol. 34, pp. 327-343, 2011.

[16] T. Tanaka, Y, Inasawa, Y, Nishioka, and H. Miyashita, "Improved primary characteristic basic function method for monostatic radar cross section analysis of specific coordinate plane," *IEICE Transactions on Electronics*, vol. E99-C, no. 1, pp. 28-35, 2016

[17] G. Bianconi, C. Pelletti, and R. Mittra, "A high-order characteristic basis function algorithm for an efficient analysis of printed microwave circuits and antennas etched on layered media," *IEEE Antennas Wireless Propag. Lett.*, vol. 12, no. 12, pp. 543-546, 2013.

[18] Z. G. Wang, Y. F. Sun, and G. H. Wang, "Analysis of electromagnetic scattering from perfect electric conducting targets using improved characteristic basis function method and fast dipole method," *J. Electromagn. Waves Appl*., vol. 28, no. 7, pp. 893-902, 2014.

[19] K. Konno and Q. Chen, "The numerical analysis of an antenna near a dielectric object using the higher order characteristic basis function method combined with a volume integral equation," *IEICE Transactions on Communications*, vol. E97-B, no. 10, pp. 2066-2073, 2014.

Effective Modeling of Tunable Graphene with Dispersive FDTD - GSTC Method

Xiaofeng Du, Huan Yu, and Mengmeng Li*

Department of Communication Engineering
Nanjing University of Science and Technology, Nanjing, 210094, China
*limengmeng@njust.edu.cn

Abstract — We propose an effective method of dispersive finite difference time domain-generalized sheet transition conditions (FDTD-GSTCs) for the modeling of electromagnetic fields from tunable graphene with nearly zero thickness. To model the tunable graphene effectively, the susceptibilities are introduced instead of its physical structure, which can be extracted from reflection or transmission coefficients. In order to model the graphene in broadband, a dispersive FDTD-GSTC method is introduced by fitting the susceptibilities with respect to frequencies with the complex-conjugate pole-residue (CCPR) pairs. Numerical results demonstrate the validity of the proposed method.

Index Terms — Broadband, dispersive, finite difference time domain, grapheme.

I INTRODUCTION

Graphene has a wide range of applications due to its excellent conductivity, good thermal stability, high electron mobility, low density, promising wave absorbing material, and easy to be tunable with biasing electrostatic or a magnetostatic field [4]. To simulate it with typical three-dimensional numerical methods will lead to very low computation efficiency [5]-[10], due to its single atom thickness. To model the thin graphene layer effectively, many techniques such as the thin dielectric sheet (TDS) [5], surface impedance boundary condition [6], sub-cell discretization technique [7], and hybrid time domain implicit–explicit method [8] are widely developed.

In recent years, generalized sheet transition conditions (GSTCs) have been widely used in the analysis of electromagnetic metasurfaces [11]-[13]. In this work, we extend the GSTC for the modeling of metasurface [17] with graphene. The complex-conjugate pole-residue (CCPR) pairs method [3] is proposed to fit the dispersive susceptibility tensors for the analysis of the wideband electromagnetic property of graphene sheet.

This paper is organized as follows: Sectopm II briefly describes the FDTD-GSTC method; Section III describes the dispersive FDTD-GSTC method in detail; numerical simulations of tunable graphene in Section IV validate the proposed method. Finally, a short conclusion is given in Section V. The results of this work are initially presented at the 2018 ACES-China conference in Beijing [16].

II FDTD-GSTC METHOD

As shown in Fig. 1, the graphene is located at *xoy* plane, the boundary conditions can be written as [1], [11]:

$$\hat{z}\times\Delta\boldsymbol{H} = j\omega\boldsymbol{P}_{\parallel} - \hat{z}\times\nabla_{\parallel}M_z, \tag{1a}$$

$$\Delta\boldsymbol{E}\times\hat{z} = j\omega\mu\boldsymbol{M}_{\parallel} - \nabla_{\parallel}\left(\frac{P_z}{\varepsilon}\right)\times\hat{z}, \tag{1b}$$

$$\hat{z}\cdot\Delta\boldsymbol{D} = -\nabla\cdot\boldsymbol{P}_{\parallel}, \tag{1c}$$

$$\hat{z}\cdot\Delta\boldsymbol{B} = -\mu\nabla\cdot\boldsymbol{M}_{\parallel}, \tag{1d}$$

where $\boldsymbol{P}$ and $\boldsymbol{M}$ are the electric and magnetic surface polarization densities, respectively. $\Delta\boldsymbol{H}$ and $\Delta\boldsymbol{E}$ represent the difference of electromagnetic field on the two sides of the graphene.

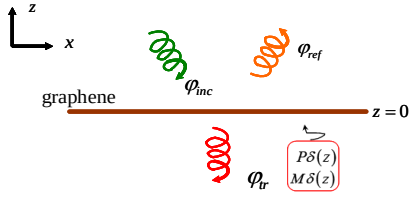

Fig. 1. Graphene located at *xoy* plane.

The electric and magnetic polarization current densities are defined as [1], [11]:

$$\boldsymbol{P} = \varepsilon\bar{\bar{\chi}}_{ee}\boldsymbol{E}_{av} + \bar{\bar{\chi}}_{em}\sqrt{\mu\varepsilon}\boldsymbol{H}_{av}, \tag{2a}$$

$$\boldsymbol{M} = \bar{\bar{\chi}}_{mm}\boldsymbol{H}_{av} + \bar{\bar{\chi}}_{me}\sqrt{\frac{\varepsilon}{\mu}}\boldsymbol{E}_{av}, \tag{2b}$$

Submitted On:October 20, 2018
Accepted On: January 26, 2019

where $\bar{\bar{\chi}}_{ee}$, $\bar{\bar{\chi}}_{em}$, $\bar{\bar{\chi}}_{me}$, and $\bar{\bar{\chi}}_{mm}$ are susceptibility tensors. $\boldsymbol{E}_{av}$ and $\boldsymbol{H}_{av}$ are the average value of electromagnetic field on the two side of the graphene.

In the particular case, we assume that the normal electric and magnetic polarization currents of graphene are zero, i.e., $P_z = 0$ and $M_z = 0$. So that the susceptibility tensors reduce to 2×2 transverse tensors. Substituting Eq. (2) into Eq. (1), we can obtain [2]:

$$\begin{pmatrix} -\Delta\tilde{H}_y \\ \Delta\tilde{H}_x \end{pmatrix} = j\omega\varepsilon \begin{pmatrix} \tilde{\chi}_{ee}^{xx} & \tilde{\chi}_{ee}^{xy} \\ \tilde{\chi}_{ee}^{yx} & \tilde{\chi}_{ee}^{yy} \end{pmatrix} \begin{pmatrix} \tilde{E}_{x,av} \\ \tilde{E}_{y,av} \end{pmatrix} + j\omega\sqrt{\mu\varepsilon} \begin{pmatrix} \tilde{\chi}_{em}^{xx} & \tilde{\chi}_{em}^{xy} \\ \tilde{\chi}_{em}^{yx} & \tilde{\chi}_{em}^{yy} \end{pmatrix} \begin{pmatrix} \tilde{H}_{x,av} \\ \tilde{H}_{y,av} \end{pmatrix}, \tag{3a}$$

$$\begin{pmatrix} \Delta\tilde{E}_y \\ -\Delta\tilde{E}_x \end{pmatrix} = j\omega\mu \begin{pmatrix} \tilde{\chi}_{mm}^{xx} & \tilde{\chi}_{mm}^{xy} \\ \tilde{\chi}_{mm}^{yx} & \tilde{\chi}_{mm}^{yy} \end{pmatrix} \begin{pmatrix} \tilde{H}_{x,av} \\ \tilde{H}_{y,av} \end{pmatrix} + j\omega\sqrt{\mu\varepsilon} \begin{pmatrix} \tilde{\chi}_{me}^{xx} & \tilde{\chi}_{me}^{xy} \\ \tilde{\chi}_{me}^{yx} & \tilde{\chi}_{me}^{yy} \end{pmatrix} \begin{pmatrix} \tilde{E}_{x,av} \\ \tilde{E}_{y,av} \end{pmatrix}, \tag{3b}$$

without loss of generality, we assume the elements are monoanisotropic and non-gyrotropic ($\tilde{\chi}_{ee}^{xy}$, $\tilde{\chi}_{ee}^{yx}$, $\tilde{\chi}_{em}^{xx}$, $\tilde{\chi}_{em}^{xy}$, $\tilde{\chi}_{em}^{yx}$, and $\tilde{\chi}_{em}^{yy}$ are equal to zero). Since the sheet is infinitesimal thin, there are no normal components of the charges and currents. As a result, the time domain expression of Eq. (3) can be simplified as:

$$J_y = \Delta H_x = \varepsilon_0 \chi_{ee}^{yy} \frac{\partial E_y}{\partial t}, \tag{4a}$$

$$J_x = \Delta H_y = \varepsilon_0 \chi_{ee}^{xx} \frac{\partial E_x}{\partial t}, \tag{4b}$$

$$K_x = \Delta E_y = \mu_0 \chi_{mm}^{xx} \frac{\partial H_x}{\partial t}, \tag{4c}$$

$$K_y = \Delta E_x = \mu_0 \chi_{mm}^{yy} \frac{\partial H_y}{\partial t}, \tag{4d}$$

where $J_p = j\omega P_p$ and $K_p = j\omega\mu_0 M_p$ with $p = x, y$ represent the polarization electric and magnetic current densities, respectively. When we insert it into the Ampere's and Faraday's laws, the FDTD updating equations as in Eq. (5) can be obtained. It can be found from Eq. (4), when the polarization susceptibilities are related to the frequencies, careful treatment of a dispersive FDTD-GSTC should be derived as will be presented in Section III.

III. DISPERSIVE FDTD-GSTC METHOD WITH CCPR PAIRS

The susceptibilitiy tensors can be extracted from the reflection and transmission coefficients [1], as a result, the susceptibility tensors are related to frequencies. In this work, the broadband susceptibilities with respect to frequencies can be fitted with the complex-conjugate pole-residue (CCPR) pairs [3]. Hence, the susceptibility tensors can be approximated as:

$$\chi(\omega) = d + \sum_{p=1}^{N} \left(\frac{c_p}{j\omega - a_p} + \frac{c_p^*}{j\omega - a_p^*} \right), \tag{6}$$

where d is a constant term, (a_p, c_p) and (a_p^*, c_p^*) are the complex-conjugate pole-residue pairs, respectively. With CCPR pairs, the polarization electric and magnetic current densities can be separated into the constant term and dispersive term:

$$\boldsymbol{J} = \boldsymbol{J}_{dis} + \boldsymbol{J}_{dis}^* + \boldsymbol{J}_{con}, \tag{7a}$$

$$\boldsymbol{K} = \boldsymbol{K}_{dis} + \boldsymbol{K}_{dis}^* + \boldsymbol{K}_{con}, \tag{7b}$$

where $\boldsymbol{J}_{con}$ and $\boldsymbol{K}_{con}$ represent constant term of electromagnetic current density. $\boldsymbol{J}_{dis}$, $\boldsymbol{J}_{dis}^*$, $\boldsymbol{K}_{dis}$ and $\boldsymbol{K}_{dis}^*$ represent two complex-conjugate pair current terms [3].

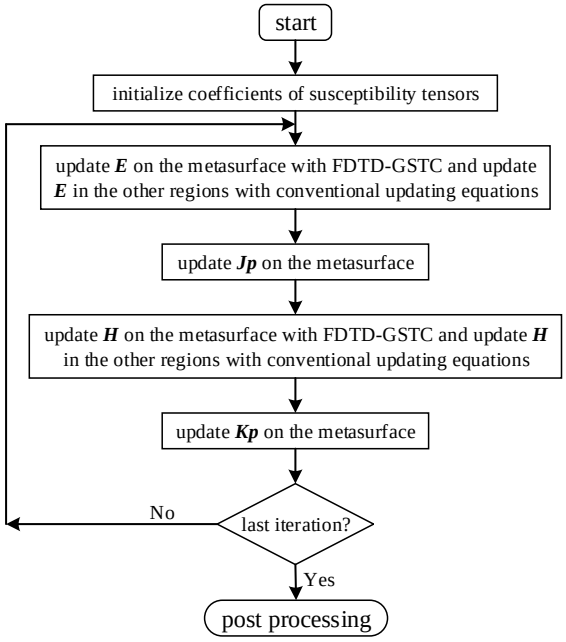

Fig. 2. A flowchart of FDTD-GSTC.

The constant term of equivalent surface currents on the graphene sheet can be solved by the traditional FDTD method [14], [15]. While the dispersive term of equivalent surface currents can be expressed by CCPR [3]:

$$\boldsymbol{J}_{p\_dis} = \varepsilon_0 \frac{c_p}{j\omega - a_p} j\omega \boldsymbol{E}, \tag{8a}$$

$$\boldsymbol{K}_{p\_dis} = \mu_0 \frac{c_{kp}}{j\omega - a_{kp}} j\omega \boldsymbol{H}. \tag{8b}$$

Assuming the graphene is located at cell of (i, j, p), Eq.

(8) in can be written in a discrete form:

$$\boldsymbol{J}_{p\_dis}^{n} = k_p \boldsymbol{J}_{p\_dis}^{n-1} + b_p \frac{\boldsymbol{E}^n - \boldsymbol{E}^{n-1}}{\Delta t}, \tag{9a}$$

$$\boldsymbol{K}_{p\_dis}^{n} = k_{kp} \boldsymbol{K}_{p\_dis}^{n-1} + b_{kp} \frac{\boldsymbol{H}^n - \boldsymbol{H}^{n-1}}{\Delta t}, \tag{9b}$$

where $k_p = \dfrac{2 + a_p \Delta t}{2 - a_p \Delta t}$, $b_p = \dfrac{\varepsilon_0 c_p 2\Delta t}{2 - a_p \Delta t}$, $k_{kp} = \dfrac{2 + a_{kp} \Delta t}{2 - a_{kp} \Delta t}$, and $b_p = \dfrac{\mu_0 c_{kp} 2\Delta t}{2 - a_{kp} \Delta t}$.

After this, we can substitute the current densities of (9) into (5), finally, the updating equation of E_y and H_y at cell (i, j, p) based on the Yee grid can be obtained as in Eqs. 10 (a) and (b). Similarly, E_x and H_x can be obtained as in Eqs. 10 (c) and (d). It should be noted here, for single layer graphene sheet without substrate $\Delta E = 0$, thus there is no need to update the magnetic equations in FDTD. The flowchart of the proposed FDTD-GSTC is shown in Fig. 2.

$$E_y^n(i,j,p) = E_y^{n-1}(i,j,p) + \frac{\Delta t}{\varepsilon_0}\left[\frac{H_x^{n-1/2}(i,j,p) - H_x^{n-1/2}(i,j,p-1)}{\Delta z} - \frac{H_z^{n-1/2}(i,j,p) - H_z^{n-1/2}(i-1,j,p)}{\Delta x}\right] - \frac{\Delta t}{\varepsilon_0}\frac{J_y(i,j,p)}{\Delta z}, \tag{5a}$$

$$H_y^{n+\frac{1}{2}}(i,j,p) = H_y^{n-\frac{1}{2}}(i,j,p) + \frac{\Delta t}{\mu_0}\left[\frac{E_z^n(i,j,p) - E_z^n(i-1,j,p)}{\Delta x} - \frac{E_x^n(i,j,p) - E_x^n(i,j,p-1)}{\Delta z}\right] - \frac{\Delta t}{\mu_0}\frac{K_y(i,j,p)}{\Delta z}, \tag{5b}$$

$$E_y^n(i,j,p) = E_y^{n-1}(i,j,p) + \frac{\Delta t}{\varepsilon_0}\frac{\varepsilon_0 \Delta z}{\varepsilon_0 \Delta z + \sum_{p=1}^{N} \mathrm{Re}(b_p) + d\varepsilon_0}\cdot\left[\frac{H_x^{n-1/2}(i,j,p) - H_x^{n-1/2}(i,j,p-1)}{\Delta z} - \frac{H_z^{n-1/2}(i,j,p) - H_z^{n-1/2}(i-1,j,p)}{\Delta x}\right]$$
$$- \frac{\Delta t}{\varepsilon_0 \Delta z}\frac{\varepsilon_0 \Delta z}{\varepsilon_0 \Delta z + \sum_{p=1}^{N} \mathrm{Re}(b_p) + d\varepsilon_0}\left[\mathrm{Re}\sum_{p=1}^{N}(1+k_p) J_{y\_dis}^{n-1}(i,j,k)\right], \tag{10a}$$

$$H_y^{n+\frac{1}{2}}(i,j,p) = H_y^{n-\frac{1}{2}}(i,j,p) + \frac{\Delta t}{\mu_0}\frac{\mu_0 \Delta z}{\mu_0 \Delta z + \sum_{p=1}^{N} \mathrm{Re}(b_{kp}) + d_k \mu_0}\cdot\left[\frac{E_z^n(i,j,p) - E_z^n(i-1,j,p)}{\Delta x} - \frac{E_x^n(i,j,p) - E_x^n(i,j,p-1)}{\Delta z}\right]$$
$$- \frac{\Delta t}{\mu_0 \Delta z}\frac{\mu_0 \Delta z}{\mu_0 \Delta z + \sum_{p=1}^{N} \mathrm{Re}(b_{kp}) + d_k \mu_0}\left[\mathrm{Re}\sum_{p=1}^{N}(1+k_{kp}) K_{y\_dis}^{n-\frac{1}{2}}(i,j,k)\right], \tag{10b}$$

$$E_x^n(i,j,p) = E_x^{n-1}(i,j,p) + \frac{\Delta t}{\varepsilon_0}\cdot\frac{\varepsilon_0 \Delta z}{\varepsilon_0 \Delta z + \sum_{p=1}^{N} \mathrm{Re}(b_p) + d\varepsilon_0}\cdot\left[\frac{H_z^{n-1/2}(i,j,p) - H_z^{n-1/2}(i,j-1,p)}{\Delta y} - \frac{H_y^{n-1/2}(i,j,p) - H_y^{n-1/2}(i,j,p-1)}{\Delta z}\right]$$
$$- \frac{\Delta t}{\varepsilon_0 \Delta z}\frac{\varepsilon_0 \Delta z}{\varepsilon_0 \Delta z + \sum_{p=1}^{N} \mathrm{Re}(b_p) + d\varepsilon_0}\left[\mathrm{Re}\sum_{p=1}^{N}(1+k_p) J_{x\_dis}^{n-1}(i,j,k)\right], \tag{10c}$$

$$H_x^{n+\frac{1}{2}}(i,j,p) = H_x^{n-\frac{1}{2}}(i,j,p) + \frac{\Delta t}{\mu_0}\frac{\mu_0 \Delta z}{\mu_0 \Delta z + \sum_{p=1}^{N} \mathrm{Re}(b_{kp}) + d_k \mu_0}\cdot\left[\frac{E_y^n(i,j,p) - E_y^n(i,j,p-1)}{\Delta z} - \frac{E_z^n(i,j,p) - E_z^n(i,j-1,p)}{\Delta y}\right]$$
$$- \frac{\Delta t}{\mu_0 \Delta z}\frac{\mu_0 \Delta z}{\mu_0 \Delta z + \sum_{p=1}^{N} \mathrm{Re}(b_{kp}) + d_k \mu_0}\left[\mathrm{Re}\sum_{p=1}^{N}(1+k_{kp}) K_{x\_dis}^{n-\frac{1}{2}}(i,j,k)\right]. \tag{10d}$$

IV NUMERICAL RESULTS

In this section, numerical simulations of graphene are shown to demonstrate the validity of the proposed dispersive FDTD-GSTC method, all the simulations are carried out on a personal computer of Intel(R) Core(TM) i3-4170 CPU with 3.7GHz and 16 GB RAM. We use Fortran to code the proposed algorithm.

A graphene with cross-shaped elements

Firstly, the graphene with cross-shaped elements is simulated, as inset in Fig. 3 (b), the dimensions of the element are: L = 48*um*, $d_1 = d_2$ = 6*um*, and the period of

the array is 60 *um*. The scattering rate of graphene sheet is 0.5 meV, the temperature is 300 K, and the biasing electric field is of 2V/nm. With the complex-conjugate pole-residue pairs method, the broadband (0.1 THz to 2 THz) susceptibilities with respect to frequencies can be fitted well as shown in Fig. 3 (a). Here, four terms are employed, and the coefficients of them are listed in Table 1, respectively.

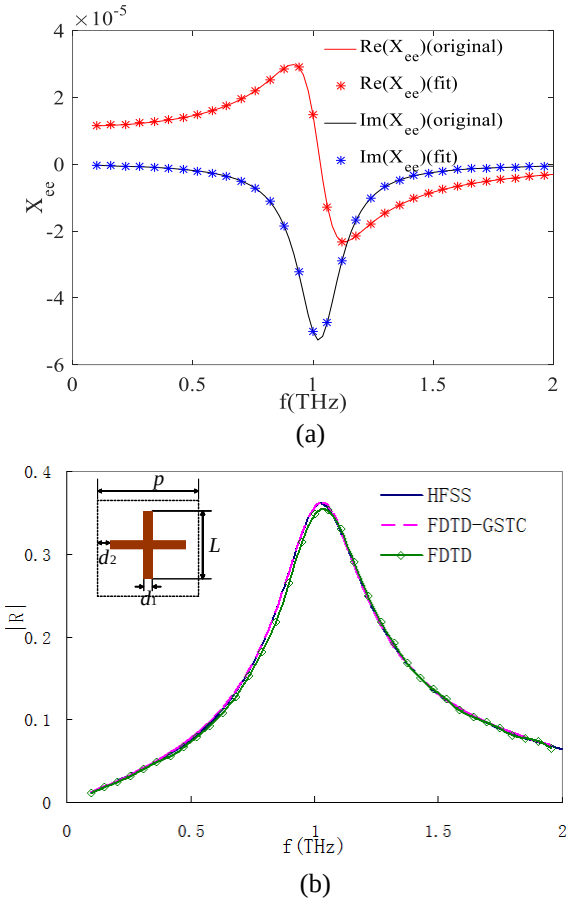

Fig. 3. Simulation of cross-shaped graphene with periodic boundary condition: (a) broadband susceptibility $\tilde{\chi}_{ee}^{xx}$ fitted by complex-conjugate pole-residue pairs, and (b) reflection coefficient by commercial software and proposed FDTD-GSTC method.

With the proposed dispersive FDTD-GSTC, the mesh size can be $dx = dy = dz = 2um$, which is much larger than conventional FDTD method [14], [15]. Figure 3 (b) plots the simulated reflection coefficients of the proposed dispersive FDTD-GSTC method and commercial software HFSS, very good agreement can be found. The simulation time and memory of FDTD and FDTD-GSTC are listed in Table 2. It can be seen that the FDTD-GSTC method requires much less number of grids and computing resources.

Table 1: Coefficients of the four terms in complex-conjugate pole-residue pairs to fit $\tilde{\chi}_{ee}^{xx} = \tilde{\chi}_{ee}^{yy}$ for the graphene sheet with cross elements (d = 4.13*e*–8)

(a_{p1}, c_{p1})	$(-1.769\times10^{12}+0j, 9.376\times10^{4}+0j)$
(a_{p2}, c_{p2})	$(-1.099\times10^{13}+0j, -4.041\times10^{6}+0j)$
(a_{p3}, c_{p3})	$(-2.866\times10^{13}+0j, 1.911\times10^{7}+0j)$
(a_{p4}, c_{p4})	$(-6.685\times10^{11}+6.217\times10^{12}j,$ $-5.575\times10^{4}-3.724\times10^{7}j)$

Table 2: Comparison of time and memory between FDTD and FDTD-GSTC

	Size of Grid (um)	Time (s)	Memory (MB)
FDTD	1×1×1	208	80
FDTD-GSTC	2×2×2	27.9	31

B graphene with asymmetrical elements

Secondly, the graphene with asymmetrical rectangular elements as inset in Fig. 4 (c) is simulated. The dimensions of the graphene element are 30*um*×18*um*, the period is 30*um*. The incident modulated Gaussian pulse is with normal propagation direction and $\hat{x}$ polarization. The scattering rate of graphene sheet is 0.96meV, the temperature is 300 K, and biasing electric field on graphene is of E = 0V/nm.

With the complex-conjugate pole-residue pairs method, the broadband (0.5 THz to 4 THz) susceptibilities $\tilde{\chi}_{ee}^{xx}$ and $\tilde{\chi}_{ee}^{yy}$ with respect to frequencies can be fitted well as shown in Figs. 4 (a) and (b). The coefficients of the four terms in complex-conjugate pole-residue pairs are listed in Tables 3 and 4.

With the proposed dispersive FDTD-GSTC, the mesh size can be $dx = dy = dz = 1um$, which is much larger than conventional FDTD method [14], [15]. The incident modulated Gaussian pulse is with normal propagation direction, Fig. 3 (c) plots the simulated reflection coefficient the proposed dispersive FDTD-GSTC method and commercial software HFSS, very good agreement can be found.

Table 3: Coefficients of the four terms in complex-conjugate pole-residue pairs to fit $\tilde{\chi}_{ee}^{xx}$ for the graphene sheet with rectangular elements (d_x = 2.94*e*–8)

(a_{p1x}, c_{p1x})	$(-3.172\times10^{10}+0j, 5.008\times10^{7}+0j)$
(a_{p2x}, c_{p2x})	$(-2.927\times10^{12}+0j, -5.269\times10^{7}+0j)$
(a_{p3x}, c_{p3x})	$(-5.9568\times10^{12}+0j, 4.524\times10^{6}+0j)$
(a_{p4x}, c_{p4x})	$(-1.141\times10^{13}+0j, -2.555\times10^{6}+0j)$
(a_{p5x}, c_{p5x})	$(-2.833\times10^{12}+3.344\times10^{13}j,$ $-4.153\times10^{5}-1.291\times10^{5}j)$

Table 4: Coefficients of the four terms in complex-conjugate pole-residue pairs to fit $\tilde{\chi}_{ee}^{yy}$ for the graphene sheet with rectangular elements ($d_y = 1.81e{-}8$)

(a_{p1y}, c_{p1y})	$(-2.341\times10^{11}+0j, 3.359\times10^{8}+0j)$
(a_{p2y}, c_{p2y})	$(-5.157\times10^{12}+0j, -4.629\times10^{7}+0j)$
(a_{p3y}, c_{p3y})	$(-1.0758\times10^{13}+0j, -2.017\times10^{7}+0j)$
(a_{p4y}, c_{p4y})	$(-1.045\times10^{12}+4.771\times10^{12}j,$ $2.147\times10^{7}-8.132\times10^{7}j)$
(a_{p5y}, c_{p5y})	$(-9.357\times10^{11}+8.878\times10^{12}j,$ $1.112\times10^{6}+2.161\times10^{6}j)$

C graphene sheet with different biasing electric fields

Thirdly, the graphene sheets with cross elements as in Section IV-A with different biasing electric fields are simulated in this part. The graphene sheet is located on the substrate with thickness of 2*um* and relative dielectric constant of 2.

As shown in Figs. 5 (a)-(c), the extracting susceptibilities ($\tilde{\chi}_{ee}^{xx} = \tilde{\chi}_{ee}^{yy}$) for the graphene sheet with biasing electrostatic field of 2 V/nm, 10 V/nm, and 20 V/nm are plotted, very good agreement between the fit and original data can be found. With the increase of static bias electric field, the peaks of reflection coefficient also gradually increase and shift to the high frequency regime as in Fig. 5 (d).

D turntable graphene sheet array

The last simulation example is a finite size graphene sheet composed of 10×10 cross elements as in Fig. 6. The observed frequencies are chosen at which the largest reflection occur, e.g., 0.9 THz, 1.18 THz, and 1.5 THz, respectively. The bistatic RCS is calculated by FDTD-GSTC and HFSS. It can be found that the results of the proposed method are in good agreement with the commercial software, while our proposed method is much more efficient as listed in Table 5.

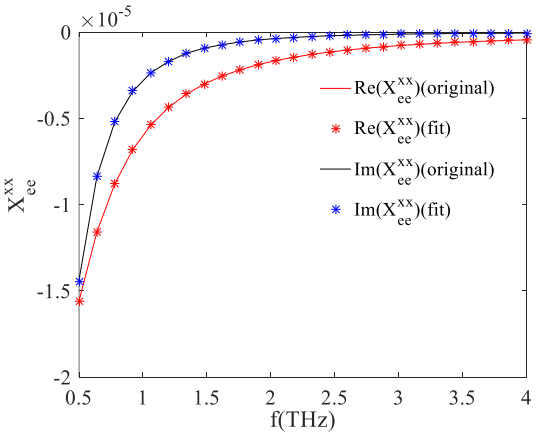

(a)

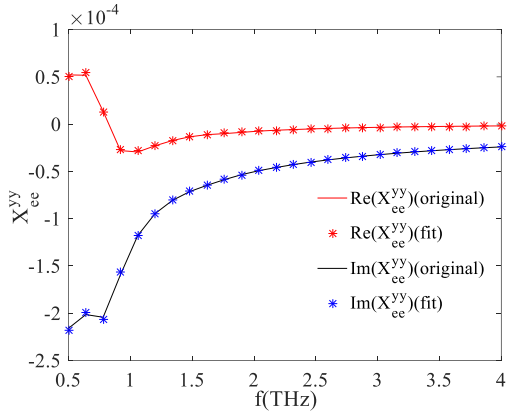

(b)

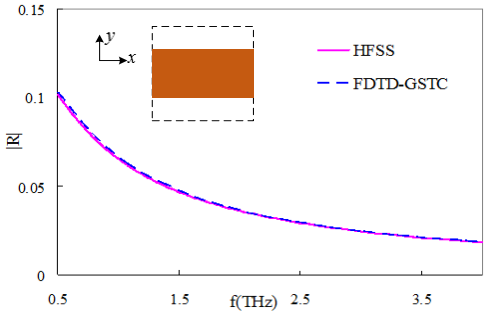

(c)

Fig. 4. Simulation of asymmetrical graphene sheet with rectangular elements: (a) extracted susceptibility $\tilde{\chi}_{ee}^{xx}$, (b) extracted susceptibility $\tilde{\chi}_{ee}^{yy}$, and (c) reflection coefficient by commercial software and proposed FDTD-GSTC method.

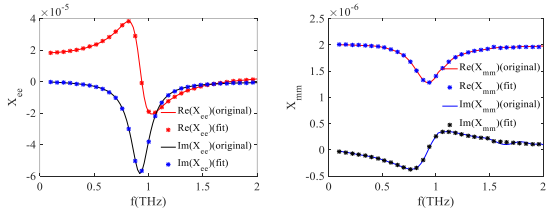

(a)

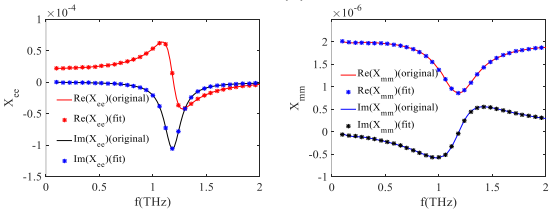

(b)

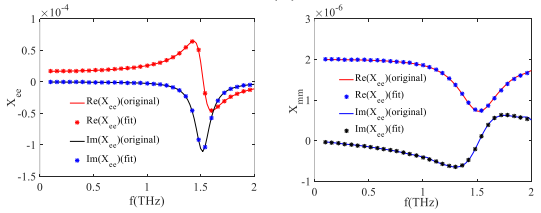

(c)

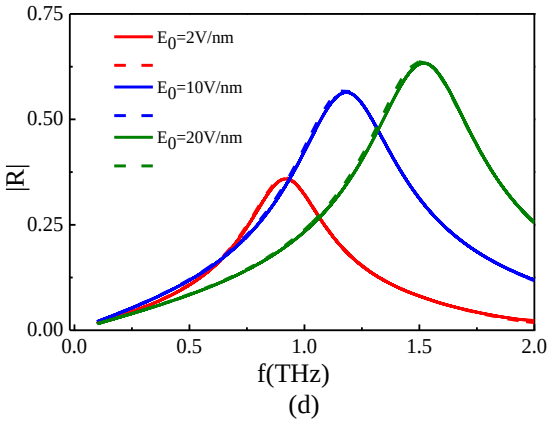

Fig. 5. Simulation of the graphene sheet with different biasing electric field: (a) susceptibilities when E = 2V/nm, (b) susceptibilities when E = 10V/nm, (c) susceptibilities when E = 20V/nm, and (d) reflection coefficients with different static biasing electric fields.

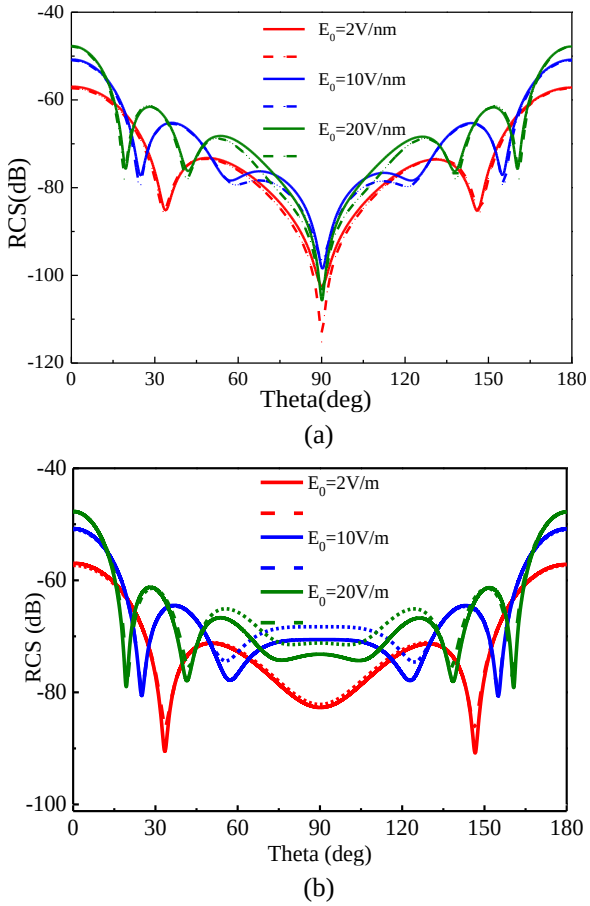

Fig. 6. Validation: bistatic RCS of finite graphene sheet composed of 10×10 cross computed by HFSS (solid line) and FDTD-GSTC (dotted line).

Table 5: Comparison of time and memory between HFSS and FDTD-GSTC

Method	Number of Elements	Time (hh:mm:ss)	Memory (GB)
HFSS	7290500	38:51:39	32
FDTD-GSTC	398×398×99	07:49:51	12

V. CONCLUSION

We proposed an effective dispersive FDTD-GSTC method to analyze the electromagnetic property of graphene by using the complex-conjugate pole-residue pairs. Typical tunable graphene sheets with cross and rectangular elements are simulated in a broadband. The accuracy of the method and the computation performance is validated with respect to commercial software.

ACKNOWLEDGMENT

This work is partially supported by Natural Science Foundation of China (61871222, 61507237); Natural Science Foundation of Jiangsu Province (BK20171429); Fundamental Research Funds for the Central Universities (30918011103).

REFERENCES

[1] K. Achouri, M. A. Salem, and C. Caloz, "General metasurface synthesis based on susceptibility tensors," *IEEE Trans. Antennas Propag.*, vol. 63, no. 7, pp. 2977-2991, July 2015.

[2] Y. Vahabzadeh, N. Chamanara, K. Achouri, et al., "Computational analysis of metasurfaces," *IEEE Journal on Multiscale and Multiphysics Computational Techniques*, vol. 3, pp. 37-49, Apr. 2018.

[3] M. Han, R. W. Dutton, and S. Fan, "Model dispersive media in finite-difference time-domain method with complex-conjugate pole-residue pairs," *IEEE Microw. Wireless Compon. Lett.*, vol. 16, no, 3, pp. 119-121, 2006.

[4] A. Geim and K. Novoselov "The rise of graphene," *Nature Mater.*, vol. 6, pp. 183-191, 2007.

[5] Y. Zhao, S. Tao, D. Ding, et al., "A time-domain thin dielectric sheet (TD-TDS) integral equation method for scattering characteristics of tunable graphene," *IEEE Trans. Antennas Propag.*, vol. 66, no, 3, pp. 1366-1373, Jan. 2018.

[6] J. C. Mak and C. D. Sarris, "A surface impedance boundary condition approach to the FDTD modeling of graphene," *IEEE Antennas and Propagation Society International Symposium (APSURSI)*, pp.902-903, July 2013.

[7] X. Yu and C. D. Sarris, "A perfectly matched layer for subcell FDTD and applications to the modeling of graphene structures," *IEEE Antennas Wireless Propag. Lett.*, vol. 11, no. 4, pp. 1080-1083, 2012.

[8] J. Chen, N. Xu, A. Zhang, et al., "Using dispersion HIE-FDTD method to simulate the graphene-based polarizer," *IEEE Trans. Antennas Propag*., vol. 24, no. 7, pp. 3011-3017, July 2016.

[9] A. Eldek, A. Z. Elsherbeni, and C. E. Smith, "Analysis of transmission and reflection from modified coplanar waveguide structures," *ACES Journal*, vol. 17, no. 2, pp. 158-165, July 2002.

[10] M. Li, C. Xia, and R. Chen, "Full-wave analysis of microstrip circuits with reciprocal matrix compression technique," *ACES Journal*, vol. 31, no. 1382-1388, Dec. 2016.

[11] E. F. Kuester, M. A. Mohamed, M. Piket-May, et al., "Averaged transition conditions for electromagnetic fields at a metafilm," *IEEE Trans. Antennas Propag.*, vol.51, no.10, pp. 2641-2651, 2003.

[12] X. Jia, X. Liu, F. Yang, et al., "An accelerated method of metasurfaces simulation by introducing susceptibilities into FDTD based on GSTCs," *arXiv* preprint *arXiv*:1710.09193, 2017.

[13] Y. Vahabzadeh, N. Chamanara, and C. Caloz "Generalized sheet transition condition FDTD simulation of metasurface," *IEEE Trans. Antennas Propag.*, vol. 66, no. 1, pp. 271-280, 2018.

[14] H. Bao and R. Chen, "An efficient domain decomposition parallel scheme for leapfrog ADI-FDTD method," *IEEE Trans. Antennas Propag*., vol. 65, no. 3, pp. 1490-1494, Mar. 2017

[15] H. Bao, D. Z. Ding, and R. S. Chen, "A hybrid spectral-element finite-difference time-domain method for electromagnetic simulation," *IEEE Antennas Wireless Propag. Lett*., vol. 16, pp. 2244-2248, 2017.

[16] X. Du, H. Yu, M. Li, and R. S. Chen, "Simulation of all dielectric metasurafce with finite thickness based on FDTD-GSTC," *2018 ACES-China Conference*, pp. 1-2, July 29-Aug. 1, 2018.

[17] M. Li, S. Li, Y. Yu, X. Ni, and R. Chen, "Design of random and sparse metalens with matrix pencil method," *Optics Express*, vol. 26, no. 19, pp. 24702-11, Sep. 2018.

Xiaofeng Du received the B.S. degree in Electrical Engineering from the Hefei University of Technology, Xuancheng, China, in 2016. She is pursuing the master degree in Electromagnetic Field and Microwave Technology in the Nanjing University of Science and Technology, Nanjing, China. Her current research interest is effective FDTD modeling of tunable metasurface.

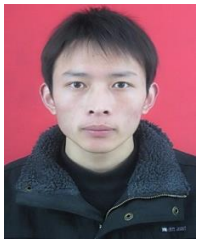

Mengmeng Li received the B.S. degree (Hons.) in Physics from Huaiyin Normal College, Huai'an, China, in 2007, and the Ph.D. degree in Electromagnetic Field and Microwave Technology from Nanjing University of Science and Technology, Nanjing, China, in 2014. From 2012 to 2014, he was a Visiting Student with the Electronics Department, Politecnico di Torino, Turin, Italy. Since 2014, he has been with the Department of Communication Engineering, Nanjing University of Science and Technology, where he has been an Associate Professor since 2017. In 2017, he was a Visiting Scholar with Pennsylvania State University, Pennsylvania, PA, USA. His current research interests include fast solver algorithms and multiscale simulations.

Li was a recipient of the Doctoral Dissertation Award of Jiangsu in 2016, the Student Paper Award at the International Conference on Microwave and Millimeter Wave Technology in 2012. He serves as an active Reviewer for the IEEE Journals and Conferences, and has been an Associate Editor for the IEEE Access.

Efficient Leapfrog SF FDTD Method for Periodic Structures at Oblique Incidence

Qi Lei, Lihua Shi, Jianbao Wang, Hailin Chen, and Shangchen Fu

National Key Laboratory on Electromagnetic Environmental Effects and Electro-optical Engineering
Army Engineering University of PLA, Nanjing, 210007, China
lqiiox@stu.xmu.edu.cn, lihuashi@aliyun.com, zwang0417@outlook.com, hylinchen@sohu.com, fshangchen@hotmail.com

Abstract ─ This paper presents an efficient explicit leapfrog implementation of the split-field (SF) finite-difference time-domain (FDTD) method for solving problems of the oblique incident plane wave on periodic structures. Firstly, by splitting only one field component, the additional time derivative terms of transformed Maxwell's equations can be eliminated. Then, by applying Peaceman–Rachford scheme, one-step leapfrog scheme and Sherman-Morrison formula, the proposed SF method is implemented in a much simpler explicit scheme than traditional SF FDTD method and some unconditionally stable methods. Furthermore, the stability condition of the proposed method is weaker than traditional SF FDTD method. The accuracy and efficiency of this method are verified by numerical results.

Index Terms ─ Finite-difference time-domain (FDTD) algorithm, modified split-field (SF) method, one-step leapfrog scheme, periodic structure.

I. INTRODUCTION

Many electromagnetic applications possess a periodicity in one or more dimensions, such as dielectric frequency selective surfaces (DFSS) [1], photonic bandgap (PBG) structures [2] and so on. The analyses of these structures using the conventional finite-difference time-domain (FDTD) method are time-consuming and memory-extensive because the periodic structures exist. The periodic boundary condition (PBC) provides a good choice to alleviate the computational burden in analyzing these structures' scattering problems [3] because only one unit cell of the periodicity need to be modeled. However, PBC is difficult to implement at the oblique incident due to a cell-to-cell phase variation between two periodic boundaries [4]. The methods that have been proposed for oblique incident are divided into two main categories: direct field methods and field transformation methods [5]. The split-field (SF) FDTD method [4], which belongs to the second category, is widely used because it is very useful and robust. Unfortunately, the Courant Friedrichs Lewy (CFL) conditions of the SF FDTD method is strict and angle-dependent. To overcome the restriction, some unconditionally stable methods [6, 7] based on implicit scheme have been introduced into the analysis of periodic structures. However, those methods all need to solve several complex implicit equations and exhibit worse numerical dispersion errors along with the increment of the time-step size. After that, Wang *et al*. present an explicit implementation of the 2-D SF FDTD method [8] by locally one-dimensional (LOD) scheme.

In this paper, by adopting modified SF method [9], Peaceman–Rachford (PR) scheme [10] and one-step leapfrog scheme [11], an efficient explicit leapfrog SF FDTD method is proposed for analyzing the oblique incident plane wave problems in periodic structures. In comparisons with the traditional SF FDTD method [4] and LOD FDTD method [7], the proposed method has better numerical performance, which is validated by the numerical examples. The rest of this paper is arranged as follows, Section II presents the derivation of formulation. In Section III, the numerical performance of the proposed method is analyzed. In Section IV, two numerical examples are demonstrated to verify the computational accuracy, efficiency and memory storage of this method by comparing with traditional SF FDTD method and periodic LOD FDTD method [7], and the conclusions are drawn in Section V.

II. FORMULATION

Supposing that an electromagnetic object has a periodic structure in *y*-direction, according to field transformation technique [3, 5], the transformed Maxwell's equations for 2-D TM wave can be obtained as follows:

$$\frac{\mu_r}{c}\frac{\partial Q_x}{\partial t} = -\frac{\partial P_z}{\partial y} + \frac{\sin\theta}{c}\frac{\partial P_z}{\partial t}, \tag{1}$$

$$\frac{\mu_r}{c}\frac{\partial Q_y}{\partial t} = \frac{\partial P_z}{\partial x}, \tag{2}$$

Submitted On: October 9, 2018
Accepted On: December 21, 2018

$$\frac{\varepsilon_r}{c}\frac{\partial P_z}{\partial t}=\frac{\partial Q_y}{\partial x}-\frac{\partial Q_x}{\partial y}+\frac{\sin\theta}{c}\frac{\partial Q_x}{\partial t}, \tag{3}$$

where $Q_x=\eta_0 H_x e^{jkyy}$, $Q_y=\eta_0 H_y e^{jkyy}$, $P_z=E_z e^{jkyy}$ and $k_y=\omega\sin\theta/c$. c is the speed of light in free space, θ is the angle of propagation for the incident field, ε_r and μ_r are relative permittivity and relative permeability, respectively.

It can be seen from equations (1) and (3) that these equations cannot be implemented yet since the time derivative terms appear in both sides of equations.

In our early work [9], a new SF method is proposed to eliminate the additional time derivative terms of equations (1)-(3) as follows:

$$\frac{\partial Q_{xa}}{\partial t}=-a_1\frac{\partial P_z}{\partial y}, \tag{4}$$

$$\frac{\partial Q_y}{\partial t}=a_1\frac{\partial P_z}{\partial x}, \tag{5}$$

$$\frac{\partial P_z}{\partial t}=a_2\left(\frac{\partial Q_y}{\partial x}-\frac{\partial Q_{xa}}{\partial y}\right)-a_3\frac{\partial P_z}{\partial y}, \tag{6}$$

where $a_1=c/\mu_r$, $b_1=\varepsilon_r\mu_r-\sin^2\theta$, $a_2=c\mu_r/b_1$, $a_3=2c\sin\theta/b_1$.

Equations (4)-(6) are self-consistent, which is simpler than the traditional SF FDTD method that need to calculate two other fields (Q_{xa} and P_{za}).

By applying the PR scheme [10], equations (4)-(6) can be split into two sub-steps as:

(n)th-(n+1/2)th step:

$$Q_{xa}^{n+1/2}+a_1a_5\frac{\partial}{\partial y}P_z^{n+1/2}=Q_{xa}^{n}, \tag{7}$$

$$Q_{y}^{n+1/2}-a_1a_5\frac{\partial}{\partial x}P_z^{n+1/2}=Q_{y}^{n}, \tag{8}$$

$$\left(1+a_3a_5\frac{\partial}{\partial y}\right)P_z^{n+1/2}=a_5\left(-a_2\frac{\partial}{\partial y}Q_{xa}^{n}+a_2\frac{\partial}{\partial x}Q_{y}^{n}\right)+P_z^{n}. \tag{9}$$

(n+1/2)th-(n+1)th step:

$$Q_{xa}^{n+1}=Q_{xa}^{n+1/2}-a_1a_5\frac{\partial}{\partial y}P_z^{n+1/2}, \tag{10}$$

$$Q_{y}^{n+1}=Q_{y}^{n+1/2}+a_1a_5\frac{\partial}{\partial x}P_z^{n+1/2}, \tag{11}$$

$$a_5\left(a_2\frac{\partial}{\partial y}Q_{xa}^{n+1}-a_2\frac{\partial}{\partial x}Q_{y}^{n+1}\right)+P_z^{n+1}=\left(1-a_3a_5\frac{\partial}{\partial y}\right)P_z^{n+1/2}, \tag{12}$$

where $a_5=\Delta t/2$ and Δt is the time step size.

In order to achieve better computational efficiency, one-step leapfrog technique [11] is introduced into the proposed method. We suppose that P_z is updated at half time steps, while Q_{xa} and Q_y are updated at integer time steps.

By substituting equations (7) and (8) into (10) and (11) respectively, the updating equations for Q_{xa} and Q_y can be got easily:

$$Q_{xa}^{n+1}=Q_{xa}^{n}-\Delta t a_1\frac{\partial}{\partial y}P_z^{n+1/2}, \tag{13}$$

$$Q_{y}^{n+1}=Q_{y}^{n}+\Delta t a_1\frac{\partial}{\partial x}P_z^{n+1/2}. \tag{14}$$

Then, substitute equation (12) in the previous time step into equation (9), the updating equation for P_z is obtained as:

$$\left(1+a_3a_5\frac{\partial}{\partial y}\right)P_z^{n+1/2}= \Delta t\left(-a_2\frac{\partial}{\partial y}Q_{xa}^{n}+a_2\frac{\partial}{\partial x}Q_{y}^{n}\right)+\left(1-a_3a_5\frac{\partial}{\partial y}\right)P_z^{n-1/2}. \tag{15}$$

To further simplify, an auxiliary field variable ρ_z is introduced as:

$$\rho_z^{n+1/2}=P_z^{n+1/2}+P_z^{n-1/2}. \tag{16}$$

Then, the (15) can be rewritten as:

$$\left(1+a_3a_5\frac{\partial}{\partial y}\right)\rho_z^{n+1/2}=\Delta t\left(-a_2\frac{\partial}{\partial y}Q_{xa}^{n}+a_2\frac{\partial}{\partial x}Q_{y}^{n}\right)+2P_z^{n-1/2}. \tag{17}$$

After that, the final implementation of the proposed leapfrog SF FDTD method is: equations (17)-(13)-(14). The field components are computed in a full time step like the conventional FDTD method, where no substep computations are needed. It means that the real iterative time step of the proposed method is Δt.

Updating $\rho_z^{n+1/2}$ from equation (17) with the PBC requires solving a perturbed bidiagonal system, which is:

$$G_1\rho_{z(i)}^{n+1/2}=d, \tag{18}$$

$$G_1=\begin{bmatrix} g_1 & & & g_2\\ g_2 & g_1 & & \\ & \vdots & & \\ & g_2 & g_1 & \\ & & g_2 & g_1 \end{bmatrix},\ \rho_{z(i)}=\begin{bmatrix} \rho_{z(i,2)}\\ \rho_{z(i,3)}\\ \vdots\\ \rho_{z(i,N_y-1)}\\ \rho_{z(i,N_y)} \end{bmatrix},\ d=\begin{bmatrix} d_{(i,2)}\\ d_{(i,3)}\\ \vdots\\ d_{(i,N_y-1)}\\ d_{(i,N_y)} \end{bmatrix},$$

where $g_1=1/2+a_3/\Delta y$, $g_2=1/2-a_3/\Delta y$, N_y is the maximum mesh number in y-direction. d is the right-hand-sides of equation (17), which is known.

To implement equation (18) explicitly, the Sherman-Morrison formula [12] can be applied as:

$$G_2 p_a=d, \tag{19}$$

$$G_2 p_b=w, \tag{20}$$

$$\rho_{z(i)}^{n+1/2}=p_a+\left(p_{a(i,N_y)}p_b\right)\left(1-p_{b(i,N_y)}\right)^{-1}, \tag{21}$$

where

$$G_2=G_1-wz=\begin{bmatrix} g_1 & & & \\ g_2 & g_1 & & \\ & \vdots & & \\ & g_2 & g_1 & \\ & & g_2 & g_1 \end{bmatrix}. \tag{22}$$

$$w=\begin{bmatrix} g_2 & 0 & \cdots & 0 \end{bmatrix}^T,\ z=\begin{bmatrix} 0 & 0 & \cdots & 1 \end{bmatrix}$$

The perturbed bidiagonal system (equation (18)) is converted into two auxiliary linear systems (equations (19) and (20)) that can be solved explicitly.

Taking the equation (19) as an example:

$$p_{a(i,2)}=d_{(i,2)}/g_1, \tag{23}$$

$$p_{a(i,j)}=\left(d_{(i,j)}-g_2 p_{a(i,j-1)}\right)/g_1 \quad 3\le j\le N_y . \qquad (24)$$

The realization of equation (20) can be handled similarly as the above-mentioned approach for equation (19). With the solution of $\rho_z^{n+1/2}$, the field components $P_z^{n+1/2}$, Q_{xa}^{n+1} and Q_y^{n+1}can be calculated explicitly by using equations (16), (13) and (14), respectively.

III. NUMERICAL PERFORMANCE ANALYSIS

A. Numerical stability analysis

The CFL condition of the proposed method can be analyzed by the Fourier method [3, 12]. Assuming a plane wave propagating in the grid, the amplification factors in free space from (n)th to (n+1)th time step can be obtained as:

$$\lambda_1=1,\lambda_{2,3}=\left(-\nu_3\pm i\sqrt{4\nu_1\nu_2-\nu_3^2}\right)\Big/2\nu_1 , \qquad (25)$$

where $i=\sqrt{-1}$, $k_x=\omega\cos\theta/c$, $m_1=c\Delta t\sin(k_x\Delta x/2)/\Delta x$, $m_2=c\Delta t\sin(k_y\Delta y/2)/\Delta y$, $\upsilon_0=2im_2\sin\theta/\cos^2\theta$, $\upsilon_1=\upsilon_0$-1, $\upsilon_2=$-υ_0-1 and $\upsilon_3=2(2(m_1^2+m_2^2)/\cos^2\theta$-1).

To make the difference scheme to be stable, the magnitude of amplification factors should be less than or equal to unity. Therefore, the CFL stability condition can be derived as:

$$\Delta t\le \cos\theta\Big/\left(c\sqrt{\Delta x^{-2}+\Delta y^{-2}}\right). \qquad (26)$$

In contrast, the stability condition of the traditional split-field FDTD method for square cell is $\Delta t\le\Delta x\cos^2\theta/c\sqrt{1+\cos^2\theta}$ [3], and its iterative time step is $\Delta t/2$. It can be seen easily that the stability condition of the proposed method is more relaxed, especially at the high incident angle.

B. Memory and computational efficiency analysis

Meanwhile, in terms of the memory used, the amount of the field components needs to be stored by the proposed method (p_a, $P_z^{n+1/2}$, $\rho_z^{n+1/2}$, Q_{xa}^n, Q_y^n) is similar to the LOD FDTD method and less than that of the traditional SF FDTD method ($Q_{xa}^{n-1/2}$, Q_{xa}^n, Q_x^n, $Q_y^{n-1/2}$, Q_y^n, $P_{za}^{n-1/2}$, P_{za}^n, P_z^n). In addition, it can be seen that the final implementation doesn't need to solve implicit equations, which is more efficient than those unconditionally stable methods [6, 7] because those methods all need to solve more than two complex implicit equations.

IV. NUMERICAL VALIDATION

For validating the accuracy and efficiency of the proposed method, the scattering properties of a PBG structure and a DFSS structure are presented, respectively.

In the first example, a PBG structure in Fig. 1 (same as [4, 7]) with four infinitely long dielectric rods is simulated. The computational domain is meshed by 308×38 uniform grids ($\Delta x=\Delta y$=0.25mm) and truncated by the PBC and the perfectly matched layer (PML) absorbing boundary condition along the y-direction and x-direction, respectively. A total-field/scattered-field (TF/SF) connecting boundary is applied to excite a plane wave and the total simulation time is chosen as 8.3 ns.

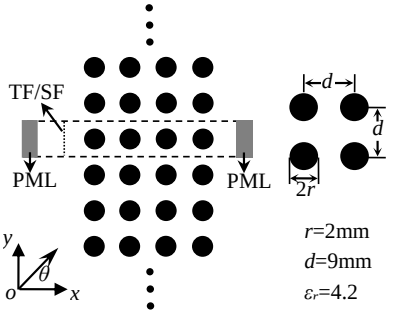

Fig. 1. Geometry of a photonic bandgap.

In this example, four different incident cases of (θ=30°, 45°, 60°and 75°) are calculated by the traditional SF FDTD method, the periodic LOD FDTD method [7] and the proposed method. The traditional SF FDTD method is used as the benchmark to examine the computational accuracy of other methods because its numerical dispersion error is the smallest. To achieve enough accuracy, the time-step sizes of the three methods are: t_1, 6×t_1 and CFLN×t_1, respectively. t_1 is half of the max time step size of traditional SF FDTD method from [3]. CFLN indicates the largest integer ratio maximum between the time-step size in proposed method from equation (26) and t_1.

The results of transmission coefficient and relative errors of the above-mentioned methods are plotted in Fig. 2. The information of the computational resources is listed in Table 1. Figure 2 shows that the numerical results calculated by the proposed method have a good agreement with traditional SF FDTD method (the relative error is below -45 dB), and the proposed method achieves better numerical dispersion performance than the LOD FDTD method. Table 1 manifests that the proposed method has high efficiency, especially at the high incident angle. Moreover, the memory storage of the proposed method is less than that of the other two methods from Table 1.

Table 1: CPU times and memory cost of the simulation of the first example

Method	Memory (kB)	CPU Time (s) (CFLN)			
		θ=30°	θ=45°	θ=60°	θ=75°
The traditional SF FDTD method	978	32.71	38.27	62.53	223.35
The LOD method	570	8.39 (6)	9.54 (6)	15.29 (6)	55.28 (6)
The proposed method	376	10.22 (2)	11.7 (2)	15.43 (3)	31.68 (5)

In the second example, to further validate the effectiveness, the proposed method is utilized to simulate the electromagnetic properties of a DFSS with two dielectric slabs (ε_{r1}=10, ε_{r2}=5) shown in Fig. 3. The computational domain is meshed by 200×20 uniform grids. The grid size, the time step size and the boundary conditions of the example are identical with the former. The total simulation time is chosen as 0.25 μs.

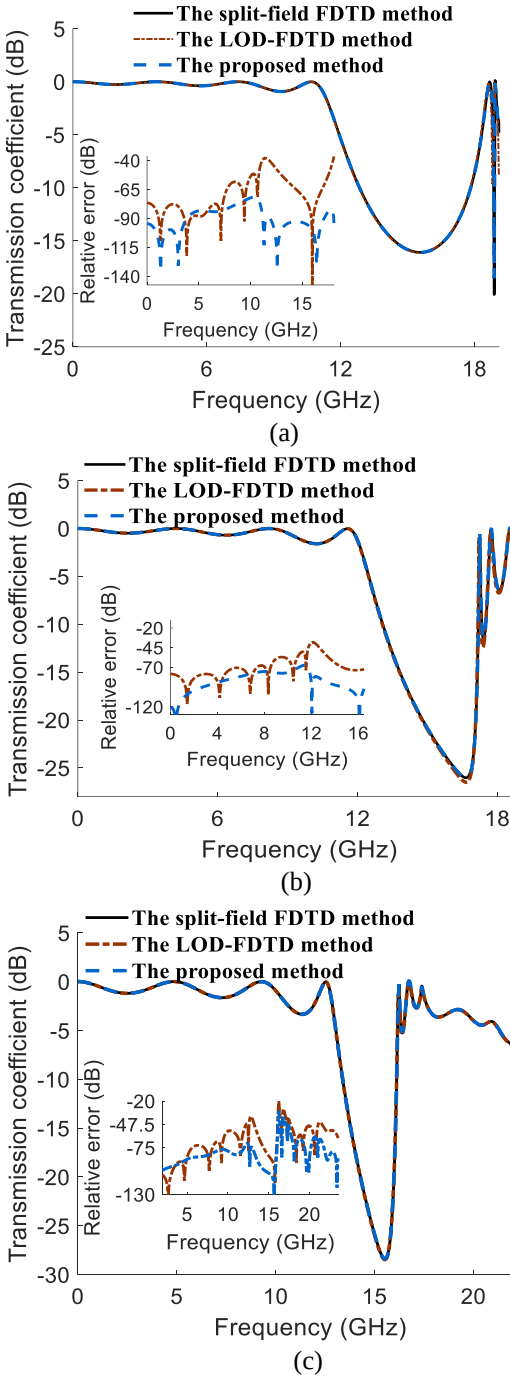

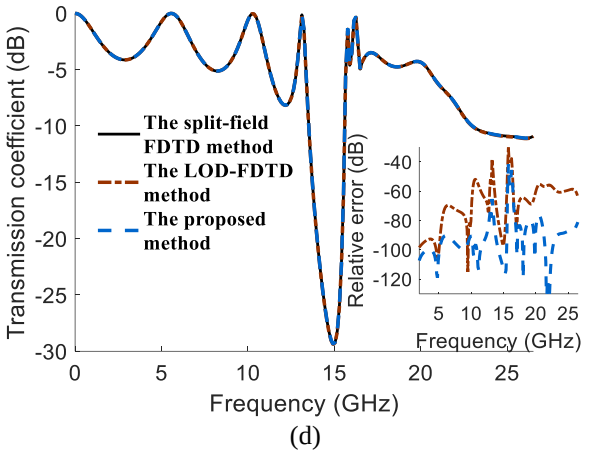

Fig. 2. Transmission coefficient and relative errors calculated by three methods: (a) θ=30°, (b) θ=45°, (c) θ=60°, and (d) θ=75°.

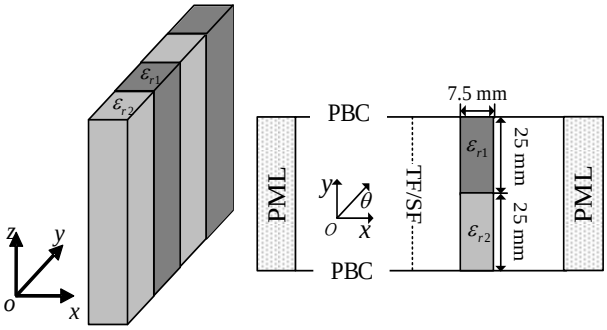

Fig. 3. Geometry of a dielectric frequency selective surfaces

Figure 4 shows the transmission coefficient and the relative error of the traditional SF FDTD method and the propose method with θ=45° and θ=75°. Table 2 provides the computational resources of the numerical simulation. It can be observed from Fig. 4 that the results of the proposed method are agreeable with the traditional SF FDTD method. Table 2 shows that the proposed method can greatly reduce runtime and memory storage compared with the traditional SF FDTD method because of the bigger time step size.

Table 2: CPU times and memory cost of the simulation of the second example

Method	Memory (kB)	CPU Time (s)	
		θ=45°	θ=75°
The traditional SF FDTD method	346	73.64	298.45
The proposed method	100	23.43	38.66

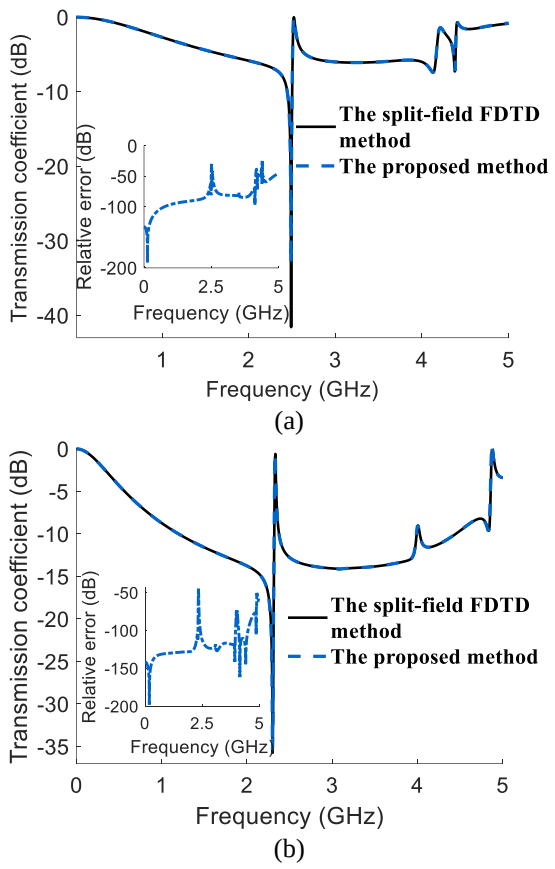

Fig. 4. Transmission coefficient and relative errors calculated by the traditional SF FDTD method and the proposed method: (a) θ=45° and (b) θ=75°.

V. CONCLUSIONS

In this paper, an efficient explicit leapfrog SF FDTD method for analyzing periodic structures' scattering problems is deduced. In comparisons with the traditional SF FDTD method and some unconditionally stable methods, the proposed method has better numerical performance and more concise implementation. Two examples verified the performance of this method in analyzing a PBG and a DFSS structure.

ACKNOWLEDGMENT

This work was supported by the National Nature Science Foundation of China under Grant 51507189, and 51477183.

REFERENCES

[1] S. Tibuleac, R. Magnusson, T. A. Maldonado, P. P. Young, and T. R. Holzheimer, "Dielectric frequency-selective structures incorporating waveguide gratings," *IEEE Trans. Microw. Theory Tech.*, vol. 48, pp. 553-561, 2000.

[2] M. P. Kesler, J. G. Maloney, B. L. Shirley, and G. S. Smith, "Antenna design with the use of photonic band - gap materials as all - dielectric planar reflectors," *Microwave & Optical Technology Letters*, vol. 11, pp. 169-174, 1996.

[3] A. Taflove and S. C. Hagness, *Advances in Computational Electrodynamics: The Finite-Difference Time-Domain Method*. 2nd ed., Norwood, MA: Artech House Publishers, 2000.

[4] J. A. Roden, S. D. Gedney, M. P. Kesler, J. G. Maloney, and P. H. Harms, "Time-domain analysis of periodic structures at oblique incidence: Orthogonal and nonorthogonal FDTD implementations," *IEEE Trans. Microw. Theory Tech.*, vol. 46, pp. 420-427, Apr. 1998.

[5] M. E. Veysoglu, R. T. Shin, and J. A. Kong, "A finte-difference time-domain analysis of wave scattering from periodic surfaces: Oblique incidence case," *J. Electromagn. Waves Appl.*, vol. 7, pp. 1595-1607, 1993.

[6] S. M. Wang, J. Chen, and P. Ruchhoeft, "An ADI-FDTD method for periodic structures," *IEEE Trans. Antennas Propag.*, vol. 53, pp. 2343-2346, July 2005.

[7] J. B. Wang, B. H. Zhou, L. H. Shi, and B. Chen, "Unconditionally stable FDTD method based on LOD scheme for analysis of 2-D periodic structures," *IEEE Trans. Antennas Propag.*, vol. 60, pp. 4003-4006, Aug. 2012.

[8] J. Wang, J. Wang, Q. Lei, L. Shi, H. Chen, and H. Liu, "Efficient implementation of 2-D split-field FDTD method for analyzing periodic structures," *IEEE Trans. Antennas Propag.*, vol. 65, pp. 3263-3266, 2017.

[9] Q. Lei, J. Wang, and L. Shi, "Modified HIE-FDTD algorithm for 2-D periodic structures with fine mesh in either direction," *IEEE Antennas Wirel. Propag. Lett.*, vol. 16, pp. 1455-1459, 2017.

[10] D. W. Peaceman, J. Rachford, and H. Henry, "The numerical solution of parabolic and elliptic differential equations," *Journal of the Society for Industrial and Applied Mathematics*, vol. 3, pp. 28-41, 1955.

[11] S. Cooke, M. Botton, T. Antonsen, and B. Levush, "A leapfrog formulation of the 3 - D ADI - FDTD algorithm," *International Journal of Numerical Modelling: Electronic Networks, Devices and Fields*, vol. 22, pp. 187-200, 2009.

[12] J. W. Thomas, *Numerical Partial Differential Equations: Finite Difference Methods*. Springer-Verlag, 1995.

Numerical De-embedding of Periodic Guided-wave Structures via SOL/SOC in FEM Algorithm

Yin Li, Danpeng Xie, and Lei Zhu

Department of Electrical Engineering
University of Macau, Macau, 519000, SAR, China
yb57430@connect.umac.mo, yb57471@umac.mo, LeiZhu@umac.mo

Abstract ─ This paper presents a 3D full-wave finite element method (FEM) combined with short-open-load (SOL) and short-open calibration (SOC) technique. Due to the effective calibration of the port discontinuities between the feeding line and periodic structure, both SOL and SOC can successfully extract the intrinsic unite-length parameters, i.e., complex propagation constants and effective characteristic impedances. Distinctively, the SOL can be easily implemented with the commercial software such as Ansys HFSS, which is widely applicable for various kinds of periodic structure. More importantly, the SOC incorporated within the FEM algorithm intrinsically reduces the requirement of the load standard in SOL. Also, the SOC in FEM will be independent with the absorbing boundary condition at the port. And the port information such as characteristic impedance and propagation constants at the designated port will not be required in advanced, thereby allowing the arbitrary implementation of non-uniform feeding structures. In order to demonstrate the efficiency and accuracy of our proposed approaches, two numerical examples are given out for verification.

Index Terms ─ Characteristic impedances, finite element method, periodic structures, port discontinuities, short-open calibration, short-open-load.

I. INTRODUCTION

Recently, a great demand for full-wave modeling and characterization of the integrated and multifunctional microwave and millimeter-wave circuits has been rapidly grown. Especially for a large number of designs with various types of periodic structures, including substrate integrated waveguide (SIW) [1], air-filled substrate integrated waveguide (AFSIW) [2-4] and metamaterials [5], etc., the high-accuracy and high-efficiency modeling approach for their guided-wave characterization become significantly important.

A traditional approach based on the Floquet theory utilizes the eigenvalue of the unit cell to characterize the infinite periodic structure [6]. However, it becomes extremely time-consuming and low-efficient when solving the eigenvalue problem of each unit cell. Although eigenmode solver has been implemented into commercial software, such as Ansys HFSS [7] and CST Microwave Studio [8], the attenuation constant and the characteristic impedance of the periodic structures still cannot be directly extracted. In this way, only the phase constant of the periodic structures can be acquired through the eigenvalue solver.

In practice, the unit cell of the periodic structure is commonly considered as an equivalent two-port network, hence the propagation characteristics of the periodic structures can be easily retrieved by the network parameters. As for realization, the port models such as lumped port and wave port are widely used to conveniently excite the two-port network. However, the lumped port models introduce an undesired port discontinuity [9, 10], due to the inaccurate description of the field at the port. Even though the wave port model can describe the filed by solving the eigenvalue problem of the cross-section at the port [11-13], the discontinuity between the feeding line and the periodic structure still exists. It will unavoidably bring in certain inaccuracy, resulting from the reflected waves back to the port [1].

Thereafter, calibration methods are accordingly conducted during the numerical modeling, aiming at the elimination of the above-described discontinuities. The so-called "double-delay de-embedding" was developed to estimate and remove out the port discontinuity [10, 14, 15]. Inspired by the calibration procedure in measurement, the numerical thru-reflect-line (TRL) calibration method was developed to effectively model the SIW devices [16, 17]. Moreover, the thru-line (TL) calibration method was also proposed for the extraction of the SIW structures [1, 18, 19]. Similarly, the through-resistor (TR) calibration method was proposed to de-embed the port discontinuities [20]. In addition, the even-odd-mode excitation was employed to analyze the port discontinuity for accurate modeling [21]. Despite that, individual limitations regarding each of the above calibration methods restrict their applicability. For

Submitted On: October 12, 2018
Accepted On: December 9, 2018

example, double-delay method needs to pre-define the format of the port discontinuities as shunt impedance, and two feeding lines in TL method must be symmetrically implemented. Electrical lengths between the line-standard and thru-standard should be determined according to the operation frequency, and the whole procedure needs to be carried out within a certain bandwidth.

As is well known, the short-open-calibration (SOC) technique was first proposed in 1997 [9], which is capable to accurately and efficiently estimate the error box by only a pair of calibration standards, named as ideal short- and open-end. It has been applied to extract the equivalent model parameters of planar circuit elements [9]. The port discontinuity and its respective feeding line are considered as an error box. After removing it out, the characteristic parameters of the periodic structures, such as coplanar waveguide (CPW) electromagnetic bandgap (EBG) [22] and CPW metamaterial structures [23], are accurately extracted.

The short-open-load (SOL) technique has been recently integrated into the 3D commercial full-wave simulator HFSS (HFSS-SOL) [24, 25, 26]. By virtue of the short, open and load standards, the periodic structures with 3D cell can be conveniently and accurately analyzed. However, the port information needs to be known or calculated in advance, whereas the realization of a load standard is usually difficult to implement. Therefore, in order to avoid the load standard element, the SOC method is further implemented in the 3D finite-element method (FEM) algorithm (FEM-SOC). It requires completely no absorbing boundary condition at the port. Also, the pre-knowledge of the port information is not needed at all. In [27], the feeding line and the port discontinuity are considered as the error box, so the characteristic parameters of the periodic structures can be extracted. In this work, two numerical examples, i.e., an AFSIW guided-wave structure modeled by HFSS-SOL and a non-uniformly-fed pin-loaded microstrip line analyzed by FEM-SOC are separately exhibited and demonstrated. In addition, the effect of the non-uniform feeding structures is discussed.

II. SOL AND SOC TECHNIQUE IN FEM

As shown in Fig. 1 (a), the equivalent circuit model of the periodic structure with *N*–unit cells fed by a pair of sources at two sides is exhibited. The longitudinal dimension of the core *N*–unit cells is $L = N \times T$, where T is the periodicity of each unit cell. The core circuit of the periodic structure can be equivalent to a uniform transmission line, whose effective guided-wave parameters include the complex propagation constant and characteristic impedance. The core circuit can be excited by the impressed source with the feeding line and port discontinuity as shown in the Fig. 1 (b).

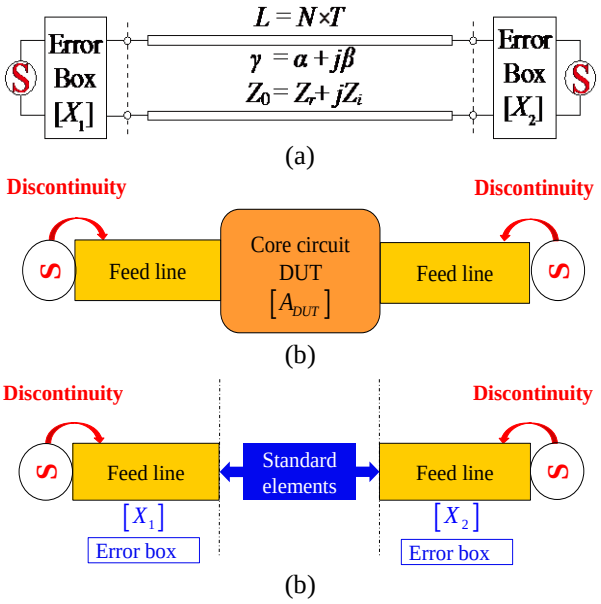

Fig. 1. Equivalent circuit model of periodic structure fed by impressed sources at two ports and its calibration process.

As shown in Fig. 1 (c), the feeding line and port discontinuity are included into the error box, which can be estimated by the standard elements and then removed out. And then, the accurate results of the core circuit can be obtained. For both SOC and SOL techniques, the feeding line and the port discontinuity are included in the two error boxes, which need to be evaluated, thus to be removed out for accurate extraction of the periodic structure. According to different calibration standards, distinctive de-embedding procedures between the SOL and SOC techniques are respectively implemented.

A. SOL de-embedding technique

As for SOL de-embedding technique, three standard elements, including short, open, and load standards, are explicitly depicted in Fig. 2. These three standards can be respectively realized by three kinds of boundary conditions, i.e., perfect electric conductor (PEC), perfect magnetic conductor (PMC), and matched load. They can be easily realized in full-wave simulator.

In terms of the error box [*X*], the four elements of its ABCD-matrix are defined as *a*, *b*, *c*, *d*. By using the transmission line theory, the input impedance for the error box loaded with the impedance Z_L can be expressed as:

$$Z_{in} = \frac{a * Z_L + b}{c * Z_L + d}. \tag{1}$$

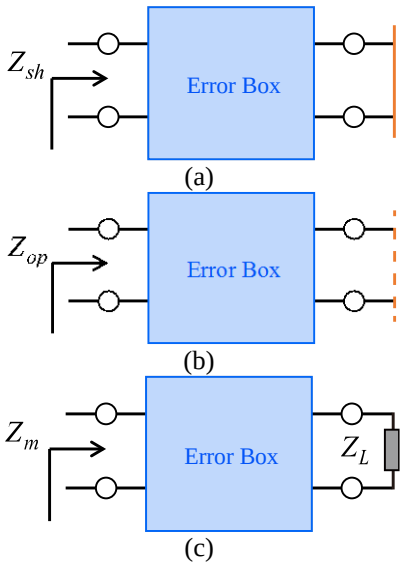

Fig. 2. The three calibration standards in SOL technique: (a) short standard, (b) open standard, and (c) load standard.

For the short-circuited element (Z_L = 0), the input impedance (Z_{sh}) can be written as:

$$Z_{sh} = \frac{b}{d}. \tag{2}$$

For the open-circuited element (Z_L = ∞), the input impedance (Z_{op}) can be written as:

$$Z_{op} = \frac{a}{c}. \tag{3}$$

For the matched-load element (Z_L = Z_m), the input impedance (Z_m) can be written as:

$$Z_m = \frac{a * Z_m + b}{c * Z_m + d}. \tag{4}$$

Since the error box is a two-port reciprocal network, an additional equation can be written as:

$$a*d - b*c = 1. \tag{5}$$

By solving the equations (1)-(5), the ABCD-matrix of the error box can be expressed as:

$$\begin{bmatrix} a & b \\ c & d \end{bmatrix} = \begin{bmatrix} cZ_{op} & \dfrac{Z_{sh}}{c\left(Z_{op} - Z_{sh}\right)} \\ c & \dfrac{1}{c\left(Z_{op} - Z_{sh}\right)} \end{bmatrix}. \tag{6}$$

Where:

$$c = \frac{\sqrt{Z_{sh} - Z_m}}{\sqrt{Z_m (Z_m - Z_{op})(Z_{op} - Z_{sh})}}. \tag{7}$$

B. SOC de-embedding technique

Different from the SOL technique, only the short and open standards are needed in SOC de-embedding process. The network parameters of *i-th* (i = 1, 2) error box can be modeled in terms of the FEM-calculated equivalent voltages, expressed as [28]:

$$[X_i] = \begin{bmatrix} \dfrac{\bar{V}_{io}' \bar{V}_{is}}{\bar{V}_{io} - \bar{V}_{is}} & -\dfrac{\bar{V}_{io}' \bar{V}_{is}}{\bar{V}_{io} - \bar{V}_{is}} \\ -\dfrac{1}{\bar{V}_{io}'} & \dfrac{\bar{V}_{io}'}{\bar{V}_{io}'} \end{bmatrix}. \tag{8}$$

Finally, by removing the ABCD-matrix of the error boxes from the whole cascading network, the desired ABCD-matrix of the core circuits can be derived. These two calibration methods are effective and efficient to estimate the ABCD matrix of the error boxes. Subsequently, the effective characteristic impedance and complex propagation constants of the discussed periodic structure can be calculated in terms of the obtained ABCD matrix (with elements a_p, b_p, c_p, d_p), such that:

$$\cosh(\gamma L) = \frac{a_p + d_p}{2}, \tag{9}$$

$$Z_0 = \sqrt{\frac{b_p}{c_p}}. \tag{10}$$

III. NUMERICAL EXAMPLES

A. Modeling of AFSIW by using HFSS-SOL

The AFSIW has advanced features such as low-loss and high power-handling capability, which can be widely used to design various kinds of microwave and millimeter wave components [2-4]. As demonstrated in Fig. 3, the cross-sectional view and top view of the AFSIW geometry are clearly shown. Different from the conventional SIW structure, the central region within the upper and lower conductor layers is partially removed out. The distance between the two rows of the metallic via-holes is W1, and the width of the air-filled region is W2. The dimension of the via-hole is *d* and the periodicity of the shorting via is *T*. Herein, the dielectric substrate Arlon AD255A with relative permittivity of ε_r = 2.55, dielectric loss tangent of tanδ = 0.0015, the height of h = 0.5 mm is selected into the design prototype.

As depicted in Fig. 4, the dispersion diagram of the AFSIW under the different air-filled ratios of W2/W1 illustrates the unique dispersive variations of the phase and attenuation constants. In order to inherently acknowledge the attenuation constant variation, here during the simulation, only the dielectric loss is brought into the modeling, without considering the conductor loss. As can be seen in Fig. 4 (a), as the air-filled region is gradually extended with *W2*/*W1* = 0.8, the attenuation constant generated by the dielectric loss is obviously reduced lower than the value of 0.1. This phenomenon validates the low-loss feature caused by the air-filled

configuration of the AFSIW structure. As further shown in Fig. 4 (b), the cut-off frequency of AFSIW as a function of the varied air-filled ratios is obtained. Also, the real and imaginary part of the characteristic impedances under different air-filled ratios are accurately extracted, as exhibited in Figs. 5 (a) and (b), respectively.

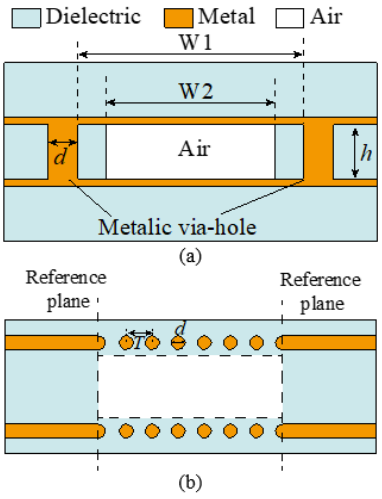

Fig. 3. The geometry of AFSIW: (a) cross-sectional view, and (b) top view of AFSIW with the feeding structures.

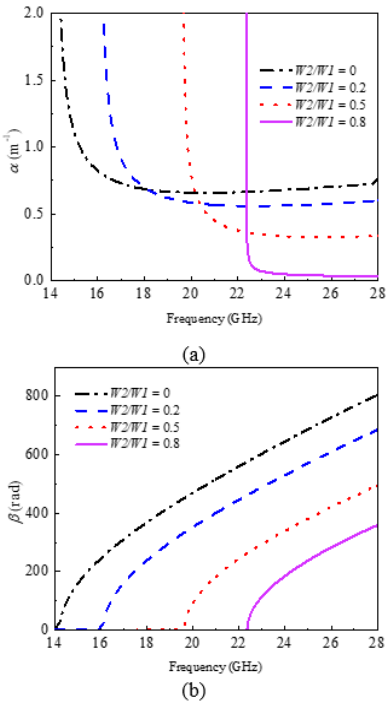

Fig. 4. The dispersion curves of the AFSIW under different dimensions of the air-filled region: (a) attenuation constant, and (b) propagation constant.

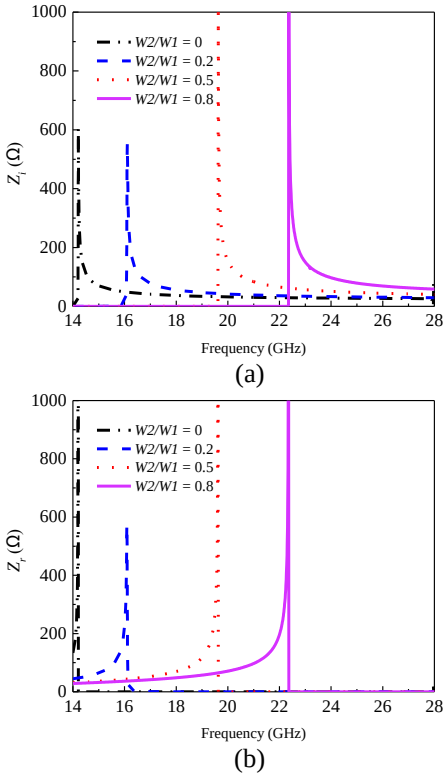

Fig. 5. The extracted characteristic impedance of the AFSIW under different dimensions of the air-filled region: (a) real part and (b) imaginary part.

B. Pin-loaded microstrip line modeled by FEM-SOC

Geometry of the microstrip line with periodical loading of shorting pins is detailly expressed in Fig. 6 (a). Here, the dielectric substrate with relative permittivity of ε_r = 2.65 and height of h = 3.0 mm is selected into the design. The key dimensional parameters of the discussed pin-loaded microstrip line are d = 1.6 mm, T = 15.0 mm, and W = 15.0 mm.

Superiorly, the FEM-SOC does not require the absorbing boundary condition at the port, and the pre-knowledge of the port information is also exempted. Thereby, arbitrary non-uniform feeding structures can be utilized for de-embedding. Here in Fig. 6 (b), two types of feeding mechanisms are used to excite the periodic structure, i.e., Case I with the uniform feeding line and Case II with the non-uniform feeding line.

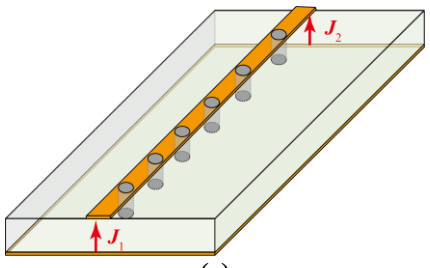

(a)

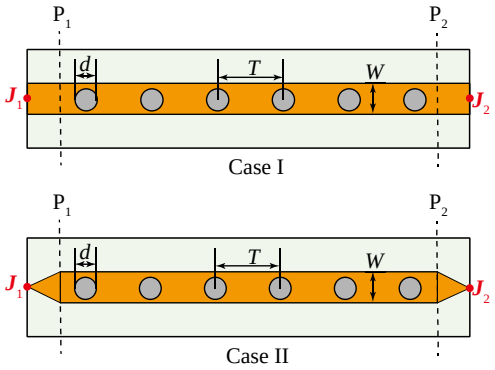

(b)

Fig. 6. Geometry of the microstrip line with the periodic shorting pins: (a) 3D view and (b) top view of the microstrip line with the periodic shorting pin with different feeding mechanisms: Case I with the uniform feeding line; Case II with the non-uniform feeding line.

As verified in Fig. 7, even if the non-uniform feeding mechanism is used, the extracted complex propagation constants and effective characteristic impedance are still remaining in good accordance with the uniform case, which reveals the strong robustness of the proposed FEM-SOC.

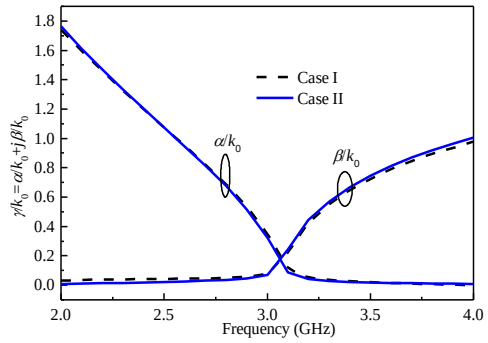

(a)

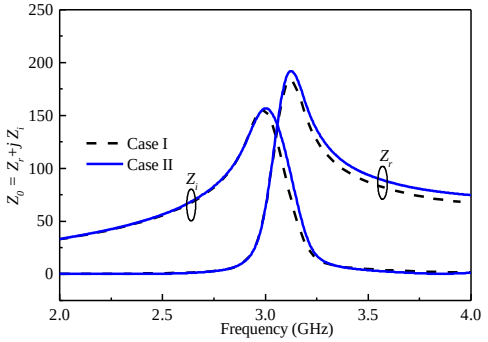

(b)

Fig. 7. The extracted parameters of the pin-loaded microstrip line under different feeding mechanisms: (a) complex propagation constants, and (b) effective characteristic impedance.

V. CONCLUSION

In this paper, de-embedding and modeling of periodic guided-wave structures using SOC/SOL technique in FEM have been presented. After removing the port discontinuities, effective propagation parameters of core periodic structures can be accurately determined. Separately, the HFSS-SOL is proved to have an extremely wide applicability, and FEM-SOC intrinsically owns a remarkable flexibility to implement the feeding structures. Evidently, these two techniques are believed to be highly effective and efficient, which can accurately characterize various kinds of guided-wave structures with periodic configurations.

ACKNOWLEDGMENT

This work was supported in part by the National Natural Science Foundation of China through the General Program under Grant 61571468, in part by the Macao Science and Technology Development Fund through the FDCT Research Grant under Grant 091/2016/A2, in part by the University of Macau through the CPG Research Grant under Grant CPG2017-00028-FST and the Multi-Year Research Grant under Grant MYRG2017-00007-FST.

REFERENCES

[1] F. Xu, K. Wu, and W. Hong, "Domain decomposition FDTD algorithm combined with numerical TL calibration technique and its application in parameter extraction of substrate integrated circuits," *IEEE Trans. Microw. Theory Techn.*, vol. 54, no. 1, pp. 329-338, Jan. 2006.

[2] N. Ranjkesh and M. Shahabadi, "Reduction of dielectric losses in substrate integrated waveguide," *Electron. Lett.*, vol. 42, no. 21, pp. 1230-1231, Oct. 2006.

[3] F. Parment, A. Ghiotto, T. Vuong, J. Duchamp, and K. Wu, "Air-filled substrate integrated waveguide for low-loss and high power-handling millimeter-wave substrate integrated circuits," *IEEE Trans. Microw. Theory Tech.*, vol. 63, no. 4, pp. 1228-1238, Apr. 2015.

[4] N. B.-Makou and A. A. Kishk, "Contactless air-filled substrate integrated waveguide," *IEEE Trans. Microw. Theory Tech*, vol. 66, no. 6, pp. 2928-2935, June 2018.

[5] C. Caloz and T. Itoh, *Electromagnetic Metamaterials: Transmission Line Theory and Microwave Applications*. John Wiley & Sons, IEEE Press, 2005.

[6] R. E. Collin, *Foundation of Microwave Engineering*. 1st ed., New York, USA: McGraw-Hill, 1966.

[7] ANSYS [Online]. Available: https://www.ansys.com

[8] CST Computer Simulation Technology [Online]. Available: http://www.cst.com/

[9] L. Zhu and K. Wu, "Unified equivalent-circuit

model of planar discontinuities suitable for field theory-based CAD and optimization of M(H)MIC's," *IEEE Trans. Microw. Theory Tech.*, vol. 47, no. 9, pp. 1589-1602, Sep. 1999.

[10] J. C. Rautio, "A de-embedding algorithm for electromagnetics," *Int. J. RF Microw. Comput.-Aided Eng.*, vol. 1, no. 3, pp. 282-287, July 1991.

[11] Z. J. Cendes and J.-F. Lee, "The transfinite element method for modeling MMIC devices," *IEEE Trans. Microw. Theory Techn.*, vol. 36, no. 12, pp. 1639-1649, Dec. 1988.

[12] P. Li, L. J. Jiang, Y. J. Zhang, S. Xu, and H. Bagci, "An efficient mode based domain decomposition hybrid 2D/Q-2D finite-element time-domain method for power/ground plate-pair analysis," *IEEE Trans. Microw. Theory Techn.*, vol. 66, no. 10, pp. 4357-4366, Oct. 2018.

[13] P. Li, L. J. Jiang, and H. Bagci, "Transient analysis of dispersive power-ground plate-pairs by DGTD method with wave port excitation," *IEEE Trans. Electromagn. Compat.*, vol. 59, no. 1, pp. 172-183, Feb. 2017.

[14] J. C. Rautio and V. I. Okhmatovski, "Unification of double-delay and SOC electromagnetic de-embedding," *IEEE Trans. Microw. Theory Techn.*, vol. 53, no. 9, pp. 289-292, Sep. 2005.

[15] J. C. Rautio, "Deembedding the effect of a local ground plane in electromagnetic analysis," *IEEE Trans. Microw. Theory Techn.*, vol. 53, no. 2, pp. 770-776, Feb. 2005.

[16] E. D. Caballero, A. Belenguer, H. Esteban, and V. E. Boria, "Thru-reflect-line calibration for substrate integrated waveguide devices with tapered microstrip transitions," *Electron. Lett.*, vol. 49, no. 2, pp. 132-133, Jan. 2013.

[17] X.-P. Chen and K. Wu, "Accurate and efficient design approach of substrate integrated waveguide filter using numerical TRL calibration technique," in *IEEE MTT-S Int. Microw. Symp. Dig.*, pp. 1231-1234, June 2008.

[18] L. Han, K. Wu, X.-P. Chen, and F. He, "Accurate analysis of finite periodic substrate integrated waveguide structures and its applications," in *IEEE MTT-S Int. Microw. Symp. Dig.*, pp. 864-867, May 2010.

[19] K. W. Eccleston, "A new interpretation of through-line (TL) calibration," *IEEE Trans. Microw. Theory and Techn.*, vol. 64, no. 11, pp. 3887-3893, Nov. 2016.

[20] L. Li and K. Wu, "Numerical through-resistor (TR) calibration technique for modeling of microwave integrated circuits," *IEEE Microw. Guided Wave Lett.*, vol. 14, no. 4, pp. 139-141, Apr. 2004.

[21] M. A. Eberspächer and T. F. Eibert, "Dispersion analysis of complex periodic structures by full-wave solution of even-odd-mode excitation problems for single unit cells," *IEEE Trans. Antennas Propag.*, vol. 61, no. 12, pp. 6075-6083, Dec. 2013.

[22] L. Zhu, "Guided-wave characteristics of periodic coplanar waveguides with inductive loading - unit-length transmission parameters," *IEEE Trans. Microw. Theory Tech.*, vol. 51, no. 10, pp. 2133-2138, Oct. 2003.

[23] J. Gao and L. Zhu, "Characterization of infinite- and finite-extent coplanar waveguide metamaterials with varied left- and right-handed passbands," *IEEE Microw. Wireless Comp. Lett.*, vol. 15, no. 11, pp. 805-807, Nov. 2005.

[24] Q.-S. Wu and L. Zhu, "Numerical de-embedding of effective wave impedances of substrate integrated waveguide with varied via-to-via spacings," *IEEE Microw. Wireless Compon. Lett.*, vol. 26, no. 1, pp. 1-3, Jan. 2016.

[25] D. Xie, L. Zhu, and X. Zhang, "An EH_0-mode microstrip leaky-wave antenna with periodical loading of shorting pins," *IEEE Trans. Antennas Propag.*, vol. 65, no. 7, pp. 3419–3426, May. 2017.

[26] L. Zhu, Q.-S. Wu, and S.-W. Wong, "Numerical SOC/SOL calibration technique for de-embedding of periodic guided-wave structures," in *2016 IEEE Int. Conf. on Comput. Electromagn.* (ICCEM), Feb. 2016.

[27] Y. Li, S. Sun, and L. Zhu, "Numerical modeling and de-embedding of non-planar periodic guided-wave structures via short-open calibration in 3-D FEM algorithm," *IEEE Access* (in Press).

[28] Y. Li and L. Zhu, "A short-open calibration method for accurate de-embedding of 3-D non-planar microstrip line structures in finite element method," *IEEE Trans. Microw. Theory Tech.*, vol. 66, no. 3, pp. 1172-1180, Mar. 2018.

On the Application of Continuity Condition in the Volume-Surface Integral Equation for Composite Closed PEC-Electrical Anisotropy Objects

Jinbo Liu [1], Zengrui Li [1], Jiming Song [2], and Limei Luo [1]

[1] School of Information and Communication Engineering
Communication University of China, Beijing, 100024, P. R. China
liuj@cuc.edu.cn, zrli@cuc.edu.cn, luolimei@cuc.edu.cn

[2] Department of Electrical and Computer Engineering
Iowa State University, Ames, Iowa 50011, USA
jisong@iastate.edu

Abstract ─The validity of the use of continuity condition (CC), combined with the volume-surface integral equation (VSIE), is studied when it is explicitly enforced on the closed perfect electric conductor (PEC)-electrical anisotropy interfaces. It is found that if the standard magnetic field integral equation (MFIE) is involved in the VSIE to model the closed PEC surfaces, the solution might be inaccurate, especially when the CC is enforced. The reason for this phenomenon is discussed, and two previously reported approaches are adopted to improve the accuracy of MFIE. Numerical results show that whether the CC is enforced or not, the improvement of the MFIE will result in more accurate VSIE solution.

Index Terms ─ Continuity condition, electrical anisotropy, method of moments (MoM), volume-surface integral equation (VSIE).

I. INTRODUCTION

Electromagnetic (EM) problems involving anisotropic dielectrics and perfect electric conductors (PECs) are of great interest in the field of EM simulation. The development of new materials has created an urgent need for accurate EM solvers for analyzing the EM radiation or scattering properties of composite PEC-complex dielectric objects. Among the numerous numerical calculation methods, the volume-surface integral equation (VSIE) [1], in conjunction of the method of moments (MoM) [2], is one of the most competitive methods to analyze the general composite objects involving both PECs and dielectrics. In addition to its advantages, the VSIE suffers from large number of unknowns since three dimensional discretization of volumetric dielectrics is required to model the dielectrics. However, lots of the composite objects are composed of PECs and dielectrics in any arbitrarily contact. For these kinds of problems, the continuity condition (CC):

$$\hat{n}(\vec{r})\bullet\vec{D}(\vec{r}) = \rho_s(\vec{r}) = -\frac{\nabla\bullet\vec{J}_S(\vec{r})}{j\omega}, \tag{1}$$

that relates the electric flux density and the surface electric current can be explicitly enforced on the PEC-dielectric interfaces to eliminate the associated volume unknowns as well as to reduce the memory usage, and the larger the size of contact surface, the more saving of the memory is expected [1, 3-6]. In (1), $j=\sqrt{-1}$, ω is angular frequency, $\vec{D}$ is the electric flux density in the dielectrics, and $\vec{J}_S$ and ρ_s are the equivalent surface electric current and charge density on the PEC surfaces, respectively. Some previous articles have focus on the use of CC. In [1, 3, 4], how the CC is adopted in the VSIE was discussed. However, whether the PEC surfaces are open or closed was not considered, and the validity was not studied rigorously. In [5], for the higher-order Legendre basis functions with the property of orthogonality, the CC can be explicitly enforced on any PEC-electrical isotropy interfaces. Nevertheless, when the lower-order basis functions are adopted, whether the use of CC is still valid was not discussed. In [6], the validity of the use of CC was investigated. It is stated that if the involved PEC surfaces are open, $\vec{J}_S$ is actually the summation of currents densities residing on both sides [12]. In other words, the single combined current $\vec{J}_S$ only has mathematical significance but no physical meaning. In this case, the explicit enforcement of CC in the VSIE might lead to inaccurate results. Besides, [6] also provides a convenient way to embed it into the context of the multilevel fast multipole algorithm (MLFMA).

Nevertheless, the previous articles focused on the objects involving electrical isotropic dielectrics. As we know, the properties of anisotropic dielectrics are very different from the isotropic ones: for inhomogeneous isotropic dielectrics, the constitutive relation between $\vec{D}$ and the electric field $\vec{E}$ is $\vec{D}(\vec{r})=\varepsilon(\vec{r})\vec{E}(\vec{r})$.The equivalent

Submitted On: October 12, 2018
Accepted On: December 21, 2018

volume electric current is defined as $\vec{J}_V(\vec{r})=[\varepsilon(\vec{r})-\varepsilon_0]\vec{E}(\vec{r})$, where the permittivity $\varepsilon(\vec{r})$ is a scalar value with the free space permittivity ε_0 [1]. On the contrary, for the inhomogeneous anisotropic dielectrics, the constitutive relation is changed into $\vec{D}(\vec{r})=\bar{\bar{\varepsilon}}(\vec{r})\cdot\vec{E}(\vec{r})$ with $\vec{J}_V(\vec{r})=\left[\bar{\bar{\varepsilon}}(\vec{r})-\varepsilon_0\bar{\bar{I}}\right]\cdot\vec{E}(\vec{r})$, while $\bar{\bar{\varepsilon}}(\vec{r})$ is a tensor, and $\bar{\bar{I}}$ is the identity tensor. From the above, although the use of CC in the VSIE for the composite PEC-electrical isotropy objects has been well verified, we still want to know whether the CC is valid when the involved dielectrics are electrical anisotropic. Because (1) conforms to the current continuity equation that is independent of the type of medium, the CC can also be adopted to the PEC-electrical anisotropy interfaces. In addition, for the SIE part of VSIE, the electric field integral equation (EFIE) is commonly adopted since it can be used to model both the open and closed PEC surfaces. For the closed PEC surfaces of composite object, the magnetic field integral equation (MFIE) can be added to the EFIE to form a well-conditioned combined field integral equation (CFIE). But since the standard MFIE is inaccurate to some extent [7-9], the application of MFIE might have a negative effect on the accuracy of VSIE solution, especially when the CC is enforced.

In this paper, the validity of explicit enforcement of CC for the objects containing PEC-electrical anisotropy interfaces is investigated. In addition, when the MFIE is involved in modeling the PEC surfaces, the calculation accuracy of the VSIE with or without enforcing the CC is discussed. Furthermore, both approaches shown in [8, 9] are adopted to improve the accuracy of MFIE, and the numerical results show that this improvement can provide more accurate VSIE solution, especially when the CC is enforced.

II. THEORY AND FOMULATIONS

Consider an arbitrary PEC surface *S*, wholly or partially covered by electrical anisotropic dielectrics with permittivity tensor $\bar{\bar{\varepsilon}}(\vec{r})$ occupying a region *V*, as shown in Fig. 1. For the convenience of analysis, it is assumed that this composite object is suspended in free space with permittivity ε_0 and permeability μ_0, and illuminated by a plane EM wave $\left[\vec{E}^i(\vec{r}),\vec{H}^i(\vec{r})\right]$ at an arbitrary angle (θ^i, φ^i).The scattering field $\left[\vec{E}^s(\vec{r}),\vec{H}^s(\vec{r})\right]$ is the superposition of fields produced by the equivalent surface electric current $\vec{J}_S$ on *S* and the equivalent volume electric current $\vec{J}_V$ in *V* as:

$$\begin{cases}\vec{E}^s(\vec{r})=\vec{E}_S^s(\vec{r})+\vec{E}_V^s(\vec{r})\\ \vec{H}^s(\vec{r})=\vec{H}_S^s(\vec{r})+\vec{H}_V^s(\vec{r})\end{cases}, \tag{2}$$

with

$$\begin{cases}\vec{E}_T^s(\vec{r})=-j\omega\vec{A}_T(\vec{r})-\nabla\varphi_T(\vec{r})\\ \vec{H}_T^s(\vec{r})=\dfrac{1}{\mu_0}\nabla\times\vec{A}_T(\vec{r})\end{cases}\quad T\in S\ or\ V. \tag{3}$$

The vector potential $\vec{A}_T$ and scalar potential φ_T are expressed as the convolutions of equivalent electric current or its divergence and the Green's function as:

$$\begin{cases}\vec{A}_T(\vec{r})=\mu_0\int_T\vec{J}_T(\vec{r}')\dfrac{e^{-jk|\vec{r}-\vec{r}'|}}{4\pi|\vec{r}-\vec{r}'|}dT'\\ \varphi_T(\vec{r})=\dfrac{j}{\omega\varepsilon_0}\int_T\nabla'\bullet\vec{J}_T(\vec{r}')\dfrac{e^{-jk|\vec{r}-\vec{r}'|}}{4\pi|\vec{r}-\vec{r}'|}dT'\end{cases}. \tag{4}$$

On the PEC surfaces *S*, the EFIE is formed based on the PEC boundary condition that requires vanishing the tangential component of total electric field as:

$$\hat{n}(\vec{r})\times\vec{E}(\vec{r})=\hat{n}(\vec{r})\times\left[\vec{E}^i(\vec{r})+\vec{E}^s(\vec{r})\right]=0\quad\vec{r}\in S. \tag{5}$$

Furthermore, for the closed PEC surfaces, the MFIE:

$$\vec{J}_S(\vec{r})-\hat{n}(\vec{r})\times\vec{H}^s(\vec{r})=\hat{n}(\vec{r})\times\vec{H}^i(\vec{r})\quad\vec{r}\in S^+, \tag{6}$$

where $\vec{r}\in S^+$ means that the field point $\vec{r}$ approaches to *S* from outside, can be added to the EFIE to form the well-conditioned CFIE as:

$$CFIE=\alpha EFIE+(1-\alpha)\eta_0 MFIE. \tag{7}$$

In (7), α ($0\leqslant\alpha\leqslant1$) is a real constant, and η_0 is the intrinsic impedance in the free space. Obviously, when α=1 or 0, the CFIE degrades into EFIE or MFIE.

The total electric field in the regions *V* is a superposition of the incident and scattering electric fields which can be written as the so-called volume integral equation (VIE):

$$\vec{E}(\vec{r})=\left[\bar{\bar{\varepsilon}}(\vec{r})\right]^{-1}\bullet\vec{D}(\vec{r})=\vec{E}^i(\vec{r})+\vec{E}^s(\vec{r})\quad\vec{r}\in V. \tag{8}$$

Thus, (7) and (8) can be combined together to build the CFIE-VIE which is a second-kind VSIE form to solve EM problems of composite objects involving closed PEC surfaces and electrical anisotropic dielectrics.

Using the Galerkin's MoM, the VSIE is converted into a matrix equation. In the implementation of this paper, the lower-order RWG basis function [10] and SWG basis function [11] are used to disperse $\vec{J}_S$ on the PEC surface and $\vec{D}$ in the dielectric region as:

$$\begin{cases}\vec{J}_S(\vec{r})=\sum_{i=1}^{N_S}I_i^S\vec{f}_i^S(\vec{r})\\ \vec{D}(\vec{r})=\dfrac{1}{j\omega}\sum_{i=1}^{N_V}I_i^V\vec{f}_i^V(\vec{r})\end{cases}, \tag{9}$$

respectively. In (9), N_S and N_V are the numbers of the RWG basis functions $\vec{f}_i^S$ and SWG basis functions $\vec{f}_i^V$, while I_i^S and I_i^V are the corresponding unknown expansion coefficients, respectively. Dispersing $\vec{D}$ instead of $\vec{J}_V$ can hold the continuity of normal component which is consistent with the boundary condition on dielectric interfaces [11]. In this case,

$$\begin{aligned}\vec{J}_V(\vec{r})&=\left[\bar{\bar{\varepsilon}}(\vec{r})-\varepsilon_0\bar{\bar{I}}\right]\bullet\left[\bar{\bar{\varepsilon}}(\vec{r})\right]^{-1}\bullet\vec{D}(\vec{r})\\ &=\frac{1}{j\omega}\sum_{i=1}^{N_V}I_i^V\left\{\bar{\bar{I}}-\varepsilon_0\left[\bar{\bar{\varepsilon}}(\vec{r})\right]^{-1}\right\}\bullet\vec{f}_i^V(\vec{r})\end{aligned}. \tag{10}$$

At the exterior boundary of dielectrics, since $\vec{D}$ is not necessarily zero, a "half" SWG basis function associated with only one tetrahedron needs to be defined [11]. However, if an exterior face of the only tetrahedron is terminated by a PEC triangular patch as well as this triangular patch exactly coincides with the exterior face, this "half" SWG function can be removed by using the CC. As mentioned in [3], according to (1) and (9), the coefficient I_p^V associated to the pth "half" SWG basis function $\vec{f}_p^S$ can be directly calculated by:

$$I_p^V = -\frac{\sum_{k\in M_S} I_k^S \nabla\bullet\vec{f}_k^S(\vec{r})}{\hat{n}(\vec{r})\bullet\vec{f}_p^V(\vec{r})}. \tag{11}$$

In (11), M_s is a set of RWG basis functions index defined on the corresponding PEC triangle. That is to say, when the CC is enforced, according to (11), the equivalent volume electric current associated to the PEC-electrical anisotropy interfaces (denoted by $\vec{J}_{VS}$) can be directly calculated by the $\vec{J}_S$ defined on the corresponding PEC surface. It is worth to mention that for the numerator of (11), since $\vec{f}_k^S$ is the RWG basis function defined over triangles, $\nabla\cdot\vec{f}_k^S$ is a constant over the whole triangle area [10]; while for the denominator, $\vec{f}_p^V$ is the SWG basis function defined over tetrahedrons, so $\hat{n}\cdot\vec{f}_p^V$ is also a constant over the tetrahedron surface [11].

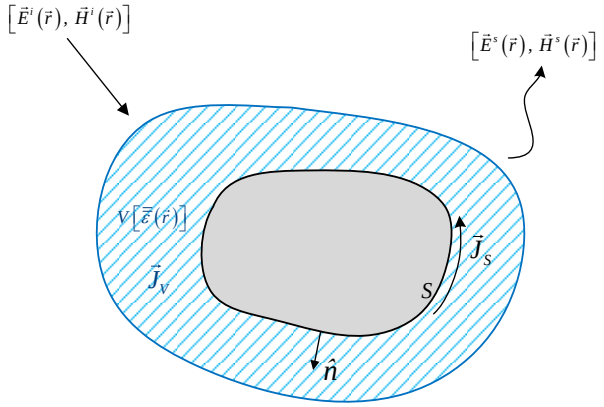

Fig. 1 Composite PEC-electrical anisotropy object under plane EM wave illumination.

III. NUMERICAL RESULTS AND DISCUSSION

In this section, we will present the bistatic radar cross section (RCS) results of a PEC sphere coated with homogeneous electrical anisotropic dielectric, while the target residual error in iterative solvers is fixed to 0.001. The Gaussian quadrature rule with 4/5 sampling points is applied to the inner or outer triangle/tetrahedron integrations during calculating the interactions between the testing and basis functions.

The radius of the PEC sphere is 0.5λ (λ is the wavelength in free space), the coating thickness is 0.075λ, and the permittivity tensor of the electrical anisotropy is:

$$\bar{\bar{\varepsilon}} = \varepsilon_0 \begin{bmatrix} 3 & -j & 0 \\ j & 3 & 0 \\ 0 & 0 & 5 \end{bmatrix}. \tag{12}$$

After discretization with an appropriate average mesh size, the total number of triangles, tetrahedrons and unknowns are 1,380, 5,955 and 15,565, respectively. The coated PEC sphere is illuminated by a θ-polarized plane wave with the incident angle θ^i=0, φ^i=0, and the observation range is $0\leqslant\theta\leqslant180°$ and φ=0. Both the CFIE-VIE and that enforced the CC (CC-CFIE-VIE) with different α values are used during the calculation, while the results are shown in Fig. 2. The exact result from Mie series is also given in this figure as a reference. It is seen that the numerical results agree well with the exact result in most angles. However, over the valley range (in this case, 137~143°), the difference of these results is evident, as shown in Fig. 3. For α=1, the results with and without CC are in excellent agreement, and the average difference of the results obtained from the CFIE-VIE and CC-CFIE-VIE over the valley range is about 0.23 dB. However, for α=0.5, the average difference of the results over the valley range is about 0.80 dB. While for α=0, this difference extends to about 0.94 dB. On the other hand, if more sampling points are used over the outer triangular integrations in the MFIE (from 4 to 16) and keep other parameters unchanged, the average differences over the valley range for α=0.5 and α=0 are reduced to 0.31 dB and 0.61 dB, respectively, as shown in Fig. 4. This phenomenon is similar to that stated in [8]: for the type of the SIE part of the VSIE, the EFIE is known to give accurate $\vec{J}_S$ with the use of RWG basis function for the PEC surfaces with arbitrary planar triangulations. On the contrary, for the MFIE, as mentioned in [7], two possible reasons may lead to the inaccuracy: 1) Overlooking the mild logarithmic singularity in the field integration with an insufficiently number of integration points inside the testing triangles; 2) The section of improper solid angle expression for the observation points. Therefore, when MFIE is involved in the CFIE-VIE (i.e., $\alpha\neq1$), the obtained $\vec{J}_S$ on the PEC surfaces may not be so accurate, leading to inaccurate $\vec{J}_{VS}$. Thus, when $\alpha\neq0$, the results from CFIE-VIE and CC-CFIE-VIE have a certain difference, and the greater proportion of MFIE occupied (i.e., the closer α is to 1), the larger the difference will be.

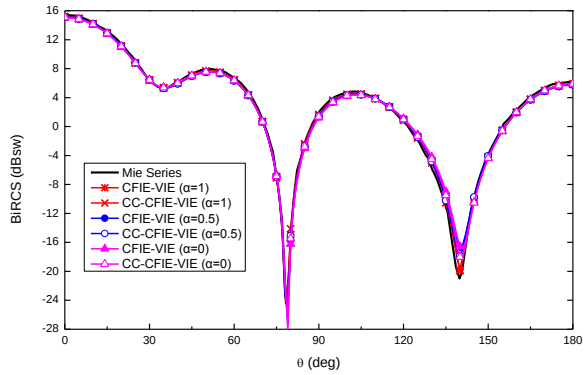

Fig. 2. Bistatic RCS for a PEC sphere of radius 0.5λ coated with 0.075λ thick homogeneous electrical anisotropic dielectric at φ=0°, illuminated by a θ-polarized plane wave with the incident angle θ^i=0, φ^i=0.

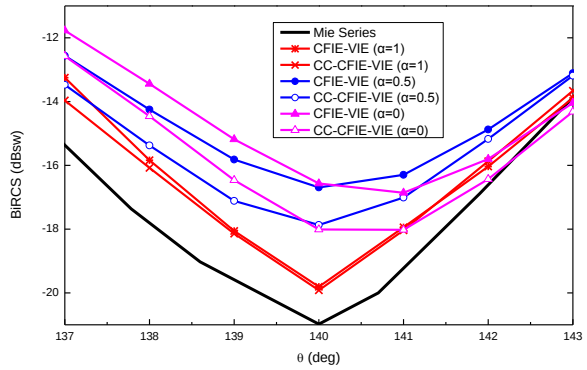

Fig. 3. Enlarged Fig. 2 at 137°⩽θ⩽143°.

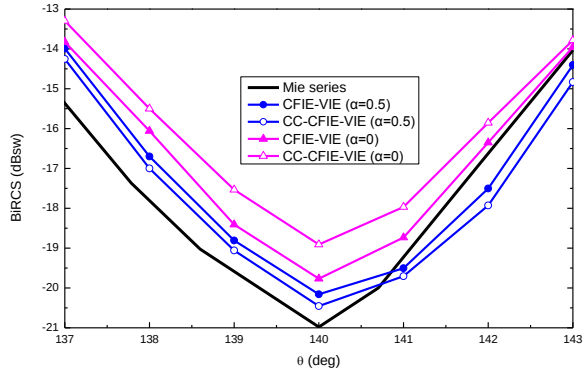

Fig. 4. Bistatic RCS of the coated PEC sphere at 137°⩽θ⩽143° and φ=0°, with 16 sampling points over the outer triangular integrations in the MFIE.

To verify the above conclusion, both of the two approaches stated in [8] and [9] are adopted to modify the standard MFIE (denoted by mMFIE): 1) extracting the logarithmic singularity during the computation of the outer integrals; 2) correcting the external solid angle of the surface at observation points. The detailed approaches can be found in [8, 9]. After the two modifications, when mMFIE is involved in the CFIE-VIE (denoted by mCFIE-VIE), more accurate $\vec{J}_S$ as well as $\vec{J}_{VS}$ are expected, and so do the numerical results. The same coated PEC sphere is calculated while the results are shown in Fig. 5. During the calculation, the Gaussian quadrature rule with 4 sampling points is applied to all the inner/outer triangular integrations. It is observed that compared to Fig. 3, the accuracy of the results have been greatly improved. In addition, the results with and without CC have a better agreement. The average differences of the results obtained from the CFIE-VIE and CC-CFIE-VIE over the valley range for α=0.5 and α=0 are reduced to 0.29 dB and 0.32 dB, respectively. From this calculation, we may draw the conclusion that accurate evaluating the matrix elements related to the MFIE part can improve the accuracy of CFIE-VIE solution, especially when the CC is enforced.

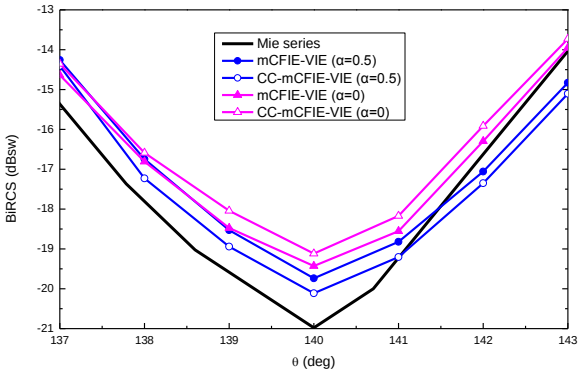

Fig. 5. Bistatic RCS of the coated PEC sphere at 137°⩽θ⩽143° and φ=0°, with the adoption of mMFIE.

IV. CONCLUSION

In this paper, the validity of explicit enforcement of CC for PEC objects coated electrical anisotropic dielectrics is investigated. It is found that possible inaccuracy may arise if the standard MFIE to model closed PEC surfaces is involved in the VSIE used, especially when the CC is enforced on the PEC-electrical anisotropy interfaces. After modifying the standard MFIE using the previously reported approaches, when the CC is enforced, more accurate equivalent surface electric current and the volume electric current associated to the PEC-electrical anisotropy interfaces are obtained.

ACKNOWLEDGMENT

This work was supported by the National Natural Science Foundation of China (61701447, 61671415, and 61331002), and the Fundamental Research Funds for the Central Universities (CUC2019B068).

REFERENCES

[1] W. C. Chew, J. M. Jin, E. Michielssen, and J. M. Song, *Fast and Efficient Algorithms in Computational Electromagnetics*. MA: Artech House, Boston, 2001.

[2] R. F. Harrington, *Field Computation by Moment Methods*. MacMillan, New York, 1968.

[3] C. C. Lu and W. C. Chew, "A coupled surface-volume integral equation approach for the calculation of electromagnetic scattering from composite metallic and material targets," *IEEE Trans. Antennas Propag.*, vol. 48, no. 12, pp. 1866-1868, Dec. 2000.

[4] K. Xiao, S .L. Chai, and L. W. Li, "Comparisons of coupled VSIE and noncoupled VSIE formulations," *Journal of Electromagnetic Waves & Applications*, vol. 25, no. 10, pp. 1341-1351, 2011.

[5] O. S. Kim, P. Meincke, O. Breinbjerg, and E. Jørgensen, "Solution of volume-surface integral equations using higher-order hierarchical Legendre basis functions," *Radio Science*, vol. 42, no. 4, pp. RS4023, 10.1029/2006RS003584.

[6] M. He, J. Liu, B. Wang, C. Zhang, and H. Sun, "On the use of continuity condition in the fast solution of volume-surface integral equation," *IEEE Antennas and Wireless Propagation Letters*, vol. 16, pp. 625-628, 2017.

[7] Ö. Ergül and L. Gürel, "Investigation of the inaccuracy of the MFIE discretized with the RWG basis functions," *Antennas & Propagation Society International Symposium*, vol. 3, pp. 3393-3396, Dec. 2004.

[8] L. Gürel and Ö. Ergül, "Singularity of the magnetic-field integral equation and its extraction," *IEEE Antennas and Wireless Propagation Letters*, vol. 4, pp. 229-232, 2005.

[9] J. M. Rius, E. Úbeda, and J. Parrón, "On the testing of the magnetic field integral equation with RWG basis functions in method of moments," *IEEE Trans. Antennas Propag.*, vol. 49, no. 11, pp. 1866-1868, Dec. 2001.

[10] S. M. Rao, D. R. Wilton, and A. W. Glisson, "Electromagnetic scattering by surfaces of arbitrary shape," *IEEE Trans. Antennas Propag.*, vol. 30, no. 5, pp. 409-418, May 1982.

[11] D. H. Schaubert, D. R. Wilton, and A. W. Glisson, "A tetrahedral modeling method for electromagnetic scattering by arbitrarily shaped inhomogeneous dielectric bodies," *IEEE Trans. Antennas Propag.*, vol. 32, no. 1, pp. 77-85, Jan. 1984.

[12] E. H. Neuman and M. R. Schrote, "On the current distribution for open surfaces," *IEEE Trans. Antennas Propag.*, vol. 31, no. 3, pp. 1550-1553, May 1983.

A Fourier Split-Step Based Wide-Angle Three-Dimensional Vector Parabolic Wave Equation Algorithm Predicting the Field Strength Over Flat and Irregular Forest Environments

Hafiz Faiz Rasool, Xiao-Min Pan*, and Xin-Qing Sheng

Center of Electromagnetic Simulation, School of Information and Electronics
Beijing Institute of Technology, Beijing, 100081, People's Republic of China
hafiz@bit.edu.cn, *xmpan@bit.edu.cn, xsheng@bit.edu.cn,

Abstract ─ This paper provides the analysis of radio wave propagation prediction over flat and irregular forest environments. A three-dimensional vector parabolic wave equation (3DPE) method is used to calculate the field strength due to the forest on a lossy ground. Forest terrains are equivalent to a series of absorbing blocks arranged along the direction of propagation. Under the assumption of forwarding propagation, a 3DPE is derived and the Fourier split-step based PE (SSPE) method is adopted to march the potentials from one aperture plane to the next. A Tukey window function is used to attenuate the fields smoothly at the upper boundary without reflections. Finally, the simulation results are compared with the analytical methods presented in the literature. The simulation results have shown the validity of the proposed algorithm.

Index Terms ─ Forest terrains, parabolic wave equation, radio wave propagation, split-step parabolic equation method, wave propagation prediction.

I. INTRODUCTION

Wave propagation is an important phenomenon in many applications. The analysis of ground wave propagation depends on the characteristics of the lower layer of the atmosphere and the terrain over which the wave propagates. Electromagnetic waves (EM) are affected by the propagation environments due to change in temperature, pressure, and humidity. Non-flat terrains, buildings, trees, and mountains also disturb the waves and lead to the variation of field strength [1].

In the rural and suburban areas, the forest is an important factor affecting the radio wave propagation over a long distance. Due to the absorption and scattering properties of the trees, the attenuation and phase shift of signals mostly happen which affects the target identification and other wireless communications greatly [2]. Therefore, it has very important practical application value to study the forest effect on wave propagation. Several empirical and deterministic methods have been presented in the literature for propagation analysis [3-5]. Empirical models require less computational effort, but these models do not consider the details of the local terrain topography. On the other hand, deterministic models require a vast amount of data regarding terrain profile, more computational resources and are more accurate than the empirical models [6,7]. The approaches based on parabolic equation (PE) are another way to predict the wave behavior, it was first introduced by Leontovich and Fock in the 1940s [8]. Later, it has become a popular method in EM wave propagation modeling. The PE method gets the environmental parameters as input, it accepts different boundary conditions (BCs) and allows to use different types of antenna patterns [9, 10]. Due to these characteristics, the PE method nowadays is a preferred method for solving radio wave propagation problems [11-13]. There are many numerical methods available to solve parabolic type wave equations such as Finite Difference method, Finite Element method, and Method of Moment in the literature [14], but the SSPE method is more suitable to solve PE for long-range propagation. This method is highly efficient both in memory usage and in runtime [15-19].

In recent years, many scholars have done some research on radio wave propagation problems in forest environments using PE method [20-25]. Still, these models are 2D in nature either it is based on scalar formulations or it has been designed for a small area.

The goal of this paper is to introduce the 3DPE method in a forest environment based on SSPE method, to predict the wave propagation due to the forest over a large area. It is shown that the 3DPE model can formulate both vertical and lateral wave propagation into account. The basic formulation of the 3DPE is discussed briefly, which is followed by the explanation of the SSPE method and the corresponding numerical implementation.

This paper is organized into five sections as follows. In the next section, the basic formulation of the wide-angle 3DPE is discussed. Section 3 presents the SSPE

Submitted On: October 24, 2018
Accepted On: April 3, 2019

solution to the proposed algorithm. In Section 4, numerical implementation steps are discussed such as initial field, domain discretization, boundary conditions, etc. Section 5 presents the simulation results and comparisons with the results presented in the literature.

II. FORMULATION OF THE 3DPE

In cartesian coordinates (*x*, *y*, *z*), considering the propagation in a homogeneous medium with refractive index *n* and supposing a time convention $e^{-i\omega t}$, where $\omega = 2\pi f$ is the radian frequency at the frequency *f*. Supposing that the fields are excited by a vertically polarized (z-oriented) sources at a given range x_0. The electric current density of the distributed source located at $x = 0$ is assumed to be $\vec{J}_z = I_0 l \delta(x)\delta(y) f^e(y,z)$, where $f^e(y,z)$ is the 2D Gaussian function, $I_0 l$ is the current moment and $\delta(\cdot)$ denote the unit delta function, respectively. Expressing the fields in terms of two z-oriented potentials, it is easy to see from Maxwell's equations that [26]:

$$E_z^e = \frac{i\eta_0}{n^2 k_0}\left(\frac{\partial^2}{\partial z^2} + k_0^2\right)\psi^e = E_z, \tag{1}$$

$$H_z^m = \frac{i}{\eta_0 k_0}\left(\frac{\partial^2}{\partial z^2} + k_0^2\right)\psi^m = H_z, \tag{2}$$

where ψ^e and ψ^m are the scalar potentials arising from the electric and magnetic currents, respectively. The superscripts "*e*" and "*m*" identify the sources (electric or magnetic) that give rise to the potentials and fields. The wavenumber and intrinsic impedance in free space are denoted by k_0 and η_0, respectively. The total fields $\vec{E} = \vec{E}^e + \vec{E}^m$ and $\vec{H} = \vec{H}^e + \vec{H}^m$ are decomposed in terms of a TEz mode and a TMz mode with constituent fields [27]:

$$\begin{aligned} E_x^e &= \frac{i\eta_0}{n^2 k_0}\frac{\partial^2 \psi^e}{\partial x \partial z}, \quad H_x^e = \frac{\partial \psi^e}{\partial y}, \\ E_y^e &= \frac{i\eta_0}{n^2 k_0}\frac{\partial^2 \psi^e}{\partial y \partial z}, \quad H_y^e = -\frac{\partial \psi^e}{\partial x}, \end{aligned} \tag{3}$$

$$\begin{aligned} E_x^m &= -\frac{\partial \psi^m}{\partial y}, \quad H_x^m = \frac{i}{\eta_0 k_0}\frac{\partial^2 \psi^m}{\partial x \partial z}, \\ E_y^m &= \frac{\partial \psi^m}{\partial x}, \quad H_y^m = \frac{i}{\eta_0 k_0}\frac{\partial^2 \psi^m}{\partial y \partial z}. \end{aligned} \tag{4}$$

Using this representation of the fields, and in a source-free region $\psi = \psi^e + \psi^m$ and thus from the Helmholtz equation, PE can be obtained as [9, 11]:

$$\left[\nabla^2 + k_0^2 n^2\right]\psi = 0, \tag{5}$$

where ∇^2 is the Laplacian operator and replacing ψ with $e^{-ik_0 x}\psi$, the wide-angle 3DPE can be obtained as [28, 29]:

$$\frac{\partial \psi}{\partial x} = ik_0(n-2) + i\sqrt{k_0^2 + \left(\frac{\partial^2}{\partial y^2} + \frac{\partial^2}{\partial z^2}\right)}\psi. \tag{6}$$

III. FOURIER SPLIT-STEP ALGORITHM

In numerical analysis, the Fourier split-step method is a type of pseudo-spectral method used to solve highly nonlinear time-dependent partial differential equations in engineering and physics applications [30]. We are briefly explaining this method as in [31]. Starting from (6) and introducing the two operator's *M* and *N* as:

$$\frac{\partial \psi}{\partial x} = \left[M(x,y,z) + N(y,z)\right]\psi, \tag{7}$$

$$M = ik_0(n-2), \quad N = i\sqrt{k_0^2 + \left(\frac{\partial^2}{\partial y^2} + \frac{\partial^2}{\partial z^2}\right)}. \tag{8}$$

Supposing that Δx is the range incremental step size, then the split-step solution at $x + \Delta x$ can be written as:

$$\psi(x+\Delta x, y, z) = e^{\int_x^{x+\Delta x} M(x,y,z)dx + \int_x^{x+\Delta x} N(y,z)}\psi(x,y,z), \tag{9}$$

the operator $[M(x,y,z) + N(y,z)]$ does not commute in this integral. With the assumption that the refractive index *n* is slowly varying at each small range step Δx in yz-plane then it can be formally expressed as [32]:

$$\psi(x+\Delta x, y, z) \simeq e^{M\Delta x + N\Delta x} = e^{M\Delta x} e^{N\Delta x}\psi(x,y,z). \tag{10}$$

In the approximated exponentials, the term $e^{M\Delta x}$ is a multiplication operator which can be solved numerically easily, while the exponential operator $e^{N\Delta x}$ is a differential operator which can be solved with the help of Fourier transform. Let $\psi = F_2^{-1}\left[F_2(\psi)\right]$, similarly,

$$e^{N\Delta x}\psi(x,y,z) = F_2^{-1}\left[F_2\left\{e^{N\Delta x}\psi(x,y,z)\right\}\right], \tag{11}$$

where F_2 and F_2^{-1} denote the 2D Fourier transforms and it's inverse Fourier transforms respectively. Equation (10) can be written as:

$$\psi(x+\Delta x, y, z) = e^{M\Delta x} F_2^{-1}\left[F_2\left\{e^{N\Delta x}\psi(x,y,z)\right\}\right], \tag{12}$$

using (8) and (12), one can get the SSPE solution for the wide-angle 3DPE as [29]:

$$\psi(x+\Delta x, y, z) = e^{ik_0\Delta x(n-2)} \times F_2^{-1}\left[e^{ik_x\Delta x} F_2\left\{\psi(x,y,z)\right\}\right], \tag{13}$$

where $k_x = \sqrt{k_0^2 - k_y^2 - k_z^2}$ is the wavenumber along the range axis for a plane wave traveling in the (k_y, k_z) direction. Here, k_y and k_z are the Fourier transform domain variables. It is the solution of an electromagnetic wave when the refractive index *n* is varying slowly at each small range step Δx in a homogeneous medium.

IV. NUMERICAL IMPLEMENTATION

In this section, we have discussed some important implementation steps for the numerical simulation of the proposed algorithm.

A. Boundary conditions

The PE model requires BCs to avoid the reflection at $z = \pm z_{\max}$ and $y = \pm y_{\max}$ along the *y* and *z* axes, respectively. An absorbing boundary condition is used in this paper as:

$$W(j,k) = w(j) \cdot w(k), \quad j = 1:N_y, k = 1:N_z, \qquad (14)$$

where *w* is the Tukey window function, with $N(N_y, N_z)$ being the Fourier transform size. [33]. Therefore, the potential at (*x*, *y*, *z*) is finally computed as:

$$\psi(i\Delta x, j\Delta y, k\Delta z) = \psi(i\Delta x, j\Delta y, k\Delta z) \cdot W(j,k). \qquad (15)$$

Besides, the forest terrain surface is assumed to be a lossy and trees are equivalent to a series of absorbing blocks arranged along the direction of propagation.

B. Domain discretization

The domains are truncated at $\pm z_{\max}$ and $\pm y_{\max}$ (maximum distance along the *y*– and *z* directions). The step size along *x*, *y*, and *z* directions defined as Δx, Δy and Δz respectively. Maximum altitude $z_{\max}$ is determined from the source/observation requirements to minimize the aliasing effects. Once $z_{\max}$ or $y_{\max}$ is decided then $k_{y\max}$ and $k_{z\max}$ are calculated from the Nyquist criterion as $z_{\max} \times k_{z\max} = \pi N$ and $y_{\max} \times k_{y\max} = \pi N$ at the same time. As $k_{y\max} = k_0 \sin\theta_{\max}$ and similarly, $k_{z\max} = k_0 \sin\theta_{\max}$, where $\theta_{\max}$ is the maximum allowable propagation angle [11]. As $\Delta z = z_{\max} / N$ and $\Delta y = y_{\max} / N$, and if $\Delta l = \sqrt{\Delta y^2 + \Delta z^2}$ then we have, $\Delta l \le \pi / k_0 \sin\theta_{\max}$ to predict the maximum propagation angle. The choice of the incremental range Δx is provided by the user and it can be as large as λ since $\psi(x, y, z)$ varies slowly along *x* in the yz-plane [26].

C. Initialization of the algorithm

The numerical solution of SSPE algorithm usually starts with the given initial potential. It relates to the field radiated by the transmitting antenna. The transformed potential provides the initial potential for the beginning of the algorithm. In this work, we generate it by a vertically polarized current source with a Gaussian aperture distribution whose electric current is I_0 and length *l*, which is given as [26]:

$$\psi^e(0^+, y, z) \approx \frac{iI_0 l}{2k_0} f^e(y,z), \qquad (16)$$

$$f^e(y,z) = \frac{1}{\sigma_z\sqrt{2\pi}} e^{-\frac{(z-H_t)^2}{2\sigma_z^2}},$$

where H_t represents the height of the transmitting antenna and σ_z is the source standard deviation used to set 3 dB elevation beamwidth of transmitting antenna. Because the magnetic current is assumed to be zero here, therefore the initial condition for ψ^m is simply $\psi^m(0^+, y, z) = 0$. The transformed potential $\tilde{\tilde{\psi}}(0^+, k_y, k_z)$ can be easily determined using Fourier transform of the current source with respect to *z*, and $\tilde{\tilde{\psi}}$ is the 2D-Fourier transform of the aperture field [26]:

$$\tilde{\psi}(0^+, 0^+, k_z) = F\left[f^e(y,z) \right] = e^{-ik_z H_t} e^{-k_z^2 \sigma_z^2/2}. \qquad (17)$$

The initial potential can be defined as a column vector with N_z elements along the z-axis, again as $\vec{J}_z$ is independent of *y* one can repeat the column of $\tilde{\psi}\left(0^+, 0^+, k_z\right)$ N_y times along the y-axis. In this way, a 2D initial potential $\tilde{\tilde{\psi}}\left(0^+, k_y, k_z\right)$ can be obtained with $N_y \times N_z$ dimension. In order to apply the impedance surface BCs on a forest terrain the image theory is applied, implying that the fields and their corresponding potentials are represented in terms of odd and even parts. This infers that the Gaussian source representation is equally split into its even and odd components, $\left(\tilde{\psi}_e\right)$ and $\left(\tilde{\psi}_o\right)$, respectively:

$$\begin{aligned} \tilde{\psi}_e(0^+, k_y, k_z) &= e^{-k_z^2 \sigma_z^2/2} \cos(k_z H_t), \\ \tilde{\psi}_o(0^+, k_y, k_z) &= -ie^{-k_z^2 \sigma_z^2/2} \sin(k_z H_t). \end{aligned} \qquad (18)$$

Neglecting the surface waves in the far zone, under this approximation the initial field is the 2D Fourier transform of the aperture field $\tilde{\tilde{\psi}}$ that satisfies the impedance boundary over the ground as [26]:

$$\begin{aligned} \tilde{\tilde{\psi}}(x, k_y, k_z) = \int_{z'=0}^{+\infty} \int_{y'=-\infty}^{+\infty} \psi(x, y', z') e^{-ik_y y'} \\ \cdot \left[e^{-ik_z z'} + \Gamma(k_z) e^{ik_z z'} \right] dy' dz', \end{aligned} \qquad (19)$$

where $\Gamma(k_z)$ is the reflection coefficient of the plane waves over an impedance terrain surface with impedance *Z* for TMz and TEz modes, which is given as:

$$\begin{cases} \Gamma_{\mathrm{TM}_z}(k_z) = \dfrac{k_z - Zk_0}{k_z + Zk_0} \\ \Gamma_{\mathrm{TE}_z}(k_z) = \dfrac{Zk_z - k_0}{Zk_z + k_0} \end{cases}, \qquad (20)$$

the normalized complex impedance of the terrain surface is given as $Z = 1\Big/\sqrt{\varepsilon_{rf} + \dfrac{i\sigma_f}{\omega\varepsilon_0}}$, where σ_f is the conductivity and ε_{rf} is the relative permittivity of the forest terrain, respectively [26, 34]. Actually, Eq. (19) is not a 2D Fourier transform, but a complicated double integration. While it can be evaluated easily with the help of fast Fourier transform (FFT) instead of evaluating double integrals. For example, the potentials are represented in terms of odd and even parts $\psi = \dfrac{\psi_e + \psi_o}{2}$. Assuming that $A = e^{-ik_z z'}$ and $B = e^{ik_z z'}$ then the integral part corresponds to z in (19) can be written as:

$$\int_{z'=0}^{+\infty} \left[A + \Gamma(k_z)B\right]\psi(x, y', z')dy'dz'. \tag{21}$$

In order to apply the FFT, changing the limit of integration from 0 to ∞ to $-\infty$ to ∞ [35]. If we add $\psi_e(x, y', z')$ and $\psi_o(x, y', z')$ together for z > 0 and z < 0 we will get back the total field ψ. In this way, we can obtain Eq. (22) by prolix deduction as given below:

$$\begin{aligned}&\int_{z'=0}^{+\infty} \left[A + \Gamma(k_z)B\right]\psi(x, y', z')dy'dz', \\ &= \int_{-\infty}^{+\infty} \frac{1+\Gamma(k_z)}{2} A\psi_e(x, y', z')dz' \\ &\qquad + \int_{-\infty}^{+\infty} \frac{1-\Gamma(k_z)}{2} A\psi_o(x, y', z')dz',\end{aligned} \tag{22}$$

substituting (22) into (19) and thus, the initial potential $\tilde{\tilde{\psi}}(0^+, k_y, k_z)$ can be obtained for the beginning of the algorithm as:

$$\begin{aligned}\tilde{\tilde{\psi}}(0^+, k_y, k_z) &= \frac{1+\Gamma(k_z)}{2}\tilde{\tilde{\psi}}_e(0^+, k_y, k_z) \\ &\quad + \frac{1-\Gamma(k_z)}{2}\tilde{\tilde{\psi}}_o(0^+, k_y, k_z).\end{aligned} \tag{23}$$

After initializing the potentials $\psi(0^+, y, z)$ at $x = 0^+$ the field values at $x(0^+ + \Delta x)$ are computed by applying the propagator $e^{ik_x \Delta x}$ to the Fourier transformed field $\tilde{\psi}(0^+, k_y, k_z)$. Hence, obtaining the field values at the successive location $x + \Delta x$ by an inverse Fourier transform as can be seen in Eq. (24) the double integration corresponds to an inverse Fourier transform where k_y and k_z are the transformation domain variables:

$$\psi(x + \Delta x, y, z) = \frac{1}{4\pi^2}\int_{-\infty}^{+\infty}\int_{-\infty}^{+\infty} e^{ik_x \Delta x}\tilde{\tilde{\psi}}(x, k_y, k_z)e^{i(k_y y + k_z z)}dk_y dk_z, \tag{24}$$

and thus, it can be solved via Split-Step Fourier algorithm which consists of a succession of Fourier and inverse Fourier transforms obtained by FFT and inverse FFT, respectively. Equations (19) and (24) are used for both ψ^e and ψ^m with the appropriate value of $\Gamma(k_z)$ chosen from (20).

V. SIMULATION RESULTS

In this section, the simulation results are presented to check the validity of the proposed algorithm. In order to validate the proposed algorithm, the simulation results are compared with the results presented by Janaswamy as Fig. 11 in [26]. Related studies can also be found in [35]. Figure 1 shows the propagation factor (PF) versus the receiver height (H_r) when a PEC knife edge is placed over the flat terrain between the transmitter and receiver as shown in Fig. 1 inset.

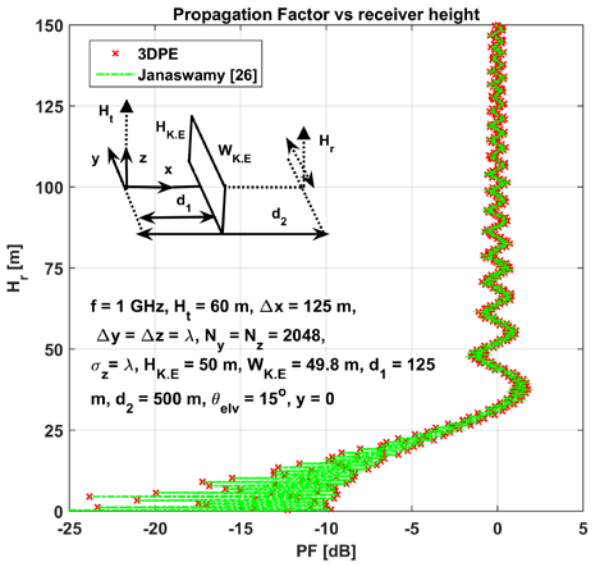

Fig. 1. Propagation factor versus vertical displacement behind a finite absorbing screen (a single knife-edge) as Fig. 11 in [26].

The knife-edge's height $(H_{K.E})$ and width $(W_{K.E})$ are 50 m (meters) and 49.8 m, respectively. The distance between the transmitter and receiver is 500 m, the distance between the transmitter and the PEC knife edge is $d_1 = 125$ m, and the distance between the knife edge and the receiver is 375 m, respectively. The field is computed at $x = x_{\max}$. Other parameters are shown in Fig. 1 inset. Compared with the reference model, the proposed model had an excellent agreement with the results presented in [26] which shows the validity of the proposed algorithm.

All the simulations were realized using a 3.4 GHz Core i7-7600 CPU workstation, 32 GB RAM. Computational time and memory used by the proposed model at different range step sizes are shown in Table 1.

Table 1: Computational time and RAM consumption (Dell 3.4 GHz Core i7-7600 CPU workstation, 32 GB RAM)

No.	Δx (m)	Ny = Nz	RAM (MB)	Time (s)
1	25	1024	626.4	28.47
2	50	1024	627.1	14.35

The second test is related to the field strength prediction over the rows of trees with uniform heights and spacing arranged along the direction of propagation on flat terrain. Field strength prediction due to the forest with non-uniform heights and equal spacing arranged along the direction of propagation on flat terrain is also presented in Fig. 4, and the last example is related to the field strength prediction due to the forest placed over three triangular-shaped mountains.

The simulation results presented in Fig. 3, Fig. 4, and Fig. 5 are compared with the analytical method namely, 3D Ray tracing method. 3D Ray tracing method is successfully applied in propagation modeling through open and closed environments, that may serve as a reference and perform validation, verification, and calibration (VV&C) [36, 37].

Figure 2 shows the geometry of the forest terrain placed in the yz-plane along the direction of propagation between the transmitter and receiver, where F_w is the forest's width and F_h is the forest's height, respectively.

Figure 3 (top) shows the geometry of the flat-shaped forest. The rows of trees with uniform heights (16 m) and separation distance (50 m) on the simulation range of 5 kilometers (km) are considered over the flat earth. The transmitting and receiving antennas are placed at the height of 16 m with 15º propagation angle in the paraxial direction. The operating frequency is considered at 900 MHz. Other operational parameters in all examples are assumed as $\Delta y = \Delta z = \lambda$, $N_y = N_z = 1024$, σ_f = 0.1 mS/m, and $\varepsilon_{rf} = 1.1$, respectively. The effect on the field strength in the presences of rows of trees on flat terrain at $F_w = 200$ m is evaluated as shown in Fig. 3 (middle) and (bottom). We can see that in the start of simulation the field values of the 3DPE method and 3D Ray tracing method are very close to the free space value, while the field values due to the 3DPE model rapidly decrease for short distance very close to the transmitter, it is may be due to the paraxial approximation in PE, it is clearly observed in Fig. 3 (bottom).

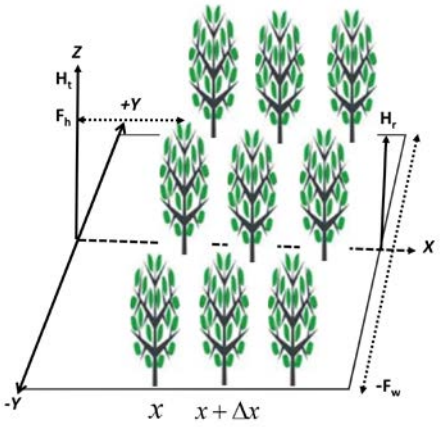

Fig. 2. Rows of trees placed in the yz-plane along the direction of propagation.

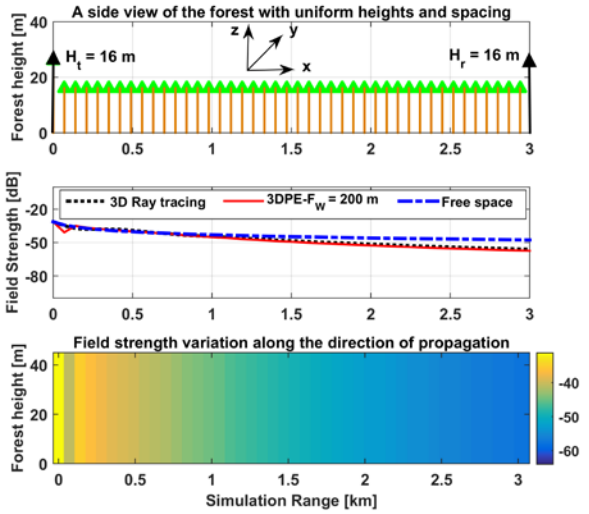

Fig. 3. A side view of the rows of trees with uniform heights and spacing on flat ground in two dimensions (top) [the third dimension, which is the lateral dimension y, is orthogonal to the plane of the paper]. Field strength prediction due to the 3D Ray tracing method and the 3DPE method (middle). Field strength prediction due to 3DPE model at F_w = 200 m (bottom).

The PE method is known to give unreliable solutions very close to the source. The region over which these errors occur is very small indeed (of the order of meters) but because the algorithm is range dependent these errors will propagate. However, preliminary experiments have indicated that the errors do not significantly affect predictions at ranges of interest [38]. The results of [39] indicate that the field degrades for a plane wave incident upon uniform height screens with equal separations as in this paper. We can see that the 3DPE results have good agreement with the 3D Ray

tracing method and the result presented in [39], but the result of the 3D Ray tracing is slightly higher, which implies it overestimates the field amplitude due to the diffracted waves.

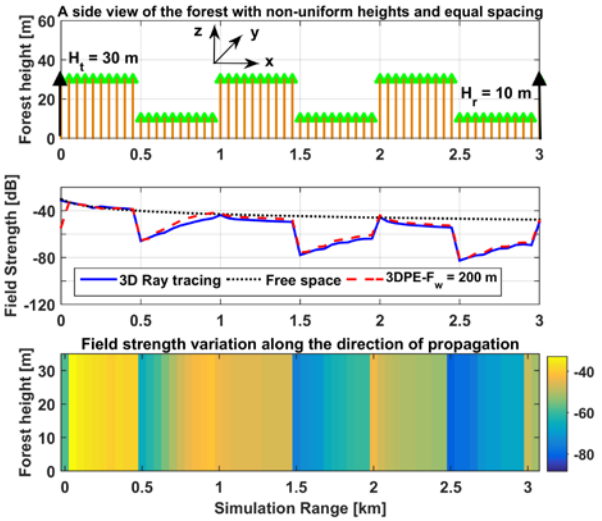

Fig. 4. A side view of the rows of trees with non-uniform heights and equal spacing on flat ground in two dimensions (top) [the third dimension, which is the lateral dimension y, is orthogonal to the plane of the paper]. Field strength prediction due to the 3D Ray tracing method and the 3DPE method (middle). Field strength prediction due to the 3DPE model at $F_w = 200$ m (bottom).

Figure 4 (top) shows the geometry of the flat-shaped forest. The rows of trees with non-uniform heights from 30 m (maximum) to 10 m (minimum) are considered with a separation distance of 50 m on the simulation range of 5 kilometers (km). The transmitting and receiving antennas are placed at the height of 30 m and 10 m respectively, with 15° propagation angle in the paraxial direction. Up to 0.5 kilometers from the transmitter the field values behave like free space and gradually decreasing due to the creeping wave effect, after 0.5 kilometers the field value increases due to the contribution of lateral waves. We can see that the 3DPE results have good agreement with the 3D Ray tracing method, but the results of the 3DPE are slightly higher, due to finite F_w. Therefore, if we increase the F_w, then we expect to see the results of the 3DPE model to agree with 3D Ray tracing results because in 3D Ray tracing method F_w is assumed infinitely long. This is equivalent to the 2DPE model which did not consider the lateral waves. The total field variation is the sum of the direct waves and reflected waves.

Figure 5 shows the geometry of the third test, it is the side view of the forest in a mountainous area with multiple rows of trees with variable heights, equal spacing and variable width distributed on three mountains surfaces. The modeling of the mountain type terrains can be found in [40].

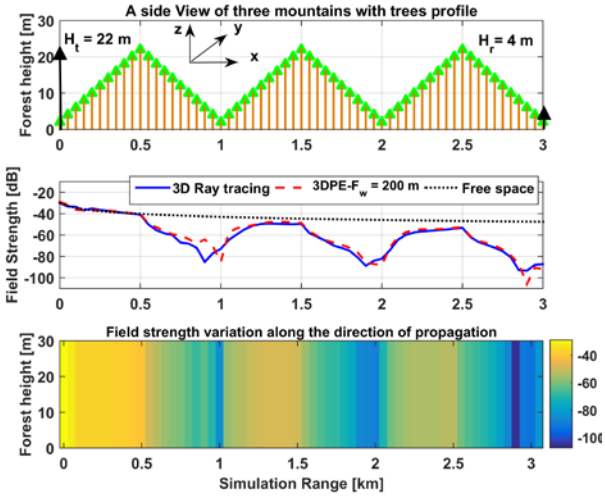

Fig. 5. A side view of the forest placed on the mountainous terrain in two dimensions (top) [the third dimension, which is the lateral dimension y, is orthogonal to the plane of the paper]. Field strength prediction due to the 3D Ray tracing method and the 3DPE method (middle). Field strength prediction due to the 3DPE model at $F_w = 200$ m (bottom).

In Fig. 5, up to 0.5 kilometers from the base station field behaves like free space, then at the first peak of mountain field behaves like a single knife-edge. The field strength minima occur at one kilometer in the 3DPE model. However, the results of 3D Ray tracing show that the ray tracing approach must be improved to handle the transition region effects and the multiple diffraction effects at very small angles.

VI. CONCLUSION

This work has demonstrated the 3DPE model that evaluates the field strength over flat and irregular forest environments. It is shown that the 3DPE model can formulate both vertically and laterally wave propagation effect in a large forest environment. Under the assumption of forwarding propagation, a wide-angle three-dimensional parabolic wave equation (3DPE) is formulated from the Helmholtz equation. The split-step parabolic equation (SSPE) method is adopted to march the potentials from one aperture plane to the next along the direction of propagation. The obtained results have a good agreement with the reference models presented in the literature. The proposed model can be generally used in both national, commercial and military applications for the analysis of radio wave propagation.

ACKNOWLEDGMENT

This work was supported in part by the National Nature Science Foundation of China (NSFC) under Grant No. 61771053 and 61421001.

REFERENCES

[1] H. L. Bertoni, *Radio Propagation for Modern Wireless Systems*. Prentice Hall PTR, New Jersey, 2000.

[2] T. Rappaport, *Wireless Communications Principles and Practice*, 2nd ed., Prentice Hall, New Jersey, 2001.

[3] T. K. Sarkar, Z. Ji, K. Kim, A. Medour, and M. Salazar-Palma, "A survey of various propagation models for mobile communication," *IEEE Antennas Propag. Mag.*, vol. 45, no. 3, pp. 51-82, June 2003.

[4] D. Liao and K. Sarabandi, "Modeling and simulation of near earth propagation in presence of a truncated vegetation layer," *IEEE Trans. Antennas Propag.*, vol. 55, no. 3, pp. 949-957, 2007.

[5] F. Wang and K. Sarabandi, "A physics-based statistical model for wave propagation through foliage," *IEEE Trans. Antennas Propag.*, vol. 55, no. 3, pp. 958-968, 2007.

[6] Y. S. Meng, Y. H. Lee, and B. C. Ng, "Study of propagation loss prediction in forest environment," *Progress in Electromagnetics. Res. B*, vol. 17, pp. 117-133, 2009.

[7] J. Zegarra, "Model Development for Wireless Propagation in Forested Environments," *Thesis and Dissertation Collection*, Naval Postgraduate School, Monterey, California, 2015.

[8] M. A. Leontovich and V. A. Fock, "Solution of the problem of propagation of electromagnetic waves along the earth's surface by the method of parabolic equation," *Academy of Sciences of the USSR: Journal of Physics*, vol. 10, pp. 13-23, 1946.

[9] M. Levy, *Parabolic Equation Methods for Electromagnetic Wave Propagation*. London, IEE Institution of Electrical Engineers, 2000.

[10] I. D. Sirkova and M. Mikhalev, "Parabolic wave equation method applied to the tropospheric ducting propagation problem: A survey," *Electromagnetics*, vol. 26, pp. 155-173, 2006.

[11] G. Apaydin and L. Sevgi, *Radio Wave Propagation and Parabolic Equation Modeling*. Wiley-IEEE Press, 2017.

[12] L. Sevgi, F. Akleman, and L. B. Felsen, "Ground wave propagation modelling: Problem-matched analytical formulations and direct numerical techniques," *IEEE Antennas Propag. Mag.*, vol. 44, no. 1, pp. 55-75, Feb. 2002.

[13] L. Sevgi, C. Uluisik, and F. Akleman, "A Matlab-based two-dimensional parabolic equation radio wave propagation package," *IEEE Antennas Propag. Mag.*, vol. 47, no. 4, pp. 164-175, Aug. 2005.

[14] X. Q. Sheng and W. Song, *Essentials of Computational Electromagnetics*. Singapore, John Wiley & Sons, 2012.

[15] F. Akleman and L. Sevgi, "A novel mom-and sspe-based groundwave-propagation field-strength prediction simulator," *IEEE Antennas Propag. Mag.*, vol. 49, no. 5, pp. 69-82, Oct. 2007.

[16] G. Apaydin and L. Sevgi, "The split-step-fourier and finite-element-based parabolic equation propagation-prediction tools: Canonical tests, systematic comparisons, and calibration," *IEEE Antennas Propag. Mag.*, vol. 52, no. 3, pp. 66-79, June 2010.

[17] G. Apaydın and L. Sevgi, "A novel split-step parabolic equation package for surface wave Propagation prediction along multi-mixed irregular terrain paths," *IEEE Antennas Propag. Mag.*, vol. 52, no. 4, pp. 90-97, Aug. 2010.

[18] O. Ozgun, G. Apaydin, M. Kuzuoglu, and L. Sevgi, "PETOOL: Matlab-based one-way and two-way split-step parabolic equation tool for radiowave propagation over variable terrain," *Computer Physics Communications*, vol. 182, no. 12, pp. 2638-2654, 2011.

[19] P. Zhang, L. Bai, Z. Wu, and L. Guo, "Applying the parabolic equation to tropospheric groundwave propagation: A review of recent achievements and significant milestones," *IEEE Antennas Propag. Mag.*, June 2016.

[20] J. F. De Souza, F. N. B. Magno, Z. A. Valente, J. C. Costa, and G. P. S. Cavalcante, "Mobile radio propagation along mixed paths in forest environment using parabolic equation," *Microwave and Optical Tech. Letters*, vol. 51, no. 4, pp. 1133-1136, Apr. 2009.

[21] P. Holm, G. Eriksson, and P. Kraus., "Wave propagation over a forest edge - parabolic equation modeling vs. measurements," *IEEE Intl. Symp. Radio Comm.*, Portugal, Sep. 2002.

[22] J. F. Souza, Z. A. Valente, F. N.B. Magno, G. P. S. Cavalcante, and J. C. Costa, "Propagation path loss through the Urban foliated semi-confined environment using parabolic equations," *IEEE Intl. Symp. on Spread Spectrum Techniques and Applications*, Brazil, Aug. 2006.

[23] M. Le Palud, "Propagation modeling of VHF radio channel in forest environments," *IEEE Military Communications Conference*, vol. 2, pp. 609-614, Oct. 2004.

[24] J. Guo, J. Wang, P. Liu, and Y. Long, "Fourier split-step parabolic equation solution of wave propagation over forest edge," *2008 Intl. Conference on Microwave and Millimeter Wave Tech.*, Nanjing, China, 21-24 Apr. 2008.

[25] V. A. Permyakov, M. S. Mikhailov, and E. S. Malevich, "Calculation of the radar station field in 3D space in the presence of forest and other

obstacles by the method of parabolic equation," *2017 Progress in Electromagnetics Research Symposium* - Spring (PIERS), Russia, 22-25 May 2017.

[26] R. Janaswamy, "Path loss predictions in the presence of buildings on flat terrain: A 3-D vector parabolic equation approach," *IEEE Trans. Antennas Propag.*, vol. 51, pp. 1716-1728, 2003.

[27] W. C. Chew, *Waves and Fields in Inhomogeneous Media*. Piscataway, NJ: IEEE Press, 1995.

[28] H. F. Rasool, X. M. Pan, and X. Q. Sheng, "Radiowave propagation prediction in the presence of multiple knife edges using 3D parabolic equation method," *Proc. ACES-China*, Aug. 2018.

[29] R. Zhang, "Study on Fourier transform methods in a 3-D parabolic equation," *IEEE GASS Symposium Proc.*, 16-23 Aug. 2014.

[30] P. Suarez, "An introduction to the split step Fourier method using MATLAB," 2016. (https://doi.org/10.13140/RG.2.1.1394.0965).

[31] F. Jensen, H. Schmidt, M. B. Porter, and W. A. Kuperman, *Computational Ocean Acoustics*. 2nd ed., ser. Modern Acoustics and Signal Processing, New York, Springer-Verlag, pp. 457-530, 2011.

[32] R. H. Hardin and F. D. Tappert, "Applications of the split-step Fourier method to the numerical solution of nonlinear and variable coefficient wave equations," *SIAM Rev*., vol. 15, no. 22, p. 423, 1973.

[33] F. J. Harris, "On the use of windows for harmonic analysis with the discrete Fourier transform," *Proc. IEEE*, vol. 66, pp. 51-83, Jan. 1978.

[34] G. P. S. Cavalcante, M. A. R. Sanches, and R. A. N. Oliveira, "Mobile radio propagation along mixed paths in forest environment," *Proceedings of IMOC*, pp. 320-324, SBMO/IEEE, 1999.

[35] K. B. Thiem, "A 3D Parabolic Equation (PE) based Technique for Predicting Propagation Path Loss in an Urban Area," *Thesis and Dissertation Collection*, Naval Postgraduate School, Monterey, California, 2001.

[36] G. Liang and H. L. Bertoni, "New approach to 3-D ray tracing for propagation prediction in cities," *IEEE Trans. Antennas and Prop.*, vol. 46, no. 6, June 1998.

[37] S. Hosseinzadeh, H. Larijani, K. Curtis, A. Wixted, and A. Amini, "Empirical propagation performance evaluation of LoRa for indoor environment," *2017 IEEE 15th International Conference on Industrial Informatics (INDIN)*, Emden, Germany, 24-26 July 2017.

[38] M. West, K. Gilbert, and R.A. Sack, "A tutorial on the parabolic equation (PE) model used for long range sound propagation in the atmosphere," *Applied Acoustics*, vol. 37 pp. 31-49,1992.

[39] L. Piazzi and H. L. Bertoni, "On screen placement for building representation in Urban environments considering 2D multiple diffraction problems," *Proc. IEEE Vehicular Technology Conference*, 1999.

[40] L. Piazzi and H. L. Bertoni, "Effects of terrain on path loss in Urban environments for wireless applications," *IEEE Trans. Antennas Propag.*, vol. 46, no. 8, pp. 1138-1147, Aug. 1998.

Hafiz Faiz Rasool received his B.Sc. and M.Sc. degrees in Electronics Engineering from the Islamia University of Bahawalpur, Pakistan in 2011 and 2015, respectively. Currently, he is a full-time Ph.D. student at the School of Information and Electronics in Beijing Institute of Technology, Beijing, China. His research interest includes fast and efficient numerical algorithms in electromagnetics.

Xiao-Min Pan received his B.S. and M.S. degrees from Wuhan University (WHU), Wuhan, China, in 2000 and 2003, respectively, and the Ph.D. degree from the Institute of Electronics, Chinese Academy of Sciences, Beijing, China, in 2006. He is a Professor in the School of Information and Electronics, Beijing Institute of Technology, Beijing, China.

Xin-Qing Sheng received his B.S., M.S., and Ph.D. degrees from the University of Science and Technology of China (USTC), Hefei, China, in 1991, 1994, and 1996, respectively. He is the Chang-Jiang Professor in the School of Information and Electronics, Beijing Institute of Technology, Beijing, China.

Fast ISAR Imaging based on High Frequency Scattered Fields from Quadratic Patches

An Wen Wu [1], Yu Mao Wu [1,*], Ya-Qiu Jin [1], Hongcheng Yin [2], Chonghua Fang [3], and Nan Zhang [1]

[1] Key Laboratory for Information Sciences of Electromagnetic Waves (MoE)
School of Information Science and Technology, Fudan University, Shanghai, 200433, China

[2] National Electromagnetic Scattering Laboratory, 100854, Beijing, China

[3] Science and Technology on Electromagnetic Compatibility Laboratory
China Ship Development and Design Center, Wuhan, 430064, China
awwu17@fudan.edu.cn, yumaowu@fudan.edu.cn*, yqjin@fudan.edu.cn, yinhc207@yahoo.com.cn, 27634073@qq.com, zhangnan16@fudan.edu.cn

Abstract ─ This paper implements the two-dimensional (2D) non-uniform Inverse Fast Fourier Transformation (NUFFT) to Inverse Synthetic Aperture Radar (ISAR) imaging. The complexity of two-dimensional NUFFT is $O(MN\log_2 MN)$, which is better than direct calculation with complexity $O(M^2N^2)$ and has controllable interpolation error. As for the echo scattered fields acquisition with respect to multiple frequencies and azimuth angles, we use physical optics (PO) method based on quadratic discretization to reduce the patch number to two orders of magnitude, compared with planar discretization. Three examples prove that the 2D imaging process has nearly equal accuracy and higher efficiency.

Index Terms ─ ISAR imaging, non-uniform FFT, physical optics, quadratic discretization.

I. INTRODUCTION

Inverse Synthetic Aperture Radar (ISAR) imaging is an important technique for further automatic target recognition (ATR) by acquiring high resolution two-dimensional or three-dimensional radar image with targets' detailed information like size, shape, structure and posture [1]. The Polar Format Algorithm (PFA) is one of the earliest imaging algorithms adopted for spotlight SAR and extensively applied in practical monostatic SAR systems [2]. The imaging algorithm contains two steps: 1) Store the scattered fields in polar form with respect to multiple frequencies and azimuth angles; 2) Apply two-dimensional inverse Fourier transform of the scattered data matrix after interpolating the scattered data into equally spaced grid.

In the electromagnetic (EM) scattering, when the target size is much larger than the wavelength, the EM scattered problems can be solved by high frequency methods [3,4]. Macdonald [5] proposed the physical optics (PO) approximation method to simulate high frequency electromagnetic scattered fields from large-scale radar targets. The PO method is executed based on three assumptions: 1) The target is meshed by sizeable planar or curved patches. The induced currents on every illuminated patch determined by the incident field and independent with each other. 2) Far-field approximation, the radius of curvature of the target is much larger than the incident wavelength. 3) Kirchhoff approximation for calculating the scattered fields. As for solving the surface integral of scattered fields, Ludwig [6] and Gordon [7] derived the analytical expression to calculate the PO scattered fields from the planar patch. Rius [8] proposed GRECO method considering the GPU's rendering function and converting the surface integral into a coherent addition of pixels. Conde [9] used the Stationary Phase Method (SPM) to radiation pattern of antennas. Wu and Chew [10,11] extended the steepest descent path method into calculating the PO integrals from the quadratic patches. In order to meet the second assumption, the planar patch size is nearly λ/8, while the quadratic patch size is 1λ or larger. The quadratic patch size is much larger than planar patch, the memory consumption is reduced with higher frequency. As for lit patch judging, Ling and Bhalla [12,13] proposed the shooting and bouncing ray technique (SBR), which calculates the intersections between the incident rays and surface element and compares the distance to determine the illuminated or shadowed part. To this day, the GPU's zbuffer technique is introduced to accelerate the shadowing process and applied in many electromagnetic calculation softwares.

Submitted On: April 25, 2019
Accepted On: June 17, 2019

Fast Fourier transforms (FFT) are widely used for many applications in engineering, science, and mathematics, which should be implemented on the uniform distributed data. However, the polar format [14] sampled scattered fields are non-uniform in Cartesian coordinate. Appropriate interpolation methods need to be implemented to transform the data into uniform distributed space. For interpolation on complex data, the complex values are divided into absolute and phase part, the interpolation method operates on two parts respectively. Therefore, the interpolation function requires linear phase response. Different from the traditional interpolation method which interpolates the complex form scattered fields, Dutt and Rokhlin [15] proposed non-uniform Fast Fourier Transformation (NUFFT) which interpolates the sequence of Fourier exponential function. [16-19] discussed the algorithm improvement and relative applications. Song and Liu implement the NUFFT into radar imaging [20] and radially encoded MR imaging (MRI) [21]. The NUFFT method interpolates the sequence of exponential function rather than the complex form scattered fields, which has least square error and higher efficiency.

In this work, the PO method for calculating scattered fields on quadratic patches is illustrated in Section II. The NUFFT method in ISAR imaging is described in Section III. Section IV shows the numerical results of three different targets with different shape and size.

II. THE PO SCATTERED FIELD ON QUADRATIC DISCRETIZATION PATCHES

A. The PO scattered fields

We consider a perfectly conducting (PEC) target illuminated by a time harmonic plane wave with time impedance e^{-iwt}. The PO scattered field can be derived from the Stratton-Chu formula:

$$\mathbf{E}_s(\mathbf{r}) = \frac{-ikZ_0 e^{ikr}}{4\pi r}\hat{\mathbf{r}} \times \hat{\mathbf{r}} \times \int_{\partial\Omega} dS(\mathbf{r}')\mathbf{J}_{\mathrm{PO}}(\mathbf{r}')e^{-ik\hat{\mathbf{r}}\cdot\mathbf{r}'}, \quad (1)$$

where, $\partial\Omega$ is the illuminated region of the target, $\mathbf{r}'$ is the position vector of the point on the region $\partial\Omega$, $\hat{\mathbf{r}}$ and r are the unit vector and the amplitude of the scattered direction, k is the wave number, Z_0 is the wave impedance of free space. The surface induced PO current $\mathbf{J}_{\mathrm{PO}}(\mathbf{r}')$ is approximated by:

$$\mathbf{J}_{\mathrm{PO}}(\mathbf{r}') = \begin{cases} 2\hat{\mathbf{n}}(\mathbf{r}') \times \mathbf{H}^{(i)}(\mathbf{r}'), & \mathbf{r}' \in \partial\Omega \\ 0, & \mathbf{r}' \notin \partial\Omega \end{cases}, \quad (2)$$

$\hat{\mathbf{n}}(\mathbf{r}')$ is the outward unit normal vector of region $\partial\Omega$, $\mathbf{H}^{(i)}(\mathbf{r}')$ is the incident magnetic field on the target surface. The incident wave has the following form:

$$\mathbf{H}^{(i)}(\mathbf{r}') = \frac{1}{Z_0}\hat{\mathbf{r}}^{(i)} \times \mathbf{E}^{(i)}(\mathbf{r}'), \quad \mathbf{E}^{(i)}(\mathbf{r}') = \mathbf{E}_0^{(i)} e^{ik\hat{\mathbf{r}}^{(i)}\cdot\mathbf{r}'}. \quad (3)$$

Then, we substitute equations (2), (3) into equation (1) and obtain the general scattered fields calculation formula:

$$\mathbf{E}_s(\mathbf{r}) \approx \int_S dS(\mathbf{r}')g(\mathbf{r}')e^{ikf(\mathbf{r}')}, \quad (4)$$

with the phase function $f(\mathbf{r}')$ and amplitude function $g(\mathbf{r}')$ that,

$$g(\mathbf{r}') = \frac{-ike^{ikr}}{2\pi r}\hat{\mathbf{r}} \times \hat{\mathbf{r}} \times \left(\hat{\mathrm{n}}(\mathbf{r}') \times \hat{\mathbf{r}}^{(i)} \times \mathbf{E}_0^{(i)}\right), \quad (5)$$

$$f(\mathbf{r}') = \left(\hat{\mathbf{r}}^{(i)} - \hat{\mathbf{r}}\right) \cdot \mathbf{r}'. \quad (6)$$

B. The quadratic discretization

For solving the integral equation (4) on quadratic patches, we have to apply affine transformation to transform every arbitrary quadratic patch into a standard square patch with parameters (ξ, η). For standard square patch, the interpolation formula for a quadratic patch:

$$\mathbf{r}'(\xi, \eta) = \sum_{j=1}^{8} N_j(\xi, \eta)\mathbf{r}_j, \quad (7)$$

$\mathbf{r}_j$ is the three-dimensional coordinates of the critical points of quadratic patch with respect to coordinate $(\mathrm{x}, \mathrm{y}, \mathrm{z})$ and $\mathbf{r}'(\xi, \eta)$ is the three dimensional coordinates with respect to parameter (ξ, η).

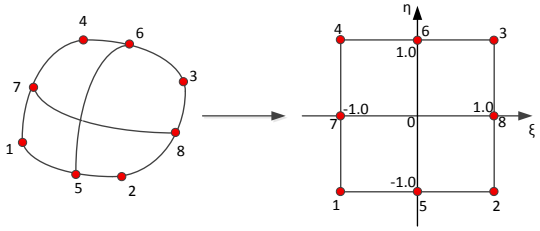

Fig. 1. The affine transformation from an arbitrary patch into a standard square patch with 8 nodes.

The standard square patch is shown in Fig. 1 above. For nodes in different place, the shape function $N_j(\xi, \eta)$ are different. For the four vertexes (j=1,2,3,4), the shape function is:

$$N_j(\xi, \eta) = \frac{1}{4}\left(1 + \xi_j\xi\right)\left(1 + \eta_j\eta\right)\left(\xi_j\xi + \eta_j\eta - 1\right), \quad (8)$$

for the middle nodes on the edge where $\xi_j = 0$ (j=5,6), the shape function is:

$$N_j(\xi, \eta) = \frac{1}{2}(1 - \xi^2)\left(1 + \eta_j\eta\right), \quad (9)$$

for the middle nodes on the edge where $\eta_j = 0$ (j=7,8), the shape function is:

$$N_j(\xi, \eta) = \frac{1}{2}(1 - \eta^2)\left(1 + \xi_j\xi\right). \quad (10)$$

We substitute equations (7-10) to equation (4), the scattered field expression of a quadratic patch is:

$$\mathbf{E}_s(\mathbf{r}) \approx \sum_{n=1}^{N} \int_{-1}^{1}\int_{-1}^{1} g_n(\mathbf{r}'(\xi, \eta))e^{ikf_n(\mathbf{r}'(\xi,\eta))}D_e d\xi d\eta, \quad (11)$$

with integral infinitesimal $D_e = \left|\mathbf{r}'_{\xi}(\xi,\eta) \times \mathbf{r}'_{\eta}(\xi,\eta)\right|$. $\mathbf{r}'_{\xi}(\xi,\eta) = \frac{\partial \mathbf{r}'(\xi,\eta)}{\partial \xi}$ and $\mathbf{r}'_{\eta}(\xi,\eta) = \frac{\partial \mathbf{r}'(\xi,\eta)}{\partial \eta}$ are the partial derivative of ξ and η.

For approximating the integral which has fixed integral domain [-1,1] ×[-1,1], we use the Lagrange interpolation polynomials to approximate the integral into closed-form formulation:

$$\mathbf{E}_s(\mathbf{r}) \approx \sum_{n=1}^{N} \int_{-1}^{1}\int_{-1}^{1} \boldsymbol{G}_n(\xi,\eta) e^{ikF_n(\xi,\eta)} d\xi d\eta, \quad (12)$$

where the function $\boldsymbol{G}_n(\xi,\eta)$ and $F_n(\xi,\eta)$ have the polynomials form on *n-th* patch as:

$$F_n(\xi,\eta) = F_0 + F_1\xi + F_2\xi^2 + F_3\eta + F_4\eta^2$$
$$\boldsymbol{G}_n(\xi,\eta) = \boldsymbol{G}_0 + \boldsymbol{G}_1\xi + \boldsymbol{G}_2\xi^2 + \boldsymbol{G}_3\eta + \boldsymbol{G}_4\eta^2. \quad (13)$$

We choose 5 points $\mathbf{r}_1, \mathbf{r}_5, \mathbf{r}_2, \mathbf{r}_8, \mathbf{r}_3$ and substitute the coordinates to equation (13) to calculate the coefficients $(F_0, F_1, F_2, F_3, F_4)$ and $(\boldsymbol{G_0}, \boldsymbol{G_1}, \boldsymbol{G_2}, \boldsymbol{G_3}, \boldsymbol{G_4})$.

C. The stationary phase method

The Stationary Phase Method (SPM) [22-24] is applied to solve the double integrals. From the geometrical theory of diffraction, when the target size is much larger than the incident wavelength, the radar scattered fields of the target is equivalent to the superposition of multiple scattering centers. Similar to the GTD model [25], the scattered field of quadric patch can be approximated by the sum of critical points: stationary phase points (points that satisfy equation (14) below and showed in Fig. 2 in detail), boundary points ($\mathbf{r}_5, \mathbf{r}_6, \mathbf{r}_7, \mathbf{r}_8$ from Fig. 1 and shown in detail in Fig. 3) and vertex points ($\mathbf{r}_1, \mathbf{r}_2, \mathbf{r}_3, \mathbf{r}_4$ from Fig. 1 and shown in detail in Fig. 4).

$$\hat{\mathbf{r}} \cdot \mathbf{r}'_{\xi}(\xi,\eta) = 0 \text{ and } \hat{\mathbf{r}} \cdot \mathbf{r}'_{\eta}(\xi,\eta) = 0. \quad (14)$$

The contributions of the stationary phase point $\boldsymbol{s}(\xi_s,\eta_s)$ is:

$$\boldsymbol{I_s} = \frac{\pi \boldsymbol{G}^s}{k} e^{-ikF^s} \sqrt{\frac{1}{\left|F^s_{\xi\xi}F^s_{\eta\eta} - \left(F^s_{\xi\eta}\right)^2\right|}} e^{-ik\frac{\pi}{4}\sigma(\delta+1)}, \quad (15)$$

where $\boldsymbol{G}^s = \boldsymbol{G}(\xi_s,\eta_s)$ and $F^s = F(\xi_s,\eta_s)$. $F_{\xi\xi}, F_{\eta\eta}, F_{\xi\eta}$ are the second parametric derivatives of $F(\xi,\eta)$. $\sigma = \text{sign}(F_{\eta\eta})$ and $\delta = \text{sign}(F_{\xi\xi}F_{\eta\eta} - (F_{\xi\eta})^2)$.

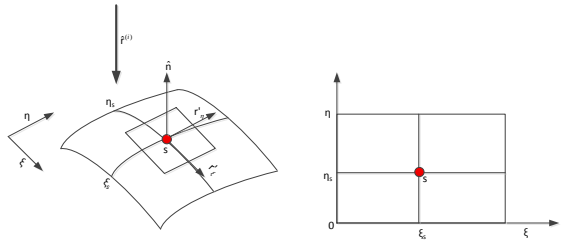

Fig. 2. Stationary phase point $\boldsymbol{s}(\xi_s,\eta_s)$ on a quadratic patch.

The contributions of the boundary point $\boldsymbol{c}(\xi_c,\eta_c)$ is:

$$\boldsymbol{I_c} = -i(-1)^{\alpha} \frac{\boldsymbol{G}^c}{k} e^{-ikF^c} \frac{1}{F^c_{\alpha}} \sqrt{\frac{2i\pi}{kF^c_{\beta\beta}}}, \quad (16)$$

where $\alpha \equiv \xi, \beta \equiv \eta$ at the boundaries $\xi = 0$ and $\xi = 1$, and $\alpha \equiv \eta, \beta \equiv \xi$ at the boundaries $\eta = 0$ and $\eta = 1$.

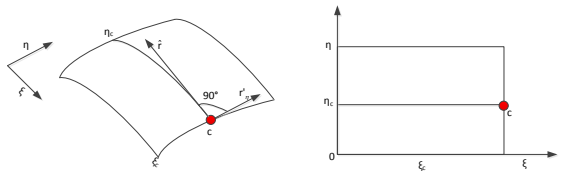

Fig. 3. Boundary point $\boldsymbol{c}(\xi_c,\eta_c)$ on a quadratic patch.

The contributions of the vertex point $\boldsymbol{v}(\xi_v,\eta_v)$ is:

$$\boldsymbol{I_v} = -\boldsymbol{G}^v e^{-ikF^v} \frac{(-1)^{\xi_v+\eta_v}}{k^2 F^v_{\xi} F^v_{\eta}}, \quad (17)$$

where $\boldsymbol{G}^v = \boldsymbol{G}(\xi_v,\eta_v)$ and $F^v = F(\xi_v,\eta_v)$. F_{ξ} and F_{η} are the parametric derivatives of $F(\xi,\eta)$.

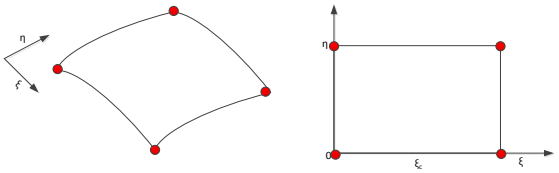

Fig. 4. Vertex point $\boldsymbol{v}(\xi_v,\eta_v)$ on a quadratic patch.

Considering all the critical points' contribution, the scattered field can be written as:

$$\mathbf{E}_s(\mathbf{r}) \approx \sum_{n=1}^{N} \boldsymbol{I^n_s} + \boldsymbol{I^n_c} + \boldsymbol{I^n_v}. \quad (18)$$

PO method calculates the scattered field of the illuminated area of the target. For lit-judging, Rius [26] used GPU's zbuffer storage to simplify the lit-judgement of the target. Fan and Guo [27] implemented the fast patch-lit-judge method in hybrid EM method with the efficient open graphics library (OpenGL).

III. NON-UNIFORMED FFT (NUFFT) IMAGING ALGORITHM

The ISAR image can be calculated by [28]:

$$I(\hat{x},\hat{y}) = \frac{1}{(2\pi)^2} \iint \mathrm{S}(f,\theta)\, e^{j2\pi K_x(f,\theta)\hat{x} + j2\pi K_y(f,\theta)\hat{y}} df d\theta, \quad (19)$$

where $\mathrm{S}(f,\theta)$ is the scattered field with respect to the different incident frequency f and azimuth angle θ, $\hat{x}$ and $\hat{y}$ are the pixel index in image domain. $K_x = \frac{2\cos\theta}{\lambda}$ and $K_y = \frac{2\sin\theta}{\lambda}$, the target reconstruction function is the 2D-IFFT with respect to K_x and K_y. The sample number of frequency f is M and azimuth angle θ is N, the

complexity of 2D-IFFT is $O(MNlog_2MN)$.

Discretize equation (19) and we form equation (20), which can be used to calculate the value of every pixel of the image. For solving the summation, the complexity is $O(M^2N^2)$:

$$I(\hat{x},\hat{y}) = \frac{1}{(2\pi)^2}\sum_{f_{min}}^{f_{max}}\sum_{\theta_{min}}^{\theta_{max}} \mathrm{S}(f,\theta)e^{j2\pi K_x(f,\theta)\hat{x}+j2\pi K_y(f,\theta)\hat{y}}. \quad (20)$$

As shown in Fig. 5 below, the sampled scattered fields are uniform on frequency−azimuth angle $k-\theta$ domain (blue points) and non-uniform on K_x-K_y domain (red points).

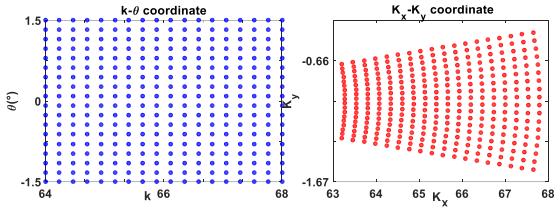

(a) (b)

Fig. 5. The sampled scattered fields distribution: (a) non-uniform distributed in K_x-K_y domain, and (b) uniform distributed in $k-\theta$ domain. We take 18 sampling points for k and θ, respectively.

Different from traditional interpolation algorithms, NUFFT method interpolates the sequence of exponential function rather than the sampled scattered fields matrix. Two-dimensional NUFFT equals to two one-dimensional NUFFT implemented in two dimensions [29,30], that is, 2D-NUFFT is the tensor product of two one-dimensional NUFFT. We just need to consider the one-dimensional Inverse Discrete Fourier Transform:

$$X_n = \frac{1}{N}\sum_{k=1}^{N} x(k)e^{j\frac{2\pi}{N}n\omega_k}, \quad (21)$$

where $\omega_k \in \left[-\frac{N}{2},\frac{N}{2}-1\right]$, $k=1,2,\dots,N$, $n=-\frac{N}{2},-\frac{N}{2}+1,\dots,\frac{N}{2}-1$. Consider the equations that every exponential function $e^{j\frac{2\pi}{N}n\omega_k}$ can be written as the sum of the nearest $(2Q+1)$ terms uniformly-spaced Fourier series:

$$s_n e^{j\frac{2\pi}{N}n\omega_k} \approx \sum_{k=[G\omega_k]-Q}^{k=[G\omega_k]+Q} x_k(\omega_k)e^{j\frac{2\pi}{GN}nk}, \quad (22)$$

where G is the oversampling factor and $(2Q+1)$ is the length of interpolation kernel. $s_n>0$ is chosen to minimize the approximation error. For this work, we choose $s_n=\cos\frac{\pi n}{GN}$. [] is the rounding operation. We substitute $n=-\frac{N}{2},-\frac{N}{2}+1,\dots,\frac{N}{2}-1$ and write the equation as equation (23).

Equation (23) is an overdetermined equation set of N linear equations with $(2Q+1)$ unknowns and $(2Q+1)\ll N$. We use the least square solution as the approximation of the solution of the overdetermined equation set. We write the equation set in simplified form:

$$B = Ax, \quad (24)$$

and the least-square solution x^* is:

$$x^* = x_k(\omega_k) = \begin{bmatrix} x_{[G\omega_k]-Q}(\omega_k) \\ x_{[G\omega_k]-Q+1}(\omega_k) \\ \vdots \\ x_{[G\omega_k]+Q}(\omega_k) \end{bmatrix} = \left(A^{\dagger}A\right)^{-1}A^{\dagger}B, \quad (25)$$

where $A^{\dagger}$ denotes the complex-conjugate transpose of matrix A. Substitute $x_k(\omega_k)$ into equation (21) and transform the non-uniform data into uniform space, as equation (26) illustrates below:

$$\begin{bmatrix} (s_{-\frac{N}{2}})e^{j\frac{2\pi}{N}\omega_k(-\frac{N}{2})} \\ (s_{-\frac{N}{2}+1})e^{j\frac{2\pi}{N}\omega_k(-\frac{N}{2}+1)} \\ \vdots \\ (s_{\frac{N}{2}-1})e^{j\frac{2\pi}{N}\omega_k(\frac{N}{2}-1)} \end{bmatrix} = \begin{bmatrix} e^{j\frac{2\pi}{GN}(-\frac{N}{2})([G\omega_k]-Q)} & e^{j\frac{2\pi}{GN}(-\frac{N}{2})([G\omega_k]-Q+1)} & \cdots & e^{j\frac{2\pi}{GN}(-\frac{N}{2})([G\omega_k]+Q)} \\ & e^{j\frac{2\pi}{GN}(-\frac{N}{2}+1)([G\omega_k]-Q)} & \ddots & \ddots & \vdots \\ & \vdots & \ddots & \ddots & \vdots \\ & e^{j\frac{2\pi}{GN}(\frac{N}{2}-1)([G\omega_k]-Q)} & \cdots & \cdots & e^{j\frac{2\pi}{GN}(\frac{N}{2}-1)([G\omega_k]+Q)} \end{bmatrix} \cdot \begin{bmatrix} x_{[G\omega_k]-Q}(\omega_k) \\ x_{[G\omega_k]-Q+1}(\omega_k) \\ \vdots \\ x_{[G\omega_k]+Q}(\omega_k) \end{bmatrix}. \quad (23)$$

Then, IFFT can be implemented on equally-spaced $x'(k)$. For 2D ISAR imaging, operate one-dimensional IFFT on range and cross range direction respectively.

For actual measurement, the incident signal is considered as step-frequency signal, pulse signal with a fixed frequency step. The amplitude and initial phase of each sample point are consistent.

$$\begin{aligned} X_n &= \frac{1}{N}\sum_{k=1}^{N} x(k)e^{j\frac{2\pi}{N}n\omega_k} \\ &= \frac{1}{Ns_n}\sum_{k=1}^{N} x(k)\left(\sum_{q=-Q}^{Q} x_{q+[G\omega_k]}(\omega_k)e^{j\frac{2\pi}{GN}n(q+[G\omega_k])}\right) \\ &= \frac{1}{Ns_n}\sum_{k=-\frac{GN}{2}}^{\frac{GN}{2}-1} x'(k)e^{j\frac{2\pi}{GN}nk}. \end{aligned} \quad (26)$$

As for the resolution, the range resolution δ_r is related to the bandwidth of the incident wideband signal, the cross range resolution δ_{cr} is related to azimuth range scan:

$$\delta_r = \frac{c}{2B}, \delta_{cr} = \frac{\lambda_c}{2\sin\Delta\varphi}, \quad (27)$$

where c is light speed in vacuum, B is the bandwidth of the incident wideband signal, λ_c is the center wavelength corresponding to center frequency f_c, $\Delta\varphi$ is the angular scan. The resolution denotes the actual distance represented by every pixel in image.

III. NUMERICAL RESULTS

We bring three targets with different size and shape to discussion, two perfect electric conductor (PEC) spheres with different radius, a glider most consisting of curved surfaces, a finely modeled ship with lots of flat surfaces. Under spherical coordinate system, θ (elevation angle) is the angle between the scattered direction and $+\hat{\mathbf{z}}$ axis. φ (azimuth angle) is the angle between the projection of the scattered direction in the xOy plane and the $+\hat{\mathbf{x}}$ axis. The scattering pattern is monostatic and incident electric field $\mathbf{E}_0^{(i)}$ polarizes along $\hat{\boldsymbol{e}}_{\boldsymbol{\theta}}$ direction.

In order to meet the Far-field approximation, the radius of curvature of the target is much larger than the incident wavelength, the planar patch size is nearly $\lambda/8$, while the quadratic patch size is 1λ or larger. We use *Altair HyperMesh 14.0* software to discretize the geometry at "second order" and "quads only" mode. Table 1 shows the patch number using planar discretization and quadratic discretization respectively. Quadratic discretization reduces the patch number to two orders of magnitude. Table 2 shows the information of the incidence and the size of three different targets.

Table 1: The numbers and sizes of patches by using the quadratic discretization and plane discretization for the different targets

Targets	**Planar Patch (λ/8)**	**Quadratic Patch (1λ)**
Two spheres	365432	5748
Glider	8901418	100389
Ship	39144518	120929

Table 2: The parameters of the incident wave and the size of three targets

Target 1: Two spheres	Radius: 0.5m 1m Center distance: 10m Patch number: 5748
Target 2: A glider	Size: 14m×14m×2m Patch number: 100389
Target 3: A ship	Size: 30m×3.5m×4.6m Patch number: 120929
Frequency center (f_c)	10GHz
θ	60°
φ	43.5°~46.5°
Bandwidth (B)	600MHz
Angular scan (Δφ)	3°
Frequency samples	128
φ samples	128
Range resolution	$\frac{c}{2B}$ =0.25m
Azimuth resolution	$\frac{\lambda}{2sin\Delta\varphi}$ =0.29m

As for the accuracy comparison, we choose the image formed by NUFFT equation (19) and by directly calculating the double integral in equation (20). For estimating the performance of the NUFFT method, we introduce the relative L_2 error to discuss:

$$e_2 = avg\left(\frac{\|\hat{I}-I\|_2^2}{\|I\|_2^2}\right), \tag{28}$$

where I is the image of direct calculation and $\hat{I}$ is the image generated by NUFFT. We calculate the average error of every pixel. The results are showed in Table 3 at the end of this chapter.

A. Two PEC sphere

Firstly, we take two PEC spheres with different radius as example. The geometry and the quadratic discretization are shown in Fig. 6. The detailed parameters are illustrated in Table 2.

Fig. 6. The geometry and the quadratic discretization of two different size spheres.

From Fig. 7 below, the 2D image generated by NUFFT and direct calculation agree well. The image tells that center sphere has smaller radius and lower amplitude. From Fig. 8, the range profile shows agreement and the two spheres can be well distinguished.

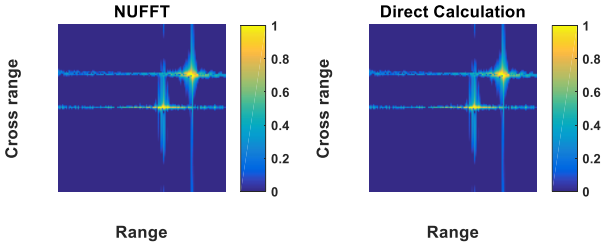

(a) (b)

Fig. 7. The comparison between: (a) NUFFT and (b) direct calculation of ISAR imaging of two PEC spheres.

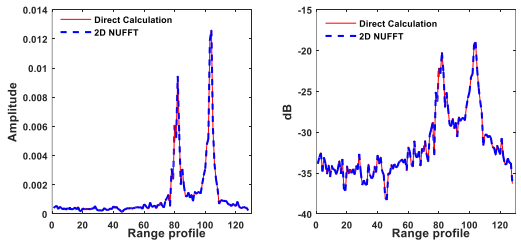

(a) (b)

Fig. 8. The range profile: (a) amplitude and (b) dBsm comparison between NUFFT and direct calculation of ISAR imaging of two PEC spheres.

B. A glider

The glider geometry and quadratic discretization are showed in Fig. 9. The geometry mostly consists of curved surface and simple struction like the streamline airframe and light wings to reduce the air friction. The comparison between NUFFT and direct calculation is illustrated in Fig. 10.

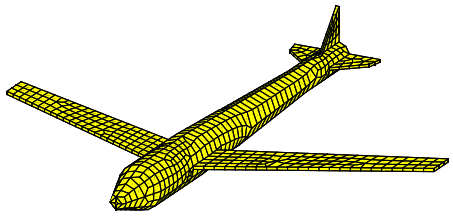

Fig. 9. The quadratic discretization of a glider.

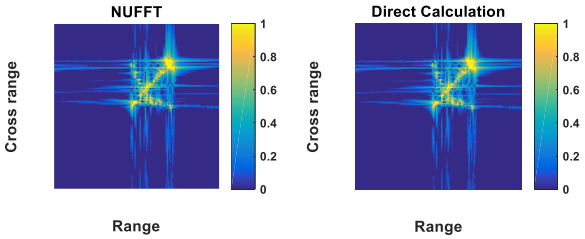

Fig. 10. The comparison between: (a) NUFFT and (b) direct calculation of ISAR imaging of a glider.

From Fig. 10, the 2D image of NUFFT and direct calculation of the glider agree very well. The image tells the detailed structure of the glider. The shape is well represented and the empennage has relatively obvious contribution. Figure 11 further verifies the scattered characteristic of the glider from range profile.

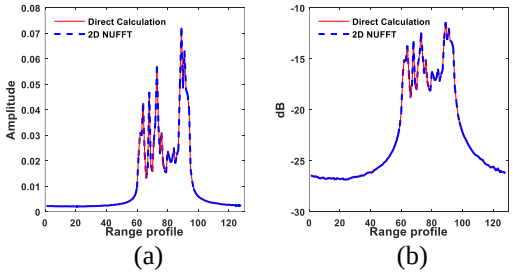

Fig. 11. The range profile: (a) amplitude and (b) dBsm comparison between NUFFT and direct calculation of ISAR imaging of a glider.

C. A ship

We take a finely modeling ship as the third example. As Fig. 12 shows, the ship is mostly composed of plane elements like the deck and control rooms in the ship. When the ship is discretized into quadratic patches, some are quite close to planar patches. We choose the same incident plane wave for test.

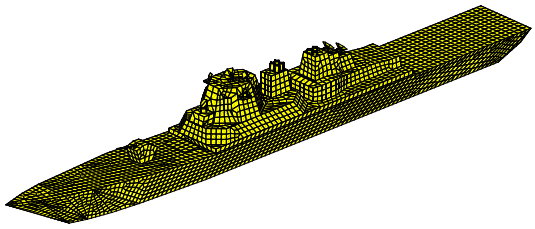

Fig. 12. The geometry and the quadratic discretization of a finely modeling ship.

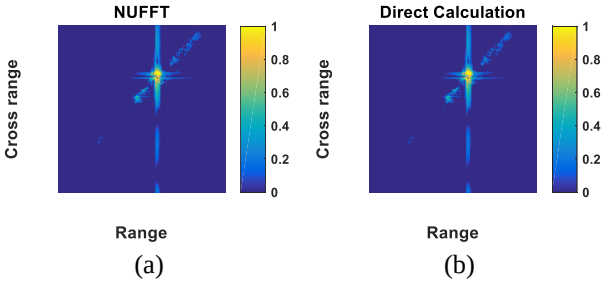

Fig. 13. The comparison between: (a) NUFFT and (b) direct calculation of ISAR imaging of a finely modeled ship.

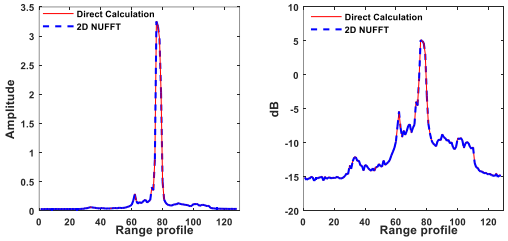

Fig. 14. The range profile: (a) amplitude (b) dBsm comparison between NUFFT and direct calculation of ISAR imaging of a finely modeled ship.

From Fig. 13, the 2D image of NUFFT and direct calculation of the ship agree well. From the ISAR image and the range profile in Fig. 14, we can tell that the middle part of the ship has the strongest contribution to the image compared with other parts. However, the structure of the ship is not very clear. The reason possibly is that the basic component of the finely modeling ship is flat, like deck and hull. The quadratic discretization generates error. We may conclude that for targets consisting of large flat surfaces, we need to choose quadratic patches combined with planar patches to finely describe the target.

The relative L_2 error shows in Table 3 below. We can tell from it that the relative L_2 error is overall quite small and increases very slowly as the increase of the interpolation kernel size Q. It indicates that the NUFFT method generates minor error, which is introduced by solving the overdetermined equations utilizing the least square solution.

Table 3: The relative L_2 error defined in equation (27) on different size of interpolation kernel determined by Q

Targets G**=2**	Q**=2**	Q**=4**	Q**=8**	Q**=16**
Two spheres	0.77%	1.09%	1.26%	1.34%
Glider	0.23%	0.43%	0.61%	0.73%
Ship	0.12%	0.19%	0.25%	0.30%

The time comparison shows in Table 4 below. NUFFT method reduces the time consumption a lot. The time consumption contains obtaining the interpolation coefficients by solving the overdetermined equations, so that the theoretical time comparison from the complexity is not fully achieved. As for the memory consumption, NUFFT has less memory usage. The CPU is Intel(R) Core (TM) i7-4790 at 3.6GHz, the simulation software is Matlab R2015b.

Table 4: The time consuming comparison between direct calculation and NUFFT on G=2, Q=4; in order to make difference more obvious, we choose the total time and memory consumption of 100 tests

	Direct Calculation	**NUFFT**
Time (second)	30.214s	14.646s
Memory (kilobyte)	296kB	212kB

IV. CONCLUSION

This work implements the two-dimensional non-uniform Inverse Fast Fourier Transformation to Inverse Synthetic Aperture Radar imaging. The complexity of two-dimensional NUFFT is $O(MN\log_2 MN)$, compared with direct computation with complexity $O(M^2N^2)$, has higher computational efficiency and nearly equal imaging accuracy. The error is controllable, generated by least squares method solving overdetermined equations. The physical optics (PO) method based on quadratic discretization reduces the patch number to one hundredth, compared with planar discretization. In general, the work achieves fast simulation for ISAR imaging on complex targets, providing basis for further automatic radar recognition (ATR).

ACKNOWLEDGMENT

This work is supported in part by National Key R&D Program of China No. 2017YFB0502703, National Natural Science Foundation of China under Grant No. 11571196, Open Research Fund of State Key Laboratory of Pulsed Power Laser Technology, Electronic Engineering Institute, State Key Laboratory of Applied Optics, Changchun Institute of Optics, Fine Mechanics and Physics.

REFERENCES

[1] Mensa, L. Dean, *High Resolution Radar Imaging*. Artech House, 1981.

[2] J. L. Walker, "Range-doppler imaging of rotating objects," *IEEE Transactions on Aerospace and Electronic Systems.*, vol. 16, no. 1, pp. 23-52, Jan. 1980.

[3] J. A. Kong, *Electromagnetic Wave Theory*. New York, NY, USA: Wiley-Interscience, 1990.

[4] Y. Q. Jin, *Electromagnetic Scattered Modelling for Quantitative Remote Sensing*. Singapore: World Science Press, 2000.

[5] H. M. Macdonald, "The effect produced by an obstacle on a train of electric waves," *Philosophical Transactions of the Royal Society of London*, vol. 212, pp. 299-337, 1913.

[6] A. C. Ludwig, "Computation of radiation patterns involving numerical double integration," *IEEE Trans. Antennas Propag*., vol. 16, no. 6, pp. 767-769, 1968.

[7] W. B. Gordon, "Far-field approximations to the Kirchhoff-Helmholtz representation of scattered fields," *IEEE Trans. Antennas Propagat.*, vol. 23, no. 7, pp. 590-592, July 1975.

[8] J. M. Rius, M. Ferrando, and L. Jofre, "High-frequency RCS of complex radar targets in real-time." *IEEE Trans. Antennas Propagat.*, vol. 41, no. 9, pp. 1308-1319, 1993.

[9] O. M. Conde, J. Perez, and M. P. Catedra, "Stationary phase method application for the analysis of radiation of complex 3-D conducting structures," *IEEE Trans. Antennas Propagat.*, vol. 49, no. 5, pp. 724-731, 2001.

[10] Y. M. Wu and W. C. Chew, "The modern high frequency methods for solving electromagnetic scattering problems," *Progr. Electromagn. Res. PIER*, vol. 156, pp. 63-82, 2016.

[11] Y. M. Wu, L. J. Jiang, and W. C. Chew, "An efficient method for computing highly oscillatory physical optics integral," *Progr. Electromagn. Res. PIER*, vol. 127, pp. 211-257, Apr. 2012.

[12] H. Ling, R.-C. Chou, and S.-W. Lee, "Shooting and bouncing rays: calculating the RCS of an arbitrarily shaped cavity," *IEEE Trans. Antennas Propagat.*, vol. 37, no. 2, pp. 194-205, Feb. 1989.

[13] R. Bhalla and H. Ling, "Image domain ray tube integration formula for the shooting and bouncing ray technique," *Radio Science*, vol. 30, no. 5, pp. 1435-1446, 1995.

[14] J. Sun, S. Mao, G. Wang, and W. Wange, "Polar format algorithm for spotlight bistatic SAR with

arbitrary geometry configuration," *Progress In Electromagnetics Research*, vol. 103, pp. 323-338, 2010.

[15] A. Dutt and V. Rokhlin, "Fast Fourier transforms for non equispaced data," *SIAM J. Sci. Comp.*, vol. 14, pp. 1368-1393, 1993.

[16] N. Nguyen and Q. H. Liu, "The regular Fourier matrices and nonuniform fast Fourier transforms," *SIAM J. Sci. Comp.*, vol. 21, no. 1, pp. 283-293, 1999.

[17] K. Natroshvili, O. Loffeld, H. Nies, A. M. Ortiz, and S. Knedlik, "Focusing of general bistatic SAR configuration data with 2-D inverse scaled FFT," *IEEE Trans. Geosci. Remote Sens.*, vol. 44, no. 10, pp. 2718-2727, Oct. 2006.

[18] Q. Liu and N. Nguyen, "An accurate algorithm for nonuniform fast fourier transform (NUFFT's)," *IEEE Microwave and Guided Wave Letters*, vol. 8, no. 1, pp. 18-20, Jan. 1998.

[19] J. A. Fessler and B. P. Sutton, "Nonuniform fast Fourier transforms using min-max interpolation," *IEEE Transactions on Signal Processing*, vol. 51, no. 2, pp. 560-574, Feb. 2003.

[20] J. Y. Song, Q. H. Liu, K. Kim, and W. R. Scott, "High-resolution 3-D radar imaging through nonuniform fast Fourier transform (NUFFT)," *Communications in Computational Physics*, vol. 1, no. 1, pp. 176-191, 2006.

[21] J. Y. Song, Q. H. Liu, S. L. Gewalt, G. Cofer, and G. A. Johnson, "Least square NUFFT methods applied to 2D and 3D radially encoded MR image reconstruction," *IEEE Transactions on Biomedical Engineering*, vol. 56, no.4, pp. 1134-1142, 2009.

[22] Y. M. Wu, L. J. Jiang, and W. C. Chew, "Computing highly oscillatory physical optics integral on the polygonal domain by an efficient numerical steepest descent path method," *Journal of Computational Physics*, vol. 236, no. 1, pp. 408-425, 2013.

[23] J. Zhang, W. M. Yu, X. Y. Zhou, and T. J. Cui, "Efficient evaluation of the physical-optics integrals for conducting surfaces using the uniform stationary phase method," *IEEE Trans. Antennas Propagat.*, vol. 60, no. 5, pp. 2398-2408, May 2012.

[24] F. S. de Adana, O. Gutierrez, I. Gonzalez, M. F. Catedra, and L. Lozano, *Practical Applications of Asymptotic Techniques in Electromagnetics*. Norwood, MA, 2011.

[25] L. C. Potter, Da-Ming Chiang, R. Carriere, and M. J. Gerry, "A GTD-based parametric model for radar scattering," *IEEE Trans. Antennas Propagat.*, vol. 43, no. 10, pp. 1058-1067, 1995

[26] J. M. Rius, A. Carbo, J. Bjerkemo, et al., "New graphical processing technique for fast shadowing computation in PO surface integral," *IEEE Trans. Antennas Propagat.*, vol. 62, no. 5, pp. 2587-2595, 2014.

[27] T. Q. Fan, L. X. Guo, and W. Liu, "A novel openGL-based MoM/SBR hybrid method for radiation pattern analysis of an antenna above an electrically large complicated platform," *IEEE Trans. Antennas Propagat.*, vol. 64, no. 1, pp. 201-209, 2016.

[28] C. Y. Dai and X. L. Zhang, "Bistatic polar format algorithm based on NUFFT method," *Journal of Electromagnetic Waves & Applications*, vol. 25, no. 17-18, pp. 2328-2340, 2011.

[29] R. Bhalla and H. Ling, "Three-dimensional scattering center extraction using the shooting and bouncing ray technique," *IEEE Trans. Antennas Propagat.*, vol. 44, no. 11, pp. 1445-1453, 1996.

[30] X. Y. He, X. Y. Zhou, and T. J. Cui, "Fast 3D-ISAR image simulation of targets at arbitrary aspect angles through nonuniform fast Fourier transform (NUFFT)," *IEEE Trans. Antennas Propagat.*, vol. 60, no. 5, pp. 2579-2602, 2012.

Design of Defective EBG Structures for Dual-Band Circular Patch MIMO Antenna Applications

Xiaoyan Zhang [1,2], Yuting Chen [1*], Haitao Ma [1], Liwei Li [1], and Huihui Xu [1]

[1] School of Information Engineering
East China Jiaotong University, Nanchang, 330013, China
xyzhang3129@ecjtu.jx.cn, *cytzgao@qq.com, 2538338841@qq.com,
liliwei_139@163.com, 164449524@qq.com

[2] State Key Laboratory of Millimeter Waves, Nanjing, 210096, China

Abstract ─ Usually, a reasonably designed electromagnetic band-gap (EBG) structure can reduce the surface wave of an antenna. However, it may take a long time to design. In this paper, a dual-band circular patch multiple-input multiple-output (MIMO) antenna on an EBG surface is proposed. Defects are simply introduced into rows and columns of the EBG cells. In this way, the band-gap bandwidth (BG-BW) of those cells can be as large as 29.2%, which enables the EBGs can cover two frequency bands with a large interval, and to generate over 25 dB isolation between the antenna elements, as well. The measured results show that the proposed antenna, incorporating defective EBGs, operates at 5.71-5.97 GHz and 6.31-6.54 GHz. The -10 dB impedance bandwidth of the antenna is extended by 28.9% and 27.8% at the low and high frequency band. In addition, its gain is enhanced by 5 dB and 6.9 dB, and its back radiation decreased by 15 dB and 10.3 dB at the resonant frequencies of 5.75 GHz and 6.44 GHz, respectively. The proposed design may have many applications in communication systems.

Index Terms ─ Defect, high impedance EBG structure, MIMO antenna, mushroom EBG structure.

I. INTRODUCTION

In recent years, multiple-input multiple-output (MIMO) technology has gained a lot of attention from scholars in the telecommunication industry, which is one of the ways to realize the 5-generation mobile communication [1, 2]. The antenna array is an important part of MIMO system. The main challenge in designing MIMO antennas is to improve the isolation between antenna elements while minimizing them as much as possible [3-5]. Generally, the smaller isolation between antennas, the smaller mutual coupling effects on them. For some special antennas, such as base station antennas, the isolation requirement is greater than 25 dB [6].

Some methods were proposed to improve the isolation between antenna elements. Ismaiel and Abdel-Rahman etched meander slots on the ground to improve the isolation [7], but it causes the frequency offset. Yu *et al.* inserted an offset circuit between feed ports [8]. However, this method will increase the complexity of the antenna design. Wang *et al.* added two pairs of *L*-shaped extensions to the background structure of the antenna [9], while the isolation is only 15 dB.

In recent years, electromagnetic band-gap (EBG) structure has been proposed to isolate antennas due to its ease of design and beneficial to reducing an antenna profile. Coulombe *et al*. embedded some coplanar EBG structures to an antenna array [10], its isolation is better than 25 dB. Qiu *et al.* introduced a perpendicular mushroom-like EBG wall to the substrate between the two patch antennas to obtain 30 dB isolation [11]. Although it is not suitable for low profile requirements, it provides a superior idea for antenna isolation design.

It is found that the wider band gap of the EBG structure, the higher isolation of the antennas. The mushroom-like EBG are usually arranged in a periodic [12] or quasi-periodic form [13]. It has many derivative structures, including a two via slot-type EBG (TVS-EBG) [14], an edge-located via EBG (ELV-EBG) [15], a modified mushroom-like EBG (MML-EBG) [16], and a complementary split ring resonator EBG (CSRR-EBG) [17]. The former two adopt the way of changing feed to improve the band-gap bandwidth (BG-BW) of the EBGs, while the latter two achieve this goal by carefully designing the shapes of the cells. Their BG-BWs comparisons are listed in Table 1. It is shown that the latter method can broaden the bandwidth more effectively. However, it may take a long time to design. In 2018, we tried to destroy the periodicity of the EBGs by introducing some defective slots only between the rows of the EBG cells to obtain a higher BG-BW [18], but the band gap was still not wide enough.

Submitted On: October 12, 2018
Accepted On: January 26, 2019

In this paper, a dual-band circular patch MIMO antenna with defective EBGs is proposed. The design of EBG structure is based on mushroom-like EBG structure that digs four half circular slots. And the defects are introduced into both rows and columns of the EBG cells. By using the proposed EBG, the bandwidth and gain can be dramatically improved.

Table 1: The lowest frequency (f_L), highest frequency (f_H) and band-gap bandwidth in different EBG structures

Ref.	Type	f_L (GHz)	f_H (GHz)	BG-BW
[14]	TVS-EBG	3.01	3.38	11.6%
[15]	ELV-EBG	3.60	4.06	12.0%
[16]	MML-EBG	5.10	6.00	16.2%
[17]	CSRR-EBG	3.31	4.33	26.7%
Proposed	—	5.68	7.62	29.2%

II. DESIGN AND ANALYSIS

A. Dual-band circular patch MIMO antenna design

Figure 1 shows a circular patch MIMO antenna in the C-band. The MIMO antenna is designed on a FR-4 substrate, whose thickness is h=2 mm and the electrical parameters are ε_r=4.4 and $tan\delta$ =0.02. The MIMO antenna is a circle patch and the radius of the circular patch is 11.5 mm. As Fig. 1 shows, the lengths and widths of slots are denoted by l_1, l_2, l_3, l_4, l_5, l_6, l_7, and d, respectively. The center of the circle patch is denoted by r_1. This antenna is excited by a coaxial cable with a 50 Ω SMA connector, it has a diameter of r_2=1 mm. The two elements of MIMO antenna distance is d_y.

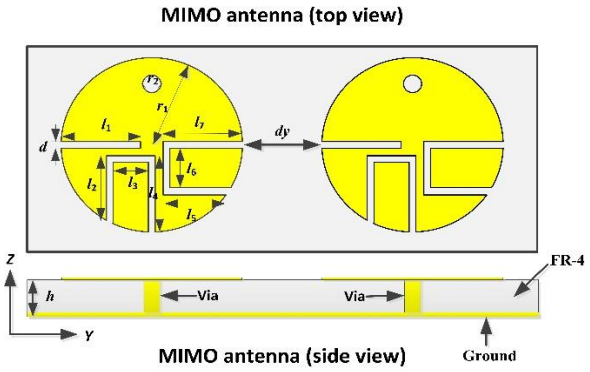

Fig. 1. Configuration and parameters of circular patch MIMO antenna and substrate, for MIMO antenna: l_1=10.5 mm, l_2=7 mm, l_3=8 mm, l_4=10 mm, l_5=7 mm, l_6=8 mm, l_7=10mm, d=0.5 mm, r_1=11.5 mm, r_2=1 mm, d_y=33.6 mm, and h=2 mm.

Figure 2 exhibits the simulated S_{11} of circular patch MIMO antenna. The MIMO antenna has two resonant modes generated at nearly 5.75 GHz and 6.44 GHz, respectively. Its bandwidth is 320 MHz at lower frequency and 200 MHz at higher frequency with a standard of S_{11} < -10 dB. The radiation efficiency of this antenna is about 73.9% at 5.75 GHz and 70.5% at 6.44 GHz, respectively.

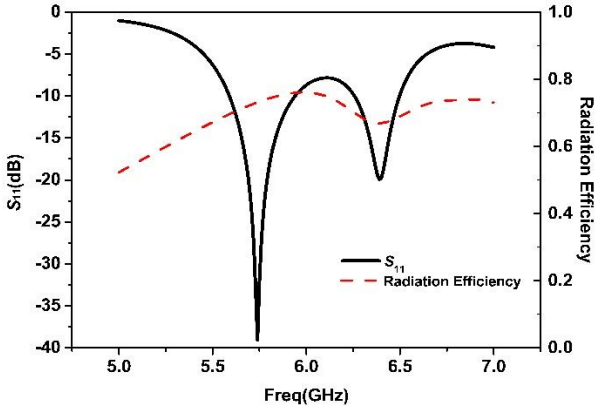

Fig. 2. S_{11} and radiation efficiency of the MIMO antenna.

B. High impedance EBG structure design

Figure 3 (a) shows the schematic of the high impedance EBG in three different cases. EBG has thickness of 2 mm with a dielectric constant of 4.4. Figure 3 (b) shows the 1×2 EBGs structure proposed. Figure 3 (c) presents the 10×16 EBG cells operating as a two-port waveguide formed by a pair of perfect electric conductor (PEC) along the z-axis and perfect magnetic conductor (PMC) along the y-axis. They are divided into seven parts: #1, #2, #3, #4, #5, #6, and #7. By changing the distances of g_x, g_y, and g_z between each part, the asymmetrically distribution of EBGs can be realized. Besides, when g_x and g_y equals dx, the EBGs are periodically arranged.

Figure 4 shows that the EBG structure can be equivalent to parallel LC resonant circuit. The gap between radiation patches of adjacent EBG structures can be equivalent to capacitance C. Because the metal through-hole connects the radiation patch with the ground structure, the current forms a loop between the radiation patch and the ground structure, which can be equivalent to the inductance L. This high impedance surface (HIS) can effectively suppress the surface wave outside the band-gap. For an EBG structure with patch width W, gap width g, substrate thickness h, the values of the L and C are determined by the following formula [19]:

$$L = \mu_0 h, \tag{1}$$

$$C = \frac{W\varepsilon_0(1+\varepsilon_r)}{\pi} cosh^{-1}\left(\frac{2W+g}{g}\right), \tag{2}$$

where ε_r is the electric constant, while ε_0 and μ_0 is the permittivity and permeability of free space, respectively.

The frequency band gap also can be predicted as:

$$\omega = 1/\sqrt{LC}, \quad (3)$$

$$\mathrm{BW} = \Delta\omega/\omega = 1/\eta\sqrt{L/C}, \quad (4)$$

where η is the free space impedance, which is 120 π.

Based on the above formulas, L is proportional to h, the band gap increases with the increasing of L, and decreases with the decreasing of L when μ_0 and η_0 are constant. W will affect the value of C when other variables are fixed. C is inversely proportional to the value of the band gap.

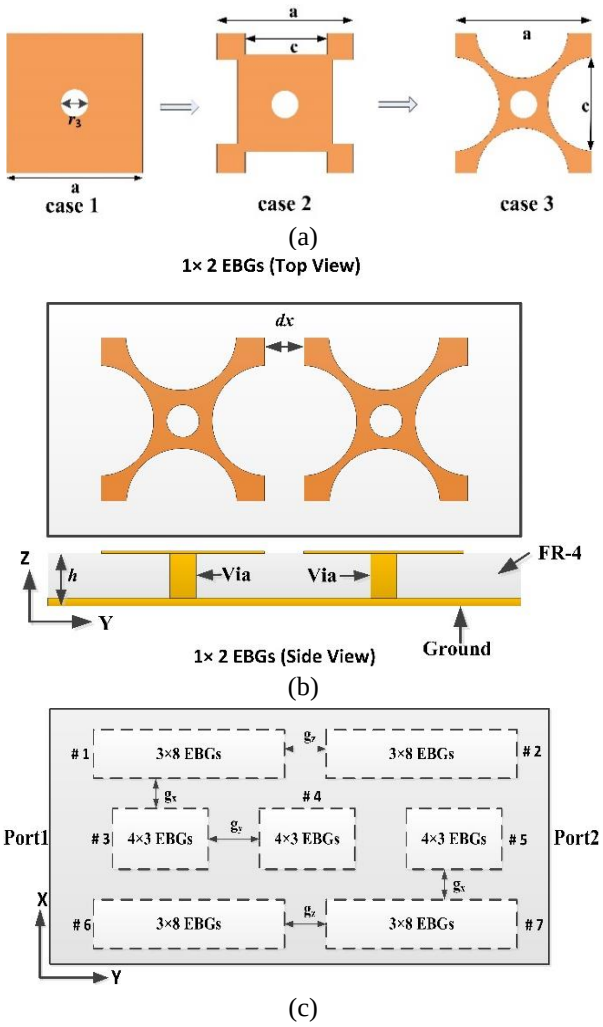

Fig. 3. (a) Configuration and parameters of the proposed EBG for high impedance EBG in the three different cases: a=6.3 mm, c=3.4 mm, r_3=1 mm, for 1×2 EBGs: dx=0.5 mm, h=2 mm; for 10×16 EBGs: g_x=5 mm, g_y=36.7 mm, and g_z=2.7 mm. (a) EBG cell in three different cases, (b) 1×2 EBGs structure, and (c) 10×16 EBGs structure.

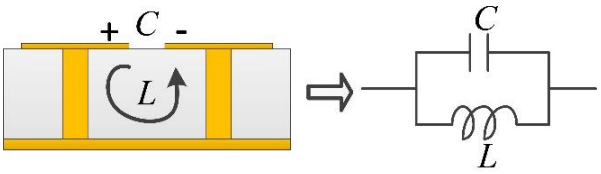

Fig. 4. Two-dimensional model for mushroom EBG type.

Figure 5 displays the effect of the slots above the electromagnetic band-gap for three cases. As seen in the above figures, under the condition of the same size, by etching circle slots on the case 3, the bandwidth of EBG is the largest. Figure 6 presents the S_{21} of proposed EBG structure. While, when g_x, g_y, and $g_z > dx$, the band-gap is broadened, because the EBG periodical structure is broken [18].

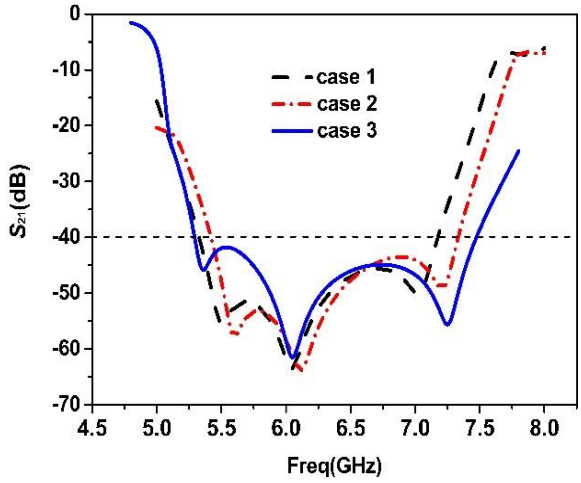

Fig. 5. Simulated S_{21} of case 1, case 2, and case 3.

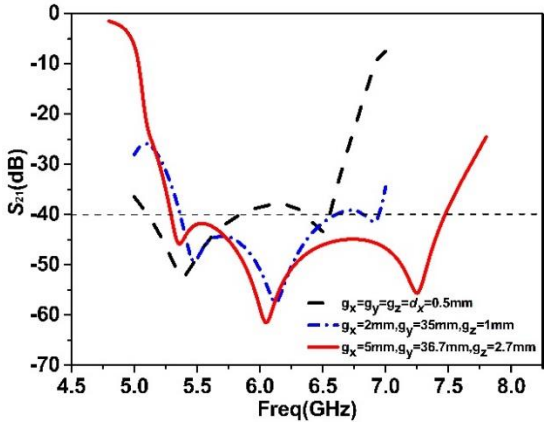

Fig. 6. S_{21} of the proposed EBG structure.

The dispersion diagrams are plotted in Fig. 7. From this diagram, the frequency band-gap between mode 1 and mode 2 is observed for the proposed EBG cell. The intersections with the light lines are used to determine the upper limit of the band-gap for the surface waves. Case 3 is proposed, the frequency of electromagnetic band gaps of the EBG structure is 5.68 GHz to 7.62 GHz, and the band gaps are 1.94 GHz.

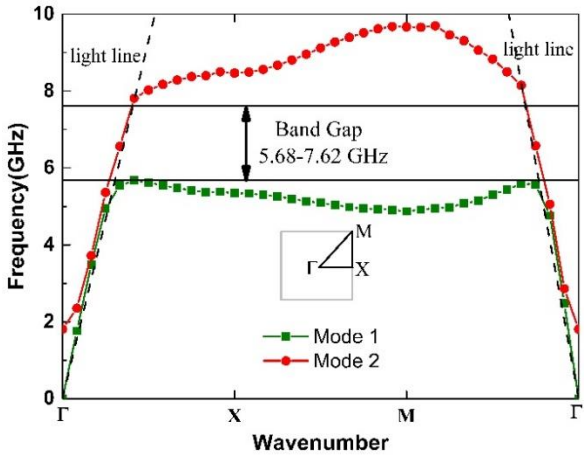

Fig. 7. Dispersion diagram for case 3.

C. A dual-band circular patch MIMO antenna with high impedance EBG structure

Figure 8 demonstrates the configuration and parameters of the proposed EBG antenna. The d_1 and d_2 equal 6.85 mm, the *Width* is 80 mm and *Length* is 135 mm.

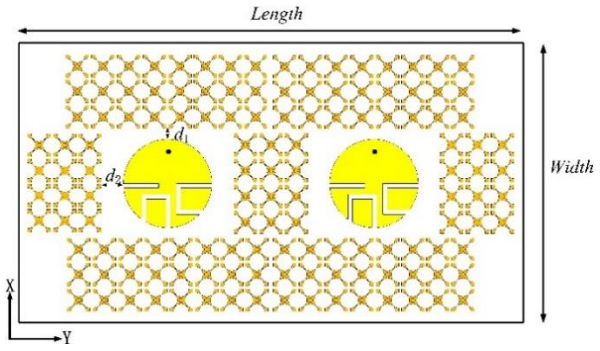

Fig. 8. Configuration and parameters of the proposed EBG antenna.

Figure 9 shows the S_{11} of the proposed EBG antenna. As can be observed, the EBG antenna bandwidth is 5.6 GHz to 6.0 GHz and 6.22 GHz to 6.46 GHz, respectively. The bandwidth is 400 MHz in low frequency and 240 MHz in high frequency, respectively. The radiation efficiency of proposed antenna is about 61.1% at 5.75 GHz and 56.1% at 6.44 GHz. Figure 10 shows the current distributions of proposed EBG antenna. It demonstrates that the proposed EBG structure can more obviously suppress the surface wave of the antenna. The radiation of the EBG antenna is clearly stronger than that of the MIMO antenna.

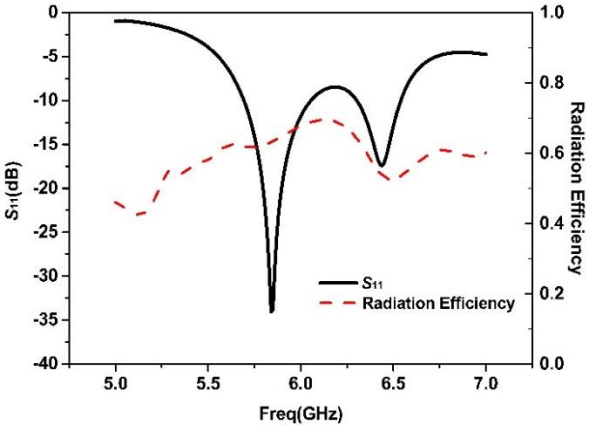

Fig. 9. S_{11} and radiation efficiency of the proposed EBG antenna.

For a MIMO antenna system, the isolation is an important parameter. It can be described as $|S_{21}|$. Figure 11 presents a slot in the ground planar of the MIMO antenna. The length and width of the slot are expressed by *glength* and *gwidth*, respectively. The MIMO antenna observed the isolation by changing the size of slot. When the *glength* equals 50 mm and *gwidth* equals 1.5 mm, the isolation of MIMO antenna can reach maximum.

Figure 12 compares the mutual coupling of the proposed EBG antenna with the MIMO antenna and slot in ground. It is shown that the proposed EBG structure is more significant in improving the mutual coupling of MIMO antenna system compared with slot in ground. Especially, at low frequency, the isolation can be enhanced by about 11.5 dB with EBG than about 0.3 dB with slot line.

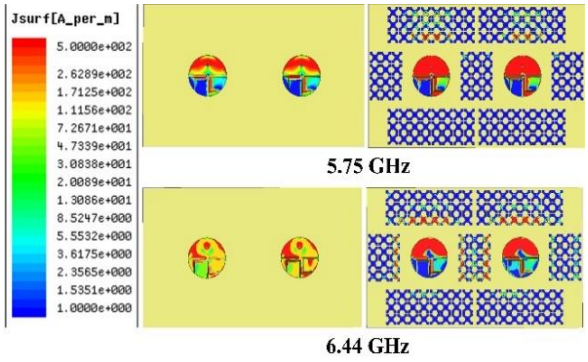

Fig. 10. Current distributions of MIMO antenna and the proposed EBG antenna at 5.75 GHz and 6.44 GHz.

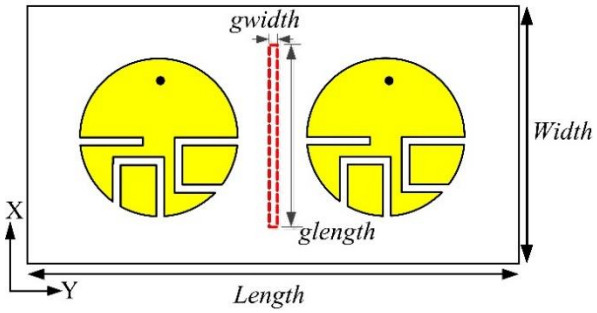

Fig. 11. Slot in ground planar of MIMO antenna.

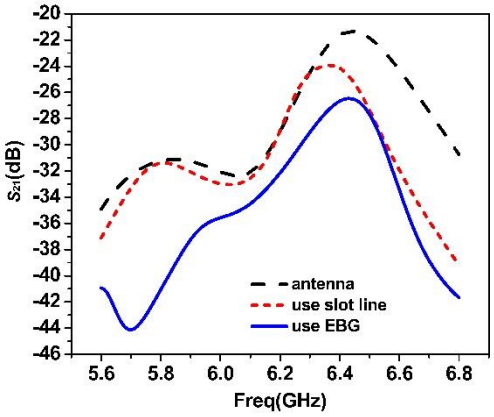

Fig. 12. Simulated isolation ($|S_{21}|$) of the proposed EBG antenna.

III. EXPERIMENTAL RESULTS AND DISCUSSION

Figure 13 depicts the photographs of the fabricated EBG antenna. Figure 14 shows the measured S_{11} of the MIMO antenna and proposed EBG antenna. The measured results show that -10 dB impedance bandwidth of the MIMO antenna is 4.5% (5.71-5.97 GHz) at the lower band and 3.6% (6.31-6.54 GHz) at the high band. When EBGs are asymmetrically arranged, the frequency bands become 5.8% (5.7-6.04 GHz) and 4.6% (6.30-6.60 GHz). Compared to the MIMO antenna, the bandwidth of proposed EBG antenna is extended by 28.9% in low frequency and 27.8% in high frequency, respectively.

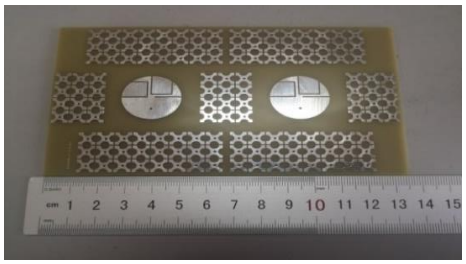

Fig. 13. Photographs of the fabricated EBG antenna.

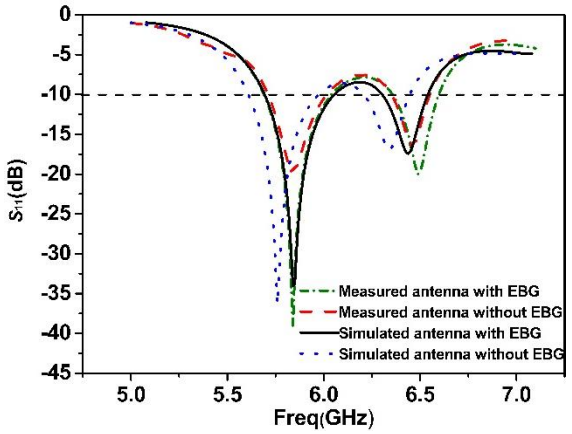

Fig. 14. Measured and simulated S_{11} of the antenna with or without EBG.

As Fig. 15 shows, when the frequency is 5.75 GHz, the gain of EBG antenna is 7 dB and the back radiation is -25 dB. The gain of MIMO antenna is 2 dB and the back radiation is -10 dB. Compared with the MIMO antenna, the gain of EBG with antenna is increased by 5 dB and the back radiation is decreased 15 dB in the E-plane. It is also shown that the cross-polarization is low at low frequency and the simulation results are basically consistent with the measured results. Figure 16 shows the gain of proposed EBG antenna is 8 dB and its back radiation is -20.5 dB at 6.44 GHz. While, the gain of traditional MIMO antenna is 1.1 dB with -10.2 dB back radiation. Compared with MIMO antenna, the gain of EBG antenna is added 6.9 dB and the back radiation is reduced 10.3 dB in the E-plane. The radiation patterns of the cross-polarization get worse at 6.44 GHz than at 5.75 GHz. There are some differences between the test results and the simulation results due to its fabrication tolerance.

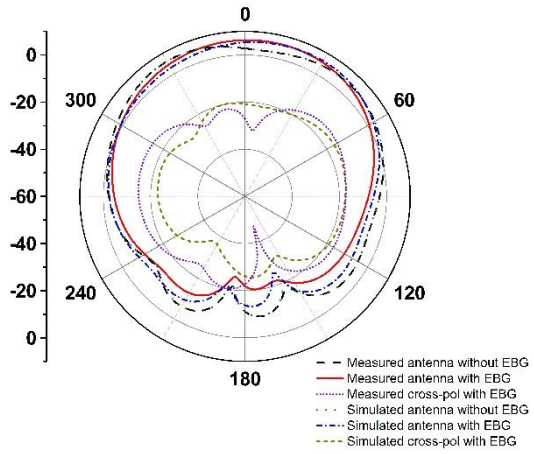

Fig. 15. Measured and simulated E-plane radiation patterns of the antenna at 5.75 GHz.

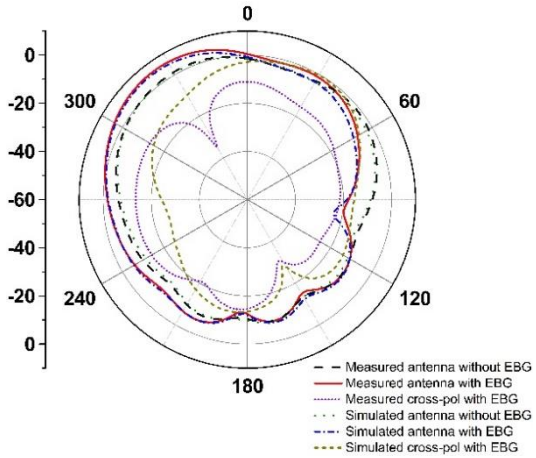

Fig. 16. Measured and simulated E-plane radiation patterns of the antenna at 6.44 GHz.

Figure 17 presents the measured and simulated isolation ($|S_{21}|$) of the proposed EBG antenna compared with MIMO antenna. The measured average isolation is around 43 dB at low frequency and 26 dB at high frequency band. Compared with the MIMO antenna, the isolation of EBG antenna is significantly improved and the measured results are in good agreement with the simulated results.

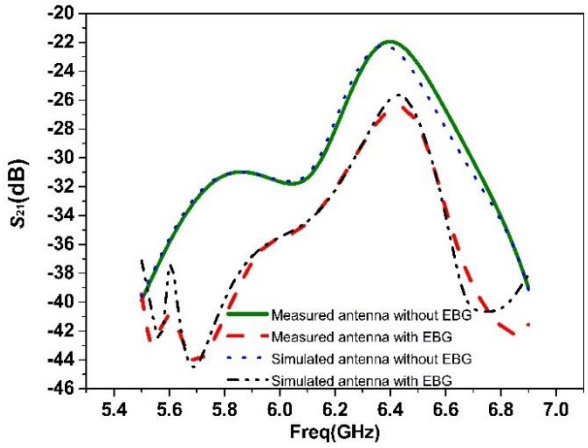

Fig. 17. Measured and simulated isolation ($|S_{21}|$) of proposed EBG antenna compared with MIMO antenna.

IV. CONCLUSION

A dual-band circular patch MIMO antenna with defective EBG structure is proposed. First and foremost, the MIMO antenna resonates at around 5.75 GHz and 6.44 GHz, the frequency covers 5.71 GHz to 5.97 GHz and 6.31 GHz to 6.54 GHz, respectively. Moreover, a high impedance EBG structure is proposed, the band gap of EBG structure is 5.68 GHz to 7.62 GHz. It can cover the frequency of the MIMO antenna. Last but not least, three rows of high impedance EBG cells are designed on the substrate to surround the MIMO antenna. By breaking the periodicity of the EBG structure, the performance parameters of the antenna will be better. The EBG with antenna has a wider bandwidth, which is extended 28.9% in low frequency and 27.8% in high frequency, respectively. In addition, the minimum isolation of the antenna is 26 dB.

The proposed EBG antenna has a higher gain and lower back radiation. When the frequency is 5.75 GHz, the gain of EBG antenna is increased 5 dB and back radiation is reduced 15 dB in the E-plane. In the H-plane, the gain of EBG antenna is increased 5 dB and back radiation is reduced 15 dB. When the frequency is 6.44 GHz, the gain of EBG antenna is increased 6.9 dB and back radiation is reduced 10.3 dB in the E-plane. In the H-plane, the gain of EBG with antenna is increased 4.5 dB and back radiation is decreased 7.7 dB. From the above results, the performance parameters of the proposed EBG antenna have been significantly improved and have a reasonable design.

ACKNOWLEDGE

The authors wish to acknowledge the supports of National Natural Science Foundation of China through Grant #61761017, #61561021, Open Project of State Key Laboratory of Millimeter Wave through Grant #K201829.

REFERENCES

[1] T. L. Marzetta, "Noncooperative cellular wireless with unlimited numbers of base station antennas," *IEEE Transactions on Wireless Communications*, vol. 9, no. 11, pp. 3590-3600, 2010.

[2] F. Rusek, D. Persson, B. K. Lau, and E. G. Larsson, "Scaling up MIMO: Opportunities and challenges with very large arrays," *IEEE Signal Processing Magazine*, vol. 30, no. 1, pp. 40-60, 2013.

[3] S. W. Su, "High-gain dual-loop antennas for MIMO access points in the 2.4/5.2/5.8 GHz bands," *IEEE Transactions on Antennas and Propagation*, vol. 58, no. 7, pp. 2412-2419, 2010.

[4] A. Al-Rawi, A. Hussain, J. Yang, M. Franzén, C. Orlenius, and A. A. Kishk, "A new compact wideband MIMO antenna—the double-sided tapered self-grounded monopole array," *IEEE Transactions on Antennas and Propagation*, vol. 62, no. 6, pp. 3365-3369, 2014.

[5] H. Li, L. Kang, Y. Xu, and Y. Z. Yin, "Planar dual-band WLAN MIMO antenna with high isolation," *Applied Computational Electromagnetics Society (ACES) Journal*, vol. 31, no. 12, pp. 1410-1415, Dec. 2016.

[6] X. Y. Zhang, G. Yang, X. R. Wang, and B. C. Li, "A dual-band and dual-polarized antenna array for 2G/3G/LTE base stations," *International Journal of RF and Microwave Computer-aided Engineering*, vol. 26, pp. 154-163, 2016.

[7] A. M. Ismaiel and A. B. Abdel-Rahman, "A meander shaped defected ground structure (DGS) for reduction of mutual coupling between microstrip antennas," *31st National Radio Science Conference (NRSC)*, Cairo, pp. 21-26, 2014.

[8] J. C. Coetzee and Y. Yu, "Design of decoupling networks for circulant symmetric antenna arrays," *IEEE Antennas and Wireless Propagation Letters*, vol. 8, no. 4, pp. 291-294, 2009.

[9] Y. Wang and Z. Du, "A printed dual-antenna system operating in the GSM1800 / GSM1900 / UMTS / LTE2300 / LTE2500 / 2.4-GHz WLAN bands for mobile terminals," *IEEE Antennas and Wireless Propagation Letters*, vol. 13, no. 1, pp. 233-236, 2014.

[10] M. Coulombe, S. F. Koodiani, and C. Caloz, "Compact elongated mushroom (EM)-EBG structure for enhancement of patch antenna array performances," *IEEE Transactions on Antennas and Propagation*, vol. 58, no. 4, pp. 1076-1086, 2010.

[11] L. Qiu, F. Zhao, K. Xiao, S. L. Chai, and J. J. Mao, "Transmit–receive isolation improvement of antenna arrays by using EBG structures," *IEEE Antennas & Wireless Propagation Letters*, vol. 11, no. 11, pp. 93-96, 2012.

[12] Z. J. Han, W. Song, and X. Q. Sheng, "Gain enhancement and RCS reduction for patch antenna by using polarization-dependent EBG surface," *IEEE Antennas and Wireless Propagation Letters*, vol. 16, pp. 1631-1634, 2017.

[13] Y. Liu, Y. W. Hao, and S. X. Gong, "Low-profile high-gain slot antenna with Fabry-Pérot cavity and mushroom-like electromagnetic band gap structures," *Electronics Letters*, vol. 51, no. 4, pp. 305-306, 2015.

[14] P. P. Bhavarthe, S. S. Rathod, and K. T. V. Reddy, "A compact two via slot-type electromagnetic band gap structure," *IEEE Microwave and Wireless Components Letters*, vol. 27, no. 5, 2017.

[15] E. Rajo-Iglesias, L. Inclan-Sanchez, J. L. Vazquez-Roy, and E. Garcia-Munoz, "Size reduction of mushroom-type EBG surfaces by using edge-located vias," *IEEE Microwave and Wireless Components Letters*, vol. 17, no. 9, pp. 670-672, 2007.

[16] A. Mousazadeh and G. H. Dadashzadeh, "A novel compact UWB monopole antenna with triple band-notched characteristics with EBG structure and two folded V-slot for MIMO/Diversity applications," *Applied Computational Electromagnetics Society (ACES) Journal*, vol. 31, no. 1, pp. 1-7, Jan. 2016.

[17] L. Peng, C. L. Ruan, and Z. Q. Li, "A novel compact and polarization dependent mushroom-type EBG using CSRR for dual/triple-band applications," *IEEE Microwave and Wireless Components Letters*, vol. 20, no. 9, pp. 489-491, 2010.

[18] X. Y. Zhang, H. T. Ma, A. Y. Zhan, L. F. Liu, Y. Xie, Y. Q. Yu, and H. W. Liu, "Design of defective electromagnetic band-gap structures for use in dual-band patch antennas," *International Journal of RF and Microwave Computer-aided Engineering*, 2018.

[19] F. Yang and Y. Rahmat-Samii, "Microstrip antennas integrated with electromagnetic band-gap (EBG) structures: A low mutual coupling design for array applications," *IEEE Transactions on Antennas and Propagation*, vol. 51, no. 10, pp. 2936-2946, 2003.

Xianyan Zhang received the B.S. degree in Applied Physics and M.S. degree in Physical Electronics from Yunnan University, Kunming, China, in 2001 and 2004 respectively, and the Ph.D. degree in Electromagnetic Field and Microwave Technology from Institute of Electronics, Chinese Academy of Sciences in 2007. Her research interests include electromagnetic computation, antenna design and wireless power transmission structure design.

Yuting Chen received the B.S. degree in School of Information Engineering from East China Jiaotong University, Nanchang, China, in 2013, and the M.S. degree in Information and Communication Engineering from East China Jiaotong University, Nanchang, China, in 2019. His research interests include electromagnetic band-gap structure, antenna design.

Haitao Ma received the B.S. degree in Applied Electronic Information Engineering from Haikou College of Economics, Haikou, China, in 2015, and the M.S. degree in Vomputer Technology from East China Jiaotong University, Nanchang, China, in 2018. His research interests also include electromagnetic band-gap structure, antenna design.

Liwei Li received the B.S. degree in Communication Engineering from Xingtan College of Qufu Normal University, Jinan, China. She is currently studying at School of Information Engineering, East China Jiaotong University. Her research interests focus on computational electromagnetic.

Huihui Xu received the B.S. degree in Communication Engineering from Chaohu University, Hefei China. She is currently studying at School of Information Engineering, East China Jiaotong University. Her research interests focus on antenna design.

High-gain Wideband Fabry-Perot Resonator Antenna Based on Single-layer FSS Structure

Zhiming Liu, Shaobin Liu*, Xiangkun Kong, Zhengyu Huang, and Xing Zhao

College of Electronic and Information Engineering
Nanjing University of Aeronautics and Astronautics, NUAA, Nanjing, 211106, P.R. China
lzmedu@foxmail.com, *lsb@nuaa.edu.cn, xkkong@nuaa.edu.cn, huangzynj@nuaa.edu.cn, elezhaoxg@163.com

Abstract ─ In this paper, a wideband Fabry-Perot (FP) resonator antenna is designed based on single-layer frequency selective surface (FSS) structure. The antenna adopts a single-layer complementary circular FSS structure as the partially reflecting surface (PRS) of Fabry-Perot resonator antenna to improve the gain. The wideband slot-coupled patch antenna is used as the source. The proposed FSS maintains a positive slope reflection phase gradient in the band of 10.3-16.0 GHz, which satisfies the realization conditions of the wideband Fabry-Perot resonator antenna. The measured results show that the 10-dB impedance matching bandwidth of the proposed Fabry-Perot resonator antenna covers 11.99-15.54 GHz (25.8%), the maximum gain is 13.16 dBi at 14.2 GHz, and the 3-dB gain bandwidth is 26.1%. The measurement results verify the feasibility of the design method.

Index Terms ─ Fabry-Perot resonator antenna, frequency selective surface, high-gain, wideband antenna.

I. INTRODUCTION

The Fabry-Perot resonator antenna is composed of a source antenna and a PRS. The Fabry-Perot antenna has the characteristics of high gain, high orientation, low profile and easy processing [1-5]. In recent years, many researchers have been attracted by the excellent performances of FP resonant cavity antenna [6-10].

In general, the reflection phase of the PRS has the characteristic of high Q value. Therefore, the gain enhancement of the FP resonator antenna is narrow-band. In order to improve the operating bandwidth of the FP resonator antenna, the PRS with the gradient structure can be used to compensate the phase in the different propagation direction, thus the PRS structure with gain enhancement in a wide band for FP resonator antenna. In [11], a single-layer FSS with quasi-periodic gradient is used as the PRS of the FP resonator antenna. The FSS structure with gradual change from the middle to the outer side can compensate the radiation phase appropriately, and the broadband FP resonator antenna with the maximum gain of 18.53 dBi and 3-dB gain bandwidth (GB) of 12.2% is realized. In [12], it applies this idea to the ground of the radiation source, and increases the gain bandwidth of the FP resonator antenna by loading the high impedance surface (HIS) on the metal ground.

In addition, the multi-layer PRS structure can also achieve bandwidth gain enhancement. In [13], a two-layer periodic structure is used as PRS of FP resonator antenna, and a broadband FP resonator antenna with a relative bandwidth of 5.1% and the maximum gain of 17.44 dBi is obtained. In [14], a multi-layer broadband FP resonator antenna fed with double slot coupling is proposed, the broadband FP resonator antenna with the fractional bandwidth of 16% and the maximum gain of 19 dBi is realized. In [15], through the exquisite design of three layer PRSs, a broadband FP resonator antenna with multi-layer PRS has the relative bandwidth of 10.7%, and it has the maximum gain of 16.9dBi. Although the FP resonator antenna with multi-layer PRS has large gain, its profile is large and its relative bandwidth is narrow.

In recent years, the PRS with positive reflection phase gradient has attracted the attention of scholars for improving the gain bandwidth of FP resonator antenna. In [16], two layers of dielectric superstrates with positive slope reflection phase gradient is used as PRS. The wideband FP resonator antenna with the relative bandwidth of 25.8% and the maximum gain of 15 dBi is realized. The antenna has good properties, but it has a high profile. In [17], a broadband FP resonator antenna with the relative bandwidth of 15% and the maximum gain of 20 dBi is proposed by using three layers periodic PRSs with positive reflection phase gradient. The FP resonator antenna formed by PRS with positive reflection phase gradient can effectively improve its 3-dB gain bandwidth, but its profile is high.

In order to expand the 3-dB gain bandwidth and reduce profile of the FP resonator antenna, a FSS with circular complementary structure is etched on both sides of the substrate as the PRS to form the FP resonator antenna in this paper. The FSS with positive reflection phase gradient in the band of 10.3-16.0 GHz, and a slot-

Submitted On: September 3, 2018
Accepted On: December 21, 2018

coupled patch antenna as the source to achieve a wideband FP resonator antenna. The measured results show that the proposed antenna with $|S_{11}|$<-10 dB of 11.99-15.54 GHz, the 3-dB gain bandwidth of 12.36-15.6 GHz, and the peak gain of 13.16 dBi.

II. FSS AND RADIATION ANTENNA

A. Numerical analysis

As shown in Fig. 1, the FP resonator is actually a semi-open resonator, which consists of a ground and a partially reflecting surface. The electromagnetic wave radiated by the source is reflected repeatedly between the upper and lower surfaces of the resonant cavity. Assuming that the incident wave with frequency of f illuminates the ground and the metal ground has total reflection properties, the reflection amplitude of ground is equal to 1. Therefore, the reflection coefficient of ground can be expressed as $e^{j\varphi_{GND}}$, where φ_{GND} is the reflection phase of ground. Meanwhile, the reflection coefficient of PRS can be expressed as $pe^{j\varphi_{PRS}}$, where p and φ_{PRS} denote reflection amplitude and reflection phase of the PRS, respectively. Considering that the source is much smaller than the overall size of the Fabry-Perot resonator, it can be approximately regarded as a point source.

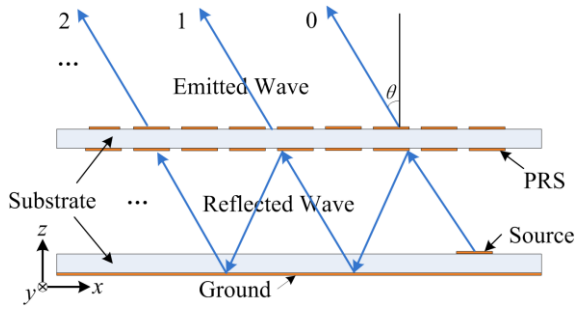

Fig. 1. The schematic diagram of Fabry-Perot resonator.

The electric field intensity of each electromagnetic wave transmitted from PRS is superimposed as [1]:

$$E=\sum_{n=0}^{\infty} f(\alpha)E_0 p^n\sqrt{1-p^2}e^{j\Theta_n}, \quad (1)$$

$$\Theta_n = n\Phi = n(-\frac{4\pi f}{c}h\cos\alpha+\varphi_{GND}+\varphi_{PRS}), \quad (2)$$

where E_0 is the amplitude of the first emitted wave, Θ_n is the total phase variations during the reflections between the ground and the PRS, n denotes the nth emitted wave, $f(\alpha)$ is the field intensity direction function, α is the incidence angle, c is the velocity of light, h is the thickness of cavity. The absolute value of field strength is expressed as:

$$|E|=|E_0|\,f(\alpha)\sqrt{\frac{1-p^2}{1+p^2-2p\cos\Phi}}. \quad (3)$$

Thus, the power pattern S is:

$$S=\frac{1-p^2}{1+p^2-2p\cos(\varphi_{GND}+\varphi_{PRS}-\frac{4\pi f}{c}h\cos\alpha)}f^2(\alpha), \quad (4)$$

when α=0°, the power pattern S becomes:

$$S=\frac{1-p^2}{1+p^2-2p\cos(\varphi_{GND}+\varphi_{PRS}-\frac{4\pi f}{c}h)}f^2(0). \quad (5)$$

The maximum power in the direction of α=0° can be obtained when:

$$\varphi_{GND}+\varphi_{PRS}-\frac{4\pi f}{c}h=2n\pi, \quad n=0,1,2....., \quad (6)$$

and the maximum power pattern is:

$$S_{max}=\frac{1+p}{1-p}f^2(0). \quad (7)$$

It can be concluded that when f, h, φ_{GND} and φ_{PRS} satisfy the resonance condition of equation (6), the FP resonator antenna will have the largest forward energy density. From equation (7), the power pattern S of FP resonator antenna is positively correlated with the reflection amplitude of the PRS, which means that as the p increases, the maximum power pattern S_{max} of the FP resonator antenna will increase.

Assuming that the directivity of the source antenna is D_0 at frequency f, and the directivity is D_s after adding a PRS above it. By equation (7), the relative directivity D can be expressed as follows:

$$D(\mathrm{dB})=10\log_{10}\left(\frac{1+p}{1-p}\right). \quad (8)$$

According to the above numerical analysis, as the f, h, φ_{GND} and φ_{PRS} satisfy the Fabry-Perot resonance condition, the FP resonance mode can be excited. The directivity of FP resonator antenna is positively correlated with the reflection amplitude of PRS. In order to obtain a large directivity of the FP resonator antenna, the reflection amplitude of the designed PRS should be as large as possible.

B. The design of FSS

From equation (6), the PRS reflection phase can be expressed as:

$$\varphi_{PRS}=\frac{4\pi h}{c}f+2N\pi-\varphi_{GND}, \quad (9)$$

where h is the thickness of the cavity, c is the velocity of light, and φ_{PRS} is the reflection phase of PRS, φ_{GND}=-π. It can be seen that when the resonant cavity height h, resonant frequency f and φ_{PRS} meet the equation (9), the FP resonance mode can be excited to achieve the gain enhancement. Therefore, the PRS with positive reflection phase gradient is the key point to design the wideband FP resonator antenna

The design of PRS structure is an important part for the wideband FP resonator antenna. In this paper, the

designed FSS acts as PRS, the proposed FSS structure is shown as shown in Fig. 2 (a). The FSS unit is composed of a circular complementary structure, p=6.5 mm, it is etched on both sides of the F_4BM220 substrate with the thickness of 1.5 mm (ε_1=2.2, tanδ=0.0007).

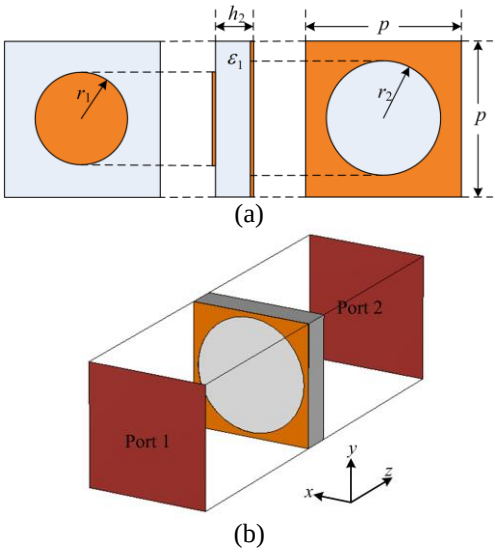

Fig. 2. The unit of FSS: (a) structure and (b) simulation model.

To analyze the characteristic of positive reflection phase gradient of FSS structure, the parameters of FSS are analyzed. Fig. 2 (b) is the schematic diagram of simulation model. Port 1 and Port 2 are set at a distance from the FSS unit, and the boundary conditions of the simulation models are set to magnetic boundary and electrical boundary in the direction of ±x and ±y, respectively. When the incident wave propagates along the +z direction, the simulated results of parameters scanning are shown in Fig. 3. In Fig. 3 (a), fixed r_2=3.0 mm, with the increase of r_1, the resonance frequency shifts to low frequency, the reflection amplitude increases slightly, the slope of the reflection phase curve is approximately the same, and the positive reflection phase gradient bands shift to the low frequency. In Fig. 3 (b), fixed r_1=2.3 mm, with the increase of r_2, the resonance frequency shifts to low frequency, the reflection amplitude decreases obviously, the slope of the reflection phase curve increases, and the positive reflection phase gradient bands also shift to low frequency. Select parameters h_2=1.5 mm, r_1=2.3 mm, r_2=3 mm, the FSS unit structure has a positive slope reflection phase gradient band in the range of 10.3-15.9 GHz, and the reflection amplitude is more than 0.58. According to the equation (9), it is known that the FP resonator antenna designed by the FSS structure can excite the FP resonance mode in a wide band, and realize the gain enhancement of the FP resonator antenna in a wide band.

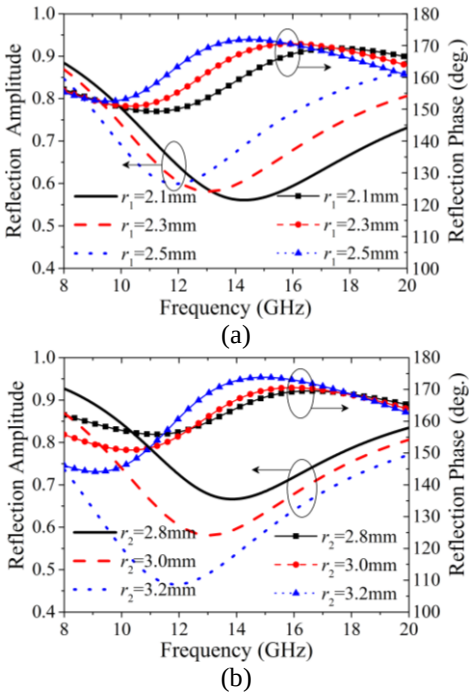

Fig. 3. The reflection coefficients of PRS: (a) r_2=3.0 mm and (b) r_1=2.3 mm.

C. Source antenna

The designed wideband source antenna is made up of a slot antenna and parasitic patch, as shown in Fig. 4. The ground and feed line of the slot antenna are etched on both sides of the F_4BM220 substrate (ε_2=2.2, tanδ=0.0007) with the thickness of 0.8 mm, respectively. The length and width of the slot antenna are W=60 mm, and the parasitic patch is placed at h_{air}=3 mm above the slot of the ground. The structural parameters are shown in Table 1. As shown in Fig. 5, the $|S_{11}|$<-10 dB of the slot-coupled patch antenna is 12.36-16.29 GHz, and the maximum gain is 8.33 dBi at 15.0 GHz. Apparently, the 10-dB impedance matching bandwidth of the source antenna is within the range of the positive slope reflection phase gradient band of the designed FSS.

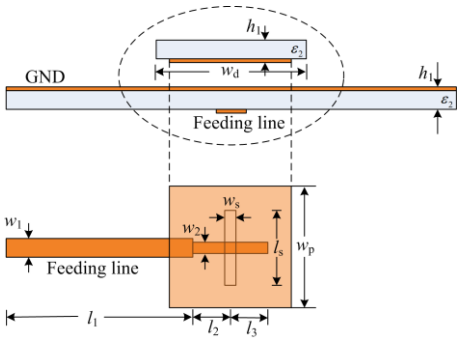

Fig. 4. The schematic diagram of the slot-coupled patch antenna.

Table 1: Parameters value of the slot-coupled patch antenna

Parameters	h_1	l_1	l_2	l_3	l_s
Value (mm)	0.8	24	6	1.7	7
Parameters	w_p	w_d	w_1	w_2	w_s
Value (mm)	5.5	10	2.3	0.9	1

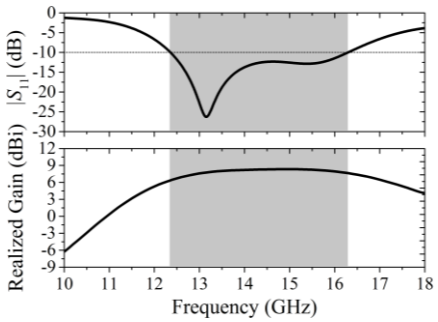

Fig. 5. The simulated results of the slot-coupled patch antenna.

III. WIDEBAND FABRY-PEROT ANTENNA

A. Wideband Fabry-Perot antenna

Based on the above design of the FSS structure and the source, an FP resonator antenna with wideband and high gain is designed. The unit of FSS element is etched in a 7×7 periodicity on the F_4BM220 substrate of W×W, and placed at h_c above the ground of slot antenna. Figure 6 is the schematic diagram of the wideband FP resonator antenna. A part of the electromagnetic wave radiated by slot-coupled patch antenna is reflected in the cavity, and part of it is transmitted through the FSS structure. When the thickness of the cavity and the reflection phase of the FSS satisfy the FP resonance condition, the gain is enhanced.

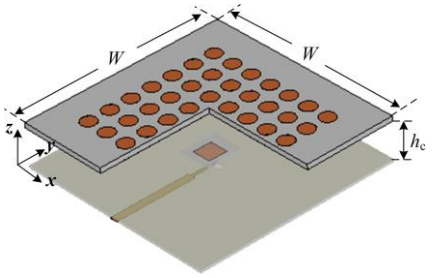

Fig. 6. The schematic diagram of the proposed antenna.

The thickness of FP cavity is an important factor that affects the performance of wideband FP resonator antenna. In order to design FP resonator antenna with good performance, the influence of different cavity thickness on the bandwidth and gain of FP resonator antenna should be taken into account.

The effect of different cavity thickness on the $|S_{11}|$ and the realized gain of FP resonator antenna is analyzed. As shown in Fig. 7 and Table 2, other parameters are fixed, as the h_c increases from 9.5 mm to 11.0 mm by step length 0.5 mm, the $|S_{11}|$<-10 dB of the designed antenna is changed from two to one, and the relative bandwidth is gradually expanded, while the 3-dB gain bandwidth is increased first and then reduced, but the maximum gain is gradually reduced. Therefore, considering the design of the wideband FP resonator antenna with large operating bandwidth and high gain, h_c=10.5 mm is selected. For this case, the proposed antenna with the 10-dB impedance matching bandwidth of 11.99-15.81 GHz (27.4%), 3-dB gain bandwidth of 11.9-15.5 GHz (26.3%), and the maximum gain of 13.26 dBi at 15.0 GHz. Meanwhile, the half-power beamwidth of 15.0 GHz of the E- and H- planes are 23.9° and 39.2°, respectively.

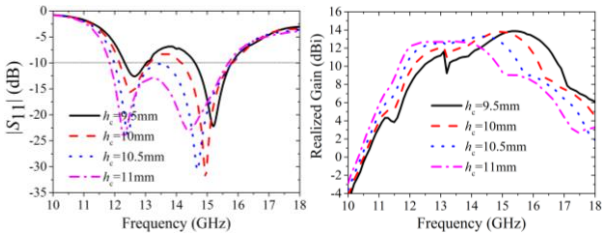

(a) (b)

Fig. 7. The simulated results of vary h_c: (a) S_{11} and (b) realized gain.

Table 2: Comparison between different h_c

h_c (mm)	$\|S_{11}\|$<-10 dB (GHz)	3-dB Gain Bandwidth (GHz)
9.5	12.32-13.02 (5.5%) 14.60-15.79 (7.8%)	13.6-16.7 (20.5%)
10.0	12.15-13.12 (7.7%) 14.16-15.82 (11.1%)	12.3-16.1 (26.8%)
10.5	11.99-15.81 (27.4%)	11.9-15.5 (26.3%)
11.0	11.84-15.68 (27.9%)	11.7-14.9 (24.1%)

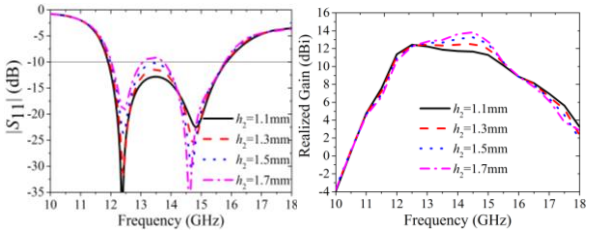

(a) (b)

Fig. 8. The simulated results of proposed antenna with different h_2: (a) $|S_{11}|$ and (b) realized gain.

The effect of h_2 on the performance of the proposed antenna is also considered. We fixed other parameters and scan the h_2 from 1.1 mm to 1.7 mm by step of 0.2 mm. The simulated results are shown in Fig. 8. It shows that when h_2 increases from 1.1 mm to 1.5 mm, the 10-dB impedance matching bandwidth of the proposed antenna remains the same basically, while as h_2 = 1.7 mm, the antenna has two operating bands with 10-dB impedance matching level. In addition, the maximum realized gain of the proposed antenna enhances with the increase of h_2. Therefore, to ensure the high performance of the proposed antenna, h_2 = 1.5 mm is selected.

B. Experiments

The designed wideband FP resonator antenna is fabricated, and its experiment is completed in the microwave anechoic chamber. The measurement scene is shown in Fig. 9.

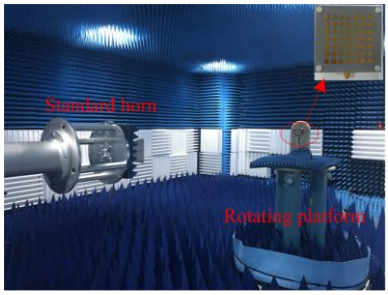

Fig. 9. The measurement scene of the proposed antenna.

Figure 10 shows that the measured and simulated results of the $|S_{11}|$ and realized gain of the proposed antenna. In Fig. 10, the measured results show that the impedance bandwidth $|S_{11}|$<-10 dB of the source antenna is 12.61-16.19 GHz, and the maximum gain is 8.18 dBi at 15.4 GHz. Meanwhile, the measured results show that the impedance bandwidth $|S_{11}|$<-10 dB of the proposed wideband FP resonator antenna is 11.99-15.54 GHz (25.8%), the 3-dB gain bandwidth is 12.36-15.6 GHz (26.1%), and the maximum gain value is 13.16 dBi at 14.2 GHz, it is approximately consistent with the simulated results.

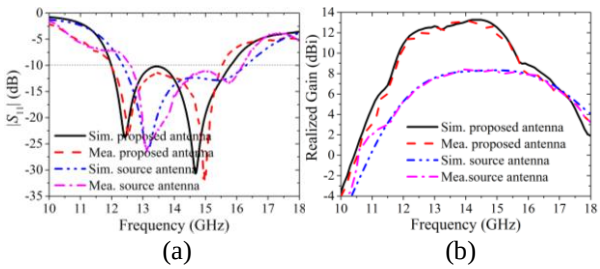

(a) (b)

Fig. 10. The comparisons of measured and simulated results: (a) S_{11} and (b) realized gain.

Also, the simulated and measured radiation patterns of the proposed antenna at 12.5 GHz, 13.5 GHz, 14.5 GHz and 15.5 GHz, respectively, in both planes are shown in Fig. 11. It can be observed that the designed antenna has good radiation pattern in the operating band. Finally, the proposed antenna is compared with the existing similar work in Table 3. It shows that the proposed antenna has a lower profile, wider operating bandwidth and the 3-dB gain bandwidth is extended.

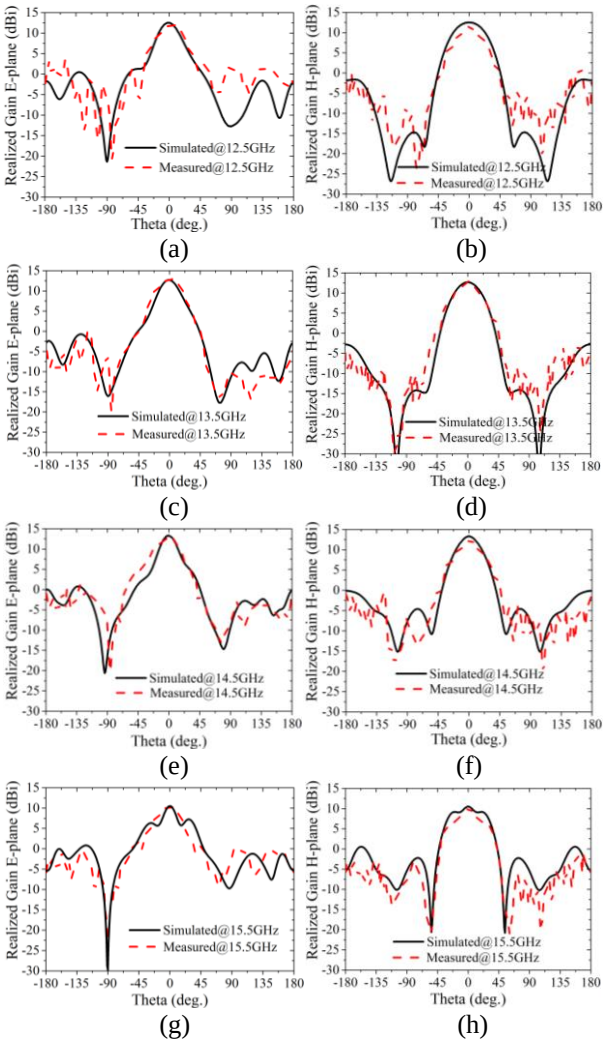

Fig. 11. The radiation patterns of the proposed antenna: (a) E-plane, (b) H-plane at 12.5 GHz, (c) E-plane, (d) H-plane at 13.5 GHz, (e) E-plane, (f) H-plane at 14.5 GHz, and (g) E-plane, (h) H-plane at 15.5 GHz.

IV. CONCLUSION

A wideband high-gain Fabry-Perot resonator antenna is designed based on single-layer FSS structure. The wideband slot-coupled patch antenna is used as the source antenna, the FSS with circular complementary structure is used to as the PRS. Moreover, the influence

of various parameters on the antenna performance is analyzed. The measured results show that the proposed antenna has the 10-dB impedance matching bandwidth of 11.99-15.54 GHz (25.8%), the 3-dB gain bandwidth of 12.0-15.6 GHz (26.1%), and the maximum gain value of 13.16 dBi at 14.2 GHz, it confirms the correctness of the simulated results.

Table 3: Comparison between the designed antenna and the existed work

Ref.	$\|S_{11}\|$<-10 dB (GHz)	3-dB GB	Height (mm)	Max. Gain (dBi)	Aperture (mm^2)	PRS Num.
[13]	13.4–14.1	5.1%	23.4	17.44	280×280	2
[15]	13–14.5	10.9%	16.44	15	80×80	3
[16]	13.6–18.4	25.8%	26.3	15	45×45	2
[17]	13.5–15.7	15%	35	20.0	80×80	3
This work	11.99-15.54	26.1%	12.8	13.16	60×60	1

ACKNOWLEDGMENT

This work was supported by Chinese Natural Science Foundation (Grant No. 61671238; No. 61471368), the Fundamental Research Funds for the Central Universities (No. NJ20160008; NS2017026), Project Funded by China Postdoctoral Science Foundation (Grant No. 2016M601802), Jiangsu Planned Projects for Postdoctoral Research Funds (Grant No. 1601009B), Aeronautical Science Foundation of China (20161852016), and the Funding of Jiangsu Innovation Program for Graduate Education (No. KYLX16_0371), the Fundamental Research Funds for the Central Universities.

REFERENCES

[1] G. V. Trentini, "Partially reflecting sheet arrays," *IRE Trans. Antennas Propag.*, vol. 4, no. 4, pp. 666-671,1956.

[2] S. Bibi, R. Saleem, A. Quddus, and M. F. Shafique, "Dual-band antenna for high gain M2M communication using PRS," *Applied Computational Electromag. Soc. J.*, vol. 32, no. 11, pp. 994-1000, 2017.

[3] Z. Liu, S. Liu, B. Bian, X. Kong, and H. Zhang, "Metasurface-based low-profile high-gain substrate-integrated Fabry-Pérot cavity antenna," *Int. J. RF Microw. Comput. Aided Eng*., p. e21583, 2018.

[4] W. Liu, Z. N. Chen, T. S. P. See, and F. Liu, "SIW-slot-fed thin beam-squint-free Fabry-Pérot cavity antenna with low backlobe levels," *IEEE Antennas Wirel. Propag. Lett.*, vol. 13, pp. 552-554, 2014.

[5] Y. Zhang, W. Yu, and W. Li, "Study on Fabry-Pérot antennas using dipole exciters," *Applied Computational Electromag. Soc. J.*, vol. 29, no. 12, pp. 1112-1116, 2014.

[6] H. H. Tran and T. K. Nguyen, "K-band planar and low-profile Fabry-Perot cavity antenna with a coupled strip-slitline feed structure," *Applied Computational Electromag. Soc. J.*, vol. 32, no. 6, pp. 542-547, 2017.

[7] Z. G. Liu, Z. X. Cao, and L. N. Wu, "Compact low-profile circularly polarized Fabry–Perot resonator antenna fed by linearly polarized microstrip patch," *IEEE Antennas Wirel. Propag. Lett.*, vol. 15, pp. 524-527, 2016.

[8] Y. F. Cheng, W. Shao, X. Ding, and M. X. Yu, "Design of tilted-beam Fabry-Perot antenna with aperiodic partially reflective surface," *Applied Computational Electromag. Soc. J.*, vol. 32, no. 5, pp. 397-404, 2017.

[9] P. Liu, J. Chen, and Y. Hu, "Accelerated storage testing and life assessment method of antenna," *Equip. Environ. Eng.*, vol. 15, no. 3, pp. 98-102, 2018.

[10] Y. Zheng, J. Gao, Y. Zhou, X. Cao, H. Yang, S. Li, and T. Li, "Wideband gain enhancement and RCS reduction of Fabry–Perot resonator antenna with chessboard arranged metamaterial superstrate," *IEEE Trans. Antennas Propag*., vol. 66, no. 2, pp. 590-599, 2018.

[11] Z. Liu, W. Zhang, D. Fu, Y. Gu, and Z. Ge, "Broadband Fabry-Perot resonator printed antennas using FSS superstrate with dissimilar size," *Microw. Opt. Technol. Lett.*, vol. 50, no. 6, pp. 1623-1627, 2008.

[12] Z. H. Wu and W. X. Zhang, "Broadband printed compound air-fed array antennas," *IEEE Antennas Wirel. Propag. Lett.*, vol. 9, pp. 187-190, 2010.

[13] C. Mateo-Segura, A. P. Feresidis, and G. Goussetis, "Bandwidth enhancement of 2-D leaky-wave antennas with double-layer periodic surfaces," *IEEE Trans. Antennas Propag.*, vol. 62, no. 2, pp. 586-593, 2014.

[14] K. Konstantinidis, A. P. Feresidis, and P. S. Hall, "Dual-slot feeding technique for broadband Fabry-Perot cavity antennas," *IET Microw. Antennas Propag.*, vol. 9, no. 9, pp. 861-866, 2015.

[15] K. Konstantinidis, A. P. Feresidis, and P. S. Hall, "Broadband sub-wavelength profile high-gain antennas based on multi-layer metasurfaces," *IEEE Trans. Antennas Propag.*, vol. 63, no. 1, pp. 423-427, 2015.

[16] N. Wang, J. Li, G. Wei, L. Talbi, Q. Zeng, and J. Xu, "Wideband Fabry-Perot resonator antenna with two layers of dielectric superstrates," *IEEE Antennas Wirel. Propag. Lett.*, vol. 14, pp. 229-232, 2015.

[17] K. Konstantinidis, A. P. Feresidis, and P. S. Hall, "Multilayer partially reflective surfaces for broadband Fabry-Perot cavity antennas," *IEEE Trans. Antennas Propag*., vol. 62, no. 7, pp. 3474-3481, 2014.

Zhiming Liu was born in Jiangxi Province, China, in 1989. He received the B.S. degree and M.S. degree from East China Institute of Technology, Fuzhou, China, in 2012 and Nanchang University, Nanchang, China, in 2015, respectively. He is currently pursuing the Ph.D. degree in College of Electronic and Information Engineering, Nanjing University of Aeronautics and Astronautics, Nanjing, China. His research interests include Antennas and Metasurface.

Shaobin Liu received the Ph.D. degree in Electronics Science and Technology from the National University of Defense Technology in 2004. However, in 2003, he was already promoted as Professor. He is currently a Professor of Electromagnetic and Microwave Technology at the Nanjing University of Aeronautics and Astronautics. His research focuses on plasma stealthy antennas, microwave, radio frequency, electromagnetic compatibility.

Xiangkun Kong received the Ph.D. degree in Communication and Information Systems from the Nanjing University of Aeronautics and Astronautics (NUAA) in 2015. He has been an Associate Professor in NUAA, since his promotion in July 2015. He used to work at the University of St. Andrews in the UK as an Academic Visitor supported by China Scholarship Council. His main research interests include the plasma stealth, plasma photonic crystal, electromagnetic properties of metamaterials, and computational electromagnetics. He has published more than 60 papers in different academic journals, including Applied Physics Letters, Optics Express, and IEEE Journal of Selected Topics in Quantum Electronics, and has been cited 1099 times.

Zhengyu Huang was born in Hunan, China, in 1986. He received the B.S. degrees in Electronic and Information Engineering from Nanchang University, Nanchang, China, in 2008 and the Ph.D. degree in Electromagnetic Environmental Effects and Electro-optical Engineering from PLA University of Science and Technology, Nanjing, China, in 2016. He has co-authored one monograph on the Associated Hermite finite-difference time-domain method and 30 peer-reviewed journal papers included in the Web of Science Core Collection. He was the recipient of the Outstanding Doctoral Dissertation Award of the PLA University of Science and Technology in 2017 and the Excellent Doctoral Dissertation Award by Lu Zhitao Academician in 2018.

He is currently an Associate Professor with Key Laboratory of Radar Imaging and Microwave Photonics, Nanjing University of Aeronautics and Astronautics, Nanjing, China. His research interests include computational electromagnetics, electromagnetic compatibility and multiphysics modeling and analysis.

Xing Zhao was raised in Tianjin, China. He received the B.Eng. degree in Information Engineering from Shanghai Jiao Tong University, Shanghai, China, in 2008, and the M.S. and Ph.D. degrees in Electronics and Computer Engineering from Hanyang University, Seoul, South Korea, in 2010 and 2014, respectively.

From 2015 to 2017, he was a Postdoctoral Research Fellow with the Department of Electrical and Computer Engineering, National University of Singapore, Singapore. He is currently an Associate Research Fellow with the College of Electronic and Information Engineering, Nanjing University of Aeronautics and Astronautics, China.

His current research interests include small antennas for 5G mobile MIMO platforms and integrated array antennas for radar system.

Design of a W-band Dual-polarization Monopulse Reflector Antenna

Wenhao Tan [1], Hao Luo [2], and Guoqiang Zhao [1]

[1] Beijing Key Laboratory of Millimeter Wave and Terahertz Techniques
Beijing Institute of Technology, Beijing, CHN100081, China
1009374960@qq.com, Zhaogq@bit.edu.cn

[2] Beijing Key Laboratory of Millimeter Wave and Terahertz Techniques
Beijing Institute of Technology, Beijing, CHN100081, China
ihlyt111@126.com

Abstract ─ This paper introduces a W-band dual-polarization reflector antenna which combines one dual-polarized transmit-receive SUM channel and two single-polarized DIFF receiving channels. The feed of the antenna consists of four OMTs (Orth Mode Transducer) to realize dual-polarization monopulse angle measurement. Four horns of the feed are combined into one radiation aperture by a coupled retracted structure to decrease side-lobes. The SUM beam gain of the proposed antenna is over 41 dBi and the aperture efficiency of 60% is achieved, cross-polarization level is better than –43 dB. The first sidelobe level is better than -30dB. The null-depth is better than -20dB.

Index Terms ─ Dual-polarization, monopulse, reflector antenna, W-band.

I. INTRODUCTION

Fully-polarization radars have more advantages in target recognition and anti-jamming compared with single-polarization radars [1]. Many kinds of dual-polarization antennas have been proposed, such as microstrip patch [2], coupling slot [3], slot array [4], horn antenna [5] and reflectarray [6]. However in high-frequency band, waveguide slot array may have a high cost and is difficult to fabricate. And in high power applications, microstrip patch is not capable for its high dielectric loss.

The millimeter-wave dual-polarization detecting system requires a dual-polarized antenna with high gain and low side-lobes that makes reflector antenna a good candidate. Compared with other antennas working at w-band, the reflector antenna has the advantages of simple manufacturing, high gain, low side lobes, and narrow beams. The key component of a dual-polarization reflector antenna is a dual-polarization feed-source. In this paper, we proposed a dual-polarization reflector antenna with good radiation performance and easy approaching.

II. GEOMETRY AND ANALYSIS OF THE PROPOSED ANTENNA

According to the principle of focusing, the reflector antenna uses the reflection of the electromagnetic wave on the paraboloid to form a plane wave-front. The geometry of the reflector antenna system is illustrated in Fig. 1.

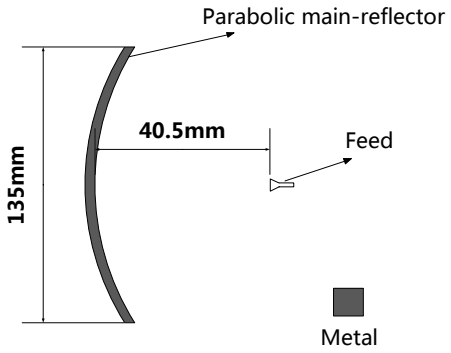

Fig. 1. Design and geometry of the antenna system.

The performance of the reflector antenna depends largely on the primary pattern of the feed, so the study of the primary radiation characteristics of the feed will benefit the overall antenna system. The proposed feed can be described in two parts, the feed net and four horns.

Figure 2 shows the working principle of the feed. In order to realize the SUM and DIFF signal processing, ports V1 and V2 receive and transmit vertically polarized wave while ports H1 and H2 receive and transmit horizontally polarized wave. Square waveguides 1, 2, 3 and 4 can transmit two kinds of orthogonal polarized waves. The sum of V1, V2 and the sum of H1, H2 make the dual-polarized sum signal of the proposed monopulse feed. The difference between V1 and V2 forms the pitch

Submitted On: October 15, 2018
Accepted On: February 9, 2019

DIFF signal, and the difference between H1 and H2 forms the azimuth DIFF signal.

The feed takes the form of four receiving and launch ports to get rid of the complex design of the comparator, and replace the analog comparator with digital comparator. Therefore this design can eliminate the insertion loss caused by the analog comparator.

There are two ways to realize dual-polarization for horn feed, cross-slot coupling or application of OMT (Orth Mode Transducer). But the isolation between different polarizations of OMT is better than cross slot coupling. And the structure of OMT is easier to fabricate.

The structure of OMT and the feed is illustrated in Fig. 3, as is shown in Fig. 3 (a), the feed source consists of four OMTs. They are combined to a radiation aperture by a coupled retracted structure. Both polarizations of the OMT structure can receive and transmit the sum signal, but the pitch different signal can only be received by the DIFF channel of one polarization, while the azimuth different signal received by the DIFF channel of the other polarization.

The structure of OMT is illustrated in Fig. 3 (b), a metal bar is designed above the coupling slot to optimize the isolation between horizontal polarization and vertical polarization.

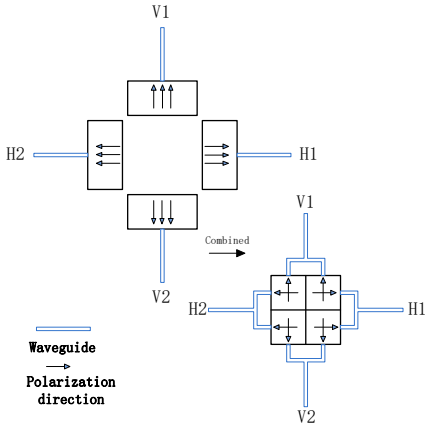

Fig. 2. Polarization direction of the feed.

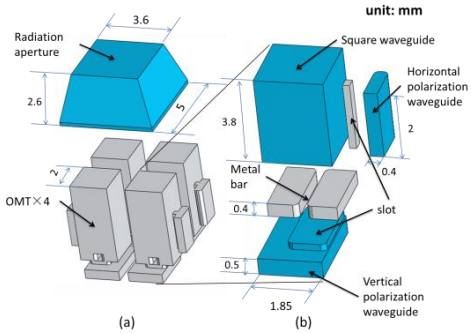

Fig. 3. (a) Structure of feed. (b) Structure of OMT.

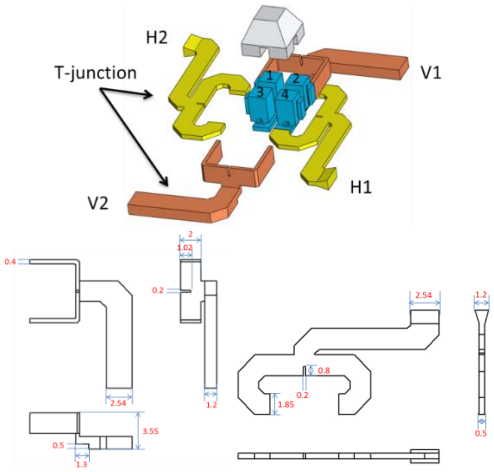

Fig. 4. Structure of the feed and the T-junction.

The structure of the feed is shown in Fig. 4, and it is the specific feed-source structure that realizes the working function shown in Fig. 2.

III. SIMULATION AND MEASUREMENT RESULTS

The simulated model is shown in Fig. 5, and Fig. 6 shows the prototype of the proposed antenna. The SUM pattern of the proposed antenna is illustrated in Figs. 7 (a), (b), and the DIFF pattern of the antenna is illustrated in Fig. 7 (b), where –M and –S represent measured and simulated result. (H) and (E) represent H-plane and E-plane. Isolation and VSWR of the feed ports are illustrated in Fig. 8.

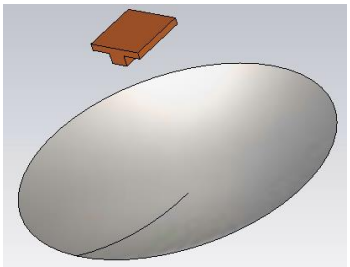

Fig. 5. Simulate model of the proposed antenna.

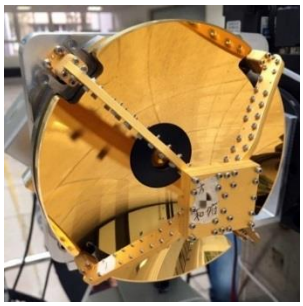

Fig. 6. Prototype of the proposed antenna.

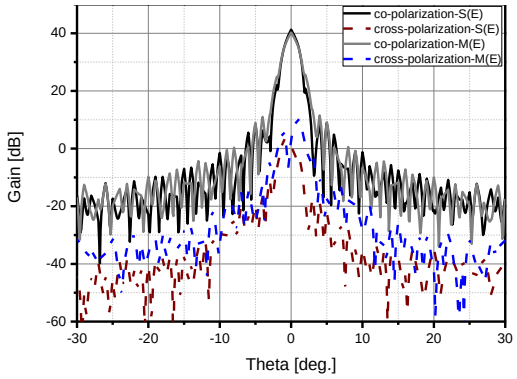

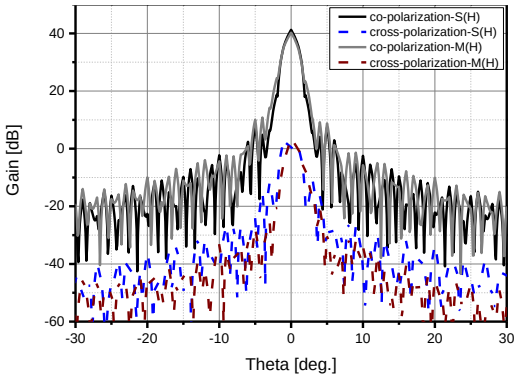

(a)

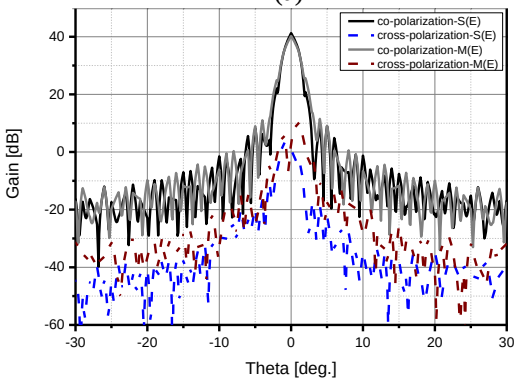

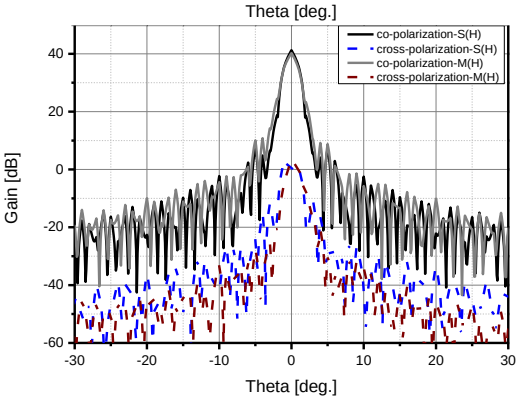

(b)

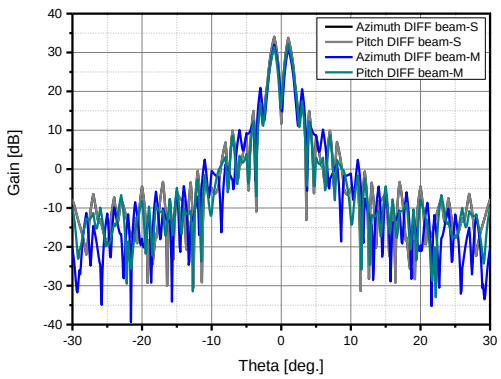

(c)

Fig. 7. (a) Vertical polarization SUM pattern. (b) Horizontal polarization SUM pattern. (c) Azimuth and Pitch DIFF pattern.

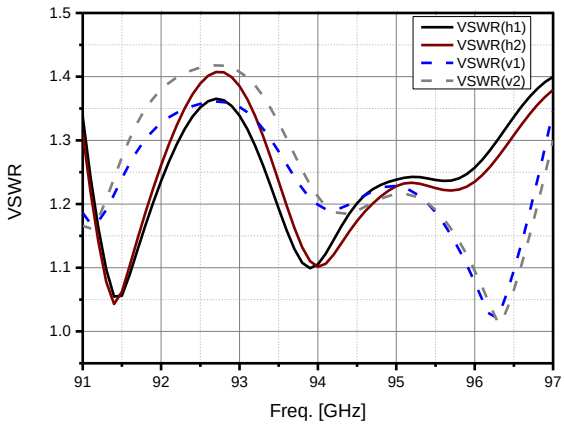

(a)

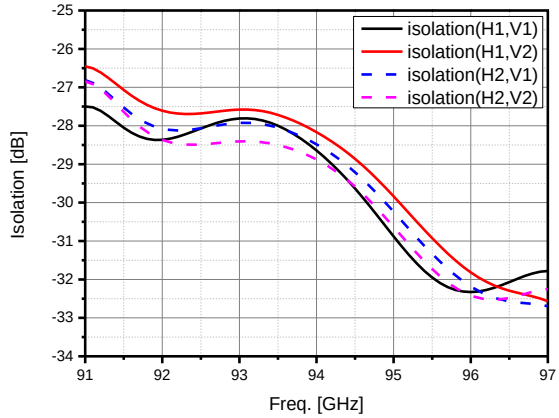

(b)

Fig. 8. (a) VSWR of the feed ports. (b) Isolation between different polarizations.

IV. CONCLUSION

In this paper, a dual-polarized monopulse reflector antenna working at W-band is demonstrated by employing a four-unit-horn with the OMTs as feed source. Simulating results verify that the polarization isolation is better than -30dB. The proposed antenna is designed and optimized in HFSS and CST. At 94GHz, the SUM beam gain is over 41dBi. Cross-polarization levels are better than -43dB and the first sidelobe level is better than -30dB. The null-depth is better than -20dB, the result reveals that the proposed antenna has excellent polarization synthesis and polarized monopulse performances further.

REFERENCES

[1] Y. Tsunemitsu, J. Hirokawa, M. Ando, Y. Miura, Y. Kazama, and N. Goto, "Polarization isolation characteristics between two center-feed single-layer waveguide arrays arranged side-by-side," *Antennas & Propagation Society International Symposium. IEEE*, 2006.

[2] P. Zheng, B. Hu, S. Xu, and H. Sun, "A W-band high aperture efficiency multi-polarized monopulse cassegrain antenna fed by phased microstrip patch quad," *IEEE Antennas and Wireless Propagation Letters*, vol. 16, pp. 1609-1613, 2017.

[3] S. K. Padhi, S. N. C. Karmakar, C. L. Law, and S. S. Aditya, "A dual polarized aperture coupled circular patch antenna using a C-shaped coupling slot," *IEEE Trans. Antennas Propag.*, vol. 51, no. 12, pp. 3295-3298, Dec. 2003.

[4] Y. Li, Z. J. Zhang, W. H. Chen, Z. Feng, and M. F. Iskander, "A dualpolarization slot antenna using a compact CPW feeding structure," *IEEE Antennas Wireless Propag. Lett.*, vol. 9, pp. 191-194, 2010.

[5] Z. X. Shen and C. Feng, "A new dual-polarized broadband horn antenna," *IEEE Antennas Wireless Propag. Lett.*, vol. 4, pp. 270-273, 2005.

[6] J. A. Encinar, et al., "Dual-polarization dual-coverage reflectarray for space applications," *IEEE Trans. Antennas Propag.*, vol. 54, no. 10, pp. 2827-2837, Oct. 2006.

Wenhao Tan (1995-), male, master candidate of Beijing Key Laboratory of Millimeter Wave and Terahertz Techniques in Beijing Institute of Technology. Major in microwave and electromagnetic fields. Research direction is millimeter wave antenna design.

Hao Luo (1990-), male, doctor candidate of Beijing Key Laboratory of Millimeter Wave and Terahertz Techniques in Beijing Institute of Technology. Major in microwave and electromagnetic fields. Research direction is millimeter wave antenna design.

Guoqiang Zhao (1976-), male, Associate Professor and Master Tutor of Beijing Institute of Technology. Research directions are Microwave millimeter wave dual polarized antenna, Microwave millimeter wave circuit and system integration, Microwave millimeter wave frequency synthesis technology, Microwave and millimeter wave target full polarization characteristics and feature extraction algorithm etc.

Design and Implementation of High Performance UWB Horn Antenna

Nan Hu [1]*, Wenqing Xie [1], Jianrui Liu [2], Shuang Liu [1], Lixin Zhao [2], and Changyong Yuan [2]

[1] A-INFO Inc., Beijing, 100084, China

[2] Chengdu A-INFO Inc., Chengdu, 610041, China
stanley@ainfoinc.com*

Abstract ─ Broadband horn antennas have been widely used in radar and communication systems. They have also been added to various state-of-the-art control systems to perform EMC measurements. EMC measurements traditionally use standard gain horn antennas for many practical reasons like needing 8 standard antennas to test a wide range of frequencies (e.g., 0.75-18 GHz). This results in space efficiency reductions (e.g., the anechoic chambers efficiency is reduced). To solve this problem, an ultra-wideband (UWB) double-ridged horn antenna is designed and tested in this study. The antenna exhibits improved gains, VSWRs, and radiation patterns. Radiation patterns maintain a single main lobe across the full band. This signifies that the designed antenna can fulfill the desired higher demands. We have fabricated the antenna and it has been applied to many related fields.

Index Terms ─ EMC, radiation patterns, ultra-wideband antenna, VSWR.

I. INTRODUCTION

Because of its simple structure, good directionality, and stable phase center, broadband horn antennas are widely used in communications, radar, electromagnetic compatibility, and electronic countermeasure applications. EMC measurements usually use standard gain horn antennas. Their use is more for practical reasons but has many problems. For example, an EMC applications require 8 standard antennas to test the frequencies 0.75-18 GHz. This reduces the space efficiency of microwave frequency anechoic chambers. To mitigate this problem, an ultra-wideband (0.7-18 GHz) double-ridged horn antenna needs to be designed. In the past, simulations of ridge horn antennas could not handle a broad operational frequency range and did not include coaxial feeds [1-3]. With the development of new and innovative antenna technology, horn antennas can achieve operational bandwidths of more than twenty times its standard bandwidth [4]. Generally, ridges are utilized to extend the single-mode operational bandwidth before the higher order modes occur [1, 2]. In the field of UWB horn antennas, most designs can obtain a frequency range from 1 to 18 GHz [5-8]. But patterns produced by this kind of antenna will begin to deteriorate above 12 GHz and the main beam splits into four large side lobes [9]. Additionally, getting a high gain, low VSWR, and small mechanical size when the operating frequency is less than 1 GHz.

To solve these problems, we designed a wideband (0.7-18 GHz) double-ridged horn antenna with metallic grid sidewalls to improve the performance at higher frequencies. The coaxial feed is utilized to make the excitation point in the center of the ridged waveguide. Test results show that the VSWR is 1.5 Typ. and 2.5 Max., the gain is 12 dBi Typ. and the radiation patterns maintain a single main lobe in the full band. The gains, VSWRs, and radiation patterns of the design ridge horn antenna were measured and we analyzed the data provided. The design was mass produced and its application was verified, with relatively ideal consistency and reliability. This demonstrates that the designed antenna can fulfill higher demands. The antenna has been fabricated and applied to many related fields.

II. DESIGN OF HIGH PERFORMANCE UWB ANTENNA

As shown in Fig. 1, a broadband dual-ridge horn antenna has been developed and manufactured. Generally horn antennas consist of three parts: coaxial dual-ridged waveguide conversion, horn section and double ridges. Table 1 shows the dimensions of the design.

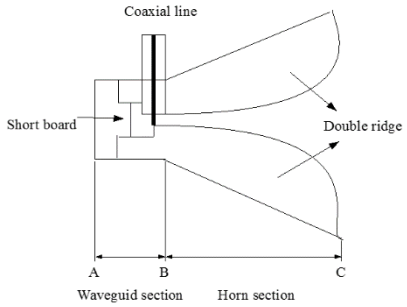

Fig. 1. Diagram of the dual-ridge horn antenna.

Submitted On: September 29, 2018
Accepted On: March 21, 2019

Table 1: New 0.7-18 GHz dual-ridge horn antenna dimensions

Figure 1 Reference	Description	Dimension
AB	Waveguide length	43 mm
BC	Horn length	230 mm
	Weight	1.5 kg

The length of the horn should be greater than half the maximum operating wavelength to ensure that high order modes are not introduced during the impedance conversion. To ensure the impedance of the coaxial feed point 50 Ω smoothly transitions to the impedance of free space, 377 Ω, the impedance of the horn section is as follows:

$$z_0 = z_{0\infty} e^{kx}, 0 \le x \le {}^{l}/_{2}, \quad (1)$$

$$z_0 = 377 + z_{0\infty}\left(1 - e^{k(1-x)}\right), {}^{l}/_{2} \le x \le l, \quad (2)$$

where l is the length of the horn segment and k is a constant. Therefore, curved shaped of the double ridge structure (of the horn section) is also generally an exponential form. The addition of a linear term in the formula for a curve can be expressed as:

$$\mathrm{y} = \mathrm{A}e^{kx} + Cx. \quad (3)$$

By letting y represent the antenna's double ridged structure, we can analyze the effect that broadening the low-frequency bandwidth and shortening the axial length of the horn section can produce. Meanwhile, the coaxial connector in coaxial double-ridged waveguide transition is generally a 50 Ω impedance connector, such as SMA or N type connector. We require that the center conductor in the coaxial line should be long enough to pass through the near ridge. The calculation formula for the coaxial cutoff frequency is as follow:

$$f_{\infty} = \frac{190.8}{\sqrt{\varepsilon_r}(D+d)}. \quad (4)$$

We can calculate the radius of the outer conductor of the coaxial conductor according to (5) [10],

$$z_0 = \frac{138}{\sqrt{\varepsilon_r}} \lg\left(\frac{b}{a}\right). \quad (5)$$

Then, we insert the center conductor into the lower ridge to ensure the electrical contact is a short circuit that achieves good impedance matching. In the straight waveguide part of the transition, a straight waveguide is added to the back end of the ridge waveguide (the length is less than half the wavelength of the maximum frequency) to reduce the frequency of the main mode transmission.

Figure 2 shows the cross-section of the straight waveguide after ridged. The design is based on conventional ridge waveguide theory [11].

Equation 6 is the cut-off frequency expression of double ridge:

$$f_c = \frac{1}{\pi\sqrt{\mu\varepsilon}\sqrt{\left(\frac{a_1}{b_1} + \frac{2C_f}{\varepsilon}\right)(a-a_1)b}}. \quad (6)$$

Equation 7 is the cut-off wavelength expression of double ridge:

$$\lambda_c = \pi\sqrt{\left(\frac{a_1}{b_1} + \frac{2C_f}{\varepsilon}\right)(a-a_1)b}. \quad (7)$$

The characteristic impedance expression of a double ridge waveguide is as follow:

$$z_0 = \frac{z_{c0}}{\sqrt{1-\left(\frac{\lambda}{\lambda_c}\right)^2}}. \quad (8)$$

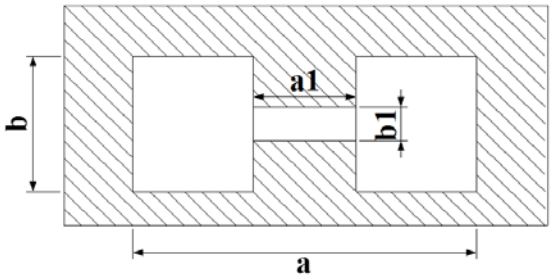

Fig. 2. Cross section of double-ridged waveguide.

First, we determine the values of the sides a/b, interval b1 and ridge width a1 in the figure. According to the curve in reference [12], the following values can be obtained from the curve: cutoff wavelength λ_{CE10} of the mode TE10, cutoff wavelength λ_{CE30} of the mode TE30 and characteristic impedance $Z_{0\infty}$ of the mode. TE10 is used when the frequency is infinitely large. Using the coaxial feed, the excitation point is located at the center of the ridge waveguide, which restrains the TE20 mode and does not excite it. Hence the available bandwidth of a double-ridged waveguide is $\lambda_{CE10}/\lambda_{CE30}$. This may be the reason why the bandwidth of the horn antenna can reach more than 25.7 octaves.

Moreover, the design of the rear cavity plays an important role in the impedance matching step of the horn's input port [13]. As shown in Fig. 3, a cross-convex block is added to the short-circuit board and embedded in the rear cavity after the mode transition step. The back end of the straight waveguide is added with a short circuit plate to form a rear cavity to reduce the effect of the reflected radiation on backward or forward radiation. Additionally, the width of the broadening transformation can be modified by adjusting the distance between the coaxial excitation, the short circuit plate and the ridge height of the short circuit section.

The existence of the inclined form forces the narrow side of the cavity to gradually expand after the mode transformation; this transition can improve the standing wave coefficient of the antenna. The presence of a wedge can effectively improve the standing wave and the high-frequency radiation patterns of the antenna. The simulated wedge and structural size of the cross-convex block can achieve ideal high frequency radiation patterns via optimization.

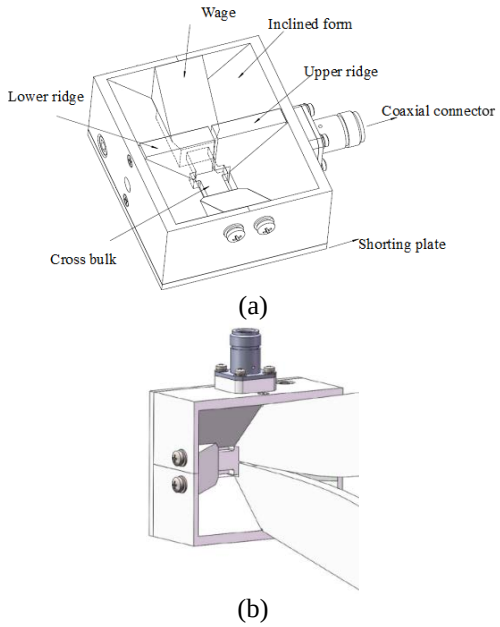

Fig. 3. Structure of rear cavity.

Figure 4 shows the actual simulation model and related parameters marked in the figure.

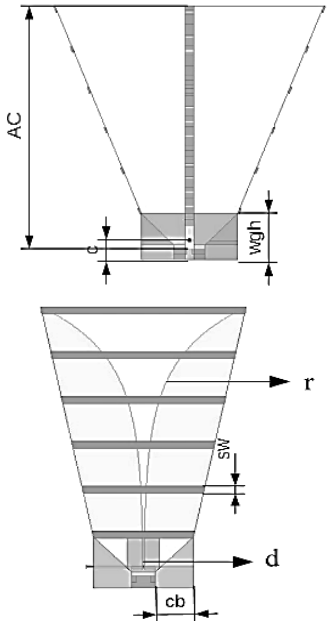

Fig. 4. Simulation model.

In Fig. 4, 'AC' is the length of ridge, c is the distance from the probe to the short board, 'wgh' is the height of the rear cavity, 'cb' is the width of the wage, 'sw' is the width of the metallic grid, 'd' is the distance between the ridges and 'r' is a parameter that influences the ridge curve.

We choose several main parameters and provide the resulting curves in Fig. 5. When the parameters take on different values from various curves, we can see the relationship between the parameters and the performance of a ridge horn antenna.

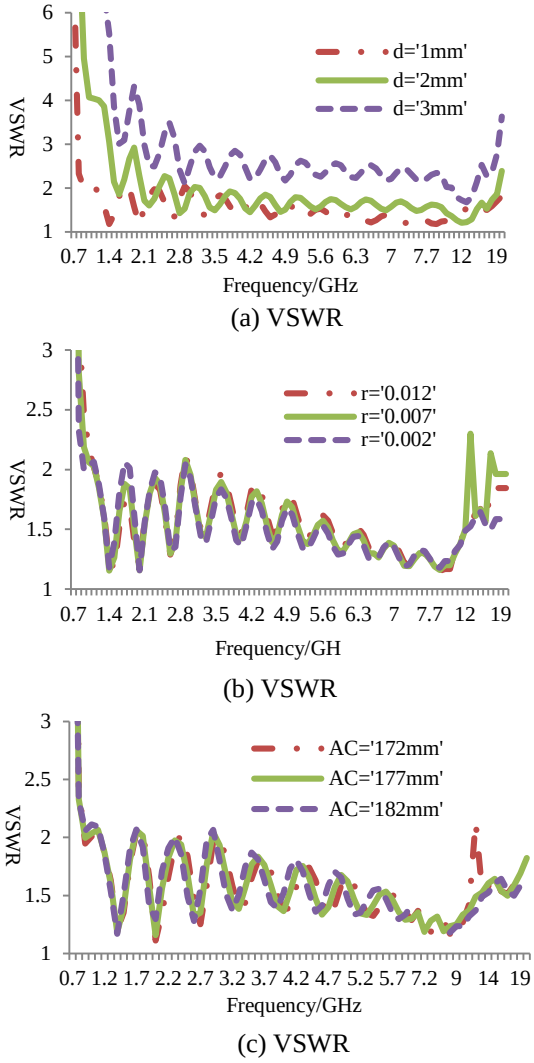

Fig. 5. Simulated VSWR of ridge horn antenna with: (a) d, (b) r, and (c) AC.

Figure 5 shows the simulation results using the main parameters, which are related to the size of the ridge. We notice that parameter d (the distance between the ridges) has the greatest influence on the performance of the horn antenna. Parameter r (the ridge curve becomes steeper as parameter r increases) and parameter AC (the length of the ridge) mainly affects the performance of the higher frequency range. We can determine the optimal size of the antenna while performing the simulation. The test results of our most current ridge horn antenna design are discussed in the next section.

III. ANTENNA SIMULATION AND TEST RESULTS

We designed a ridge horn antenna with a 0.7-18 GHz operational frequency band and manufactured it as shown in Fig. 10 [13]. Double ridged horn antennas are highly sensitive to the tolerances during the machining and assembly stages. Different gaps implemented in the flared waveguide section will affect antenna performance [14]. Thus, great care is required when assembling the antenna components. We found via simulation that removing the narrow side wall of the traditional horn antenna can not only reduce weight, but also improves the gain and high-frequency directional pattern. After optimizing the design, the narrow sidewall is replaced by five evenly distributed narrow metal pieces. The final simulation and the measurement results validate the design goals.

The VSWR curves and the gain of the antenna, both simulated and measured, are shown in Fig. 6 and Fig. 7. The results show that the VSWR of the antenna is under 2.1:1 over the 0.75-18 GHz frequency range and the maximum value is 6.6 at 700 MHz. The gain is between 3.1 and 15.35 dBi for the entire design frequency band. The gain curve is flat and there are no large fluctuations.

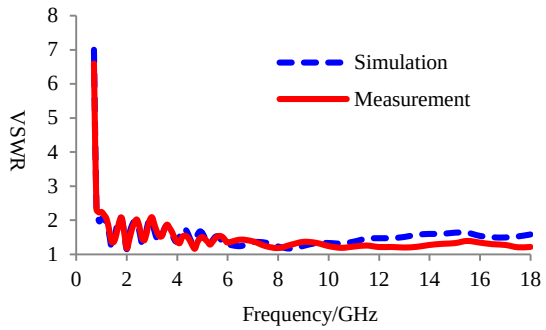

Fig. 6. VSWR.

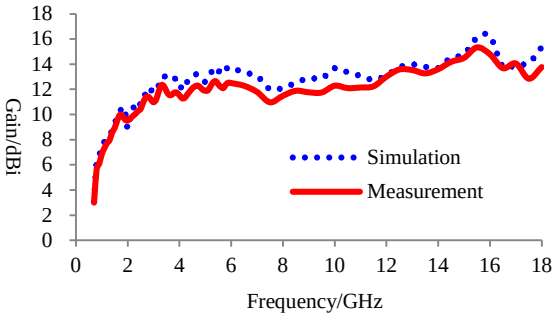

Fig. 7. Gain.

Figure 8 shows the E field of designed broadband horn antenna at 0.7 GHz and 18 GHz.

Figure 9 shows the simulation and measured patterns of the newly designed double-ridge horn antenna at 0.7 GHz, 10 GHz, and 18 GHz.

From Fig. 8 and Fig. 9, the measured results agree with the simulation results. The main lobe on the H-plane and E-plane pattern does not break apart (split) in the full frequency band.

Figure 10 shows the antenna mechanical structure. The specific dimensions of the antenna are: an 244 × 160 mm area of the flared surface, a 92 × 77 mm area for the bottom of the waveguide section, a 43 mm long waveguide section, a 230 mm axial length of the horn, and a weight of approximately 1.5 kg. The antenna can use SMA female or N type female coaxial connectors, which can withstand an average power of 50 W and 300 W, respectively.

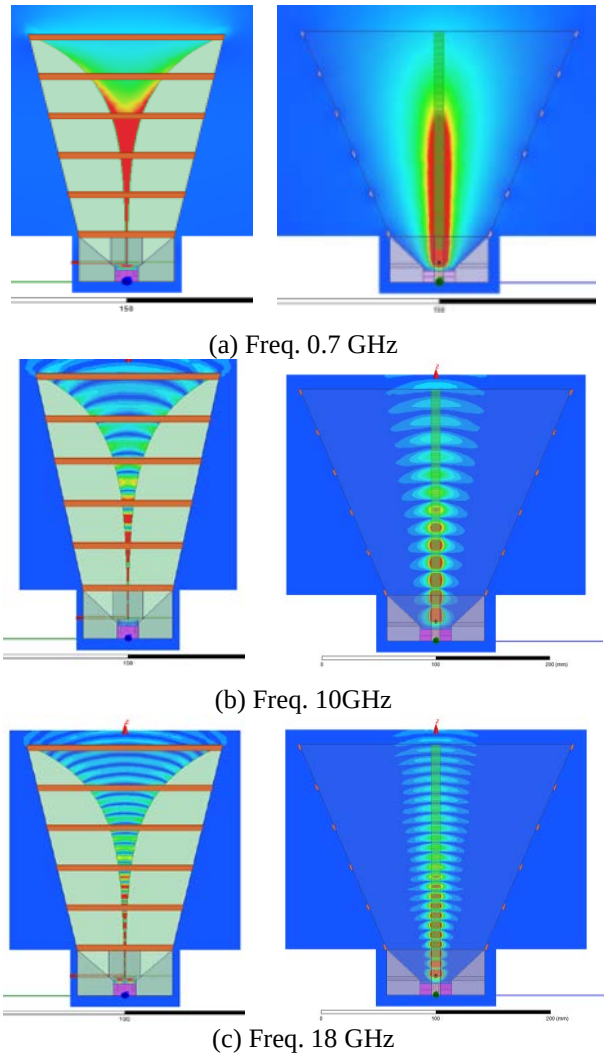

(a) Freq. 0.7 GHz

(b) Freq. 10GHz

(c) Freq. 18 GHz

Fig. 8. E Field of designed broadband horn antenna.

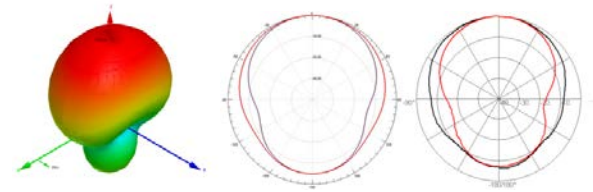

(a) Freq. 0.7 GHz

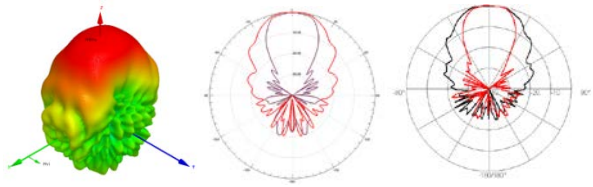

(b) Freq.10 GHz

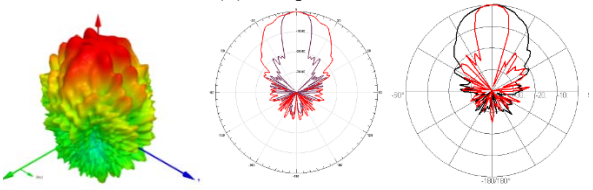

(c) Freq. 18 GHz

Fig. 9. Patterns: simulation (left) and measured (right).

Fig. 10. Photographs of fabricated horn antenna.

IV. CONCLUSION

To provide high UWB performance, an ultra-wideband horn antennas, typically used to measure electromagnetic compatibility in laboratory environments, are designed, tested and analyzed via a variety of methods. An example of a UWB double ridge horn antenna prototype is developed and tested. Both the simulation and test results are satisfactory. The VSWR of the antenna is under 2.1:1 over the frequency range of 0.75-18 GHz and the maximum value is 6.6 at 700 MHz. The gain varies between 3.1 and 15.35 dBi in the entire designed frequency band. The patterns don't split in full operational frequency range. The antenna is under mass production and widely used in microwave anechoic chambers, EMC testing environments, electronic counter measurement environments, and materials testing laboratories.

REFERENCES

[1] S. B. Cohn, et al., "Properties of ridged wave guide," *Proc. IRE.*, vol. 35, no. 8, pp. 783-788, Aug. 1947.

[2] K. L. Walton, et al., "Broadband ridged horn design," *Microw. J.*, pp. 96-101, 1964.

[3] A. Hizal and U. Kazak, "A broadband coaxial ridge horn antenna," in *Proc. 19th EUR. Macrowave Conf. Turnbrige Wells*, U.K., pp. 247-252,1889.

[4] C. Wang, Y. Zhang, and G. Guo, "Ridge horn antenna with adjustable metallic grid sidewalls and cross-shaped back cavity," *IEEE Antenna and Wireless Propagation Letters*, pp. 1221-1225, Nov. 2015. DOI 10.1109/LAWP.2015.2502578.

[5] C. Bruns, et al., "Analysis and simulation of a 1-18 GHz broadband double-ridged horn antenna," *IEEE Trans. Electromagn. Compat.*, vol. 45, no. 1, pp. 55-60, Feb. 2003.

[6] C. Bruns, et al., "Full wave analysis and experimental verification of a broad band ridged horn antenna system with parabolic reflector," in *IEEE Antennas and Propagation Soc. Int. Symp.*, vol. 4, pp. 230-233, 2001.

[7] B. Jacobs, J. W. Odendaal, and J. Joubert, "An improved design for a 1-18GHz double-ridged waveguide horn antenna," *IEEE Trans. Antennas Propagat.*, 2012.

[8] J. Huang, "The design and realization of wide band double-ridged horn antenna," *University of Chinese Academy of Sciences*, 2014.

[9] C. Bruns, P. Leuchtmann, and R. Vahldieck, "Comprehensive analysis and simulation of a 1-18 GHz broadband parabolic reflector horn antenna system," *IEEE Trans. Antennas Propagat.*, vol. 51, no. 6, pp. 1418-1422, June 2003.

[10] L. Liu, Y. Li, and S. Zhang, "Design of a wide-band double-ridged standard horn antenna," *Trans. Tech. Publications*, vol. 687-691, pp. 4019-4023, 2014.

[11] T.-S. Chen, "Calculation of the parameters of ridge waveguides," *IRE Trans. Microwave Theory Tech.*, pp. 953-959, 1957.

[12] C. Bruns, P. Leuchtmann, and R. Vahldieck, "Analysis and simulation of a 1-18GHz broadband double-ridged horn antenna," *IEEE Trans. Electro-magn. Compat.*, pp. 45:55-60, 2003.

[13] H. Nan, "Ultra-wideband horn antenna," China, H01Q13/02, Patent No: CN201621014310.X, 2017.

[14] B. Jacobs, J. W. Odendaal, and J. Joubert, "The effect of manufacturing and assembling tolerances on the performance of double-ridged horn antennas," *Centre for Electromagnetism University of Pretoria*, South Africa, July 2010.

Nan Hu (M'17-SM'18) received the B.E. degree in Electronic Engineering from Chengdu University of Information Technology, Chengdu, China, in 2001. Since 2001, he has been the CTO of A-INFO Inc. (www.ainfoinc.com). Hu is a Senior Member of IEEE and Chinese Institute of Electronics (CIE) and a Member of ACES. He has served as a Member of Technical Committee on Antenna Measurements of IEEE AP-S and a Committee Member of Antenna Branch of CIE (CIE-ANT). Since 2014, he has served as a Reviewer for some journals including the IEEE T-AP, ACES Journal & Conference, Journal of Electromagnetic Waves and Applications, IET Microwaves, Antennas & Propagation, and IET Electronics Letters. He has served as a Session Chair of ACES-china 2018. He has served on editorial/review boards of several journals and conferences.

His research interests include Ultra wideband antennas, Antenna Array, Transmit array, Reflectarray, Metasurface, Metamaterial, EBG Structures, RF/Microwave and mm-wave components, and waveguide components.

Wenqing Xie received the B.S. degree from Beijing Normal University, in 2002, and the M.S. degree from the Chinese Academy of Sciences, in 2005. Since 2016, he has been the Marketing Manager of A-INFO Inc. (www.ainfoinc.com).

His research interests include ultra wideband antennas, design and application of microwave, millimeter-wave, and terahertz-wave antennas, 5G antennas and RF technology, 5G communication antenna and measurement, and material testing. He is a Senior Member of the Chinese Institute of Electronics and a member of IEEE.

Investigation of the RCS for Finite Bandpass Frequency Selective Surface

Chengran Fang [2], Xiuzhu Ye [1], Yan Zhang [4], Qian Wang [3], Jingcheng Zhao [4], Naixin Zhang [4], Hao Jiang [4], Cheng Jin [1], and Ming Bai [4]

[1] Department of Electronics and Information Engineering
Beijing Institute of Technology, Beijing, 100081, China
xiuzhuye@outlook.com

[2] Sino-French Engineer School
Beihang University, Beijing, 100191, China

[3] The Aeronautical Science Key Lab of High-Performance Electromagnetic Windows
The Research Institute for Special Structures of Aeronautical Composite AVIC, Jinan, 250023, China

[4] Department of Electronics and Information Engineering
Beihang University, Beijing, 100191, China

Abstract ─ Frequency selective surface (FSS) with finite size behaves differently compared to an ideal infinite one, due to the influence of fringe effect, while there exist little study concerning this subject. RCS radiation can serve as a critical indicator of the FSS performance which can quantitatively reveal the mechanism of the fringe effect. This paper presents the study of RCS for FSS with finite structures. RCS for different sized FSS with different configurations under plane wave illumination are studied qualitatively. The result reveals the frequency selectivity and fringe effect of finite FSS. Quantitative functional relations between fringe effect and dimension of FSS are first summarized for monolayer FSS. A new case is then picked and tested to verify the validity of the functional relations. The relations are also extended to multilayer FSS. It turns out that the relations are general properties of finite FSS excited by plane waves.

Index Terms ─ Finite FSS, fringe effect, multilayer FSS, RCS.

I. INTRODUCTION

Frequency selective surface (FSS) is a kind of spatial filtering structure, through which the electromagnetic wave of a specific frequency range can pass, while the others are reflected. Basically, an ideal frequency selective surface is composed of identical patches or unit elements periodically arranged in a two-dimensional infinite array. The special electromagnetic properties possessed by FSS is unique in the electromagnetic domain. FSSs are able to react differently to electromagnetic waves according to frequency, angle of incidence and polarization. Therefore, FSS can behave as "spatial" filters. By well designing the structure of FSS, we can adjust their behaviors in order to satisfy some engineering requirements.

A large variety of FSS is used in parabolic antennas, radomes, THz technologies, etc. In general, there are two main usages of FSS, one of them is to realize the frequency multiplexing, the other is to reduce the RCS of a structure, or stealth technology [1,2]. According to the number of layers, FSS can be divided into monolayer FSS and multilayer FSS. Monolayer FSS contains only one layer of the periodic structure and is easy to be machined. Therefore, it is well developed and widely used. Figure 1 presents some examples of different types of unit elements [1]. It should be noticed that the complementary of these elements are also eligible FSS units due to Babinet's principle.

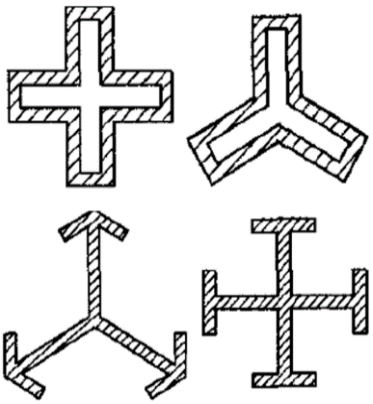

Fig. 1. Four examples of FSS unit elements.

Submitted On: October 14, 2018
Accepted On: April 1, 2019

However, monolayer FSS is hard to achieve large constant bandwidth, flat top and fast roll-off. A multilayer FSS is the combination of a series of well-designed monolayer FSS. One of the motivations for multilayer FSS is to incorporate different properties of each FSS layers. Thus, multilayer FSS can achieve large bandwidth and fast roll-off more easily than a single monolayer FSS [3]. The design and performance analysis of multilayer FSS become the main trend of contemporary research [4]. Therefore, to evaluate the fringe effect for both types of FSSs, in this paper, we have chosen a bandpass FSS with cross aperture units for monolayer FSS, and a broad bandwidth bandpass filter designed in [5] for multilayer FSS. The dimension and configuration of these FSS are presented in Section II.

Traditional research methods usually assume that the FSS is an infinite array. Because of fringe effect, the actual electrical performance of the finite FSS differ from theoretical predictions, and one cannot take full advantage of FSS peculiarities. In order to manipulate the finite FSS, additional attention should be paid to the perturbation caused by the fringe effect. Radar cross-section (RCS) is a measure of detectability of an object [6,7]. Since FSS is an important component of stealth technology, bi-static RCS is chosen as a key indicator of eligibility of FSS [8] to reveal the scattering mechanism of the fringes quantitatively. Hence, a profound comprehension of the bi-static RCS formed by excited FSS is necessary, and we will concentrate on the RCS deform caused by the fringe effect.

In this paper, we study the RCS of finite FSS by simulating a series of finite FSS in commercial software CST. Qualitative analyses about the propagation of E field and bi-static RCS are first conducted to show the fringe effect of finite FSS. The main lobe magnitude and angular width of RCS are then analyzed quantitatively. The main contribution of this paper is that the relations between the dimension of FSS and the fringe effect is summarized and validated. This work can serve as theoretical guidance to the designing and machining of FSS which is finite in size practically.

II. FSS CONFIGURATION

In this study, a unit element with cross aperture is chosen for monolayer FSS. Figure 2 illustrates the dimensions of one unit. We first investigate the frequency selectivity of this unit element. Regarding S-parameters of infinite FSS composed of this unit, the periodic boundary condition is applied to the unit in the simulation. As shown in Fig. 4, the unit element forms into a monolayer FSS with passband 8-12 GHz.

For multilayer FSS, we have chosen an FSS unit composed of 5 layer patches and two types of dielectric mediums as illustrated in Fig. 3. The round or hollow patches are 5 FSS units, and the red and blue materials are dielectric mediums (Some parts of the multilayer FSS are set to be solid red in Fig. 3 to emphasize the 3D structure of FSS). The geometric parameters of the multilayer FSS are as listed in Table 1.

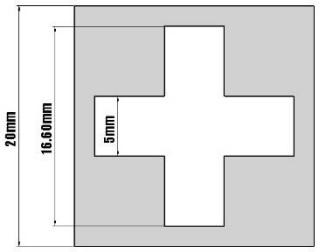

Fig. 2. The dimension of square FSS with cross aperture.

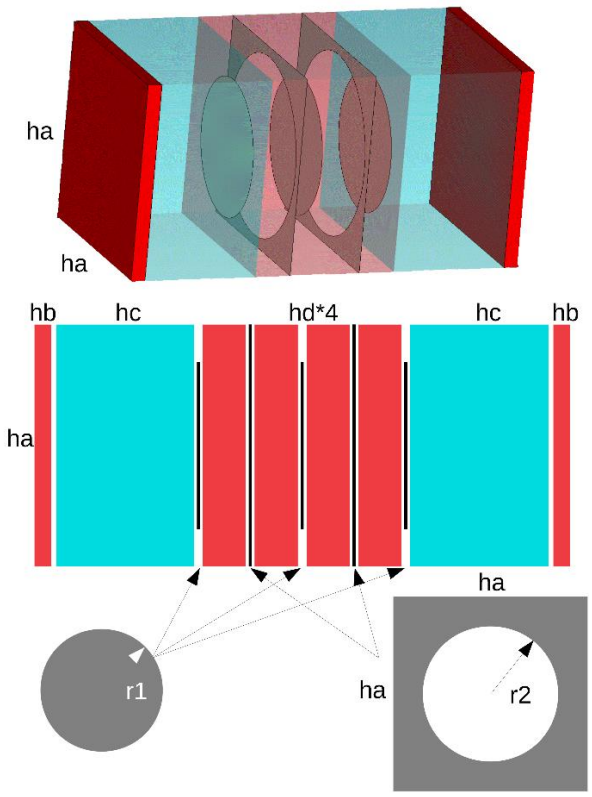

Fig. 3. The configuration of the multilayer FSS unit.

Table 1: Geometric parameters of multilayer FSS (mm)

ha	hb	hc	hd	r1	r2
8.4	0.6	4.8	1.5	2.9	3.8

Similarly, the periodic boundary condition is applied in order to obtain S-parameters of the multilayer FSS (see Fig. 4). It is evident that the bandwidth of the multilayer FSS is large and flat with passband 8-12 GHz. In this study, different sized FSS are excited by plane wave at frequency ranging from 5 GHz to 15 GHz, and three frequency points (5, 10, 15 GHz) in the passband and stopband are selected deliberately.

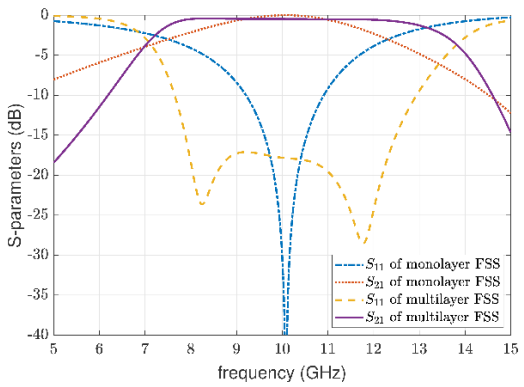

Fig. 4. S-parameters of infinite FSS.

III. QUALITATIVE ANALYSIS OF RCS

Before we conduct RCS analysis of FSS, it is helpful to verify the frequency selectivity of FSS and get the first impression of fringe effect. Two finite monolayer FSS with different number of units are excited by plane wave with frequency ranging from 5 GHz to 15 GHz. Figure 5 illustrates the propagation of E field sampling in the three frequency points (5, 10, 15 GHz). Left images are results of small size (5x5 units) FSS and right images are results of large size (10x10 units) FSS.

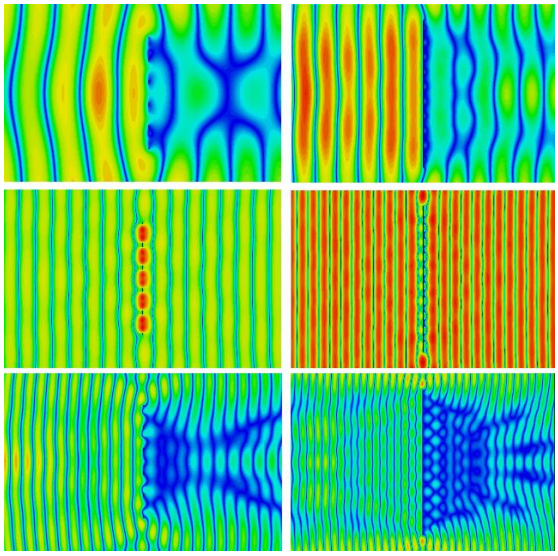

Fig. 5. E field propagation with 5x5 units FSS (left), 10x10 units FSS (right) in 5 GHz (first row), 10 GHz (second row) and 15 GHz (third row).

It is clear that all sizes of FSS present a frequency selectivity and fringe effect. In fact, the incident plane wave will be partly reflected by FSS in the backward direction and partly transmitted in the forward direction. At passband, the incident wave should pass through the FSS totally without reflection. At stopband, the incident wave should be reflected back and there should be no wave at the back of the FSS. Due to the diffraction of electromagnetic wave around finite FSS, the cancellation cannot be perfect, and the deform of plane wave can be observed in Fig. 5.

Concerning the bi-static RCS analysis, we first compare RCS simulation results of finite FSS, perfect electric conductor (PEC) slab and dielectric slab in order to analyze the transmission performance of FSS. The relative permittivity of the dielectric slab is 1.2. Moreover, the sizes of the PEC slab and dielectric slab are the same as the comparative finite FSS. Figures 6 and 7 show the bi-static RCS simulation results for 5x5 monolayer and 12x12 multilayer FSS.

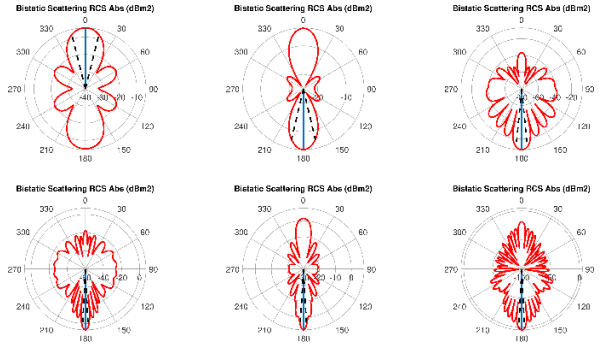

Fig. 6. Bi-static RCS of monolayer FSS (left), PEC (center) and dielectric slab (right) in 5 GHz (first row) and 10 GHz (second row).

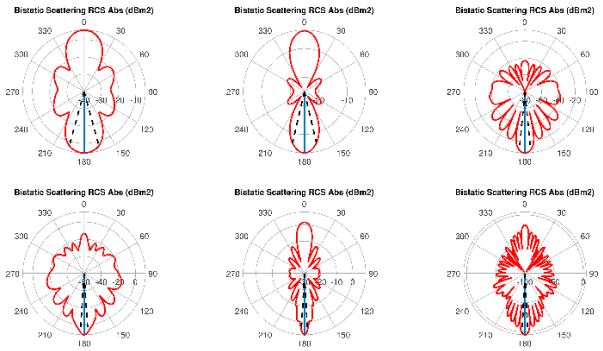

Fig. 7. Bi-static RCS of multilayer FSS (left), PEC (center) and dielectric slab (right) in 5 GHz (first row) and 10 GHz (second row).

It can be seen that the bi-static RCS of both monolayer and multilayer FSS are similar to that of PEC in the stopband and resemble that of the dielectric slab in the passband. This phenomenon can be explained by the physical bandpass property of the FSS. The differences between them mainly lie in the magnitude and the angular width of the main lobe and shape of the side lobe. A further study also shows that the bigger the size of FSS is, the smaller the differences are in both stopband and

passband. As a result, we can concentrate on the main lobe study in the quantitative analysis.

IV. QUANTITATIVE ANALYSIS OF RCS

A. Main lobe magnitude

In this section, we will study the relationship between the main lobe magnitude of RCS and the dimension of FSS. Main lobe magnitude is the maximal value in the main lobe of RCS which represents the intensity of the transmitted or reflected wave. As we found in Section III, the fringe effect will badly reduce the magnitude of main lobe in both passband and stopband. Therefore, it is worthy to find a quantitative relation of main lobe magnitude and the dimension of FSS.

In order to capture the physical and electrical size of FSS, we introduce a dimensionless quantity,

$$\alpha = \frac{FSS\ surface}{FSS\ perimeter \times wavelength}, \quad (1)$$

to quantify the FSS dimension. Within the formula, FSS surface quantifies the area of the finite FSS including areas of apertures and conductors; FSS perimeter is the whole length of the border around finite FSS. RCS of each FSS is simulated and sampled at different frequencies.

We first study the main lobe magnitude of RCS generated by a group of different sized monolayer FSS. The quantitative relations of the main lobe magnitude with respect to α are shown in Fig. 8. Three frequency points (5, 10, 15 GHz) are chosen. It can be verified that the larger α is, the larger is the magnitude of main lobe and the less is the fringe effect.

Besides, we fit the results to third degree polynomials in order to quantitatively capture the fringe effect. It turns out that the relations between α and main lobe magnitude can be properly represented by third degree polynomials since the correlation coefficients are all very close to 1. The case of 30x30 FSS, which is out of the range of the training set, is also simulated and predicted to verify the prediction performance of the curves. Table 2 shows the result. The relatively small errors present the good performance of prediction formula.

Furthermore, the third-degree polynomial relation can be extended to multilayer FSS. The RCS main lobe of different sized multilayer FSS which are excited by plane wave are simulated. The same pattern is also found in this case. Figure 9 provides the figures of RCS main lobe magnitude in relation to multilayer FSS dimension. The polynomial pattern is clear, and this fact generates the result found in monolayer FSS to multilayer FSS.

B. Angular width

In addition to the main lobe magnitude, the angular width of RCS main lobe which represents the directivity of the reflected or transmitted wave is also a key factor of FSS. The angular width is defined as the angle between the two directions where the radiation is dropped by 3 dB regarding the maximum radiation in the main lobe direction [6].

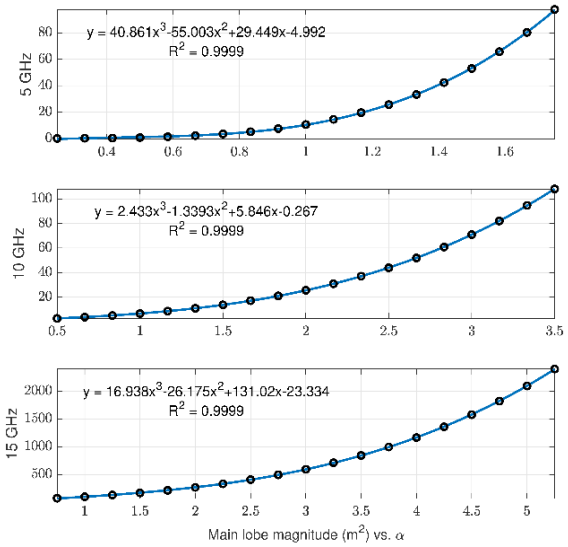

Fig. 8. The relations between the main lobe magnitude and the dimension of monolayer FSS.

Table 2: Comparison between true values of main lobe magnitude and predicted values

30x30 FSS	True Values	Predicted Values	Error
5 GHz	$395m^2$	$363.3m^2$	8.02%
10 GHz	$314m^2$	$299.6m^2$	4.58%
15 GHz	$6920m^2$	$6632.7m^2$	4.15%

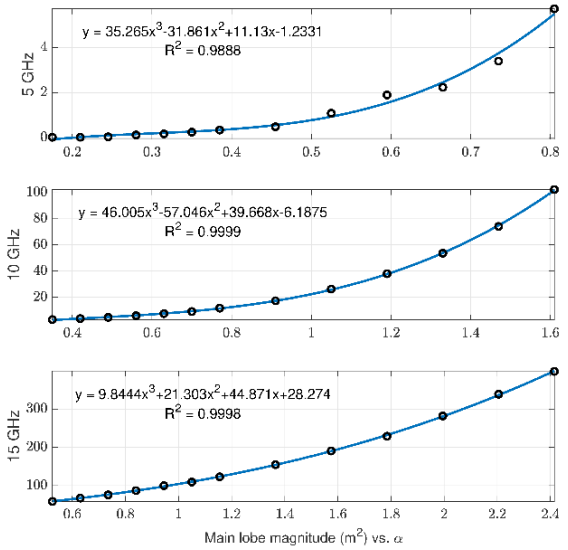

Fig. 9. The relations between the main lobe magnitude and the dimension of multilayer FSS.

Different sized monolayer FSS are excited by plane wave, and we calculate the angular width of RCS main lobe. The relations between angular width and dimension of FSS in 3 frequencies are illustrated in Fig. 10. It can be seen that the angular width shrinks with the increase of FSS dimension. This means that the directivity of transmitted wave ameliorates with the enlargement of FSS size. The fact fits our intuition since the transmitted wave is a plane wave with impulse function shaped RCS for an infinite FSS.

We also fit the results to three polynomial equations. The polynomial equations and correlation coefficients are presented in Fig. 10. We found that the angular width is inversely proportional to the dimension of monolayer FSS and the correlation coefficients are quite close to 1. In order to verify the prediction performance, we compare the true value with the predicted value in the case of 30x30 FSS in Table 3.

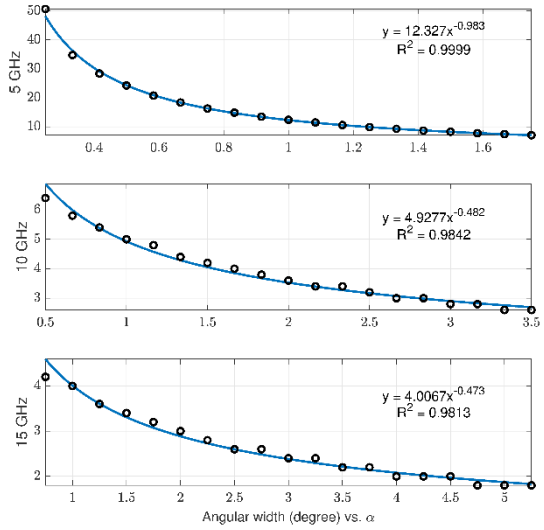

Fig. 10. The relations between the main lobe magnitude and the dimension of multilayer FSS.

Table 3: Comparison of true value of main lobe magnitude and predicted value

30x30 FSS	True Value	Predicted Value	Error
5 GHz	5	5.01	0.16%
10 GHz	2	2.27	13.4%
15 GHz	1.4	1.54	10.3%

Moreover, the inversely proportional relation can also be generated to multilayer FSS. In the case of multilayer FSS illuminated by plane wave, we plot the angular width with respect to FSS dimension (see Fig. 11). We can also find the inversely proportional relation with high correlation coefficient.

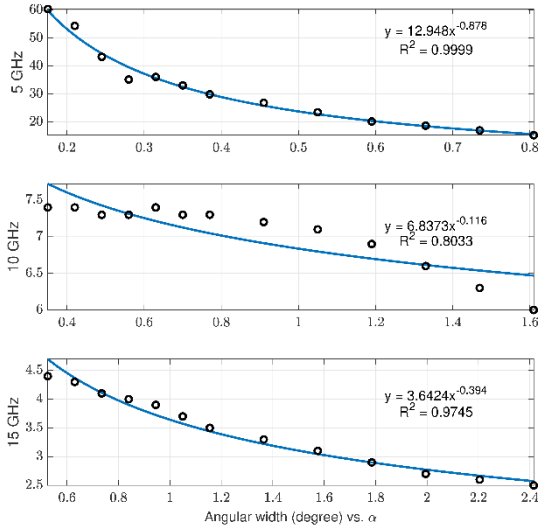

Fig. 11. The relations between the main lobe magnitude and the dimension of multilayer FSS.

V. CONCLUSION

This paper presents a study of RCS properties for finite FSS. Some main characters of RCS for frequency selective surfaces are captured in the analyses. We choose two typical bandpass FSS representing monolayer FSS and multilayer FSS respectively. A qualitative analysis is first conducted. The simulations reveal that the selectivity of FSS and fringe effect will perturb RCS radiation of finite FSS. Some quantitative relations are found afterward, and the relations are verified by concrete instances. The fitted curve found in monolayer FSS can also be extended to multilayer FSS. It means that the discovered relations are general properties of finite FSS regardless of the FSS design. The result can serve as a guideline for design and machining of practical FSS.

ACKNOWLEDGMENT

This work is supported by the National Natural Science Foundation of China under Grant No. 61401009 and Grant No. 61671032 and the Aeronautical Science Foundation of China under Grant 20161851009.

REFERENCES

[1] B. A. Munk, *Frequency Selective Surfaces: Theory and Design*. John Wiley & Sons, 2005.

[2] A. N. Silva, et al., "Simple and efficient design of reconfigurable FSS with triangular patch elements," *Applied Computational Electromagnetics Society Symposium-Italy (ACES), 2017 International, IEEE*, 2017.

[3] B. Liang and M. Bai. "Subwavelength three-dimensional frequency selective surface based on

surface wave tunneling," *Optics Express*, vol. 24, no. 13 pp. 14697-14702, 2016.

[4] M. Jin and M. Bai. "On the transmitted beam degradation through FSS in the working band by plane-wave spectrum computation and evaluation," *Applied Computational Electromagnetics Society Journal*, vol. 31, no. 9, 2016.

[5] X. Liu, et al., "On the improvement of angular stability of the 2nd-order miniaturized FSS structure," *IEEE Antennas and Wireless Propagation Letters*, vol. 15, pp. 826-829, 2016.

[6] E. F. Knott, *Radar Cross Section Measurements*. Springer Science & Business Media, 2012.

[7] J. Su, et al., "Ultra-wideband and polarization-insensitive RCS reduction of microstrip antenna using polarization conversion metasurface," *Applied Computational Electromagnetics Society Journal*, vol. 32, no. 6, 2017.

[8] R. Mittra, C. H. Chan, and T. Cwik, "Techniques for analyzing frequency selective surfaces-A review," *Proceedings of the IEEE*, vol. 76, no. 12, pp. 1593-1615, 1998.

Chengran Fang received the B.S. degree from Sino-French Engineer School, Beihang University, Beijing, China, in 2016. He is currently working towards the M.S. degree with the Department of Electronics and Information Engineering, Beihang University, Beijing.

His research interests include computational electromagnetics, inverse problem and machine learning.

Xiuzhu Ye (S'11-M'12) received the B.E. degree in Telecommunication Engineering from Harbin Institute of Technology, Harbin, China, in 2008 and the Ph.D. degree from Department of Electrical and Computer Engineering in National University of Singapore, Singapore, in 2012.

From 2012 to 2013, she worked in Department of Electrical and Computer Engineering, National University of Singapore as a Research Fellow. Since 2013, she worked as Assistant Professor in Beihang University. Since 2019, she has been an Associate Professor with School of Information and Electronics, Beijing Institute of Technology. Her research areas are electromagnetic inverse problems, microwave imaging methods, antenna designing and radar techniques.

Ye has served on review boards of various technical journals, including IEEE Transactions on Antenna and Propagation, IEEE Transactions on Microwave Theory and Techniques, Radio Science and Optics Express.

Reduction of Mutual Coupling for Broadband Vivaldi Antennas Using Characteristic Modes Analysis and Lumped Loads

Zhenpeng Ma and Qi Wu

School of Electronic and Information Engineering
Beihang University, Beijing, 100191, China
mazhp@buaa.edu.cn, qwu@buaa.edu.cn

Abstract ─ A method to reduce mutual coupling for broadband Vivaldi antennas is presented in this paper. Theory of characteristic modes is used to analyze the surface currents on the Vivaldi antennas which may contribute to mutual coupling, and inductive loads are used to suppress these modes. Mutual coupling between adjacent Vivaldi antennas is reduced by 10~20 dB on average in a wide bandwidth. Three configurations, including the classical design, design with slot, and design with inductive loads are studied. Numerical and experimental results are presented to verify the effectiveness of this method, which ensures that the method has very little influence to normal operation of Vivaldi antennas.

Index Terms ─ Characteristic modes analysis, lumped loads, mutual coupling, Vivaldi antenna.

I. INTRODUCTION

Mutual coupling between antennas has been studied extensively due to the widespread use of multi-antenna system, such as the multiple input multiple output systems, modern vehicles and antenna systems on aircraft. Strong mutual coupling may result in performance degradation of wireless systems. The method to reduce mutual coupling in these systems is limited by a number of factors. For example, for airborne antenna system, the distance between antennas is under restrictions of the space, so it is unrealistic to reduce mutual coupling by increasing the distance between antennas. Therefore, it is necessary to find a method to analyze mutual coupling and mitigate it with little influence to the normal operation of antennas.

Theory of characteristic modes was proposed in 1960s [1, 2], and this theory is found to be effective to analyze and reduce mutual coupling of antennas [3, 4]. Surface currents on the antenna can be separated into several modes, and the contributions of each mode to mutual coupling are evaluated through modal mutual admittance [3]. Lumped loads can be used to suppress specific modes which contribute to mutual coupling, so that the mutual coupling will be reduced with little influence to normal operation of antennas.

Vivaldi antenna is a kind of broadband antenna, which can be designed to cover the frequency range from 500 MHz to 7 GHz [5, 6]. Vivaldi antenna is practical because it has simple construction, wide band-width and relatively high gain [7]. It can be used in the array form for enhanced performance and functionality. Therefore, Vivaldi antenna has been widely used in radar and other wireless systems. However, in a shared aperture, the mutual coupling between antennas tends to be strong and is possible to affect the normal work of the antenna array. So it deserves consideration that how to reduce mutual coupling in wide frequency band.

Although there are a few works for the reduction of mutual coupling between antennas based on the theory of characteristic modes, they usually consider only a few frequency points, i.e., in a relatively narrow band. The method presented in this paper, on the other hand, analyzes the mode current at different frequency points, and then find the critical places where the eigencurrents have large contribution to mutual coupling. And based on this analysis, the reduction of mutual coupling for Vivaldi antennas on the broadband is realized.

The remaining parts of this paper are organized as follows. In Section II, theory of characteristic modes is introduced and modal mutual admittance for Vivaldi antennas is analyzed. In Section III, characteristic mode analysis (CMA) for Vivaldi antennas is shown, and a method is proposed to reduce mutual coupling in a wide bandwidth. Some numerical and experimental results are presented in Section IV. Short conclusions are discussed in Section V.

II. CMA OF MUTUAL COUPLING FOR VIVALDI ANTENNAS

A. The theory of characteristic modes

According to the theory of characteristic modes, surface currents on a conducting body can be decomposed into infinite number of current modes by the eigenvalue equation:

Submitted On: October 14, 2018
Accepted On: December 25, 2018

$$X[\mathbf{J}_n] = \lambda_n R[\mathbf{J}_n], \quad (1)$$

where X, R are the imaginary and real parts of operator Z respectively. The operator Z is linear and symmetric and can be obtained from the electric field integral equation (EFIE), which can be written as [8]:

$$-\mathbf{E}^i_{\tan} = (-\mathrm{j}\omega\mathbf{A} - \nabla\Phi)_{\tan}, \quad (2)$$

with the vector magnetic potential defined as:

$$\mathbf{A}(\mathbf{r}) = \frac{\mu}{4\pi}\int_S \mathbf{J}\frac{e^{-jk\mathbf{R}}}{\mathbf{R}}dS', \quad (3)$$

and the scalar electric potential as:

$$\Phi(\mathbf{r}) = \frac{1}{4\pi\varepsilon}\int_S \sigma\frac{e^{-jk\mathbf{R}}}{\mathbf{R}}dS'. \quad (4)$$

The operator Z can be written from EFIE as:

$$\mathbf{Z}(\mathbf{J}) = [\mathrm{j}\omega\mathbf{A}(\mathbf{J}) + \nabla\Phi(\mathbf{J})]_{\tan}. \quad (5)$$

Using the method of moment (MOM) and Rao-Wilton-Glisson (RWG) basis functions, eigenvalue λ_n and eigencurrent $\mathbf{J}_n$ can be solved from (1). From the theory of eigenvalue equation, it can be proved that $\mathbf{J}_n$ is orthogonal on the conducting body surface.

Surface currents on the conducting body under a specified excitation can be decomposed as:

$$\mathbf{J} = \sum_n \alpha_n \mathbf{J}_n, \quad (6)$$

where α_n is modal weighting coefficient. By substituting (6) into (1) and using the orthogonal property of $\mathbf{J}_n$, α_n can be rewritten as:

$$\alpha_n = \frac{\langle \mathbf{E}^i_{\tan}, \mathbf{J}_n \rangle}{(1+\mathrm{j}\lambda_n)}. \quad (7)$$

From (6) and (7), the surface currents on the conducting body can be represented by a linear superposition of weighted eigencurrents. Recent researches show that eigencurrents have interesting physical insights and different eigencurrents have different contributions to mutual coupling. Mutual coupling can be reduced by suppressing the eigencurrents that contribute to mutual coupling much. Hence, it deserves a consideration that how to evaluate the contribution to mutual coupling from a certain eigencurrent.

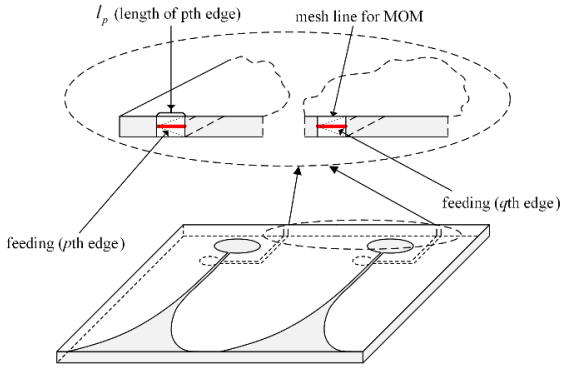

Fig. 1. Illustration of the structure of Vivaldi antennas.

B. Modal mutual admittance for Vivaldi antennas

Modal mutual admittance for general antenna pairs is discussed in [3], which represents the contribution of each mode to the mutual coupling. For Vivaldi antennas, its modal mutual admittance is computed by a similar approach.

Structure of Vivaldi antennas discussed in this paper is shown as Fig. 1. The electromagnetic wave is radiated from the slot line and the antennas are fed by a microstrip line. In order to compute the characteristic modes, the antennas are meshed into a series of triangles using RWG basis functions. Antenna 1 is fed by the port located at the pth edge with length l_p, and antenna 2 is fed by the port located at the qth edge with length l_q. The mutual admittance between antenna 1 and antenna 2 can be expressed as:

$$Y_{21} = \sum_{n=1}^{\infty}\frac{I_n(p)I_n(q)l_p l_q}{1+j\lambda_n}, \quad (8)$$

where $I_n(p)$ and $I_n(q)$ are the nth order eigencurrents at the pth and qth edge, and λ_n is the nth order of eigenvalue. From (8), the modal mutual admittance can be written as:

$$Y^n_{21} = \frac{I_n(p)I_n(q)l_p l_q}{1+j\lambda_n}. \quad (9)$$

From (9), the contribution to mutual coupling of each mode can be evaluated at separated frequency points. Taking account of wide bandwidth of Vivaldi antennas, modal mutual admittance at several frequency points need to be considered. Therefore, the eigencurrents contributed to mutual coupling much at different frequency points need to be suppressed. In order to suppressed a certain mode, lumped loads such as inductive loads usually are used [8]. The position of lumped loads can be obtained from CMA.

III. A REDUCTION OF MUTUAL COUPLING FOR VIVALDI ANTENNAS USING CMA

The size and structure of Vivaldi antennas discussed in this paper is shown as Fig. 2. The size of one Vivaldi element is 140 mm × 220 mm × 0.8 mm. Relative permittivity of the dielectric substrate is 2.65. The bandwidth of Vivaldi element is from 1 GHz to 3 GHz. The antenna is fed by microstrip line with a width of 2.2 mm, which is also the length of the pth and qth edge. Two Vivaldi elements are placed side by side and the mutual coupling between the two antennas is strong. It can be noticed from the structure that, possibly mutual coupling is mainly caused more from the ground plane, rather than from the space. Therefore, analyzing the eigencurrents on the ground plane will be efficient.

To find out the eigencurrents which contribute mainly to the mutual coupling, the modal mutual admittance at several frequent points is calculated from (9) and is

shown in Table 1. It can be noticed from Table 1 that the modal mutual admittance of different modes has similar order of magnitudes, which means that they have similar contributions to mutual coupling. Hence, it is necessary to observe several eigencurrents in order to find out how to suppress eigencurrents effectively. The eigencurrents with large modal mutual admittance at 1.12 GHz is shown in Fig. 3.

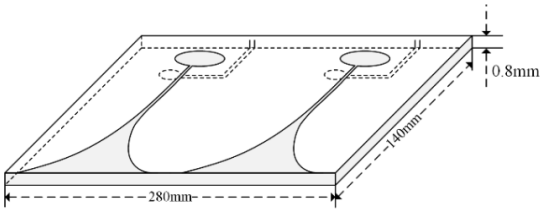

Fig. 2. Illustration of the size and structure of Vivaldi antennas.

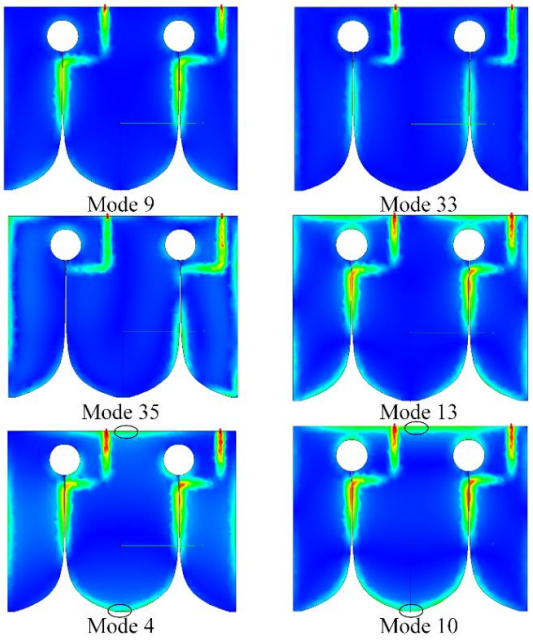

Fig. 3. Distributions of eigencurrents with relatively large modal mutual admittance.

From Fig. 3, it can be observed that these eigencurrents have similar distributions in the tapered slot area of Vivaldi antennas. Because the normal work condition of antennas needs to be guaranteed, it needs to be noticed that the current in the work area has better not been affected. From the current distributions of modes 4 and 10, the edges between the two antennas, which are shown by ellipses in Fig. 3, are likely to need attention. Although modes 4 and 10 don't have largest modal mutual admittance, they have the same order of magnitudes as the largest one. In addition, the modes which have the largest modal mutual admittance, such as modes 9 and 33 only have current distributions in the place of work area. It is difficult to deal with these modes. Therefore, it is significant to analyze these modes like modes 4 and 10. By analyzing eigencurrents at other frequency points, which is shown in Fig. 4, the place that is marked tends to be significant to mutual coupling. We can control the current on such place to suppress corresponding eigencurrent, and then, the mutual coupling will be mitigated.

From the research in [3, 4], lumped loads such as inductive loads are usually utilized to suppress eigencurrent. For Vivaldi antennas, inductive loads might be a choice. However, because the surface current tends to choose the path with lower impedance, only inductive may be not effective enough. A slot between the two antennas is necessary [3].

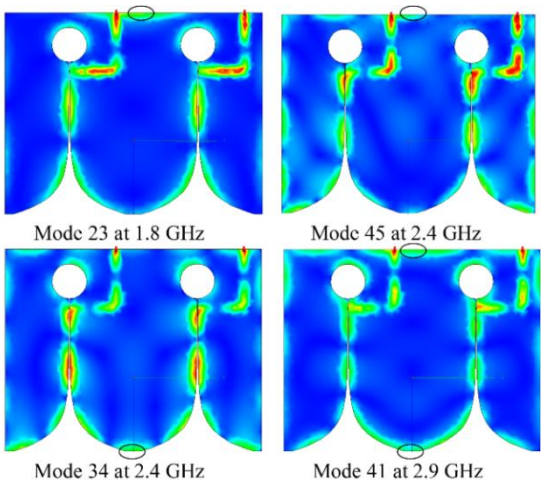

Fig. 4. Eigencurrents with similar current distributions at other frequencies considered.

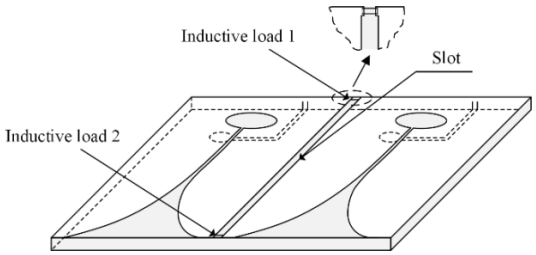

Fig. 5. Illustration of optimized antenna with slot and inductive loads.

Table 1: MMA of two Vivaldi antennas

1.12	Mode 9	Mode 33	Mode 35	Mode 13	Mode 4	Mode 10
GHz	6.87e-3	4.32e-3	3.42e-3	2.79e-3	2.58e-3	1.88e-3
1.8	Mode 41	Mode 23	Mode 29	Mode 10	Mode 36	Mode 17
GHz	4.36e-3	3.91e-3	3.39e-3	3.04e-3	2.21e-3	2.15e-3
2.4	Mode 45	Mode 28	Mode 13	Mode 19	Mode 34	Mode 32
GHz	1.95e-3	1.52e-3	1.44e-3	1.44e-3	1.28e-3	1.28e-3
2.9	Mode 50	Mode 49	Mode 36	Mode 31	Mode 24	Mode 41
GHz	3.73e-3	2.93e-3	2.26e-3	1.73e-3	7.29e-4	4.47e-4

The adopted plan is shown in Fig. 5. A slot is cut out between the two antennas. On the two edges of the slot, two inductive loads are placed respectively. In this way, the eigencurrents at different frequency points will be suppressed on these places, so that the mutual coupling should be reduced in the wide work band.

IV. NUMERICAL SIMULATION AND EXPERIMENTAL VERIFICATION

A. Numerical simulation for Vivaldi antennas

To verify the effectiveness, numerical simulation is completed by HFSS. It can be noticed that the slot between the two antennas will also contribute to the reduction of mutual coupling, hence it is necessary to compare results of antennas with only slot and antennas with slot and inductive loads. The value of the two inductive loads are confirmed as 2.3 nH for load 1 and 10.8 nH for load 2, by parametric scanning to get a relatively better performance for mutual coupling. The results of S-parameter are shown in Fig. 6, and the radiation patterns at 1.12 GHz and 2.4 GHz are shown in Fig. 7 respectively.

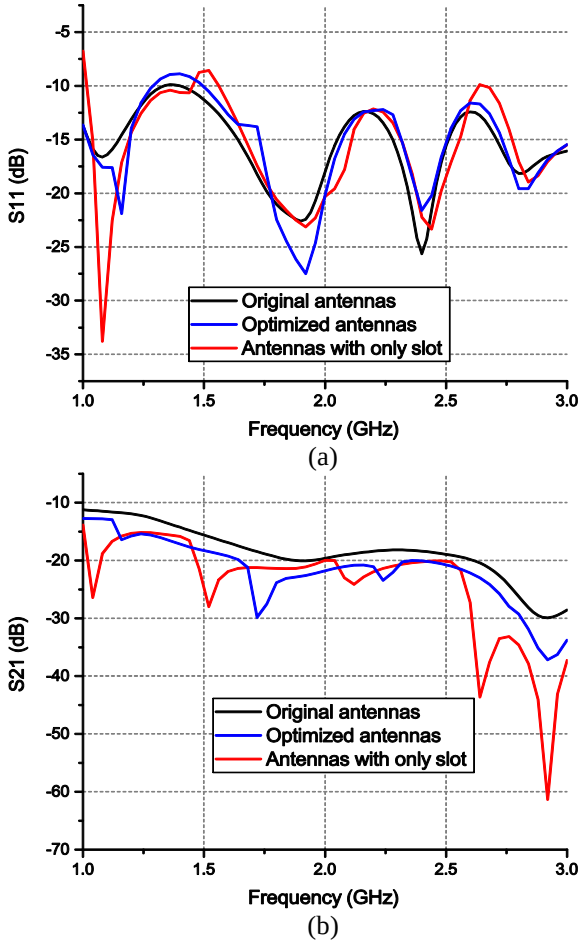

Fig. 6. S-parameters of the 3 kinds of Vivaldi antennas: (a) S11 and (b) S21.

As shown in Fig. 6 (a), for S11, there is no significant difference among the three antennas, which means that the normal work condition is not changed a lot. The S21 parameter of the optimized one with inductive loads is reduced in the whole work band of Vivaldi antennas. It can be observed that the mutual coupling at 2.7 GHz is reduced by about 30 dB. Furthermore, the mutual coupling from 1 GHz to 3 GHz is lower than -15 dB. Compared to the antennas with only slot, which is shown in blue lines in Fig. 6 (b), it can be observed that the optimized antennas with loads perform better, especially in the high frequency band.

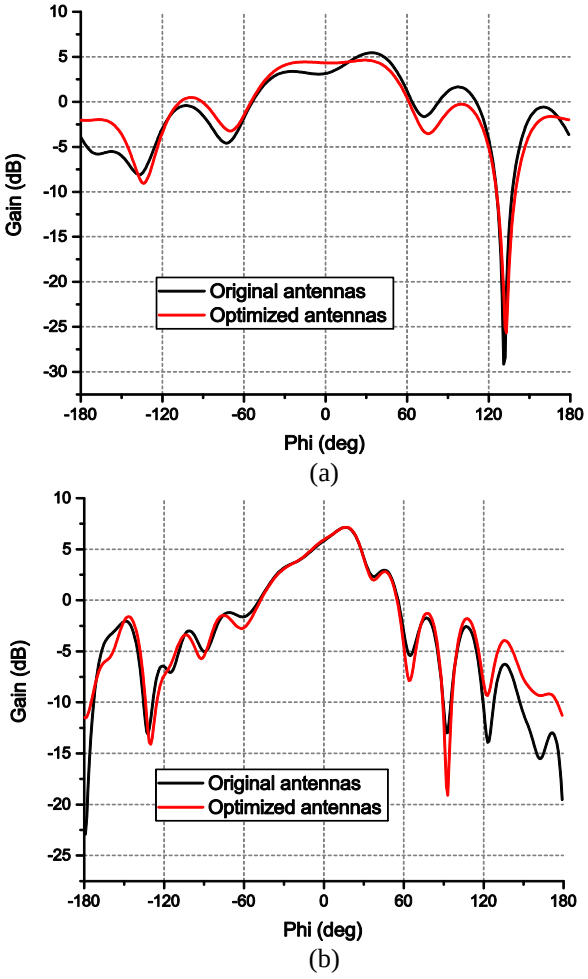

Fig. 7. Radiation pattern of Vivaldi antennas at: (a) 1.12 GHz and (b) 2.4 GHz.

This illustrates that the inductive loads indeed play a role in reducing mutual coupling.

From Fig. 7, it can be noticed that the symmetry of the radiation pattern is better after optimizing, mainly due to the reduction of the mutual coupling at 1.12 GHz. This is a good result because this means that the radiation characteristic of antennas is easier to predict and will improve the performance of the Vivaldi array. At 2.4

GHz, the mutual coupling of antennas is reduced by only 2 dB, and the radiation patterns of original and optimized antenna array are similar. This is result from the similar work mode currents, which are hardly influenced by the inductive loads.

B. Experiment verification

In order to verify the simulation, the Vivaldi antennas are fabricated and measured. The photographs of original and optimized antennas are shown in Fig. 8, and the result of experiment is shown in Fig. 9.

From Figs. 9 (a) and (b), it can be noticed that the S-parameters agree well between measured and simulated. As shown in Fig. 9 (c), the mutual coupling is reduced by 20 dB at most at about 1.6 GHz, and the mutual coupling is bellower than -15 dB almost in the whole work band.

V. CONCLUSION

In this paper, a CMA-based method for reducing mutual coupling of Vivaldi antennas in a wide band is proposed. The MMA of Vivaldi antennas is analyzed. The modes which has large modal mutual admittance at several frequency points are observed. By comparing the eigencurrents which contribute to mutual coupling much, the critical places of those modes are found. Inductive loads are used to suppress such eigencurrents so that the mutual coupling can be reduced.

(a)

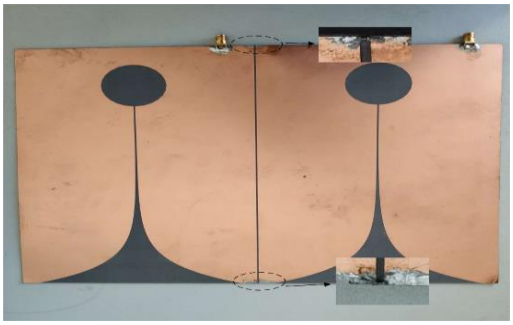

(b)

Fig. 8. Photograph of: (a) original antennas, and (b) optimized antennas with slot and inductive loads.

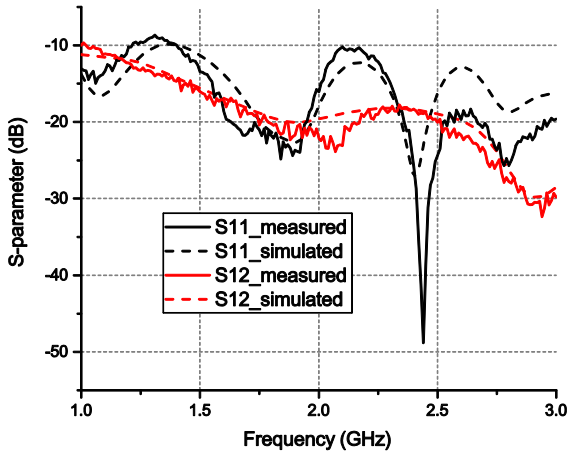

(a)

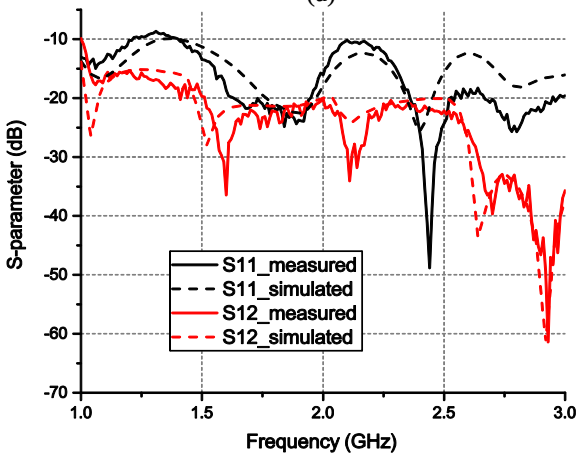

(b)

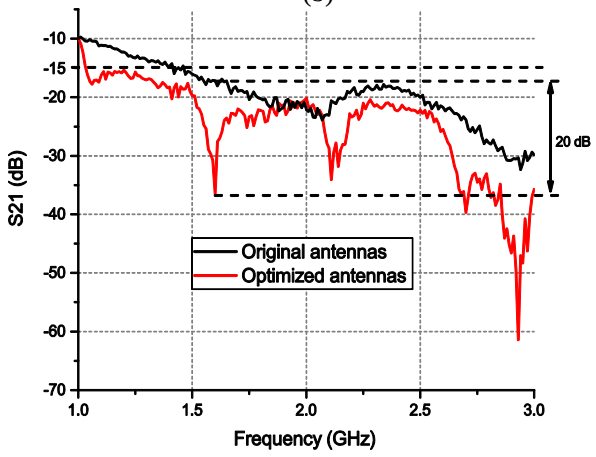

(c)

Fig. 9. The result of (a) Simulated and measured S-parameter of original antennas (b) Simulated and measured S-parameter of optimized antennas, and (c) compared for measured S21 between original antennas and optimized antennas.

Numerical and experimental results are shown to

verify this method. The mutual coupling of Vivaldi antennas is reduced effectively in the frequency range of 1 to 3 GHz. In addition, radiation pattern performs better after optimization. The results show that CMA is effective to reduce mutual coupling of broadband antennas.

ACKNOWLEDGMENT

This work was supported in part by National Key Research and Development Program of China under Grant of 2017YFF0204903.

REFERENCES

[1] R. J. Garbacz and R. H. Turpin, "A generalized expansion for radiated and scattered fields," *IEEE Transactions on Antennas Propagation*, vol. 19, no. 3, pp. 348-358, May 1971.

[2] R. Harrington and J. Mautz, "Theory of characteristic modes for conducting bodies," *IEEE Transactions on Antennas Propagation*, vol. 19, no. 5, pp. 622-628, Sep. 1971.

[3] Q. Wu, W. Su, Z. Li, and D. Su, "Reduction of out-of-band antenna coupling by characteristic mode analysis," *IEEE Transactions on Antennas Propagation*, vol. 64, no. 7, pp. 2732-2742, 2016.

[4] P. Liang and Q. Wu, "Characteristic mode analysis of antenna mutual coupling in the near-field," *IEEE Transactions on Antennas Propagation*, in Press.

[5] J. Shin and D. H. Schaubert, "A parameter study of stripline-fed Vivaldi notch-antenna arrays," *IEEE Transactions on Antennas and Propagation*, vol. 47, no. 5, pp. 879-886, May 1999.

[6] S. Kasturi and D. H. Schaubert, "Effect of dielectric permittivity on infinite arrays of single-polarized Vivaldi antennas," *IEEE Transactions on Antennas and Propagation*, vol. 45, no. 2, pp. 351-358, Feb. 2006.

[7] K. Ebnabbasi, D. Busuioc, R. Birken, and M. Wang, "Taper design of Vivaldi and co-planar tapered slot antenna (TSA) by Chebyshev transformer," *IEEE Transactions on Antennas and Propagation*, vol. 60, no. 5, pp. 2252-2259, May 2012.

[8] S. M. Rao, D. R. Wilton, and A. W. Glisson, "Electromagnetic scattering by surfaces of arbitrary shape," *IEEE Transactions on Antennas and Propagation*, vol. AP-30, no. 3, May 1982.

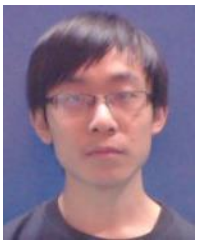

Zhenpeng Ma received the B.S. degree from Beihang University (BUAA), Beijing, China in 2017. He is currently pursuing master's degree in Beihang University. His current research interests include characteristic mode analysis and antenna mutual coupling. He was a volunteer in ACES China, 2018.

Qi Wu received the B.S. degree from East China Normal University, and Ph.D. degree from Shanghai Jiao Tong University in 2004 and 2009, respectively. He joined the faculty of Beihang University, in 2009, now he is an Associate Professor. During 2014 and 2016, he was an Alexander von Humboldt Fellow at Technical University of Hamburg, Germany.

Wu has authored over 40 journal papers, one book in Chinese and holds 10 Chinese patents. His research interests include broadband antennas, computational electromagnetics, and related EMC topics.

Wu received several awards including the Young Scientist Award from the International Union of Radio Science (URSI) in 2011, the Nominee Award for Excellent Doctoral Dissertation from the National Minister of Education in 2012. Wu was the TPC Co-chair of ACES China 2018.

Development of Microstrip Structure and Microstrip Sensor for Measurement of Transient Electromagnetic Pulse

Jinhong Wei, Shoulong Zhang, Zhen Liu, Youjie Yan, Tingyong Jiang, and Fanghong Huang

Northwest Institute of Nuclear Technology
Xi'an 710049, China
17600809313@163.com

Abstract ─ In this paper, a type of microstrip structure and sensor based on the microstrip structure are designed, fabricated and tested for the measurement of transient electromagnetic pulse. The voltage on the terminal load of microstrip line illuminated by a plane wave is analyzed, and a method of recovering the incident electric field is presented to recover the transient electromagnetic pulse by numerical processing. The proposed microstrip structures are set on the shielding boxes. The start of microstrip structure 1 without substrate is short circuited, and the start of microstrip structure 2 with substrate is matched. The induced voltage is acquired from the ends of microstrip structures. The simulated results and the measured results verify that the microstrip structures can be used to measure the transient electromagnetic pulse with rise time of $\geq$ 1 ns. The simulated results show that the microstrip structures have wide bandwidths of 1.5 GHz and 2.5 GHz, respectively. In addition, the simulated effective heights show consistency with the measured effective heights. The microstrip sensors, built by adding the electro-optical conversion modules into the shielding boxes, have good fidelity and can be used to measure high-altitude electromagnetic pulse (HEMP).

Index Terms ─ Effective height, HEMP, microstrip structure, sensor, transient electromagnetic pulse.

I. INTRODUCTION

Transient electromagnetic pulse (EMP) [1] has the fast rise time and high amplitude. It is easy to be coupled into the internal electronic system, and can disrupt or damage critical electronic facilities over an very large area. HEMP and ultra-wideband short pulse (UWB-SP) are two kinds of typical transient electromagnetic pulses [2-5]. In order to reveal the characteristics of transient electromagnetic fields, clarify the effect of electromagnetic pulse on the electronic equipment, evaluate the performance of electromagnetic protection, and then seek for some important means of electromagnetic protection. The time domain measurement theory and technologies of transient electromagnetic field have become one of the focal points in the region of EMP attack and protection.

The key technology in transient electromagnetic field measurement is to transform pulse field into voltage or current signal undistorted. The capabilities of the receiving antenna directly affect the test system to measure the pulsed field. TEM horn is used as the receiving antenna for UWB-SP recommended by NIST (National Institute of Standards and Technology) [6]. Within the time window of TEM horn, its output voltage waveform is identical to the incident electric field. The effective height of TEM horn is incalculable analytically and has to be calibrated by standard field or multi antenna method. When used in a narrow space, TEM horn may be too large to ignore the disturbance caused by the receiving antenna. The rise time of HEMP defined by IEC standard 61000-2-9 is 2.5±0.5 ns, the pulsewidth is 23±5 ns [7]. E-field sensor, D-Dot are the most commonly used electric field sensor for HEMP measurement [8-9]. Currently, the active E-field sensors based on the electrically small antenna need the matching networks of high impedances. The narrow frequency band of the networks becomes the limitation of the whole measurement systems [10]. The output of a D-dot sensor is proportional to the time rate of change of the measured field, and an integration operation has to be applied so as to restore the pulse shape of the electric field. In addition, the connection with balun, integral module, and electro-optical converting module further increases the overall size of the system.

VNIIOFI (All-Russian Research Institute for Optical and Physical Measurements) suggested using microstrip lines for measurement of EMP waveform parameters [11]. They developed the theory of microstrip transducers (IPPL-L) [12], carried out the experimental investigations and worked out the production technology [13-14]. One advantages of transducers is the flat transient response during the time window that is twice the time taken for the signal to propagate along the microstrip line. The output signals of the transducers replicate the E-field signal and any integration device is not necessary. Therefore, microstrip transducers are

Submitted On: September 23, 2018
Accepted On: January 26, 2019

optimal to record the UWB-SP. However, for the measurement of HEMP, since the duration time of the pulse waveforms are up to 100 ns or even more, the transducers lack a long enough time window to restore the incident waveform.

In this paper, two novel microstrip structures and microstrip sensors are proposed. The sensors adopt microstrip structures as the receiving antennas. The incident electric field can be recovered from the output signal recorded by the receiving antenna by the method of numerical processing. With the characteristics of wide bandwidth, good fidelity and compact sizes, they can be used to measure transient electromagnetic pulse.

II. STRUCTURE DESIGN

A. Microstrip line coupling to electromagnetic wave

Consider a microstrip line consisting of a conductor of length l and a ground plane parallel to the conductor, which are separated by a dielectric plate with the thickness h and the relative dielectric permittivity ε_r. Both of ends are loaded with impedances Z_1 and Z_2 respectively. The microstrip line is illuminated by a linearly polarized uniform plane wave as seen in Fig. 1.

Assume that $w << a$, $h << l$, and $h << a$, since the vector E of the incident field is perpendicular to the microstrip line carrier, it lies in the incidence plane, which corresponds to the case of vertical or parallel polarization. Thereby, the Poynting's P is parallel to the carrier plane. The voltage on the load Z_2 induced by the plane wave is representable in the form:

$$u(l,t)=\frac{E_0 h(1+\rho_2)}{2}\sum_{k=0}^{\infty}(\rho_1\rho_2)^k\cdot \{[\frac{(1-\frac{1}{\varepsilon_r})}{\sqrt{\varepsilon_e}-1}-\frac{1}{\varepsilon_r}]\cdot[f(t-\frac{2lk\sqrt{\varepsilon_e}+l}{c})-f(t-\frac{(2k+1)l\sqrt{\varepsilon_e}}{c})]- \rho_1[\frac{(1-\frac{1}{\varepsilon_r})}{\sqrt{\varepsilon_e}+1}+\frac{1}{\varepsilon_r}]\cdot[f(t-\frac{(2k+1)l\sqrt{\varepsilon_e}}{c})-f(t-\frac{2l(k+1)\sqrt{\varepsilon_e}+l}{c})]\} \quad ,(1)$$

where E_0 is an external field strength of the incidence wave outside the dielectric substrate, f is the function determining a pulse waveform. c denotes light speed, ε_e is the equivalent dielectric constant of microstrip line. ρ_1 and ρ_2 are the reflection coefficients at both ends of the microstrip line,

$$\rho_1=\frac{Z_1-Z_c}{Z_c+Z_1},\ \rho_2=\frac{Z_2-Z_c}{Z_c+Z_2}\ . \quad (2)$$

Ignore the transmission loss of the current signal on the microstrip line. When $Z_1=0$, $Z_2=Z_c$, thus $\rho_1=-1$, $\rho_2=0$, analyzing (1) for the case of the dielectric layer being absent, and the induced voltage on the terminal load Z_2 can be expressed as:

$$U_{without\_sub}=-\frac{E_0 h}{2}[f(t-\frac{l}{c})\ -f(t-\frac{3l}{c})]. \quad (3)$$

When $Z_1=Z_c$, $Z_2=Z_c$, thus $\rho_1=0$, $\rho_2=0$, analyzing (1) for the case of the dielectric layer being present, the induced voltage on the terminal load Z_2 can be written as:

$$U_{with\_sub}=\frac{E_0 h}{2}[\frac{1-\frac{1}{\varepsilon_r}}{\sqrt{\varepsilon_e}-1}-\frac{1}{\varepsilon_r}]\cdot[f(t-\frac{l\sqrt{\varepsilon_e}}{c})-f(t-\frac{l}{c})]. \quad (4)$$

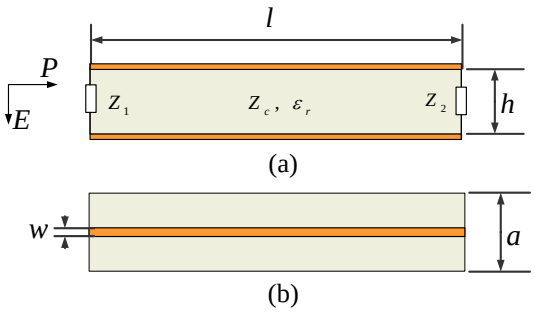

Fig. 1. Microstrip line illuminated by a plane wave: (a) side view and (b) top view.

B. The method of recovering the incident electric field

Based on (3) and (4) that the voltage signals can be expressed as the superposition of two voltage signals. If the two voltage signals are expressed as $V(t)$ and $-V(t-t_0)$ respectively, where t_0 expressed as the delay time, (3) and (4) can be representable in the form:

$$U(t)=V(t)-V(t-t_0)\ . \quad (5)$$

Further, we can get,

$$V(t)=\sum_{n=0}^{k}U(t-nt_0)+V(t-(k+1)t_0)\ . \quad (6)$$

When $(k+1)$ t_0 is longer than the duration of the voltage signal $V(t)$, $V(t-(k+1)\ t_0)$ is after $V(t)$, the $V(t)$ can be get from the equation:

$$V(t)=\sum_{n=0}^{k}U(t-nt_0)\ ,\quad t<(k+1)t_0\ . \quad (7)$$

Combining Equations (3) and (4), we can get:

$$\sum_{n=0}^{k}U_{without\_sub}(t-\frac{2nl}{c})=-\frac{h}{2}E_0 f(t-\frac{l}{c}) =-h_{eff1}E_0 f(t-\frac{l}{c}),\quad t<(k+1)\frac{2l}{c} \quad ,(8)$$

$$\sum_{n=0}^{k}U_{with\_sub}(t-n\frac{l\sqrt{\varepsilon_e}-l}{c})=\frac{h}{2}(\frac{1-\frac{1}{\varepsilon_r}}{\sqrt{\varepsilon_e}-1}-\frac{1}{\varepsilon_r})\cdot E_0 f(t-\frac{l}{c}) =h_{eff2}E_0 f(t-\frac{l}{c}),\quad t<(k+1)\frac{l\sqrt{\varepsilon_e}-l}{c} \quad ,(9)$$

$$h_{eff1}=\frac{h}{2}\ , \quad (10)$$

$$h_{eff2}=\frac{h}{2}(\frac{1-\frac{1}{\varepsilon_r}}{\sqrt{\varepsilon_e}-1}-\frac{1}{\varepsilon_r})\ . \quad (11)$$

Where h_{eff1} and h_{eff2} are the theoretical effective heights, which are mainly determined by h. From (8) and (9), the amplitude E_0 and the waveform f of the incident electric field can be calculated respectively.

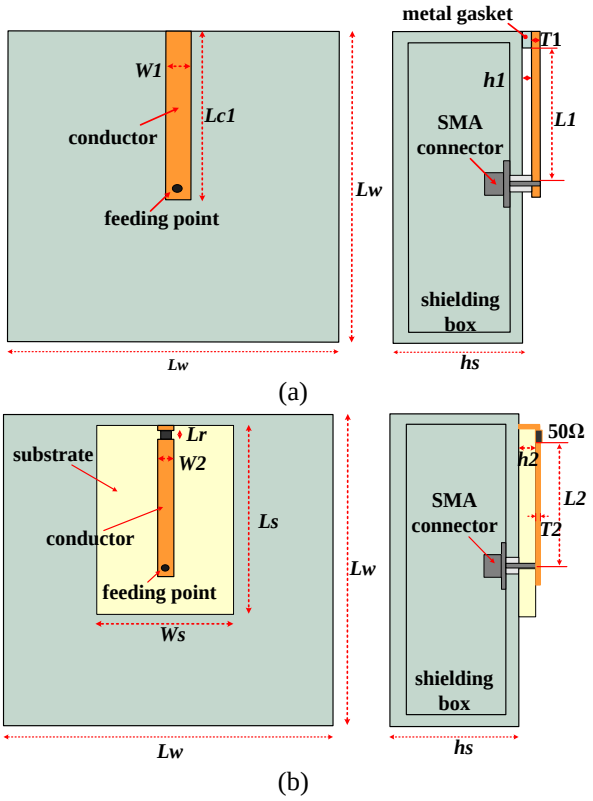

Fig. 2. Geometry of microstrip structures (the left is top view; the right is side view): (a) microstrip structure 1, and (b) microstrip structure 2.

C. The geometry of microstrip structures

The geometry of the microstrip structure without the substrate is shown as Fig. 2 (a). A shielding box occupying a size of 100×100×30 mm^3, which is equivalent to the ground plane of the microstrip line, is used to hold electro-optical conversion circuits. At the start of the microstrip structure, the conductor is connected to the top surface of the shielding box through a metal gasket with a size of 4.3 × 4 × 1 mm^3 for short circuit (Z_1=0). The end of the microstrip structure is connected to a 50 Ω SMA connector for the transmission of the induced voltage $U_{without\_sub}$. The effective length $L1$ of the conductor is 45 mm, corresponding to a delay time t_0 of 0.3 ns. The geometry of microstrip structure 2 with a substrate is shown in Fig. 2 (b). The substrate is a microwave composite substrate with relative permittivity ε_r = 9.8 and loss tangent σ < 0.001 and is equipped on the upper surface of the shielding box. A 50 Ω resistor is loaded at the start of the microstrip structure to match it with the microstrip structure. Similarly, a 50 Ω SMA connector is connected to the end of the conductor to output the induced voltage U_{with_sub}. Both of the feeding positions of microstrip structures are set on the middle point of the upper surface of the shielding boxes. The effective length $L2$ of the conductor is 43 mm, corresponding to a delay time t_0 of 0.225 ns.

The final dimensions of two microstrip structures are summarized in Table 1.

Table 1: Dimensions of microstrip structures

Parameter	Value (mm)	Parameter	Value (mm)
L1	45	*L2*	43
h1	1	*h2*	3.175
T1	1	*T2*	0.035
W1	4.2	*W2*	3
Lc1	52	*Lr*	1
hs	30	*Ls*	60
Lw	100	*Ws*	40

III. PERFORMANCE SIMULATION

A. The recovered waveforms of two microstrip structures

The performances of the microstrip structures are studied by the Microwave CST studio based on the time-domain finite integration technique [15]. To study the performance of the microstrip structures, a simulation model of mono-cone structure which can generate UWB-SP is built, as shown in Fig. 3.

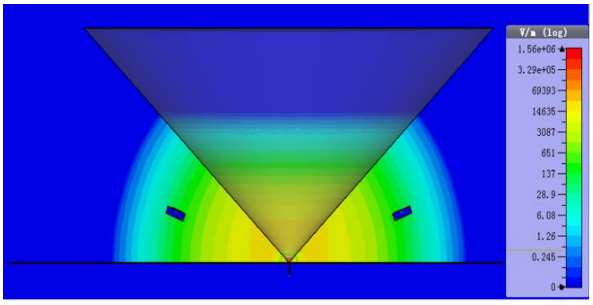

Fig. 3. Microstrip structure 1 (the right) and microstrip structure 2 (the left) activated by the electric field generated by the mono-cone structure.

The mono-cone structure is a variation of the infinite biconical transmission line, which contains a cone with half cone-apex angle of θ_h = 47° and generatrix length of 1.5 m, a ground plane with a size 3 × 3 m. The dominant mode in the biconical line is the spherical TEM mode. Both of the microstrip structures are placed on the working area of the mono-cone structure symmetrically, where r = 0.65 m, θ = 21°. At this position, there is a clear time or time window of about 6 ns. Within the time window, the reflections from the ends of the cone and the

ground plane cannot affect the electromagnetic field of this position. Otherwise, the end reflections cannot be neglected.

A bipolar pulse with the rise time of 1 ns and the peak-to-peak width of 1.4 ns is set as the excitation signal and is sent into the mono-cone structure by a coaxial line under the ground plane. In order to monitor the output voltages, two voltage probes are set between the inner conductor and the outer conductor of coaxial lines connected to the SMA connectors in the shielding boxes, where the ends of the coaxial lines are matched with waveguide ports. According to (8) and (9), the recovered waveforms of two microstrip structures can be calculated, respectively. Figure 4 shows the comparison between the excited waveform and the recovered waveforms of two microstrip structures.

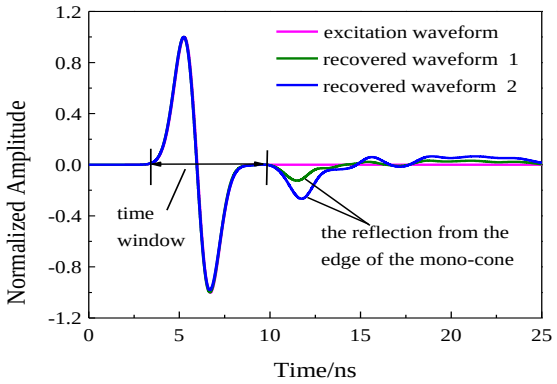

Fig. 4. The comparison between the recovered waveforms and the excited waveform.

As illustrated in Fig. 4, the recovered waveforms are highly consistent with the incident waveform within the time window of the mono-cone structure. The waveforms after the time of 10 ns are from the reflection of the edge of the mono-cone structure. The result reveals that the method of recovering the incident electric field mentioned above is effective and can be used to recover the waveform of the transient electromagnetic pulse.

B. Bandwidths of microstrip structures

From (8), (9), and (2), under the conditions that the feeding positions are well matched, the start is well short circuited for microstrip structure 1, and the start is well matched for microstrip structure 2, the amplitude responses are flat and the phase responses are linear. Thus, the incident electric fields will be recovered without distortion.

Actually, with the increase of the working frequency, the parasitic inductance and the parasitic capacitance of both ends of microstrip structure cannot be ignored, destroying the conditions. So, instead of the incident electric field formed by the mono-cone structure, a signal peak pulse with the upper frequency limit of 2.5 GHz is adopted as the excitation signal. Fourier transform is used to calculate the spectrums of the excited signal and the recovered voltage. Then, the transfer functions of two microstrip structures can be calculated. The results are shown in Fig. 5.

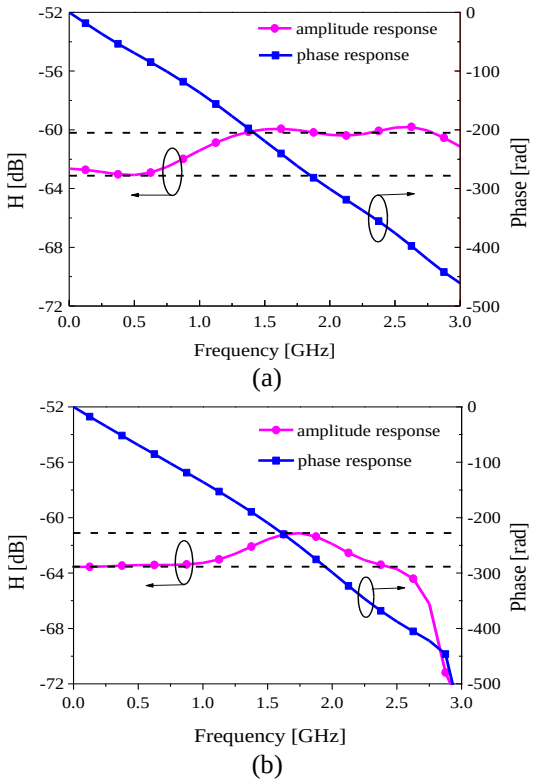

Fig. 5. Transfer functions of two microstrip structures: (a) microstrip structure 1, and (b) microstrip structure 2.

It can be seen from Fig. 5 that the bandwidth of -3 dB is DC~1.5 GHz for microstrip structure 1, and DC~2.5 GHz for microstrip structure 2. In these ranges, the amplitude response is approximately flat and the phase response is approximately straight line, satisfying the distortionless condition mentioned above approximately. The results signify that the microstrip structures have wide bandwidth for the measurement of transient electric field.

C. Effective heights of microstrip structures

Assuming that the recovered voltage is $U(t)$, and the excited electric field is $E(t)$, the effective height h_{eff} of microstrip structure defined as the ratio of $U(t)$ and $E(t)$ can be calculated. A signal peak pulse with the spectrum from DC to 1.5 GHz is used as the excited signal. The simulated and theoretical h_{eff} (h_{eff1} and h_{eff2}) are listed in Table 2. The simulated values are larger than the theoretical values. The reason is that the theoretical

analysis does not consider the effect of the height of the shielding box and the thickness of the conductor.

Table 2: Effective heights of microstrip structures

Microstrip Structures	Simulated h_{eff} (mm)	Theoretical h_{eff} (mm)
1	0.67	0.50
2	0.81	0.75

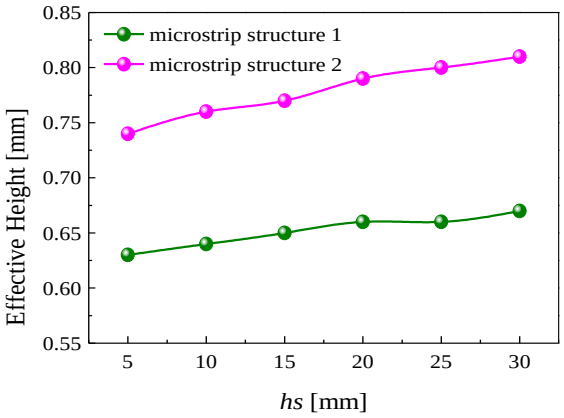

Fig. 6. The influence of height of shielding box on the effective height.

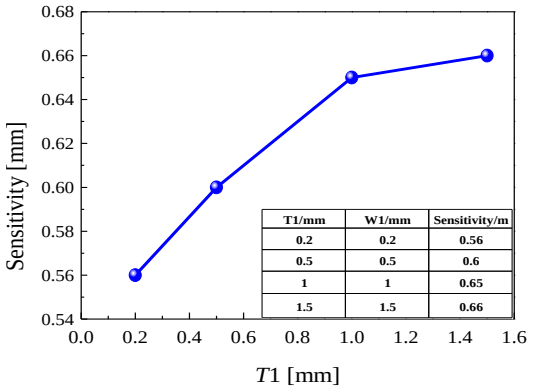

Fig. 7. The influence of the dimension of the conductor on the effective height.

Figure 6 presents the effective heights of microstrip structures with different *hs* of shielding box. Figure 7 shows the influence from the dimension of the conductor of microstrip structure 1 on the effective height. It is clear that the thickness of the conductor is thinner, and the height of the shielding box is lower, the simulated effective height is closer to the theoretical effective height.

IV. EXPERIMENTAL VERIFICATION

A. Calibration of the microstrip structures

To verify the simulation results, the proposed microstrip structures, as shown in Fig. 8, have been fabricated and tested by the time-domain electromagnetic pulse standard field generation setup [16].

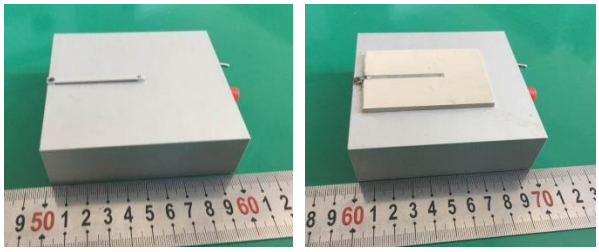

Fig. 8. The photos of microstrip structures. (Microstrip sensors can be built by adding the electro-optical conversion modules into the shielding boxes): (a) microstrip structure 1, and (b) microstrip structure 2.

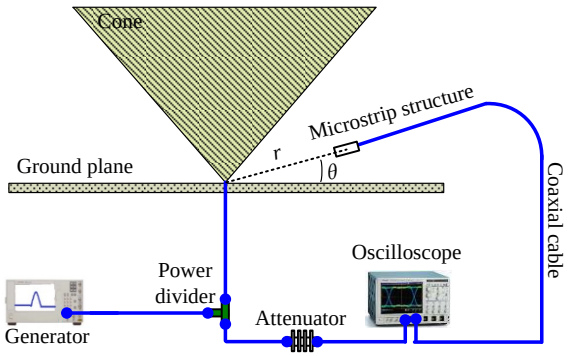

Fig. 9. Experiment system.

The experiment system is built up as shown in Fig. 9. The standard field generation setup is based on a monocone. It can produce a calculated electric field that only depends on the geometry parameter and the generator. Microstrip structure 1 is positioned on the working area of r = 0.65 m, θ = 21° with a time window of about 6 ns, while microstrip structure 2 is positioned on the working area of r = 0.8 m, θ = 21° with a time window of about 5 ns. A double peak pulse with the rise time of 1 ns and the peak-to-peak width of 2 ns, whose frequency spectrum is covered by the simulated bandwidth of the microstrip structures, is used as the excited signal. The output signals of microstrip structures are transmitted to channel 2 of the oscilloscope via a coaxial cable. Channel 1 of the oscilloscope can be used to monitor the incident electric field of the working area as the reference signal. To quantify the comparison between the recovered signal $U(t)$ from the output signal and the reference signal $V(t)$. The root mean square deviation σ is used [17]:

$$\sigma = \sqrt{\int_T [u(t-t_0)-v(t)]^2 dt \Big/ \int_T v^2(t)dt}\,, \qquad (12)$$

where,

$$u(t) = U(t) / \sqrt{\int_T U^2(\tau) d\tau}, \quad (13)$$

$$v(t) = V(t) / \sqrt{\int_T V^2(\tau) d\tau}, \quad (14)$$

are normalized functions, T is the time window, and t_0 is the time shift of $V(t)$ relative to $U(t)$ wherein the value of σ is minimal.

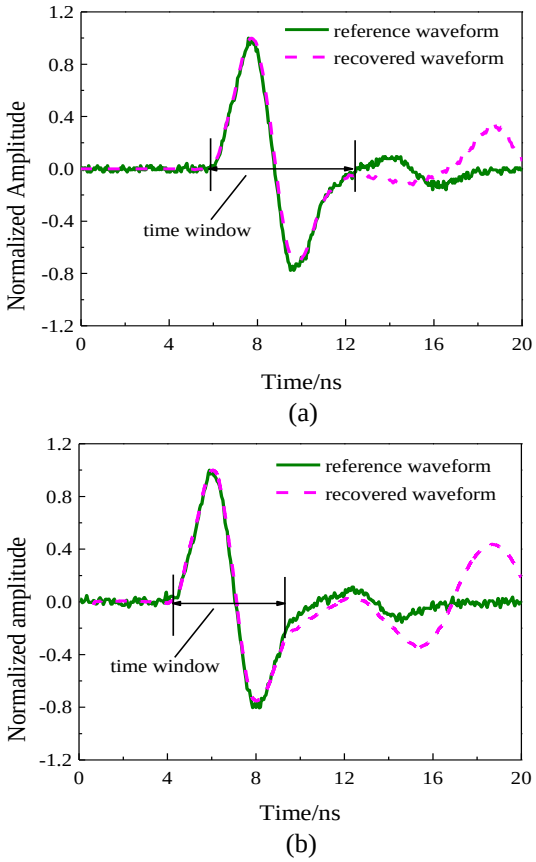

Fig. 10. The comparison of waveforms between the reference waveform and the recovered waveform: (a) microstrip structure 1, and (b) microstrip structure 2.

Figure 10 shows a comparison of waveforms between the reference waveform and the recovered waveform. As shown in Fig. 10, within the time window, the recovered waveforms from both microstrip structure 1 and microstrip structure 2 are highly similar to the corresponding reference waveforms. For the waveforms of structure 1, the RMS deviation σ is 6.9%. For the waveforms of microstrip structure 2, the RMS deviation σ is 5.8%. The waveforms outside the time window are mainly from the reflections at the edge of the monocone. The measured results show that the microstrip structures have good waveform fidelity.

The peak-to-peak values of the reference signal $V(t)$ and the recovered signal $U(t)$ are used to compute the effective height according to Eq. (15),

$$h_{eff} = \frac{U(t) r \sin(\pi/2 - \theta)}{1.2 V(t)}. \quad (15)$$

For microstrip structure 1, the mean value of the effective height is 0.69 mm. The difference between the measured value and the simulated value is less than 3%. For microstrip structure 2, the mean value of the effective height is 0.78 mm, and the difference is less than 4%. The measured results show good consistency with the simulated results. The proposed microstrip structures can capture the transient electromagnetic field with the fast rise time of ≥1 ns.

B. Response of the microstrip sensors

According to the experimental results above, electro-optical conversion modules [18], whose lower cutoff frequency is lower than 1 kHz and the upper cutoff frequency is higher than 350 MHz, are added into the shielding boxes of the microstrip structures to build the microstrip sensors.

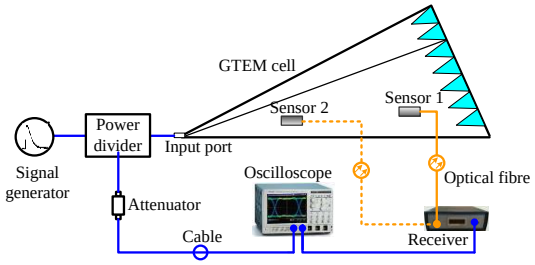

Fig. 11. Experiment test setup in GTEM cell.

As shown in Fig. 11, the GTEM cell [19] with VSWR<1.5 GHz in the range of 1 KHz ~ 3 GHz, as the standard electro-magnetic field generating device, is used to test the response of the microstrip sensors. The signal generator is used to simulate the HEMP source and can generate a pulse with a rise time of 2 ns and a pulsewidth of 20 ns.

The output voltages of microstrip structures are converted into optical signals to transmit with a fibre and recorded by channel 2 of a digital oscilloscope, which can further improve the anti-interference ability for EMP during the transmission of signals. Channel 1 of the oscilloscope is used to monitor the source waveform. According to (8) and (9), the output signals are processed to get the recovered signals. The offset [20] from the noise of the electro-optical conversion circuit, the fibre and the oscilloscope are calculated and then compensated.

Figure 12 shows the comparison between the recovered waveforms and the source waveforms. It can be seen from Fig. 12 (a) that the recovered waveform from microstrip sensor 1 is basically consistent with the source waveforms. According to the IEEE Standard 1597.1 [21], the application of the feature selective validation techniques (FSV) gives for this comparison

the following values: GRADE = 2 and SPREAD = 2. The reason why the falling edge of the recovered waveform is different from that of the source waveform is from the reflection of the end of the GTEM cell. Microstrip sensor 2 is closer to the input port, which has a longer clear time than microstrip sensor 1. Figure 12 (b) illustrates that the recovered waveform is in agreement with the source waveform within the clear time. The RMS deviation σ is 5.3%. The FSV GRADE and SPREAD are 2 [22-23]. If the clear time is enough long, the falling edge of the source waveform can be recovered completely. These results indicate that the microstrip sensors can be used to measure HEMP.

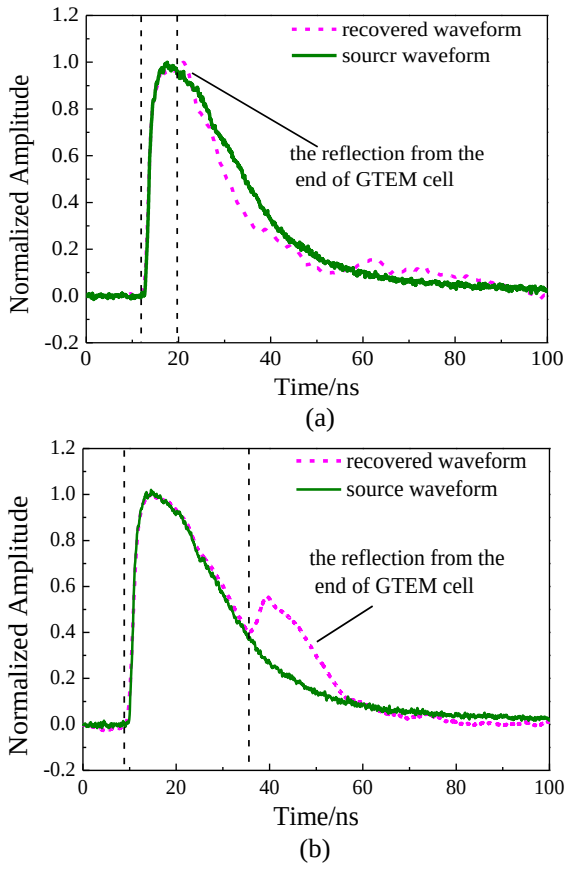

Fig. 12. The comparison between the recovered waveforms and the source waveforms: (a) microstrip structure 1 and (b) microstrip structure 2.

V. CONCLUSION

In order to detect the transient electric field, one type of microstrip structure and microstrip sensor is presented in this paper. The induced voltage on the end load of microstrip line is analyzed. The amplitude and the waveform of the incident electric field can be calculated from the induced voltage by the method of recovering the incident electric field. The proposed microstrip structures are set on the shielding boxes. The start of microstrip structure 1 without substrate is short circuited, and the start of microstrip structure 2 with substrate is matched. The induced signals are outputted via the 50 Ω SMA connectors attached to the ends of the microstrip structures. The performances of two microstrip structures are simulated in the simulation model of a mono-cone structure and measured in the monocone. The simulated and the measured results confirm that the microstrip structures can capture the transient electromagnetic field with the fast rise time of ≥1 ns by the method mentioned above. In addition, the calibrated effective heights show consistency with the simulated effective heights. The reasons for the difference between the simulated effective heights and the theoretical effective height are analyzed. The simulated bandwidths of microstrip structure 1 and microstrip structure 2 are DC~1.5 GHz and DC~2.5 GHz, respectively. The measured results show that the microstrip sensors, built by adding the electro-optical conversion circuit into the shielding boxes, can measure HEMP, displaying its important role in the EMP effect and protection researches.

REFERENCES

[1] C. E. Baum, "Reminiscences of high-power electromagnetics," *IEEE Transactions on Electromagnetic Compatibility*, vol. 49, no. 2, 2007.

[2] IEC 6100-2-13, *High-Power Electromagnetic Environment—Radiated and Conducted*, 2005.

[3] S. T. Song, "Simulation and analysis of HEMP coupling effect on a wire inside an apertured cylindrical shielding cavity," *ACES Journal*, vol. 27, no. 6, pp. 505-515, 2012.

[4] W. A. Radasky, "Introduction to the special issue on high-power electromagnetics (HEMP) and intentional electromagnetic interference (IEMI)," *Electromagnetic Compatibility IEEE Transactions* vol. 46, no. 3, pp. 314-321, 2004.

[5] X. Zhou, "Calculation of transient responses of EMP on transmission lines," *ACES-China 2017*, Suzhou, China, Aug. 2017.

[6] J. R. Andrews, "UWB signal sources, antennas & propagation," *Wireless Communication Technology, 2003. IEEE Topical Conference on. IEEE*, pp. 439-440, 2003.

[7] Electromagnetic Compatibility (EMC) – Part 2: Environment - Section 9: Description of HEMP environment - Radiated disturbance, International Electrotechnical Commission, IEC61000-2-9: 1996.

[8] Y. S. Jiang, "Research on calibration accuracy of D-Dot transient electric field sensor," *Antenna Measurements & Applications (CAMA), 2017 IEEE Conference on. IEEE*, pp. 69-71, 2017.

[9] W. Feser, "A potential free spherical sensor for the measurement of transient electric fields," *IEEE Transactions on Power Apparatus and Systems*, vol. PAS-103, no. 10, Oct. 1984.

[10] Z. Cui, "E-field sensor design for subnanosecond fast transient," *Environmental Electromagnetics, 2012 6th Asia-Pacific Conference on. IEEE*, 2012.
[11] S. V. Tikhomirov and K. Y. Sakharov, "A standard system for producing very-short electromagnetic pulses with a rise time of 20 psec," *Measurement Techniques*, vol. 53, no. 7, pp. 809-812, 2010.
[12] K. Y. Sakharov, "A picosecond pulsed electric field strength measuring transducer," *Measurement Techniques*, vol. 57, no. 2, pp. 201-205, 2014.
[13] K. Y. Sakharov, "A measuring system for characterization of radar-absorbing materials with sounding ultra-short electromagnetic pulses over the range 0.1-40 GHz," *Microwave Techniques (COMITE), 2015 Conference on. IEEE*, 2015.
[14] S. A. Podosenov and A. A. Sokolov, "Linear two-wire transmission line coupling to an external electromagnetic field. I. Theory," *IEEE Transactions on Electromagnetic Compatibility*, vol. 37, no. 4, pp. 559-566, 1995.
[15] CST STUDIO SUITE™ 2014, CST AG, Germany, www.cst.com, 2014.
[16] Y. Yan, "Study of the time-domain electromagnetic pulse standard field generation setup and its application," *Review of Scientific Instruments*, vol. 89, no. 7, 2018.
[17] E. V. Balzovsky, "Dual polarized receiving steering antenna array for measurement of ultra-wideband pulse polarization structure," *Review of Scientific Instruments*, vol. 89, no. 3, 2016.
[18] J. Wei, "Development of transient electric field sensor based on microstrip line," *Microwave and Millimeter Wave Technology (ICMMT), 2018 IEEE International Conference on. IEEE*, Chengdu, China, May 2018.
[19] Electromagnetic compatibility (EMC) – Part 4-20: Testing and measurement techniques – Emission and immunity testing in transverse electromagnetic (TEM) waveguides, IEC61000-4-20: 2010.
[20] L. Yao, "Implementation of a measurement system on field uniformity of transient electromagnetic field," *IEEE Electromagnetic Compatibility Magazine*, vol. 5, no. 1, pp. 43-49, 2016.
[21] IEEE, Standard for Validation of Computational Electromagnetics Computer Modeling and Simulations, Standard IEEE 1597.1-2008, June 2008.
[22] A. Orlandi, G. Antonini, C. Ritota, and A. P. Duffy, "Enhancing feature selective validation (FSV) interpretation of EMC/SI results with grade-spread," in *Proc. 2006 IEEE Int. Symp. Electromagn. Compat.*, vol. 2, pp. 362-367, 2006.
[23] A. P. Duffy and A. Orlandi, "The influence of data density on the consistency of performance of the feature selective validation (FSV) technique," *J. Appl. Comput. Electromagn. Soc.*, vol. 21, no. 2, pp. 164-172, 2006.

Jinhong Wei was born in 1991 in Yunnan, China. He received his B.Sc. degree from Xi'an Jiaotong University, Xi'an, China, 2014, and the M.S. degree from Northwest Institute of Nuclear Technology, Xi'an, China, in 2016. He has been an Engineer in Northwest Institute of Nuclear Technology, Xi'an, China. His current research interests include the transient electromagnetic measurement and antenna design.

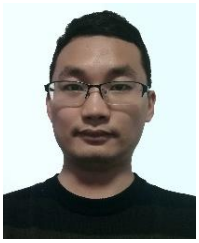

Shoulong Zhang received the M.S. degree from Army Engineering University, Shijia-zhuang, China, in 2014. He has been an Engineer in Northwest Institute of Nuclear Technology, Xi'an, China. His current research interests include EMP measurement and RF circuit design.

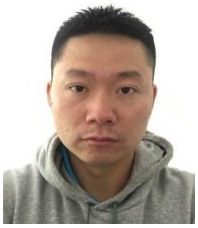

Zhen Liu received his B.Sc. degree in Electronics Engineering and Computer Science from Peking University, Beijing, China, 2010, and the M.S. degree from National University of Defense Technology, Changsha, China, in 2012. He has been an Engineer in Northwest Institute of Nuclear Technology, Xi'an, China. His current research interests include time-domain electromagnetics and its applications.

Youjie Yan received the Ph.D. degree at the University of Electronic Science and Technology of China, Chengdu, China, in 2018. He has been an Associate Research Fellow in Northwest Institute of Nuclear Technology, Xi'an, China. His research interests include the time-domain electromagnetics and the electromagnetic compatibility.

Tingyong Jiang received the Ph.D. degree from Tsinghua University, Beijing, China, in 2016. He has been a Senior Engineer in the Northwest Institute of Nuclear Technology, Xi'an, China. His current research interests include time-domain electromagnetics and the electromagnetic compatibility.

Fanghong Huang received the M.S. degree in Measurement Techniques and Instruments from National University of Defense Technology, Changsha, China, in 2016. She has been an Engineer in the Northwest Institute of Nuclear Technology, Xi'an, China. Her current research interests include time-domain electromagnetics and its applications.

Field-to-Wire Coupling Model for Wire Bundles with Strongly Non-uniform Path

Xinwei Song [1], Donglin Su [2*], Junjun Wang [2], and Bing Li [2]

[1] School of Electrical and Information Engineering
Beijing University of Civil Engineering and Architecture, Beijing, 102616, China
songxinwei@bucea.edu.cn

[2] School of Electronic and Information Engineering
Beihang University, Beijing, 100191, China
*sdl@buaa.edu.cn, wangjunjun@buaa.edu.cn, bingli@buaa.edu.cn

Abstract ─ This paper presents a field-to-wire coupling model for wire bundles with strongly non-uniform path. Previous studies on multi-conductor transmission lines (MTL) are mainly confined to uniform or weakly non-uniform path, which is sometimes not the case in practice. In this paper, the external and internal characteristics of the wire bundle are decomposed by a mode transformation method, of which the advantage is the transformation matrices do not vary with the non-uniform path. The external characteristics correspond to common-mode (CM) components, modeled as an equivalent single wire running in the same path with the bundle above the reference ground. The internal characteristics correspond to differential-mode (DM) components, modeled as a uniform MTL system composed of the original wires in the bundle. In this way, the effects of the non-uniform path and the external field only exist in the CM model. Mode conversion caused by the dielectric coating and terminals is modeled with equivalent circuits. The proposed model is validated with a bundle of curved wires above a PCB board.

Index Terms ─ Field-to-wire coupling, mode conversion, mode transformation, strongly non-uniform path, wire bundle.

I. INTRODUCTION

The wire bundle is a widely used medium for data/power transmission between different devices, PCBs or equipment in information and communication systems. Field-to-wire coupling is a main path for electromagnetic interferences entering the systems. Many methods have been developed to deal with the field coupling problem for wire bundles. The most fundamental one is the multi-conductor transmission line theory (MTLT) [1]. Other methods made improvements based on this theory, such as the reduction technique at high frequency [2], the modeling method for random bundle of twisted-wire pairs [3], the modeling method for cable bundle with lacing cords [4] and the analysis of undesired asymmetries and non-uniformities [5]. In these studies, the wiring path of the bundle is assumed to be uniform or weakly non-uniform. It is sometimes not the case in practice. Wires inside a bundle are often parallel to each other, but the whole bundle may not always be parallel to the reference ground. It means that the per-unit-length parameters in MTLT vary greatly along the wire bundle. Moreover, the height of the bundle from the reference ground may not be electrically small. In this case, only full-wave methods or other methods derived from Maxwell's theory, such as transmission-line super theory (TLST) [6], can deal with this problem, but they are complex and not so efficient. To this end, a modeling method for field-to-wire coupling of wire bundles with strongly non-uniform path is proposed in this paper.

The proposed method decomposes the wire bundle and its reference ground into two parts. One is an equivalent single wire running in the same path with the bundle above the reference ground; the other is a uniform MTL system composed of the original wires in the bundle. In this way, the non-uniform path only exists in the first part and can be dealt with by method of moments (MoM) [7]. The above model decomposition is achieved by mode transformation. Different from the modal analysis in MTLT, the mode transformation proposed here is independent with the height of the bundle from the reference ground. Thus, it is suitable for the analysis of wire bundles with non-uniform path. The two parts of the model are called common-mode (CM) and differential-mode (DM) components in mode domain respectively, since they are corresponding to the external and internal characteristics of the wire bundle. The coupling between CM and DM components will occur if terminals are unbalanced or dielectric coating exists [8]. This is characterized by controlled sources in this paper.

The rest of this paper is organized as follows. In

Submitted On: October 14, 2018
Accepted On: January 26, 2019

Section II, the fundamental mode transformation method for a wire bundle with strongly non-uniform path is introduced. Models for the resulted CM and DM components are built. Mode conversion caused by the dielectric coating and terminals is characterized by equivalent circuits. The proposed modeling method is experimentally validated in Section III. Conclusions are drawn in Section IV.

II. MODELING METHOD

A wire bundle with strongly non-uniform path above the ground is shown in Fig. 1. To model this system, mode transformation is applied to decompose the system into CM and DM components. This is illustrated in the case of bare wires firstly. Then, the dielectric coating and the terminal are considered and modeled with equivalent circuits.

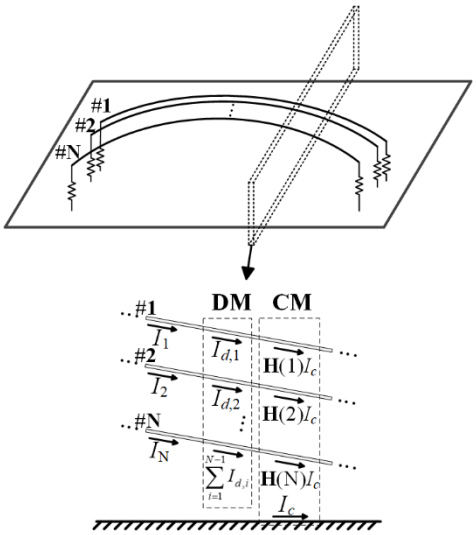

Fig. 1. A wire bundle with strongly non-uniform path above the ground.

A. Mode transformation

In this subsection, the wires are assumed to have no coating. An infinitely small area of the system under analysis is shown in Fig. 1. Currents of the wires are divided into CM current I_c and DM currents $I_{d,i}$ $(i=1,2,...,N-1)$ in the following way:

$$\begin{bmatrix} I_1 \\ I_2 \\ \vdots \\ I_{N-1} \\ I_N \end{bmatrix} = \underbrace{\begin{bmatrix} & 1 & 0 & \cdots & 0 \\ & 0 & 1 & \cdots & 0 \\ \mathbf{H} & \vdots & \vdots & \ddots & \vdots \\ & 0 & 0 & \cdots & 1 \\ & -1 & -1 & \cdots & -1 \end{bmatrix}}_{\mathbf{T}_I} \begin{bmatrix} I_c \\ I_{d,1} \\ I_{d,2} \\ \vdots \\ I_{d,N-1} \end{bmatrix}, \quad (1)$$

where **H** is the current division vector. The *i*th $(i=1,2,...,N)$ element of **H**, **H**(i), denotes the ratio of CM current in wire #i to total CM current. **H** is similar to the current division factor *h* (also known as imbalance factor [9]). Concerning to two-conductor transmission lines (TLs) with the reference ground, $\mathbf{H}=[h;1-h]$. Voltages of the wires are also divided into CM voltage V_c and DM voltages $V_{d,i}$ $(i=1,2,...,N-1)$. The corresponding relationship can be obtained by the equivalence of the transmitted power:

$$\begin{aligned} &[V_1,V_2,\ldots,V_N]\cdot\left[I_1^*,I_2^*,\ldots,I_N^*\right]^T \\ &=\left[V_c,V_{d,1},\ldots,V_{d,N-1}\right]\cdot\left[I_c^*,I_{d,1}^*,\ldots,I_{d,N-1}^*\right]^T, \end{aligned} \quad (2)$$

and is,

$$\begin{bmatrix} V_c \\ V_{d,1} \\ V_{d,2} \\ \vdots \\ V_{d,N-1} \end{bmatrix} = \underbrace{\begin{bmatrix} & \mathbf{H}^T & & & \\ 1 & 0 & \cdots & 0 & -1 \\ 0 & 1 & \cdots & 0 & -1 \\ \vdots & \vdots & \ddots & \vdots & \vdots \\ 0 & 0 & \cdots & 1 & -1 \end{bmatrix}}_{\mathbf{T}_V^{-1}} \begin{bmatrix} V_1 \\ V_2 \\ \vdots \\ V_{N-1} \\ V_N \end{bmatrix}. \quad (3)$$

In the above mode transformation, the external field and DM components are decoupled, and CM and DM components are decoupled, if the dielectric coating and the terminal are not considered. CM components of the system can be equivalent to a single wire running in the same path with the bundle above the reference ground, and DM components can be modeled as uniform *N*-conductor TLs with wire #N as the reference conductor, shown in Fig. 2. In this way, CM components can be modeled by MoM, and DM components can be modeled by MTLT.

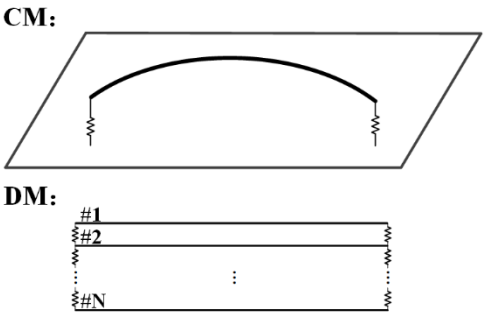

Fig. 2. Models for CM and DM components of the system in Fig. 1.

Then the left problem is how to obtain **H**. Since CM voltages on all conductors are the same, the following relationship can be obtained:

$$\sum_{k=1}^{N} j\omega L_{ik}\mathbf{H}(k)I_c = \sum_{k=1}^{N} j\omega L_{mk}\mathbf{H}(k)I_c \quad (i,m=1,2,...,N), \quad (4)$$

where L_{ik} (L_{mk}) is the per-unit-length self-inductance of

wire #i (#m) if $i=k$ ($m=k$), or the per-unit-length mutual-inductance between wire #i (#m) and #k if $i\neq k$ ($m\neq k$). For the infinitely small area in Fig. 1, L_{ik} (L_{mk}) can be expressed by the formulas in [1]:

$$\mathbf{L}=\frac{\mu_0}{2\pi}\begin{bmatrix}\ln\frac{2D}{r_1} & \ln\frac{2D}{d_{12}} & \cdots & \ln\frac{2D}{d_{1N}}\\ \ln\frac{2D}{d_{21}} & \ln\frac{2D}{r_2} & \cdots & \ln\frac{2D}{d_{2N}}\\ \vdots & \vdots & \ddots & \vdots\\ \ln\frac{2D}{d_{N1}} & \ln\frac{2D}{d_{N2}} & \cdots & \ln\frac{2D}{r_N}\end{bmatrix}, \tag{5}$$

where D is the distance between the wire bundle and the ground, d_{ij} $(i,j=1,2,...,N)$ is the distance between wire #i and #j, and r_i is the radius of wire #i. (5) is based on the assumption that the wire bundle is not close to the ground, and the wires are not close to each other. Generally, the results will be accurate enough if $D\geq 2d$ and $d\geq 4r$. (4) can be simplified as:

$$\mathbf{L}\cdot\mathbf{H}=[c]_{N\times 1}, \tag{6}$$

where c is an unknown constant. Thus, combining (5), (6) with $\sum_{k=1}^{N}\mathbf{H}(k)=1$, $\mathbf{H}$ can be calculated by:

$$\begin{bmatrix}\ln r_1 & \ln d_{12} & \cdots & \ln d_{1N}\\ \ln d_{21} & \ln r_2 & \cdots & \ln d_{2N}\\ \vdots & \vdots & \ddots & \vdots\\ \ln d_{N1} & \ln d_{N2} & \cdots & \ln r_N\end{bmatrix}\mathbf{H}_0=\begin{bmatrix}1\\1\\\vdots\\1\end{bmatrix}, \tag{7}$$

$$\mathbf{H}=\mathbf{H}_0\Big/\sum_{i=1}^{N}\mathbf{H}_0(i). \tag{8}$$

It can be seen that $\mathbf{H}$ is independent with D, and the transformation matrices $\mathbf{T}_I$, $\mathbf{T}_V$ are invariant despite the non-uniform wiring path. The above derivation of $\mathbf{H}$ can also be expressed with the aid of the per-unit-length capacitance $\mathbf{C}$ in a similar way for $\mathbf{C}=\mu_0\varepsilon_0\mathbf{L}^{-1}$. The equivalent radius r_c of the single wire in the CM model can be obtained by combining the following relationship with (7):

$$j\omega\frac{\mu}{2\pi}\ln\frac{2D}{r_c}\cdot[1]_{N\times 1}\cdot I_c=j\omega\mathbf{L}\cdot\mathbf{H}\cdot I_c, \tag{9}$$

and is,

$$r_c=e^{1\Big/\sum_{i=1}^{N}\mathbf{H}_0(i)}. \tag{10}$$

B. Model for the effect of the dielectric coating

For wires with dielectric coating, $\mathbf{C}\neq\mu_0\varepsilon_0\mathbf{L}^{-1}$. Thus, different $\mathbf{H}$ will be obtained when we calculate it from $\mathbf{L}$ and $\mathbf{C}$. In this case, mode conversion between CM and DM occurs, as described in [8].

Before the introduction of the model for dielectric coating, $\mathbf{H}$ derived from $\mathbf{C}$ (denoted as $\mathbf{H}_e$) is described. The coated wire is equivalent to a bare wire with the equivalent electric radius r_e [10]:

$$r_e=a^{\frac{1}{\varepsilon_r}}b^{1-\frac{1}{\varepsilon_r}}, \tag{11}$$

where a is the radius of the conductor, b is the radius of the whole wire, and ε_r is the relative permittivity of the coating. In this way, $\mathbf{H}_e$ can be calculated by (7) and (8) with r replaced by r_e .

Corresponding to $\mathbf{H}_e$, $\mathbf{H}$ derived from $\mathbf{L}$ is denoted as $\mathbf{H}_m$, and the magnetic radius is denoted as r_m (equal to the conductor radius a). If $\mathbf{H}_e$ is chosen as the $\mathbf{H}$ in transformation matrices $\mathbf{T}_I$, $\mathbf{T}_V$, the mode conversion caused by coating will be represented by series voltage sources. If $\mathbf{H}_m$ is chosen, the mode conversion will be represented by grounded parallel voltage sources. The two representation are both feasible, and the former is chosen in this paper. Thus, the transformation matrices are:

$$\mathbf{T}_I=\left(\mathbf{T}_V^{-1}\right)^T=\begin{bmatrix}1 & 0 & \cdots & 0\\ 0 & 1 & \cdots & 0\\ \mathbf{H}_e & \vdots & \vdots & \ddots & \vdots\\ 0 & 0 & \cdots & 1\\ -1 & -1 & \cdots & -1\end{bmatrix}. \tag{12}$$

The series and parallel voltages of CM and DM components generated by the CM current are:

$$\left[V_{sc},V_{sd,1},V_{sd,2},\ldots,V_{sd,N-1}\right]^T=\left[V_{sc},\mathbf{V}_{sd}\right]^T=\mathbf{T}_V^{-1}\cdot\mathbf{L}\cdot j\omega\mathbf{H}_eI_c, \tag{13}$$

$$\left[V_{pc},V_{pd,1},V_{pd,2},\ldots,V_{pd,N-1}\right]^T=\left[V_{pc},\mathbf{V}_{pd}\right]^T=\mathbf{T}_V^{-1}\cdot j\omega\mathbf{H}_e\Delta I_c/\mathbf{C}(r_e). \tag{14}$$

A transfer inductance vector $\mathbf{L}_t$ is defined to describe the relation between series voltage sources and the CM current, $\mathbf{V}_{sd}=j\omega\mathbf{L}_tI_c$. $\mathbf{L}_t$ can be derived from (13):

$$\mathbf{L}_t=\frac{\mu_0}{2\pi}\begin{bmatrix}\ln\frac{d_{N1}}{r_1} & \ln\frac{d_{N2}}{d_{12}} & \cdots & \ln\frac{d_{N,N-1}}{d_{1,N-1}} & \ln\frac{r_N}{d_{1N}}\\ \ln\frac{d_{N1}}{d_{21}} & \ln\frac{d_{N2}}{r_2} & \cdots & \ln\frac{d_{N,N-1}}{d_{2,N-1}} & \ln\frac{r_N}{d_{2N}}\\ \vdots & \vdots & \ddots & \vdots & \vdots\\ \ln\frac{d_{N1}}{d_{N-1,1}} & \ln\frac{d_{N2}}{d_{N-1,2}} & \cdots & \ln\frac{d_{N,N-1}}{r_{N-1}} & \ln\frac{r_N}{d_{N-1,N}}\end{bmatrix}\mathbf{H}_e. \tag{15}$$

The equivalent circuit for this effect is shown in Fig. 3. Theoretically, there should also be CM voltage sources induced by DM currents, but this effect is weak and

neglected for simplification.

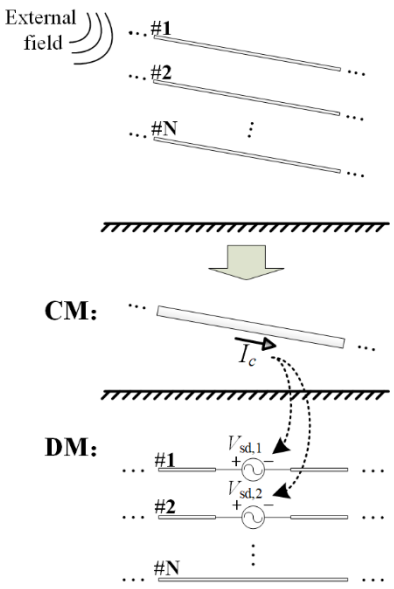

Fig. 3. Model for the effect of the dielectric coating.

The equivalent magnetic and electric radii of CM components, r_{cm} and r_{ce}, can be obtained from the V_{sc} and V_{pc} in (13) and (14):

$$r_{cm} = e^{\mathbf{H}_e^T \cdot \mathbf{A}_m \cdot \mathbf{H}_e}, \tag{16}$$

$$r_{ce} = e^{\mathbf{H}_e^T \cdot \mathbf{A}_e \cdot \mathbf{H}_e}, \tag{17}$$

where

$$\mathbf{A}_{m(e)} = \begin{bmatrix} \ln r_{m(e)1} & \ln d_{12} & \cdots & \ln d_{1N} \\ \ln d_{21} & \ln r_{m(e)2} & \cdots & \ln d_{2N} \\ \vdots & \vdots & \ddots & \vdots \\ \ln d_{N1} & \ln d_{N2} & \cdots & \ln r_{m(e)N} \end{bmatrix}. \tag{18}$$

C. Model for the terminal

Terminals of the CM and DM models in Fig. 2 are obtained by [11]:

$$\mathbf{Z}_{cd} = \mathbf{T}_v^{-1} \cdot \mathbf{Z} \cdot \mathbf{T}_I = \begin{bmatrix} z_c & [z_{ti}] \\ [z_{ti}]^T & [z_{dij}] \end{bmatrix} \quad (i, j = 1, 2, \ldots, N-1), \tag{19}$$

where $\mathbf{Z}$ is the original terminal impedance matrix and $\mathbf{Z}_m$ is the impedance matrix in mode domain. z_c is the CM load, z_{dij} $(i = j)$ is the DM load between wire #i and #N, and z_{dij} $(i \neq j)$ is the DM load between wire #i and #j. Unbalanced terminals will also cause mode conversion [12]. z_{ti} represents the coupling (or conversion) between CM and DM on terminals. The corresponding model is shown in Fig. 4.

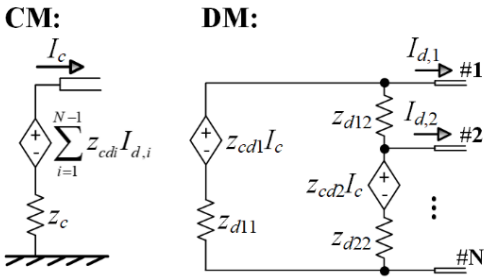

Fig. 4. Model for the terminal.

III. EXPERIMENTAL VALIDATION

The proposed modeling method in Section II is validated with a bundle of four curved wires shown in Fig. 5.

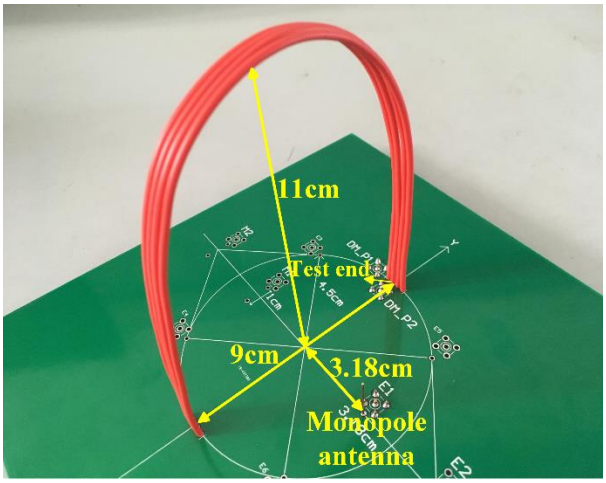

Fig. 5. A bundle of curved wires above a PCB board for experimental validation.

The wire bundle is connected to a double-face PCB. The four wires are the same. Their conductor radius is 0.465 mm, the outer radius is 1.05 mm, and the relative permittivity of the coating is 3.4. The distance between adjacent wires is about 3 mm. The length of the wires is 27 cm. Both ends of each wire are terminated with 51 Ω chip fixed resistors, except the test end. A spectrum analyzer (Keysight N9918A FieldFox Handheld Microwave Combination Analyzer) is connected to the test end through a coaxial connector on the back of the PCB board. External fields are generated by the monopole antenna on the PCB. The antenna is fed by a signal generator (R&S SMF 100A signal generator) providing 0-dBm power. The length of the antenna is 1.7 cm. The induced currents measured on the test end are compared with the proposed model. The results are shown in Fig. 6. It can be seen that the results obtained from measurements and the proposed model agree well.

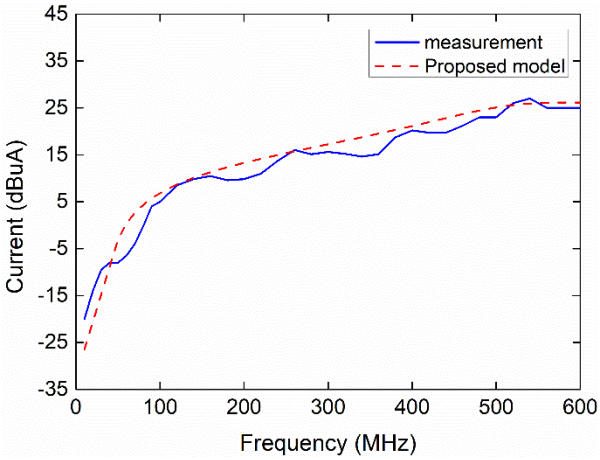

Fig. 6. The induced currents on the test end obtained from measurements and the proposed model.

IV. CONCLUSION

A field-to-wire coupling model for wire bundles with strongly non-uniform path is built in this paper. As the wiring path is one of the external characteristics, a mode transformation method is proposed to decompose the external and internal characteristics of the wire bundle. In this way, the corresponding CM and DM components are obtained. The former is modeled as an equivalent single wire running in the same path with the bundle above the reference ground. The latter is modeled as a uniform MTL system composed of the original wires in the bundle. External fields only excite the CM components. The non-uniform path only exists in the CM model and can be easily dealt with by MoM. Mode conversion caused by the dielectric coating and terminals are modeled as controlled voltage sources. Although the presented method focuses on the field-to-wire coupling problem, it can be readily extended to the counterpart radiation problem.

ACKNOWLEDGMENT

This work is sponsored by National Natural Science Foundation of China (No. 61771032) and Civil Aircraft Projects of China (No. MJ-2017-F-11).

REFERENCES

[1] C. Paul, *Analysis of Multiconductor Transmission Lines*. 2nd ed., Wiley-IEEE Press, New Jersey, 2007.

[2] G. Andrieu, L. Kon, F. Bocquet, B. Dmoulin, and J. P. Parmantier, "Multiconductor reduction technique for modeling common-mode currents on cable bundles at high frequency for automotive applications," *IEEE Trans. Electromagn. Compat.*, vol. 50, no. 1, pp. 175-186, Feb. 2008.

[3] G. Spadacini, F. Grassi, and S. A. Pignari, "Field-to-wire coupling model for the common mode in random bundles of twisted-wire pairs," *IEEE Trans. Electromagn. Compat.*, vol. 57, no. 5, pp. 1246-1254, Oct. 2015.

[4] P. Manfredi, D. D. Zutter, and D. V. Ginste, "Analysis of nonuniform transmission lines with an iterative and adaptive perturbation technique," *IEEE Trans. Electromagn. Compat.*, vol. 58, no. 3, pp, 859-867, June 2016.

[5] F. Grassi, P. Manfredi, X. Liu, J. Sun, X. Wu, D. V. Ginste, and S. A. Pignari, "Effects of undesired asymmetries and nonuniformities in differential lines," *IEEE Trans. Electromagn. Compat.*, vol. 59, no. 5, pp. 1613-1624, Oct. 2017.

[6] H. Haase, T. Steinmetz, and J. Nitsch, "New propagation models for electromagnetic waves along uniform and nonuniform cables," *IEEE Trans. Electromagn. Compat.*, vol. 46, no. 3, pp. 345-352, Aug. 2004.

[7] R. F. Harrington, *Field Computation by Moment Methods*. IEEE Press Series on Electromagnetic Waves, New York, 1993.

[8] B. Li, D. Su, J. Wang, and X. Song, "Common- and differential-mode conversion induced by asymmetry and dielectric coating in a transmission line system," *IEEE Trans. Electromagn. Compat.*, vol. 59, no. 3, pp. 988-991, June 2017.

[9] T. Watanabe, O. Wada, T. Miyashita, and R. Koga, "Common-mode current generation caused by difference of unbalance of transmission lines on a printed circuit board with narrow ground pattern," *IEICE Trans. Commun.*, vol. E83-B, no. 3, pp. 593-599, Mar. 2000.

[10] B. D. Popovic, M. B. Dragovic, and A. R. Djordjevic, *Analysis and Synthesis of Wire Antennas*. Research Studies Press, New York, 1982.

[11] J. Wang, X. Song, D. Su, and B. Li, "Near-field radiation calculation of irregular wiring twisted-wire pairs based on mode decomposition," *IEEE Trans. Electromagn. Compat.*, vol. 59, no. 2, pp. 600-608, April 2017.

[12] A. Sugiura and Y. Kami, "Generation and propagation of common-mode currents in a balanced two-conductor line," *IEEE Trans. Electromagn. Compat.*, vol. 54, no. 2, pp. 466-473, Apr. 2012.

Xinwei Song received the B.S. and Ph.D. degrees in Electronic and Information Fngineering from Beihang University, Beijing, China, in 2012 and 2018, respectively. She is currently a Lecturer with the School of Electrical and Information Engineering, Beijing University of Civil Engineering and Architecture, Beijing, China.

Her research interests include numerical modeling and measurements of transmission lines, and electromagnetic compatibility.

Donglin Su received the B.S., M.S., and Ph.D. degrees in Electronic Engineering from Beihang University (BUAA), Beijing, China, in 1983, 1986, and 1999, respectively. In 1986, she joined the Faculty of School of Electronics and Information Engineering, BUAA, where she is currently a Full Professor. From 1996 to 1998, she was a Visiting Scholar with the Department of Electronic Engineering, University of California, Los Angeles (UCLA), Los Angeles, CA, USA, under the BUAA–UCLA Joint Ph.D. Program.

Her research interests include the numerical methods for microwave and millimeter-wave integrated circuits and systematic electromagnetic compatibility design of various aircrafts.

She is a senior member of the Chinese Institute of Electronics. She is the General Chair of 2018 International ACES Symposium. She is also the Chair of Beijing Chapter of the IEEE Antennas and Propagation Society and the Deputy Chair of the Antennas Society, Chinese Institute of Electronics.

Junjun Wang received the B.E. degree from Shandong University of Technology, Shandong, China, and M.E. degree from Shanghai University, Shanghai, China, in 1999 and 2002 respectively, and the Ph.D. degree at School of Electrical and Electronic Engineering, Nanyang Technological University, Singapore, in 2006, all in Electronic Engineering. From 2005 to 2008, she worked at Sony Electronics (Singapore) as a Senior R&D Engineer. Since 2009, she has been an Associate Professor with the School of Electronic and Information Engineering, Beihang University, Beijing, China.

Her research interests include design of integrated in-package and on-chip antennas, electromagnetic compatibility, wireless energy harvesting and radio frequency circuits.

Bing Li received the B.S. and Ph.D. degrees in Electronic and Information Engineering from Beihang University, Beijing, China, in 2011 and 2017, respectively. He currently works as a Post-doctoral Scholar with the School of Electronic and Information Engineering, Beihang University, Beijing, China.

His research interests include numerical modeling of transmission lines, field coupling analysis, and computational electromagnetics.

Necessity of Charge Measurement for Radiation Evaluation of Transmission Lines

Bing Li [1], Xinwei Song [2], and Donglin Su [1*]

[1] School of Electronic and Information Engineering
Beihang University, Beijing, 100191, China
bingli@buaa.edu.cn, *sdl@buaa.edu.cn

[2] School of Electrical and Information Engineering
Beijing University of Civil Engineering and Architecture, Beijing, 102616, China
songxinwei@bucea.edu.cn

Abstract — This paper attempts to arouse people's attention to charge measurement in electromagnetic compatibility, especially when evaluating the radiation of transmission lines (TLs). Usually the total current (or common-mode current) is supposed to represent the potential radiation of a TL system. However, it is proved that the measurement of charge, which is the dual source quantity of current, is also necessary to evaluate radiation in this paper. Only when the current and charge are both obtained, the radiation field could be determined accurately. First of all, it is pointed out that charge information could not be properly obtained by current measurement. Although charge could be derived from current theoretically, the error transferred from current to charge could be great for measurement. Then, the error transferred from current to near field (which reflects the charge distribution) is studied by simulation of a typical TL case. And it is proved that such error could be reduced effectively if current is modified by charge. In addition, another important reason for charge measurement is given as limited measurement points, since the standing waveform on TLs cannot be determined by current only. Finally, a possible method for charge measurement is proposed.

Index Terms — Charge measurement, radiation, transmission lines.

I. INTRODUCTION

The radiation of transmission lines is an important problem in electromagnetic compatibility (EMC). In many studies, the radiation of wires, cables or other transmission line systems is considered to be determined by current [1]–[6]. For example, a cable is modeled according to the terminal current in [1]. In MIL-STD-461 [7] and CISPR 25 [8], the high frequency conducted emission (CE) is based on current measured with current probe. However, compared with current, the other field source quantity—charge receives very little attention. Current (without charge) is considered sufficient to describe everything in transmission line radiation. Usually, there are two main reasons for this idea:

1) The charge conservation law indicates that charge and current could be derived from each other, which means the charge information may be obtained by current.

2) The electric field generated by the given current distribution [9] is:

$$\boldsymbol{E} = -j\omega\mu \iint_S \boldsymbol{J}\frac{e^{-jkR}}{4\pi R}\mathrm{d}s - \nabla\left(\frac{1}{\varepsilon}\iint_S \sigma\frac{e^{-jkR}}{4\pi R}\mathrm{d}s\right), \quad (1)$$

which indicates that the contribution of charge to electric field gets lower at higher frequencies.

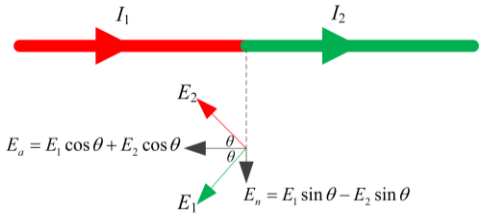

Fig. 1. Axial and normal components of the electric field generated by two current segments on the symmetric plane.

However, the two reasons are not always correct. Here we take the electric field as the example to explain. As a simple example, the electric field generated by two connected current segments on the symmetric plane are shown in Fig. 1. In the near-field region, the axial components of the electric fields generated by the two segments have the same direction, hence $E_a \propto I_1 + I_2$. For E_a, the relative error (RE) is limited:

Submitted On: October 14, 2018
Accepted On: December 25, 2018

$$\frac{\Delta E_a}{E_a}=\frac{\Delta I_1+\Delta I_2}{I_1+I_2}\le \max\left\{\frac{\Delta I_1}{I_1},\frac{\Delta I_2}{I_2}\right\}. \tag{2}$$

However, for E_n, the RE is:

$$\frac{\Delta E_n}{E_n}=\frac{\Delta I_1-\Delta I_2}{I_1-I_2}. \tag{3}$$

Obviously, the error is out of control and even approaches infinity since $I_1-I_2\approx 0$ if $I_1\approx I_2$. That means the electric field generated by charge does not always reduce as the frequency gets higher. The same problem exists for Reason 1, since the charges at the connection node is also determined by I_1-I_2. (Actually the normal field E_n just right represents the node charge.)

The error transfer from current to electric field is analyzed and discussed in Section II. After that, current is modified with charge, which proves to effectively reduce the errors in Section III. An additional reason for charge measurement is given in Section IV. Finally, a possible method for charge measurement is proposed in Section V.

II. ERRORS TRANSFER FROM CURRENT TO ELECTRIC FIELD

For different parameter settings, the field errors caused by current errors are shown and explained. This discussion helps to understand how the errors happen, and when the errors have to be corrected.

Fig. 2. The transmission line system and the field region under test.

The transmission line system in Fig. 2 is taken as the example. By default, the length of the wire is L = 1m, the height from the ground plane is h = 1cm and the radius is r = 1mm. A voltage source V_s = 1V is connected at the left terminal. The load is connected at the right terminal, which is set to be $R_L = Z_c$ by default. $Z_c = 60ln(2h/r)$ is the characteristic impedance of the transmission line. Electric fields in the rectangle range $0.1\text{m}\le x\le 0.9\text{m}$ and $0\le y\le 0.2\text{m}$ on the ground (GND) plane are calculated based on integral equations [9]. Since the system is symmetric by the *xOz* plane, only one side on the *y* axis is considered. Fields near the two terminals are not considered, because the currents are calculated by transmission line theory (TLT) [10], which are violated on the terminals and may lead to incorrect results.

The default frequency is set to be f = 100MHz. With the default settings, the current distribution along the wire could be easily obtained with TLT:

$$I(x)=\frac{1}{Z_c}\left(Ae^{-j\beta x}-Be^{j\beta x}\right), \tag{4a}$$

where

$$A=\frac{1}{2}\frac{(R_L+Z_c)e^{j\beta L}}{R_L\cos\beta L+Z_c\cdot j\sin\beta L}V_s, \tag{4b}$$

$$B=\frac{1}{2}\frac{(R_L-Z_c)e^{-j\beta L}}{R_L\cos\beta L+Z_c\cdot j\sin\beta L}V_s, \tag{4c}$$

$$\beta=\frac{2\pi f}{v}. \tag{4d}$$

Here v is the phase velocity of the transmitted wave, which is usually equal to velocity of light c.

Then the wire is divided into 80 segments with known currents. With (1), the electric field generated by each segment and its mirror segment current could be calculated , then sums up to be the total electric field on the field point, as shown in Fig. 3.

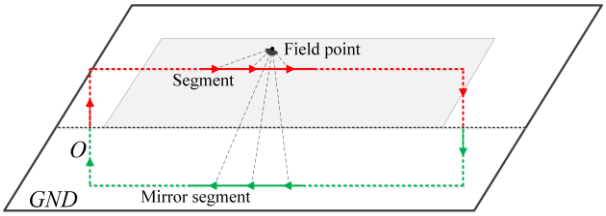

Fig. 3. Field calculation of the transmission line system.

To observe the error transferring from current to field, a random 1% error is added to each segment current and the simulation is redone. To avoid the fortuity, the same process is done by 100 times and average values of the REs are taken as the results.

Firstly, it is obvious that 1% (40dB) errors for currents could lead to much larger errors for fields. This is because fields are determined by I_1-I_2 (or the charge) to a certain extent as introduced in Section I. Another phenomenon is that the REs get smaller as field points get further from the wire. The reason is that the field close to the wire tends to be determined by the local charge density, while the field far from the wire tends to be determined by the general charge density. For a certain segment current, the effect caused by the error is carrying the charge from one end to the other. As further from the wire, the field becomes less sensitive to such charge movement, which means the errors would be smaller.

There-in-after, RE of the electric field would be shown for each group of parameter settings.

A. Frequency *f*

Besides the default 100MHz, three other frequencies, 25MHz, 50MHz and 200MHz, are also selected to demonstrate the influence of frequency on the REs of the electric field. The electric fields for the four cases are all shown in Fig. 4. Obviously, the errors become smaller as frequency gets higher. When frequency gets higher, differences between adjacent segment currents ($I_1 - I_2$) become larger, which means real value of charges and electric fields would be larger. Simultaneously, the absolute errors keep invariant, which leads to the reduction of the REs.

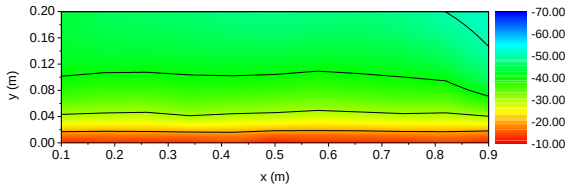

(a) f = 25MHz

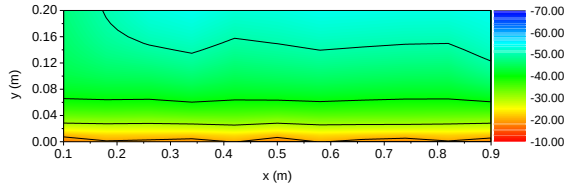

(b) f = 50MHz

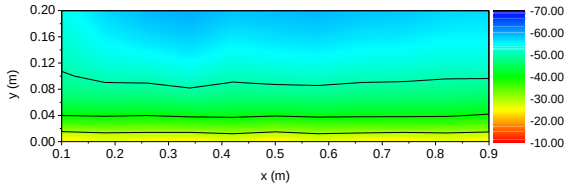

(c) f = 100MHz

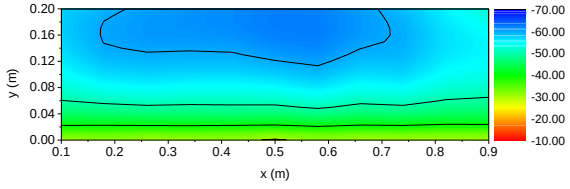

(d) f = 200MHz

Fig. 4. Relative errors (dB) of the field at different frequencies.

B. Height *h*

The REs of the electric field for three heights 0.5cm, 1cm (default) and 2cm are shown in Fig. 5. At y = 0, the REs of electric field tightly rely on h. However, at y = 0.04m, the REs of the three cases are all about –40dB. In other words, the influence of h declines very fast as the field point gets further from the wire. The explanation is that the REs depend on the strict point-wire distance $d' = \sqrt{d^2 + h^2}$. When d is small (close to the wire), $d' \approx h$; when d is large (far from the wire), $d' \approx d$.

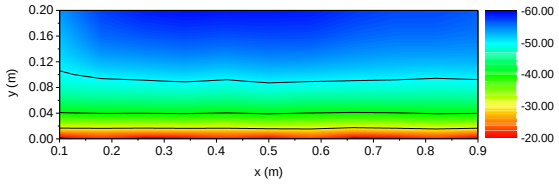

(a) h =0.5cm

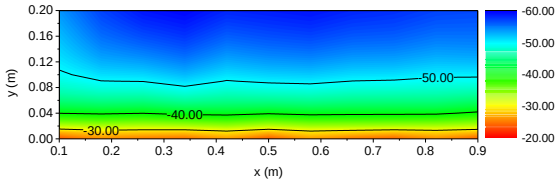

(b) h =1cm

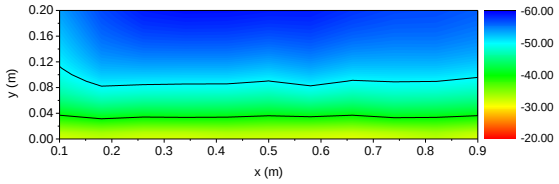

(c) h =2cm

Fig. 5. Relative errors (dB) of the field with different heights.

C. Radius *r*

The radius actually has no influence on the REs. In TLT, r is only related to Z_c, where $Z_c = 60ln(2h/r)$. As long as Z_L keeps equal to Z_c, the current distribution has no relation with the specific value of r.

D. Coating

Dielectric coating is quite common for transmission lines. In the aspect of current/charge distribution, the effect of coating is that it decreases the phase velocity v of the transverse electromagnetic (TEM) wave traveling along the wires. Here, the phase velocity is set as v=0.5c (c is the light speed in vacuum). The REs of electric fields is given in Fig. 6 (calculated with the modified Green function in [11]), compared with the default case.

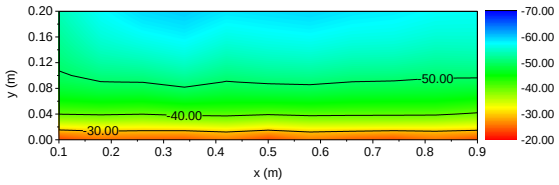

(a) v=c

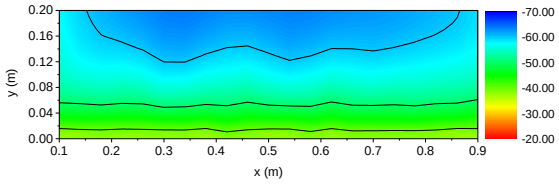

(b) v=0.5c

Fig. 6. Relative errors (dB) of the field with different phase velocities.

Obviously, the existence of coating reduces the REs. Similar to *f*, the coating could also change the differences of adjacent segment currents $I_1 - I_2$. $I_1 - I_2$ depends on β, where $\beta = 2\pi f / v$. In other words, both f and the coating influence the REs by changing β. The REs in Fig. 4 (d) (f=200MHz) and Fig. 6 (b) (v=0.5c) are quite similar, which also proves this standpoint.

The permittivity of the coating may be frequency dependent, which means v varies at different frequencies. However, this effect is not evident at the low frequencies the transmission line analysis concerns. Another possible effect of the coating is dielectric loss, which may lead to the attenuation of the wave in transmission. In this condition, the true value and error change in equal proportion and RE remains unchanged.

E. Terminal Load R_L

In the default settings, R_L is set to be equal to Z_c, which makes the magnitude of current along the wire invariant. This setting helps to demonstrate the effects of other parameters. But in practice, the terminal load is more possible to be open or short. To avoid the extreme conditions, a 10Ω load and a 10kΩ load are used to represent the short and open states, respectively. The REs of electric fields is given in Fig. 7, compared with the default cases.

Since R_L is set as nearly short (10Ω) or open (10kΩ), standing wave forms along the wire. The nodes and antinodes of the voltage have been marked in Fig. 7. The REs near the voltage nodes are quite large while those near the antinodes are much smaller. At the voltage nodes (which are also the current antinodes), the current is largest while the voltage and charge density are the smallest. Therefore, the RE becomes evidently large. Yet at the voltage antinodes, the condition is the exact opposite. That is why such a big difference of REs forms along the wire.

Here it seems that the error is not severe at voltage antinodes. However, that is because till now we have been discussing relative errors, where the small current here makes the added error value also small there. Considering absolute errors, the problem may be as serious at voltage antinodes. Actually, in many cases the errors in the measurement system are absolute, such as the receiver thermal noise. For a low-current system, like open-ended wire or dipole antenna, the current may be too small and submerged by the noise, hence charge becomes the only measurable quantity.

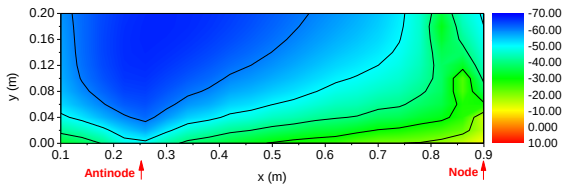

(a) R_L=10Ω

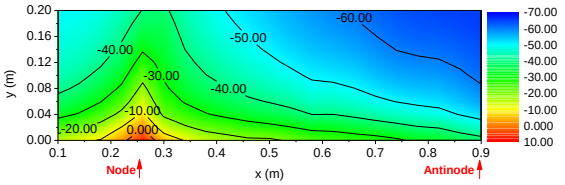

(b) R_L =10kΩ

Fig. 7. Relative errors (dB) of the field along the wire with approximately short and open terminal loads. (Nodes and antinodes of the voltage are marked).

III. CURRENT MODIFICATION WITH CHARGE DENSITY

Since small errors of current may lead to large errors of electric field, an applicable way to eliminate this effect is to directly measure the current difference ($I_1 - I_2$), which actually represents the charge deposited on the connection node of the two current segments $Q = 1/j\omega(I_1 - I_2)$. That is why charge measurement is necessary for such cases.

Another problem left is that how to include charge density information in the modeling. Currents have already been measured and charge densities are another group of constraints for the currents. This makes the problem over determined. Here, we manage to modify the currents with the charge density with minimum changes on the currents.

Still taking the case in Fig. 2 as the example, the current vector $\boldsymbol{I} = [I_1; I_2; ...I_N]$ (the number of segments N=80 here) represents segment currents from left to right on the wire. The 1% error has been added to each element of $\boldsymbol{I}$. Then the charge density vector $\boldsymbol{Q} = [Q_1; Q_2; ...Q_{N-1}]$, which represents charges on connection nodes, could be obtained:

$$\mathbf{Q} = \frac{1}{j\omega}\mathbf{T}\mathbf{I}, \tag{5}$$

where

$$\mathbf{T} = \begin{bmatrix} 1 & -1 & & & \\ & 1 & -1 & & \\ & & \ddots & \ddots & \\ & & & 1 & -1 \end{bmatrix}_{(N-1)\times N}. \tag{6}$$

Assuming the measured charge density is $\boldsymbol{Q}'$, the modification current vector $\Delta\boldsymbol{I}$ could be obtained with

$$\boldsymbol{T}\Delta\boldsymbol{I} = \boldsymbol{Q}' - \boldsymbol{Q}. \tag{7}$$

Notably, (7) is an underdetermined equation. With the command $\Delta\boldsymbol{I} = \boldsymbol{T} \setminus (\boldsymbol{Q}' - \boldsymbol{Q})$ in Matlab, the minimum norm solution of $\Delta\boldsymbol{I}$ could be obtained, which means changes on the currents is minimized. After that, the modified current vector could be derived:

$$\boldsymbol{I}' = \boldsymbol{I} + \Delta\boldsymbol{I}. \tag{8}$$

The REs of electric field before and after the current modification are shown in Fig. 8. It could be seen that

the errors are effectively suppressed (about 20dB) at the field points close to the wire.

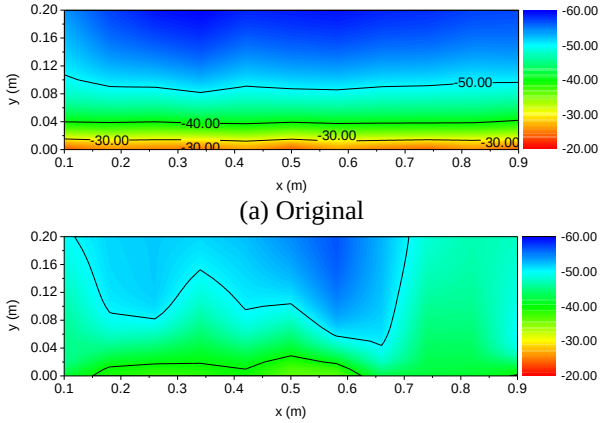

(a) Original

(b) Modified

Fig. 8. Relative errors (dB) of the field calculated with the original and modified currents at f =100MHz.

IV. ANOTHER REASON FOR CHARGE MEASUREMENT

The discussion above is all about the error caused by the lack of charge measurement, where we assume that the current along the whole transmission line could be measured. However, the measuring positions are usually limited in practice because of site conditions or time-consuming. In many cases, the measurement could only be done close to the source port. This is another reason for charge measurement, because we will see only current cannot determine the standing waveform of a transmission line. The charge information is also needed.

First of all, we must point out that for the common-mode of a transmission line system, the terminals are usually short or open. Therefore, standing-wave is the normal state. As shown in Fig. 9, if only the current value is known, how could we know the total current distribution is A, B or C?

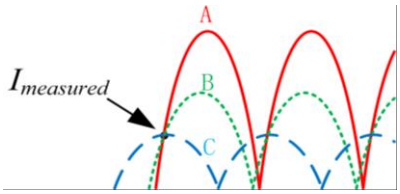

Fig. 9. Possible current distributions on a transmission line if current is measured at only one point.

However, if the charge is also known on the test point, the distribution could be determined. The spatial differentiation of current distribution $\boldsymbol{I}$ is related to charge distribution $\boldsymbol{\rho}$ with:

$$\frac{\partial}{\partial x}\boldsymbol{I} = j\omega\boldsymbol{\rho}, \tag{9}$$

which helps to determine the waveform. As shown in Fig. 10, the waveform could be determined as B (the green curve) this time. Therefore, charge measurement is also necessary in the conditions that measuring points are limited.

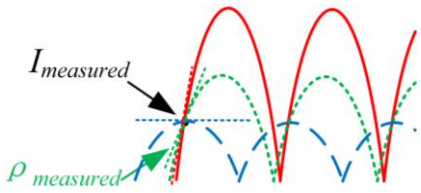

Fig. 10. The waveform could be determined with both $\boldsymbol{I}$ and $\boldsymbol{\rho}$ measured.

V. A PROPOSED METHOD FOR CM CHARGE MEASUREMENT

The current probe measures the total current (or the so-called common-mode current) by sensing the magnetic field surrounding the transmission lines. Similarly, the charge could be measured by testing electric field, which could be done by a near-field electric probe. However, there is another problem here. What we want is only the CM component, while measurement with the electric probe inevitably contains the DM component. To eliminate the DM component, a simple method is introduced here: adding a thin metal ring around the wires. Similar to a 'Faraday cage', the metal ring could sum up the charges on all wires, which could simultaneously eliminate the DM component and homogenize the CM component around the lines.

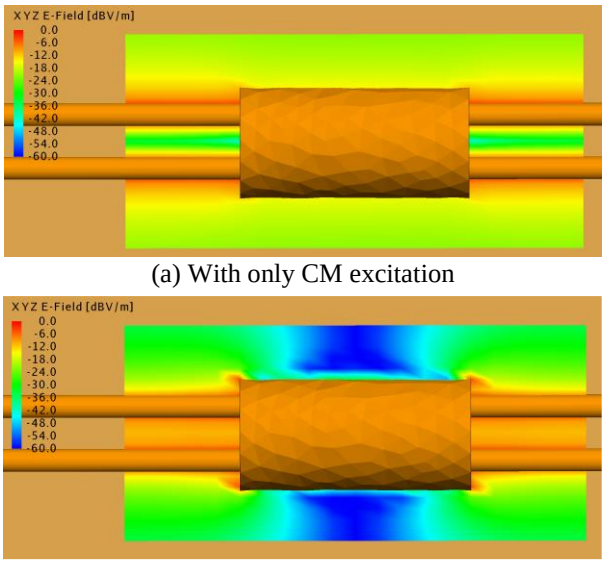

(a) With only CM excitation

(b) With only DM excitation

Fig. 11. Normalized field generated by only CM or DM component near the metal ring.

To indicate the effect of the metal ring, the near field of the wire pair with only CM or DM component is shown in Fig. 11 (simulated by FEKO). For the DM component, the ring suppress the field effectively, since we can see the field with the ring exceeds the field without the ring for about 10dB. While for the CM component, the ring has even no influence on the field value along the wire. This result proves that a circular metal ring with an electric field probe could be a possible device for charge measurement.

VI. CONCLUSION

This paper aims to discuss the necessity of charge measurement for the radiation evaluation of a transmission line. The key point here is whether current information is enough to accurately predict the near field. Usually we believe current is enough because charge information is implicitly included in current except DC. This assertion is right theoretically. However, the error transferred from current to charge could be very large, since the charge is determined by the difference of the current. The error transferred from the current to the field (or the charge) in a transmission line system is discussed in detail. And it is also proved that the error may be suppressed effectively if the charge information is added. Another reason for charge measurement is that only current cannot determine the whole standing wave along a transmission line and charge information is also needed. A possible method for charge measurement is also proposed in this paper.

In computational electromagnetics (CEM), current is also the data that usually used to characterize the potential radiation of transmission lines, such as in CST Cable Studio. However, it could be better to store or exchange both current and charge information for lower frequencies. Using only current means much higher accuracy of current is needed to represent the charge correctly. Moreover, note that current accuracy may not completely reflect the performance of a CEM method or software.

ACKNOWLEDGMENT

This work is sponsored by National Natural Science Foundation of China (No. 61771032) and Civil Aircraft Projects of China (No. MJ-2017-F-11).

REFERENCES

[1] K. W. Kam, A. Radchenko, and D. Pommerenke, "On different approaches to combine cable information into near-field data for radiated-field estimation," *IEEE Trans. Electromagn. Compat.*, vol. 56, no. 2, pp. 276-285, Apr. 2014.

[2] C. Su and T. H. Hubing, "Imbalance difference model for common-mode radiation from printed circuit boards," *IEEE Trans. Electromagn. Compat.*, vol. 53, no. 1, pp. 150-156, Feb 2011.

[3] T. Matsushima, T. Watanabe, Y. Toyota, R. Koga, and O. Wada, "Prediction of EMI from two-channel differential signaling system based on imbalance difference model," *2010 IEEE International Symposium on Electromagnetic Compatibility*, pp. 413-418, July 2010.

[4] H. Ke, K. Morishita, T. Hubing, N. Kobayashi, and T. Harada, "Modeling radiated emissions due to power bus noise from circuit boards with attached cables," *IEEE Trans. Electromagn. Compat.*, vol. 51, no. 2, pp. 412-416, May 2009.

[5] C. A. Nucci, F. Rachidi, and M. Rubinstein, "An overview of field-to-transmission line interaction," *ACES Newsletter*, vol. 22, no. 1, pp. 9-27, 2007.

[6] J. Jia, Z. Lai, J. Lei, and Q. Wang, "Stochastic Radiation Model for Cable Bundle with Random Wires," *ACES Journal*, vol. 31, no. 3, pp. 279-287, Mar. 2016.

[7] *MIL-STD-461F: Requirements for the Control of Electromagnetic Interference Characteristics of Subsystems and Equipment*, U.S. Dept. of Defense Std., 2007.

[8] *CISPR 25: Limits and Methods of Measurement for the Protection of Onboard Receivers*, 3rd, International Electrotechnical Commission (IEC) Std., 2008.

[9] R. F. Harrington, *Field Computation by Moment Methods*. IEEE Press Series on Electromagnetic Waves, New York: IEEE Press, 1993.

[10] C. R. Paul, *Analysis of Multiconductor Transmission Lines*. 2nd ed., New York: Wiley-IEEE Press, Oct. 2008.

[11] B. D. Popović, M. B. Dragović, and A. R. Djordjević, *Analysis and Synthesis of Wire Antennas*. New York: Research Studies Press, 1982.

Bing Li received the B.S. and Ph.D. degrees in Electronic and Information Engineering from Beihang University, Beijing, China, in 2011 and 2017, respectively. He currently works as a Post-doctoral Scholar with the School of Electronic and Information Engineering, Beihang University, Beijing, China.

His research interests include numerical modeling of transmission lines, field coupling analysis, and computational electromagnetics.

Xinwei Song received the B.S. and Ph.D. degrees in Electronic and Information Engineering from Beihang University, Beijing, China, in 2012 and 2018, respectively. She is currently a Lecturer with the School of Electrical and Information Engineering, University of Civil Engineering and Architecture, Beijing, China.

Her research interests include numerical modeling and measurements of transmission lines, and electromagnetic compatibility.

Donglin Su received the B.S., M.S., and Ph.D. degrees in Electronic Engineering from Beihang University (BUAA), Beijing, China, in 1983, 1986, and 1999, respectively. In 1986, she joined the Faculty of School of Electronics and Information Engineering, BUAA, where she is currently a Full Professor.

Her research interests include the numerical methods for microwave and millimeter-wave integrated circuits and systematic electromagnetic compatibility design of various aircrafts.

She is a senior member of the Chinese Institute of Electronics. She is the General Chair of 2018 International ACES Symposium. She is the Chair of Beijing Chapter of the IEEE Antennas and Propagation Society and the Deputy Chair of the Antennas Society, Chinese Institute of Electronics.

A Low-loss Wideband Filtering Coupler with Patterned Substrate Integrated Suspended Line (SISL) Technology

Li Ma [1], Yongle Wu*[1], Mingxing Li [2], Weimin Wang [2], and Yuanan Liu [2]

[1] State Key Laboratory of Information Photonics and Optical Communications, School of Electronic Engineering
Beijing University of Posts and Telecommunications, Beijing, 100876, China
mali2013@bupt.edu.cn, wuyongle138@gmail.com

[2] Department of Electronic Engineering, Beijing Key Laboratory of Work Safety Intelligent Monitoring
Beijing University of Posts and Telecommunications, Beijing, 100876, China
lmxdx1990@163.com, wangwm@bupt.edu.cn, yuliu@bupt.edu.cn

Abstract ─ A wideband filter-integrated coupler has been presented using the substrate integrated suspended line structure with patterned substrate. This coupler is composed of a two-line coupled line, two variant coupled lines, and four three-line coupled lines at each port. The SISL structure is composed of five print circuit boards, connected together by metal via holes. There is a hollowed substrate between two air cavities to reduce the loss. For further explanation, two wideband filtering SISL couplers operating at different operating frequencies with equal/unequal power divisions are designed and simulated, of which a specific coupler working at 1.66 GHz with a relative bandwidth of about 52.56% is fabricated and measured. The experimental results agree well with the theoretical and simulation ones. This proposed coupler has many advantages such as self-packaged, low loss, filter integration, arbitrary power division ratio, and inherent DC-block function.

Index Terms ─ Filtering coupler, microwave components, patterned substrate, substrate integrated suspended line (SISL), wide band.

I. INTRODUCTION

Branch-line coupler (BLC) has become an essential part in the RF/microwave circuits and systems, which has found a wide utilization in balanced power amplifier [1], balanced mixer [2], and frequency discriminator [3]. Nowadays, with the rapid development of 5G and satellite communication, multiple-antenna systems, such as isophoric sparse arrays [4] and massive MIMO arrays [5], have brought forward higher requirements on the feed network of antenna and antenna array. As a critical part of the feed network, BLC has been used for Butler matrix for beam forming network [6], exciting multiple modes of the multimode multi-element antenna [7], and so on. Thus, multi-function integration, such as filtering, power splitting/combining, unequal power-division ratio, flatness of amplitude and phase differences, has been more and more important for application, among which the filtering-integrated coupler has attracted more and more interests of researchers. The conventional method to realize filtering function is cascading filtering units with the coupler, for example, reference [8] uses net-type resonator to construct a rat-race coupler with bandpass response, and reference [9] utilized coupled resonator to design the filtering 180º hybrid. Recently, other technologies like substrate integrated waveguide (SIW) [10] and low temperature co-fired ceramic (LTCC) [11] are also introduced into the design of filtering coupler. But the aforementioned design methods cannot realize broad bandwidth, filtering function and low loss property at the same time.

The substrate integrated suspended line (SISL) structures [12-13] are composed of multi-layer print circuit boards. There are two air cavities on both sides of the core circuit, so the field of the circuit is mainly distributed in the air. Besides, the substrate of the core circuit is hollowed with specific shape. Thus, both the dielectric loss and the radiation loss of the suspended line are relatively smaller than the ones of microstrip line (ML) and strip line. In [12], a novel compact branch-line coupler has been designed using the SISL technology, and in [13], SISL and double-sided SISL (DSISL) inductors with patterned substrate are proposed. Compared with conventional metal-cavity structure, SISL technology has solved many problems, showing an excellent performance on cost, weight, support of the substrate, and so on.

In this paper, a wideband filter-integrated coupler using substrate integrated suspended line (SISL) technology has been designed, simulated, and fabricated. As an expansion of the authors' previous work in [14], we chose two specific couplers as examples to further explain the design and advantages of the SISL coupler. This coupler improved the origin transmission-line

Submitted On: September 25, 2018
Accepted On: December 27, 2018

structure in [15] for size reducing. Besides, with the help of the patterned SISL technology, loss can be narrowed. And the comparison of the losses between the proposed one and conventional one is also given. This low-loss SISL coupler can also realize filter integration, flexible power division ratio, and inherent DC-block function at the same time. Compared with the former work of the authors in [14], this work explains the design procedures in detail and provides two design examples with experimental result, in which the properties of this coupler such as low loss, flexible power division ratio, etc. have been verified. Besides, we discuss the influence of physical circuit parameters on the properties of the coupler and give the design procedures. The first SISL coupler named *Example A* works at 1.66 GHz with 7 dB power division, and the other named *Example B* is designed with 3.50 GHz operating frequency and equal power division. Both simulation and measured results coincide well with each other. Moreover, this low-loss wideband filtering BLC can be applied to many situations of wireless communication systems.

II. WIDEBAND FILTERING SISL COUPLER

The design method of the proposed wideband filter-integrated coupler can be divided into two parts. Firstly, we design and optimize the SISL structure according to the technology in [12]. Secondly, the basic circuit of the wideband filtering coupler is designed and discussed. Finally, we combine these two procedures together and take the overall simulation and optimization of the SISL coupler.

A. SISL structure

The SISL structure contains five double-side print circuit boards, which are fixed together by several screws as shown in Fig. 1. The five substrate layers, named as *Substrate* 1, 2, 3, 4, and 5, have created totally ten metal planes named as *G*1, *G*2, …, *G*10 from top to bottom. *Substrate* 1 and 5 act as electromagnetism shields for the SISL structure, with *G*1, 2, 9, and 10 being ground planes. *Substrate* 2 and 4 provide two air cavities on the upper and lower of the suspended circuit. The air cavities are actually a kind of open slot of the substrate, which are surrounded by via holes. *Substrate* 3 acts as the suspended substrate. The basic circuit of the wideband filtering coupler, which would be discussed in the next part, is etched on *G*5. The field of the circuit on *G*5 is mainly distributed on the two air cavities on *Substrate* 2 and 4, with a boundary brought by the metal holes surrounding the air cavities. The dielectric of *Substrate* 3 possesses low loss tangent and is hollowed according to the shape of the coupler, thus both radiation loss and substrate loss can be greatly reduced [13].

B. Core circuit of the wideband filtering coupler

The primary circuit of the broadband filter-integrated coupler on *G*3 is shown in Fig. 2. The coupler has both horizontally and vertically symmetric layout, composed of one two-line coupled line in the center, two deformed coupled lines at the top and bottom sides, and four three-line coupled lines connected to the ports. The coupler can also achieve wideband filtering function, inherent DC-block between the ports, and unequal power division. The power division ratio can be altered by tuning w_1 and w_2. For further explanation, two design examples with different design requirements have been designed and simulated.

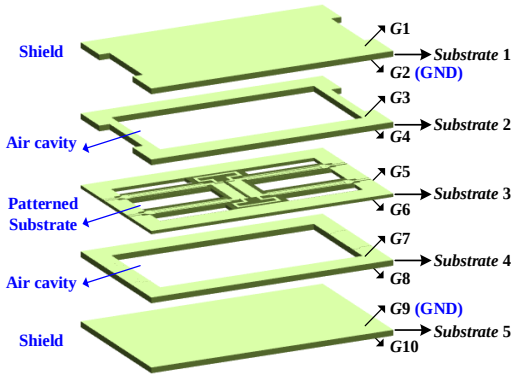

(a)

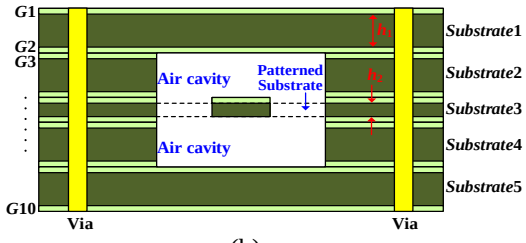

(b)

Fig. 1. The SISL construction of the proposed coupler: (a) 3D layout and (b) cross section.

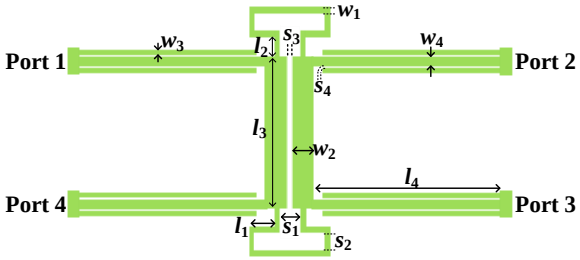

Fig. 2. The circuit configuration of the wideband filtering coupler.

III. DESIGN EXAMPLES

A. Example A

The first case of the SISL coupler named *Example A* works at 1.66 GHz with 7 dB power division, which

has been discussed in [14]. The material of *Substrate* 1, 2, 4, and 5 is chosen as FR-4, with the dielectric constant ε_r being 4.4, the thickness h_1 being 1.5 mm, and loss tangent being 0.02. *Substrate* 3 is designed to be F4B, whose dielectric constant ε_r being 2.65, the thickness h_2 being 0.254 mm, and loss tangent being 0.001.

When designing the specific structure of the SISL coupler, we define the demands of the coupler first, namely operating frequency and power division ratio. The operating frequency of the coupler is related to the lengths of the coupled lines. When the working frequency of a specific coupler is determined, the lengths of l_1, l_2, l_3, and l_4 can be defined. Considering that the power division ratio is affected mainly by the width of w_1 and w_2, they can be determined by repeated simulations using ADS Momentum. Then other parameters will be chosen by the optimization of HFSS Optimetrics Analysis.

Then the physical parameters of the *Example A* can be defined as follows (with units of mm): w_1=1, l_1=3.5, l_2=3, s_1=2, s_2=2, w_2=5, l_3=30, s_3=0.2, w_3=0.8, w_4=1.4, l_4=33, s_4=0.2, w_a=33, l_a=8, w_b=35, l_b=19, w_c=85.8, l_c=52. The structure of *Example A* is illustrated in Fig. 3, in which the total configuration of the SISL structure is shown in Fig. 3 (a), while the circuit of the coupler is shown in Fig. 3 (b). The simulated results are given in Fig. 4 [14]. From these curves, we can see that this coupler can realize wideband filtering function and possesses flat phase difference. The relative bandwidth is about 52.56% with S_{11} lower than -15 dB.

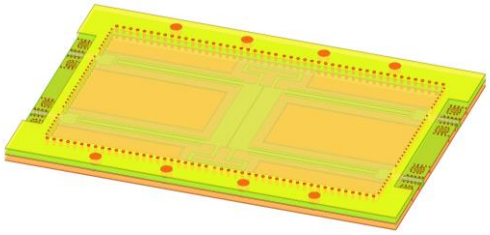

(a)

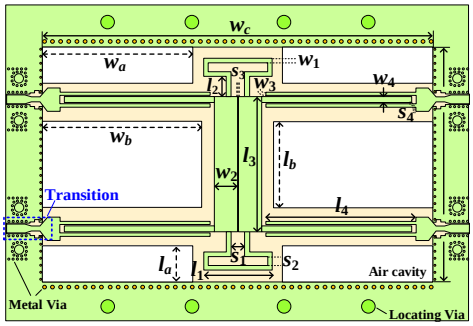

(b)

Fig. 3. The constructions of *Example A*. (a) The overall structure, and (b) the main circuit of the coupler on *G*3.

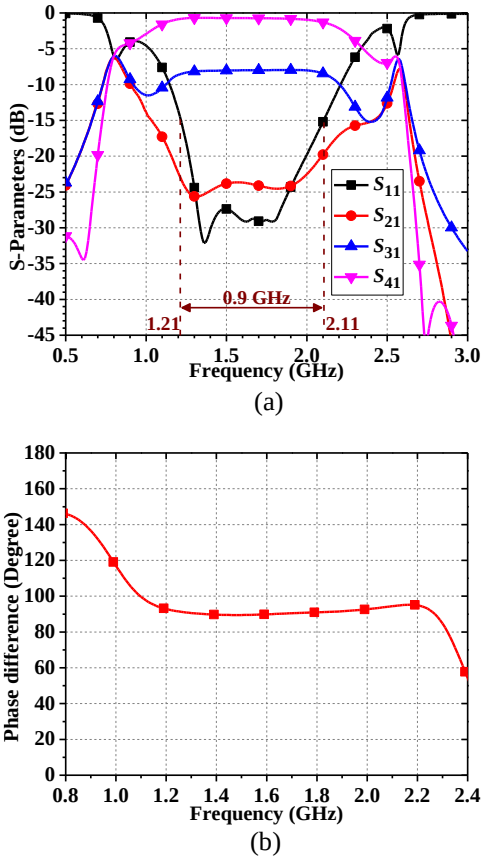

(a)

(b)

Fig. 4. The calculated results of *Example A* [14]. (a) The S-parameters, and (b) phase difference.

The loss of the coupler can be defined as [12],

$$Loss = 1 - |S_{11}|^2 - |S_{21}|^2 - |S_{31}|^2 - |S_{41}|^2. \quad (1)$$

Then we calculate the losses of the designed SISL coupler and conventional microstrip line coupler, which are shown in Fig. 5 [14] for comparison. As we can see, the SISL coupler has a lower loss than the microstrip line one.

The relationship between the power division ratio and the line width of w_1 and w_2 would be further discussed. As shown in Fig. 6, as the increasing of w_1, the power division ratio will decrease. While in Fig. 7, the variation trend of the power division ratio along with the line width w_2 is contrary to the one in Fig. 6. That is, the power division ratio increases with the increasing of the line width w_2.

B. Example B

When designing *Example B*, equal power division and higher operating frequencies are considered. The substrate and configuration of the multi-layer structure are chosen to be the same as those in *Example A*. The physical parameters of the *Example B* can be simulated and optimized by ADS Momentum and HFSS as follows

(with units of mm): w_1=2.5, l_1=3, l_2=2, s_1=2, s_2=1.7, w_2=3.5, l_3=17, s_3=0.2, w_3=0.8, w_4=1.3, l_4=20, s_4=0.2, w_a=20, l_a=8, w_b=22, l_b=12.5, w_c=57.8, l_c=37.4. The SISL structure of the *Example B* is shown in Fig. 8 (a), while the circuit of the coupler is shown in Fig. 8 (b).

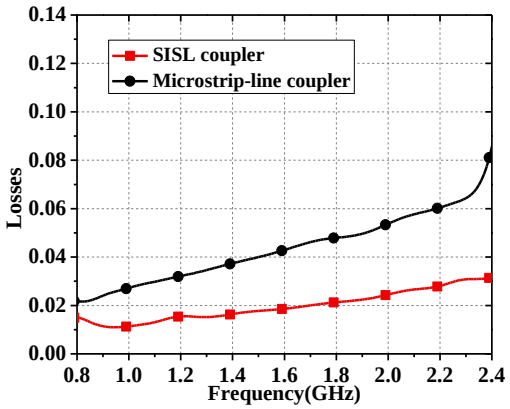

Fig. 5. The losses of SISL coupler and ML coupler [14].

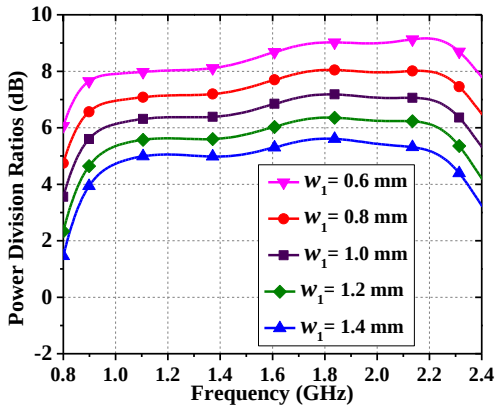

Fig. 6. The power division ratios of the SISL coupler width varies w_1 when w_2 = 5 mm.

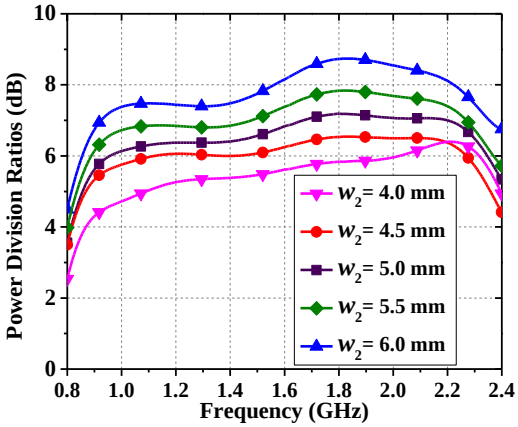

Fig. 7. The power division ratios of the SISL coupler width varies w_2 when w_1 = 1 mm.

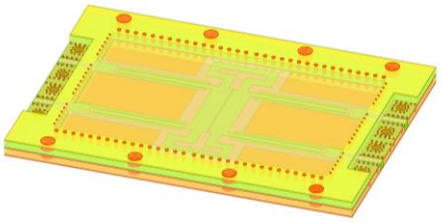

(a)

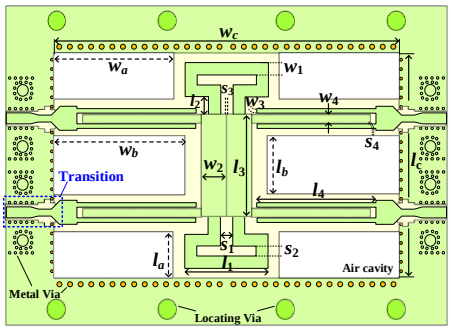

(b)

Fig. 8. The constructions of *Example B*. (a) The overall structure, and (b) the main circuit of the coupler on *G*3.

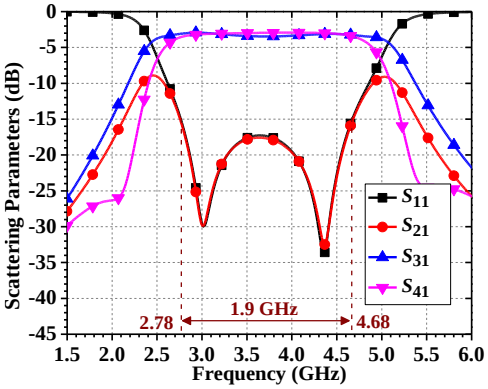

(a)

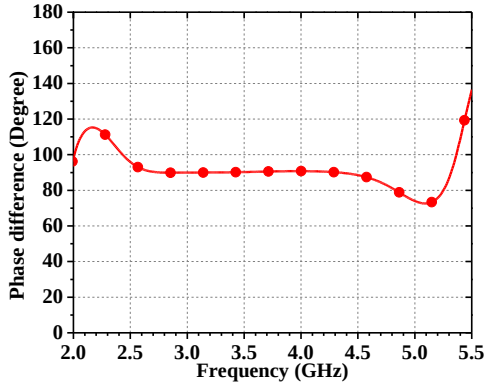

(b)

Fig. 9. The calculated results of *Example B*. (a) The S-parameters, and (b) phase difference.

The simulated scattering parameters and phase difference are shown in Figs. 9 (a) and (b), respectively. It can be observed that this coupler possesses a relative bandwidth of 54.28% with S_{11} lower than -15 dB and a flat phase difference. So, the wideband filtering coupler has been realized.

IV. MEASURED RESULTS

In order to verify the performance of the SISL wideband filer-integrated coupler, we take *Example A* as an experimental case. The design parameters of the coupler are all the same as those explained in Section III.A. The photograph of the fabricated SISL coupler is illustrated in Fig. 10. The size of the coupler is about 110.2×70×6.254 mm^3. Figures 11 (a) and (b) are the simulated and measured S-parameters and phase differences of the coupler in *Example A*, separately. As we can see from the figures, the coupler works at 1.66 GHz, with a power division of about 7 dB. The coupler has good matching and isolation and possesses a relative bandwidth of about 49.398% with S_{11} lower than -15 dB. In addition, the major features and advantages of this SISL wideband filtering BLC compared with other reported ones are listed in Table 1.

V. CONCLUSION

In this paper, a compact wideband filter-integrated coupler is designed, simulated and fabricated using the patterned substrate integrated suspended line technology. The design and optimization procedures of the coupler have been explained in detail, and two cases with different operating frequencies of 1.66/3.5 GHz and unequal/equal power division ratios were designed as examples. The loss of the designed couplers was greatly reduced compared with that of traditional ones. Then for further verification, a specific SISL coupler working at 1.66 GHz with 7 dB power division and 52.56% relative bandwidth was designed and fabricated. The measured scattering parameters and phase difference coincided well with the theory and the simulated results. This coupler has the advantages such as self-package, low loss, filter integration, and flexible power division ratio, which is propitious to the applications in the microwave circuits and wireless communication systems.

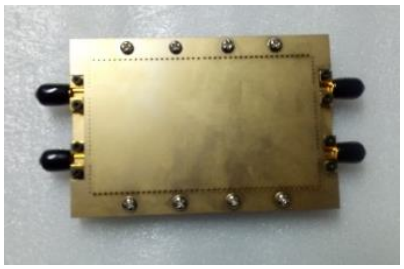

Fig. 10. The photograph of the SISL coupler.

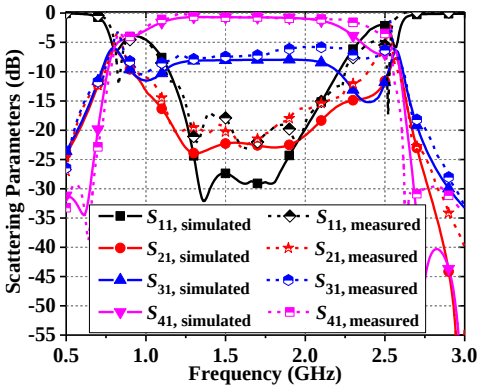

(a)

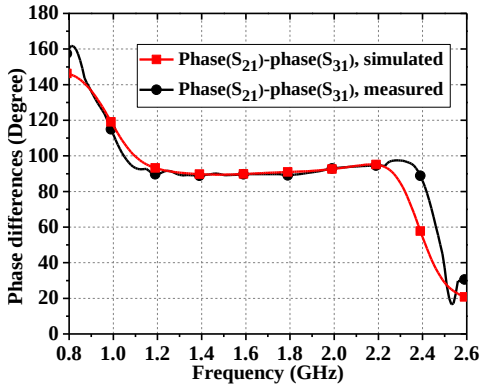

(b)

Fig. 11. The simulated and measured results of the wideband filtering SISL coupler. (a) The S-parameters, and (b) phase difference.

Table 1: Performance comparison of the proposed SISL wideband filtering BLC with other reported ones

Refs.	BW*	IL (dB)	Technology	Self-Packaged
[8]	19%	1.38	PCB	No
[9]	10%	0.7	PCB	No
[10]	2.5%	1.9	SIW	No
[11]	8.6%	1.8	LTCC	Yes
This work	49.398%	0.655	SISL	Yes

*: with return loss < -15 dB.

ACKNOWLEDGMENT

This work was supported in part by National Natural Science Foundations of China (No. 61671084, and No. 61821001), Guangzhou Major Projects of Industrial Technology of China (Research and Development of Large-scale Multi-beam Antenna Array for 5G Massive MIMO Communication). This paper is an expanded version from the International Applied Computational Electromagnetics Society (ACES) Symposium, Beijing, China, July 2018 [14].

REFERENCES

[1] A. Grebennikov, *RF and Microwave Power Amplifier Design*. New-York: McGraw-Hill, 2015.

[2] H. Ebrahimian, M. Ojaroudi, N. Ojaroudi, and N. Ghadimi, "Distributed diode single-balanced mixer using defected and protruded structures for doppler radar applications," *Applied Computational Electromagnetics Society (ACES) Journal*, vol. 30, no. 3, pp. 313-318, Mar. 2015.

[3] S. Moon, I. Yom, and H. Lee, "K-band phase discriminator using multiport downconversion for monopulse tracker," *IEEE Microw. Wireless Compon. Lett.*, vol. 27, no. 6, pp. 599-601, June 2017.

[4] A. F. Morabito and P. G. Nicolaci, "Optimal synthesis of shaped beams through concentric ring isophoric sparse arrays," *IEEE Antennas Wireless Propag. Lett*., vol. 16, pp. 979-982, Oct. 2017.

[5] B. Yang, Z. Yu, Y. Dong, J. Zhou, and W. Hong, "Compact tapered slot antenna array for 5G millimeter-wave massive MIMO systems," *IEEE Trans. Antennas Propag*., vol. 65, no. 12, pp. 6721-6727, Dec. 2017.

[6] S. Karamzadeh, V. Rafii, M. Kartal, and B. Virdee, "Modified circularly polarised beam steering array antenna by utilised broadband coupler and 4×4 butler matrix," *IET Microw., Antennas Propag.*, vol. 9, no. 9, pp. 975-981, June 2015.

[7] D. Manteuffel and R. Martens, "Compact multimode multielement antenna for indoor UWB massive MIMO," *IEEE Trans. Antennas Propag*., vol. 64, no. 7, pp. 2689-2697, July 2016.

[8] W.-H. Wang, T.-M. Shen, T.-Y. Huang, and R.-B. Wu, "Miniaturized rat-race coupler with bandpass response and good stopband rejection," in *IEEE MTT-S Int. Microw. Symp. Dig.*, Boston, MA, USA, pp. 709-712, June 2009.

[9] C. Lin and S. Chung, "A compact filtering 180˚ hybrid," *IEEE Trans. Microw. Theory Tech*., vol. 59, no. 12, pp. 3030-3036, Dec. 2018.

[10] Y. Cheng and Y. Fan, "Compact substrate-integrated waveguide bandpass rat-race coupler and its microwave applications," *IET Microw. Antennas Propag.*, vol. 6, no. 9, pp. 1000-1006, June 2012.

[11] K. Wang, X. Liu, Y. Li, L. Lin, and X. Zhao, "LTCC filtering rat-race coupler based on eight-line spatially-symmetrical coupled structure," *IEEE Access*, vol. 6, pp. 262-269, 2018.

[12] Y. Wang, K. Ma, and S. Mou, "A compact branch-line coupler using substrate integrated suspended line technology," *IEEE Microw. Wireless Compon. Lett.*, vol. 26, no. 2, pp. 95-97, Feb. 2016.

[13] L. Li, K. Ma, and S. Mou, "Modeling of new spiral inductor based on substrate integrated suspended line technology," *IEEE Trans. Microw. Theory Tech.*, vol. 65, no. 8, pp. 2672-2680, Aug. 2017.

[14] L. Ma, Y. Wu, C. He, W. Wang, and Y. Liu, "A wideband filter-integrated coupler using substrate integrated suspended line (SISL) technology with patterned substrate," in *International Applied Computational Electromagnetics Society (ACES) Symposium*, July 2018.

[15] Y. Wu, L. Jiao, Y. Du, and Y. Liu, "Wideband filter-integrated coupled-line coupler with unequal power division and inherent DC-block function," *Microw. Opt. Technol. Lett.*, vol. 58, no. 1, pp. 121-123, Jan. 2016.

Li Ma received the B.S. degree in Electronic Science and Technology from Beijing University of Posts and Telecommunications (BUPT), Beijing, China, in 2017, where she is currently pursuing the Ph.D. degree. In September 2017, she started her research as a graduate at BUPT. Her research interests include microwave passive components and multi-layer technology.

Yongle Wu received the B.Eng. degree in Communication Engineering and the Ph.D degree in Electronic Engineering from Beijing University of Posts and Telecommunications (BUPT), Beijing, China, in 2006 and 2011, respectively. From April to October in 2010, he was a Research Assistant at the City University of Hong Kong, Kowloon, Hong Kong. In 2011, he joined the BUPT and becomes currently a Full Professor in the School of Electronic Engineering. His research interests include microwave components and wireless systems design.

Mingxing Li received his B.S. degree in College of Information Science and Technology from Henan University of Technology (HAUT), Zhengzhou, China, in 2015. In September 2015, he started his research as a graduate at BUPT and is currently working toward the Ph.D. degree at the same university. His research interests include microwave passive components, RF and radar systems.

Weimin Wang received the B.S. degree in Communication Engineering, the M.S. degree in Electromagnetic Field and Microwave Technology and the Ph.D degree in Electronic Science and Technology from Beijing University of Posts and Telecommunications (BUPT), Beijing, China, in 1999, 2004 and 2014, respectively. In 2014, she joined BUPT. She is currently a Lecturer in the School of Electronic Engineering, BUPT. Her research interests include electromagnetic field and MIMO OTA measurement.

Yuanan Liu received the B.E., M.Eng., and Ph.D. degrees in Electrical Engineering from University of Electronic Science and Technology of China, Chengdu, China, in 1984, 1989 and 1992, respectively. In 1984, he joined the 26th Institute of Electronic Ministry of China to develop the inertia navigating system. In 1992, he began his first Post-doctor position in EMC lab of Beijing University of Posts and Telecommunications (BUPT), Beijing, China. In 1995, he started his second Post-doctor in Broadband Mobile Lab of Department of System and Computer Engineering, Carleton University, Ottawa, Canada. From July, 1997, as Professor, he is with Wireless Communication Center of College of Telecommunication Engineering, BUPT, Beijing, China, where he is involved in the development of next-generation cellular system, wireless LAN, Bluetooth application for data transmission, EMC design strategies for high speed digital system, and Electromagnetic interference (EMI) and Electromagnetic Susceptibility (EMS) measuring sites with low cost and high performance.

A Study on Equivalent Circuit Model of RF Discharge Based on Multi-Physics Field

Xinkai Fu, Fei Dai*, and Ruitao Hu

School of Electronic and Information Engineering
Beihang University, Beijing, 100191, China
*daphige@buaa.edu.cn

Abstract ─ Belongs to EMC problems, the equivalent circuit model of RF discharge is studied. By establishing the correlation between circuit parameters of equivalent circuit and plasma characteristics, this paper conducts a brief analysis on the RF discharge mechanism with different frequencies.

Index Terms ─ Equivalent circuit model, multi-physics simulation, RF discharge.

I. INTRODUCTION

Once loses control and precaution, excessive electromagnetic energy not only cause electromagnetic interference, but also have a damaging effect on some specific targets, which is generally known as hazards of electromagnetic radiation. The US military standard MIL-STD-464C [1] has proposed HERF (Hazards of electromagnetic radiation to fuel), but the mechanism of HERF still lacks in-depth studies yet.

HERF is an interactive result of multiple physical fields including electromagnetism, plasma science, combustion science, hydrodynamics and thermodynamics. From the macroscopic chronological perspective of the interaction, the mechanism of HERF can be roughly divided into three processes: electromagnetic coupling, discharge and ignition. When the discharge coupled by electromagnetic is sufficient to ignite, the HERF problem will occur and cause unpredictable damage.

There is still a lot of work about the hazard mechanism of HERF like electromagnetic coupling, discharge and combustion, and the RF discharge is one of the keys. Since the discharge of HERF comes from electromagnetic coupling instead of ESD (electro-static discharge), this process belongs to RF discharge. The breakdown characteristic of RF discharge is very different from ESD due to different frequency. There is a critical frequency during RF breakdown process [2]:

$$f_{c0} = \frac{\mu_e E}{\pi d}, \tag{1}$$

where E is the amplitude of the alternating electric field, d is the distance between the gap and μ_e is the electron mobility. While the frequency is higher than f_{c0}, free electrons cannot reach the electrode before the polarity of the electric field changes, which may reduce the electron dissipation rate, and change the breakdown characteristics. However, the specific regular of this process is unclear yet.

To quantitatively study the characteristics of RF discharge, it is necessary to extract core parameters of the discharge. Many scholars have carried out research [3-5] and experiments [6-9] on the relationship between the discharge parameters and the circuit parameters including voltage, current, equivalent plasma resistance from voltage and current. But these equivalent circuit models of discharge are conductivity models, which are only suitable for DC discharge, and not suitable for the RF discharge problem discussed in this paper.

According to the previous qualitative research [10] and reference [11], RF discharges have different physical characteristics with different frequencies. As the definition of current and electron, current can evaluate the characteristics of electron number density during RF discharge.

Aiming to overcome the quantitative research of RF discharges, this paper studies and analyzes the breakdown characteristic of RF discharge under the same amplitude with different frequency. Because the traditional electromagnetic simulation software cannot calculate the discharge breakdown model, multi-physics simulation software COMSOL is selected. This paper gives the calculation method of the equivalent AC capacitance form the discharge structure considering a typical structure of aircraft fuel tank oil-inlet and nozzle. By analyzing the equivalent circuit, the gas conductivity can be clearly seen and the discharge characteristic under different frequencies can be obtained. Finally, the breakdown characteristics of RF discharge in the whole frequency band are analyzed and summarized through a large number of simulations.

Submitted On: October 15, 2018
Accepted On: January 26, 2019

II. EQUIVALENT CIRCUIT MODEL BASED ON ELECTROMAGNETIC FIELD THEORY

A. Equivalent circuit model

Unlike the stable electric field of DC discharge, the electric field of the RF discharge is alternating where the frequency determines the characteristics of the breakdown process. After the RF discharge occurs, the gas medium has a capacitive effect because of the RF electromagnetic field, so the equivalent circuit structure of RF discharge is different from the DC discharge.

In addition to the conductance component of the plasma gas, there is the AC capacitance component equivalent from the high frequency electromagnetic structure. So, the equivalent circuit structure of the RF discharge is a capacitor parallel conductance circuit like Fig. 1.

According to the characteristics of the parallel circuit, the total terminal current is divided into two parts:

1) The current of the capacitor is the displacement current, which is generated by the neutral medium after the breakdown of the gas. While the electron density of gas is small, the displacement current can be constant during the breakdown process;

2) The current of the conductance is the electron current, which is generated by the free electron motion after breaking down. The conductance can characterize the plasma characteristics of gas breakdown discharge. The equivalent conductance in this paper can be calculated from the total terminal current, excitation voltage and equivalent capacitance, and it is one of the most important parameters.

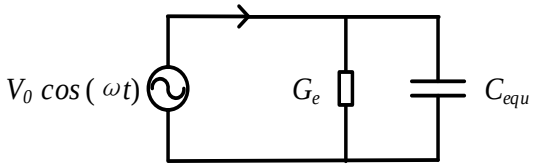

Fig. 1. The equivalent circuit model of RF discharge.

B. Equivalent AC capacitor structure

There are three necessary conditions for the accidental ignition of fuel by electromagnetic radiation [12]: proper ratio of fuel vapor and air, discharge produced by Electromagnetic radiation which has enough length and heat to ignition. These conditions indicated that HERF may occur in the gap between the carrier aircraft fuel tank oil-inlet and nozzle.

Referring to the structure of aircraft fuel tank oil-inlet and nozzle [13-14], two concentric cylindrical plates are selected as the two poles of discharge reactor. With a thin layer of dielectric attached on the metal surface of fuel tank oil-inlet and nozzle, two dielectric plates are added outside the gap to compose the model like Fig. 2. The electromagnetic field between the two cylindrical electrode plates is approximately uniform in the θ direction.

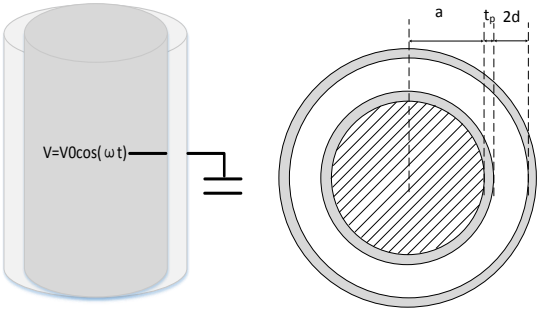

Fig. 2. Cross-sectional structure of the cylinder.

The inside radius of cylindrical plate a is 145mm, the dielectric layer thickness t_p is 0.1mm, the gap between aircraft fuel tank oil-inlet and nozzle $2d$ is 1.8mm and the length of the cylinder l is 150mm. Since l is much longer than the gap $2d$, the edge effect of electromagnetic field distribution can be ignored in the simulation process. So, the three-dimensional simulation model can be simplified to one-dimensional axisymmetric model.

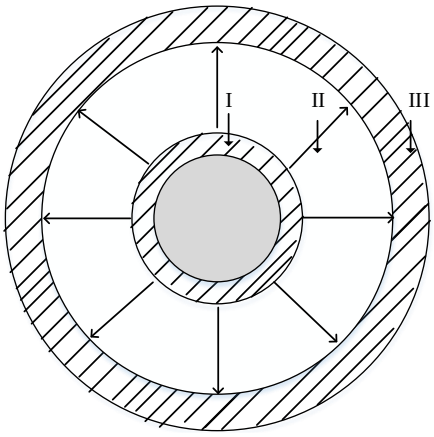

Fig. 3. The gap structure of the cylinder when $z = l/2$.

The gap structure can be simplified as the cross-sectional distribution when $z = l/2$ like Fig. 3, half of the distance between two plates is d, and the thickness of plates is t_p. Because no free charge distributes in I, II and III regions, the field line of electric displacement vector should be continuous, and it is easy to know that the modulus of electric displacement vector in region I, II, and III regions is inversely proportional to the radius:

$$|D| = \frac{A}{r}, \tag{2}$$

where D is the electric displacement vector, A is a constant and r is the radius.

So, the electric fields in the direction of the r-axis can be calculated:

$$E_{\mathrm{I}} = E_{\mathrm{III}} = \frac{A_1}{r}, \tag{3}$$

$$E_{\mathrm{II}} = \frac{A_2}{r}, \tag{4}$$

where $E_{\mathrm{I}}, E_{\mathrm{II}}, E_{III}$ are the electric fields of the three region.

Here are the boundary conditions in z = 0:

$$V_0 = -\int_0^{2d+2t_p} E_r(z,t)|_{z=0} dr, \tag{5}$$

$$D_I|_{r=\mathrm{a}+t_p} = \varepsilon_0\varepsilon_r E_I = \varepsilon_0\varepsilon_g E_{II} = D_{II}|_{r=a+t_p}. \tag{6}$$

The key parameter can be calculated:

$$\begin{cases} A_1 = \dfrac{V_0}{ln\frac{(a+t_p)+(a+2t_p+2d)}{a(a+t_p+2d)} + \frac{\varepsilon_r}{\varepsilon_g} ln\frac{(a+t_p+2d)}{(a+t_p)}} \\ A_2 = \dfrac{\varepsilon_r}{\varepsilon_g} A_1 \end{cases}, \tag{7}$$

where V_0 is the amplitude of the excitation voltage, a, t_p, d are the structural parameters as Fig. 2 shown, ε_g is the relative dielectric constant of the gas and ε_r is the relative dielectric constant of the dielectric layer. In this paper, ε_g is 1 and ε_r is 10.

Terminal voltage and terminal current are obtained by integration of electric and magnetic fields in the gap:

$$\begin{aligned} \mathrm{u} &= \int_a^{a+2t_p+2d} E_r dr \\ &= \left[\mathrm{A}_1 \ln\frac{(a+t_p)(a+2t_p+2d)}{a(a+t_p+2d)} \cos\left(\beta_r \frac{l}{2}\right) + \right. \\ &\left. \mathrm{A}_2 \ln\frac{a+t_p+2d}{a+t_p} \cos\left(\beta_g \frac{l}{2}\right)\right] \cos\omega t, \end{aligned} \tag{8}$$

$$\mathrm{i} = -2\int_0^{2\pi} H_\theta r d\theta = -\frac{4\pi A_1}{\eta_r} \sin\left(\beta_r \frac{l}{2}\right) \sin\omega t. \tag{9}$$

According to the AC capacitance theory [15], with the increase of the frequency, different order Taylor expansions of the trigonometric function can obtain different equivalent circuit model. For example, the first-order approximation is a capacitance model, and the second-order approximation is a capacitive-inductor series circuit model.

Take the first-order approximation as an example and put the structural parameters into the equation. The first-order approximate cut-off frequency calculation result is 60MHz and the capacitance is 0.669nF:

$$\beta_r \frac{l}{2} < 5\% \cap \beta_g \frac{l}{2} < 5\%, \tag{10}$$

$$\mathrm{C} = \frac{2\pi\varepsilon_0\varepsilon_r l}{\ln\frac{(a+t_p)(a+2t_p+2d)}{a(a+t_p+2d)} + \frac{\varepsilon_r}{\varepsilon_g}\ln\frac{a+t_p+2d}{a+t_p}}. \tag{11}$$

The equivalent conductance is calculated from the terminal current and capacitance by multi-physics simulation results, and it is affected by the degree of ionization. Therefore, the RC equivalent circuit can identify discharge breakdown characteristics. The conductance represents the degree of ionization between the gap, and the terminal current represents the discharge characteristics.

III. RF DISCHARGE MECHANISM

A. Parameters of simulation model

The plasma module of multi-physics simulation in COMSOL was selected to analyze the mechanism of RF discharge [16]. The excitation signal is $\mathrm{V} = -600[\mathrm{V}]\sin(\omega t)$, the gaseous pressure is 1 atmosphere and the temperature is 400K [17].

According to research, the conductance of the equivalent circuit model grows in proportion to the frequency, which means that the degree of ionization is proportional to the frequency. And there are five different breakdown physical characteristics found under the same excitation voltage with different frequency.

B. Terminal current

Referring to the foregoing analysis, the waveform of the total terminal current on the electrode can represent the breakdown characteristic of discharge and determine whether breakdown occurs and analyze the degree of ionization.

According to the simulation results below, the first-order approximate cut-up frequency of the equivalent capacitance, there are five different waveforms of the terminal current generated by the excitation of 600V, representing different breakdown characteristics.

1) 1 Hz ~ 23.4 kHz: as shown in Fig. 4, the terminal current from simulation result is completely consistent with the analytical solution of the extracted capacitor, which means that the current of the equivalent conductance component is almost negligible and there is no breakdown.

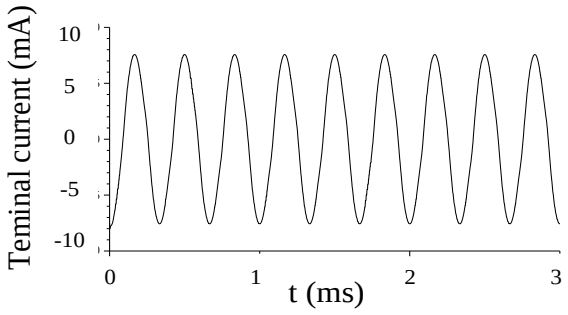

Fig. 4. Terminal current at 3kHz.

2) 23.4 kHz ~ 120 kHz: compared with the values above, the cyclical mutation of terminal current illustrates cyclical discrete breakdown. There is a process of breakdown, maintenance, and extinction during every half cycle like Fig. 5.

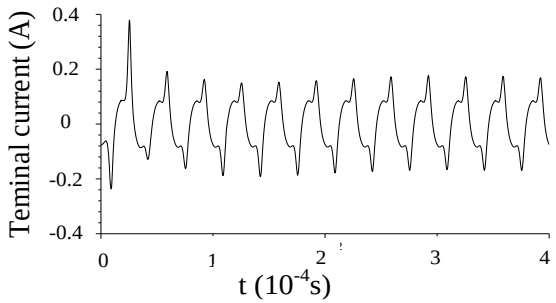

Fig. 5. Terminal current at 30kHz.

3) 120 kHz ~ 1.5 MHz: as shown in Fig. 6, the duration of breakdown per half cycle is getting longer and longer, until the plasma from collision is enough to maintain a continuous breakdown the excitation of 600V.

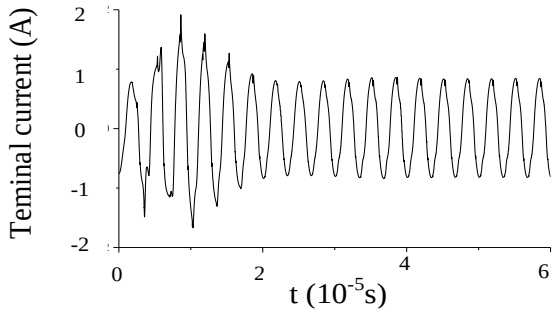

Fig. 6. Terminal current at 300kHz.

4) 1.5 MHz ~ 12 MHz: Fig. 7 indicates that the continuous collision of electrons will accumulate more new electrons, which may increase the ionized plasma over time. The initial current value is the same as the displacement current, which means that the accumulated plasma is not enough to breakdown argon at the initial stage of accumulation effect.

Under this special accumulation effect, the breakdown process is gradual and there is no clear breakdown state. It is necessary to determine a certain threshold to judge whether electrons are accumulated enough.

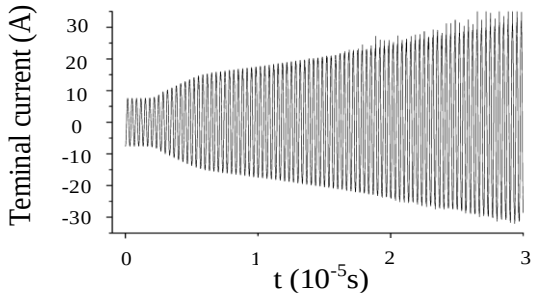

Fig. 7. Terminal current at 3MHz.

5) 12 MHz ~ 60 MHz: as shown in Fig. 8, under these frequencies, the accumulation effect will lead to a qualitative change while it reaches a certain level, which is called electron avalanche effect breakdown. The ionization of electrons will suddenly intensify when electron avalanche effect breakdown occurs.

It is worth noting that the cut-off frequency calculated by the Equation (1) is 12.1 MHz, which is the same as the multi-physics simulation result, the accuracy of the plasma portion can be verified.

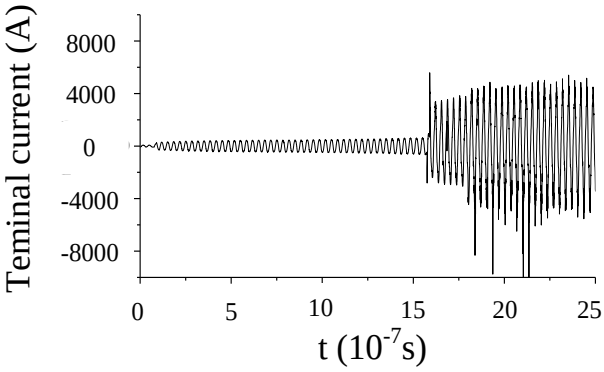

Fig. 8. Terminal current at 30MHz.

C. Equivalent conductance

The equivalent conductance of the ionized gas can be solved based on the total terminal current and the displacement current. The conductance can analyze the conductivity of the plasma and the breakdown characteristics. Following is a brief analysis from conductance.

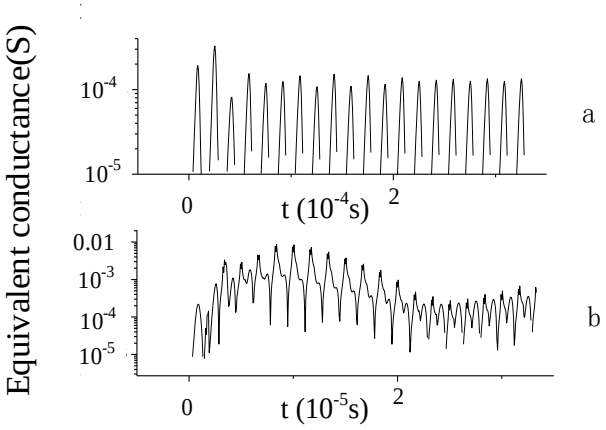

Fig. 9. Conductance of cyclical discrete breakdown at 30kHz (a), and continuous breakdown at 300kHz (b).

Figure 9 indicates the case of periodic discrete breakdown and continuous breakdown. During the cyclical discrete breakdown process, the conductance changes discretely between a small conductance at breakdown and infinitesimal conductance at unbroken.

Under the condition of the continuous breakdown, the gas remains in a conductive state, and the conductivity at larger magnitude of the excitation voltage is greater than when the amplitude is small.

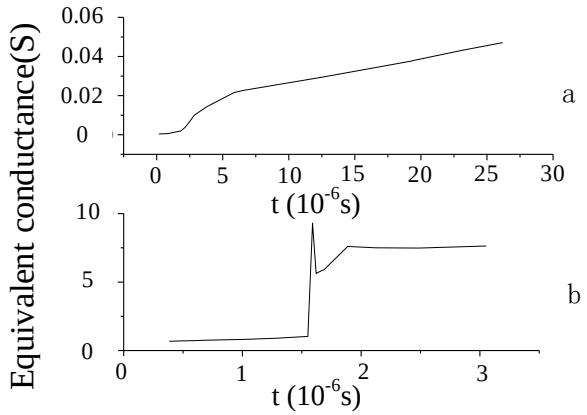

Fig. 10. Conductance of accumulation effect at 3MHz (a), and avalanche effect at 30MHz (b).

As shown in Fig. 10, during the cumulative effect and avalanche effect breakdown process, the conductivity of the gas gradually increases with the breakdown process at the same excitation voltage amplitude. This proves the most essential difference between RF discharge and DC discharge, and that RF discharge is more harmful to the HERF problem.

IV. CONCLUSION

A method of multi-physics simulation is proposed to analyze the mechanism of RF discharge. Through the equivalent models, some important conclusions can be obtained by simulation results.

When the structure of Aircraft Fuel Tank oil-inlet and Nozzle is coupled by the RF field, its electromagnetic structure can be equivalent to different orders LC circuit under different frequency.

There are different breakdown characteristics with different frequencies at the same excitation voltage, and the characteristics can be analyzed by the equivalent circuit. In general, the higher the frequency, the breakdown will be easier, and the degree of ionization will be higher.

Research shows that there are five different breakdown states under different frequencies excited at 600V. With cumulative effect, high frequency discharge process appears above 1MHz, the degree of ionization changes significantly. With electron avalanche effect, high frequency discharge process appears above 10MHz, the degree of ionization will suddenly intensify nearly 10 times. And these situations are related to the breakdown time.

ACKNOWLEDGMENT

This work is supported in part by the National Natural Science Foundation of China. (Grant No. 61571027, 61427803), and supported by the 2011 Collaborative Innovation Center.

REFERENCES

[1] MIL-STD-464C, Electromagnetic environmental effects requirements for systems, pp. 11-17, 2010.

[2] X. Xueji and Z. Dingchang. *Gas-Discharge-Physics*. Fudan University Press, pp. 268-292, 1996.

[3] M. A. Lieberman, "Analytical solution for capacitive RF sheath," *IEEE Trans. Plasma Sci*., vol. PS-16, pp. 638444, 1988.

[4] V. A. Godyak and N. Stemberg, "Dynamic model of the electrode sheaths in symmetrically driven RF discharges," *Phys. Rev. A*, vol. 42, pp. 2299-2312, 1990.

[5] M. A. Lieberman and S. E. Savas, "Bias voltage in finite length, cylindrical and coaxial radio-frequency discharges," J. *Vacuum Sci. Technol*., vol. A8, pp. 1632-1641, 1990.

[6] C. M. Horwitz, "RF sputtering voltage division between two electrodes," *J. Vacuum Sci. Technol*., vol. AI, pp. 60-68, 1983.

[7] A. J. Van Roosmalen, "Plasma parameter estimation from RF impedance measurements in a dry etching system," *Appl. Phys. Lett*., vol. 42, pp. 416-418, 1983.

[8] A. I. Van Roosmalen, W. G. M. van den Hoek, and H. Kalter, "Electrical properties of planar RF discharges for dry etching," *J. Appl. Phys*., vol. 58, pp. 653458, 1985.

[9] K. D. Allen, H. H. Sawin, M. T. Mocella, and M. W. Jenkins, "The plasma etching of polysilicon with CFsCVargon discharges: I. Parametric modeling and impedance analysis," *J. Electrochem. Soc*., vol. 133, pp. 2315-2325, 1986.

[10] X. Feng, F. Dai, and X. Fu, "A study on the mechanism of hazards of high intensity radiated field to fuel based on multi-physics field," *Progress in Electromagnetics Research Symposium IEEE*, Fall 2018.

[11] X. Feng and F. Dai, "A study on RF discharge characteristics of argon in multi-physics field," *Applied Computational Electromagnetics Society Symposium IEEE*, 2017.

[12] C. Qiong, *Electromagnetic Compatibility Engineering Handbook*. Beijing, National Defense Industrial Press, pp. 196-200; 1255-1256, 1993.

[13] HB5942-86, Size Standard for Aircraft Pressure Refueling Joints, 1986.

[14] HB6130-87, Aircraft Pressure Refueling Dimensions Standard, 1987.

[15] S. Doling and X. Shuguo, *Electromagnetic Fields and Waves*. Higher Education Press, pp. 315-339, 2009.
[16] Cn.comsol.com. [Online]. Available: http://cn.comsol.com/model/dielectric-barrier-discharge-8637. [Accessed: 20 Jan. 2017].
[17] X. Fu, F. Dai, and F. Zhou, "A study on equivalent circuit model of RF discharge between the oil-inlet and nozzle of aircraft fuel tank," *Applied Computational Electromagnetics Society Symposium IEEE*, 2018.

Xinkai Fu receive the B.Eng. degree in Electronic Engineering from Beihang University, Beijing, China, in 2016, and he is currently working towards the M.S. degree in the same university.

His research interests include the microwave technology, EMC technology, as well as Multiphysics simulation.

Fei Dai receive the Ph.D. degree in Circuits and Systems from Beihang University, Beijing, China, in 2007. He joined the Electromagnetic Compatibility Laboratory at Beihang university, Beijing, in 2007, where he is currently an Associate Professor.

His research interests include the EMC technology, microwave technology, and antennas technology.

Ruitao Hu receive the B.Eng. degree in Electronic Engineering from Beihang University, Beijing, China, in 2017, and he is currently working towards the M.S. degree in the same university.

His research interests include EMC technology and Multiphysics simulation.

A Novel Classification Method Based on Adaboost for Electromagnetic Emission

Jing Nie, Shunchuan Yang, Qiang Ren, and Donglin Su

Institute of Electromagnetic Compatibility Technology
Beihang University, Beijing, 100191, China
niejing0209@163.com, scyang@buaa.edu.cn, qiangren@buaa.edu.cn, sdl@buaa.edu.cn

Abstract **—** Abundant characteristics information of equipment or systems could be obtained from electromagnetic emission data. In this paper, those typical characteristics, like harmonics, damped oscillations, of electromagnetic emission are classified via the adaptive boosting (Adaboost) algorithm and they are validated through measurement results. Based on the "basic emission waveform theory", three types of the basic fundamental elements, characteristics-harmonic, narrowband and envelope-of complex emission in frequency domain, are considered in our proposed method. By taking weights combination patterns to effectively improve the classification performance of a single classifier, quite high classification accuracy could be achieved by Adaboost algorithm in our simulations. In our study, 100% precision classification accuracy of three types of characteristics could be obtained using Adaboost with 13 decision tree weak-classifiers. Compared with other classification methods, the Adaboost algorithm with decision tree weak-classifier used to classify typical characteristics of electromagnetic emission is the most accurate. At the same time, it is very effective to process the measured data. Only through the classification of multiple emission signals can identification and positioning of electromagnetic interference sources further.

Index Terms **—** Adaboost, classification, electromagnetic emission characteristics, classification probability, signal component.

I. INTRODUCTION

The electromagnetic emission is the key parameter to evaluate the performance of equipment and systems. Once the emission characteristics of the system is obtained through numerical simulations or meansurements, useful information to indicate its performance could be extracted [1]. In [2], the "basic emission waveform theory" was proposed to identify the basic emission sources of complex systems [2]. Various emissions are characterized with and decomposed into four basic elements including square wave, sine wave, damped oscillation, and spike wave according to physical sources, which are interpreted as the emission waveforms of different types of circuit elements. Then, based on such decomposition, the performance could be evaluated. Therefore, the emission characteristics of any equipment can be obtained by analyzing its electromagnetic emission. However, to the best of the authors' knowledges, how to identify those fundamental elements are not yet addressed. We have reported our premiliary results in [2]. In this paper, comprehensive studies are carried out and compared with measurements.

The location of the interference source has always been a common concern of researchers. Therefore, when we extract the characteristics of the collected electromagnetic emission signals, can we determine which emission source does the characteristics correspond to? The classification model in this paper is to identify and classify the characteristics so as to further correspond to the emission source. Various classfication approaches have been extensively investigated [3], [4], [5], [6]. In recent years, the machine learning (ML) based methods have been paid special attention to, since MLs could extract hidden pattern and characteristics embedding in a large number of data [4]. Therefore, they are widely used in data mining, image processing, medical diagnosis and etc. [7]. Many machine learning methods are used in signal processing and cybernetics [8], [9]. However, to the authors' knowledge, they are seldom used to analyze the emission and their characteristics in electromagnetic compatibility field. In this paper, we explore the possibility of using the ML method to analyze the electromagnetic emission characteristics through the machine learning algorithm, more specifically, with Adaboost.

The paper is organized as follows. In Section II, four basic waveforms proposed the "basis emission waveform theory" are summarized and the new classification method is illustrated in detail. In Section III, numerical cases are carried out to validate the proposed method. In Section IV, its effectinveness is further confirmed by the good agreement with experiment data. At last, we draw

Submitted On: October 14, 2018
Accepted On: January 26, 2019

some conclusions in Section V.

II. BASIC ELECTROMAGNETIC EMISSION CHARACTERISTICS AND CLASSIFICATION

A. Electromagnetic emission characteristics from basic emission waveform theory

As indicated by "basic emission waveform theory", no matter how complex the electromagnetic emission is, the number and type of basic emission sources are limited, which are generally in some limited forms. By categorizing numerious circuits and their electromagnetic emission, the basic waveforms are cast into four types in the time domain: square waves, sine waves, damped oscillations, and spike waves [2,10].

Based on the above-mentioned emission sources, the relationship between the basic emission waveforms in time domain and the typical circuit characteristics in frequency domain are further clarified in this paper. First of all, square wave (clock signal) is the principal function signals in the digital circuit, which always possesses the characteristic of harmonics or an overall lift in the frequency domain. A typical waveform from the measured data of a crystal oscillator module is shown in Fig. 1 (a).

An analog circuit module is generally used for amplification, mixing, detection, and other related purpose. The overall data should have sine signals, which often own the characteristic of narrowband or even single frequency in the frequency domain, as shown in Fig. 1 (b), which is generated by the sine signal with random noise from the signal generator.

In addition, impedance mismatch leads to damped oscillations in the circuit. The damped oscillation signals present the characteristic of envelope in frequency domain, as shown in Fig. 2, which is generated by the damped oscillation signal with random noise from signal generator.

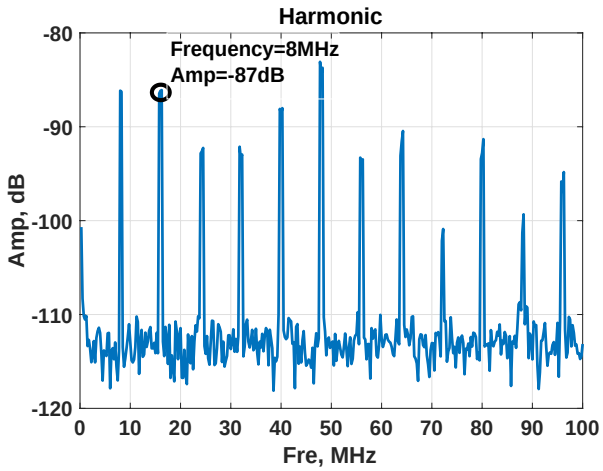

(a)

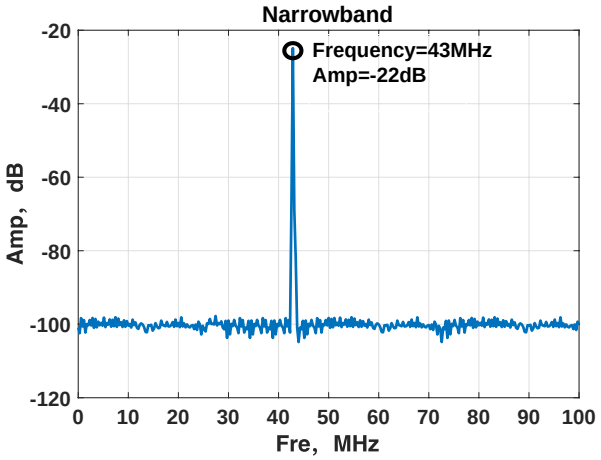

(b)

Fig. 1. (a) Harmonics characteristic, and (b) narrowband characteristic in frequency domain.

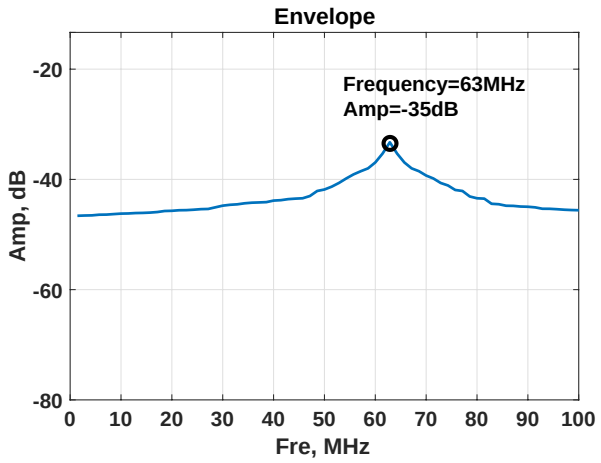

Fig. 2. Envelope characteristic in the frequency domain.

B. Feature recognition and classification based on Adaboost algorithm

The Adaboost algorithm is an iterative procedure that combines many weak-classifiers to the powerful Bayesian classifier C(x). Starting with the unweighted training sample data, the Adaboost constructs a weak-classifier to produce class labels. If a training data point is misclassified, the weight of that is named as training [11]. In addition, original Adaboost algorithm was further extended to the multi-class case in [12]. In this paper, we select this method to analyze the emission characteristics. The pseudo code of the algorithm is listed as follows.

1) Initialize the observation weights:

$$\omega_i = 1/n, i = 1,2,3 \ldots, n. \quad (1)$$

2) For $m = 1$ to M:
   a) Fit a classifier $T^{(m)}(x)$ to the training data using weights ω_i.
   b) Compute:

$$err^{(m)} = \sum_{i=1}^{n} \omega_i \cdot II\left(c_i \neq T^{(m)}(x_i)\right) / \sum_{i=1}^{n} \omega_i. \quad (2)$$

c) Compute:

$$\alpha^{(m)} = log\frac{1-err^{(m)}}{err^{(m)}} + log(K-1). \quad (3)$$

d) Set,

$$\omega_i \leftarrow \omega_i \cdot exp\left(\alpha^{(m)} \cdot II\left(c_i \neq T^{(m)}(x_i)\right)\right), \quad i = 1,2,\ldots,n. \quad (4)$$

e) Re-normalize ω_i.

3) Output:

$$C(x) = argmax_k \sum_{m=1}^{M} \alpha^{(m)} \cdot II\left(T^{(m)}(x_i) = k\right). \quad (5)$$

Different weak-classifier often generate different classification effects. In our research, decision tree and decision stump are used as weak-classifiers to study a small group of samples and nonlinear data of electromagnetic emission.

III. THE VERIFICATION OF ELECTROMAGNETIC EMISSION CHARACTERISTICS CLASSIFICATION

In this part, 300 groups of typical frequency characteristics data and their labels, which are the ideal waveforms from signal generator, have been used as the training data set, respectively. Harmonics, narrowband and envelope are considered and each has 100 groups.

Corresponding to Part II B, Equ. (1) n = 300, initial sample data weights are $1/300$, m is the number of weak classifiers, K = 3 is data types. Equation (3) ensures the weight update direction is greater than 0. For the m-th classifier being trained, according to Equ. (4), the weight of misclassified data is increased, while the weight of correctly classified data is reduced. The redistributed weight data is used to train the next classifier. Finally, the combination training result of weak classifiers with the highest probability of correct classification is obtained from Equ. (5). While, 110 groups of data in three types and their corresponding labels, which are similar to real emission, are chosen as testing data.

The classification accuracy:

$$A(h,y) = \frac{1}{n}\sum_{i=1}^{n} 1\{h(x^{(i)}) = y^{(i)}\}. \quad (6)$$

For training data (x, y), $y = 1,2,3,\ldots d$, where x is the electromagnetic emission characteristics data, y is the type of such data, namely label, d is the number of labels for classification and $h(x)$ is the classification label generated by training and prediction of Adaboost, n is the total number of sample x. So the training error is $E(h,y) = 1 - A(h,y)$.

The decision tree classifier assigns the parameter $\gamma_j, j = 1,2,\ldots,J$. to several mutually disjoint regions (attributes J), which can be expressed as:

$$F(x,\Theta) = \sum_{j=1}^{J} \gamma_j I(x \in R_j), \quad (7)$$

and

$$\Theta = argmin \sum_{j=1}^{J} \sum_{x \in R_j} E(y_j, \gamma_j). \quad (8)$$

Θ in Equ. (7) and Equ. (8) represents the parameter that minimizes the empirical risk, namely, the one that minimizes the training error of one classifier. And the objective function is:

$$F(x) = arg \min_{1 \le y \le d} E(h,y) = \frac{1}{n}\sum_{i=1}^{n} 1\{h(x^{(i)}) \neq y^{(i)}\}. \quad (9)$$

It is worth mentioning that different weak classifiers have different results. Decision stump weak classifier makes a single decision on characteristics data, that is, only one split is needed for judgment. Decision tree weak classifier judges characteristics from multiple angles, such as amplitude and frequency interval, and needs to be split into multiple disjoint spaces for judgment. Based on the nonlinearity and amplitude-frequency characteristics of electromagnetic emission data, the two kind weak-classifers are chosen to analyze. When using different numbers of decision tree weak-classifiers, the accuracy is increasing gradually and stabilizing at 100%, which implies that the classification results match the actual classification of the testing data completely. The optimal number of decision tree weak-classifiers in this algorithm is 13, as shown in Fig. 3 (a).

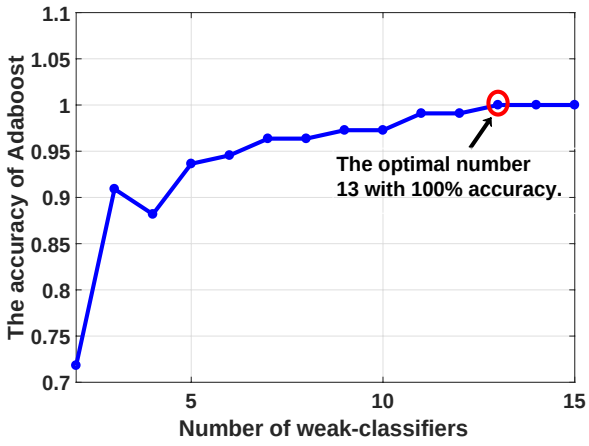

(a)

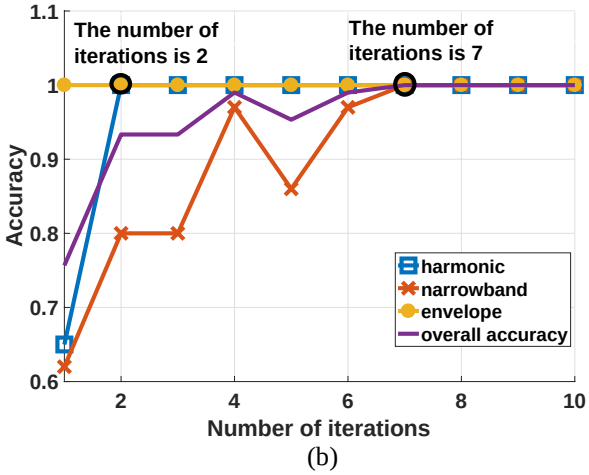

(b)

Fig. 3. (a) The accuracy with the number of weak-classifiers, and (b) the accuracy of three varieties characteristics with the number of iterations.

When using the same number of the decision tree weak-classifiers, the accuracy changes with the iteration number. It's clear from Fig. 3 (b) that the envelope characteristic shows the fastest identification, then followed by the harmonic and narrowband. The Table 1 shows the accuracy of different algorithms, which proves Adaboost-DecisionTree to be optimal.

Table 1: Accuracy of different algorithms

Alogritm	Single Classifier	13 Classifiers
SVM	0.8369	--
Adabost-Decision Stump	0.5636	0.6273
Adaboost-DecisionTree	0.8000	1.0000

IV. VERIFICATION

In this section, the author conducted radiation emission tests on three types of electronic equipments in a 10-meter semi- anechoic chamber, which are intercom, computer host and shielding device, then applied the Adaboost algorithm to classify signals under different conditions, including single type signal classification and mixed types signal classification.

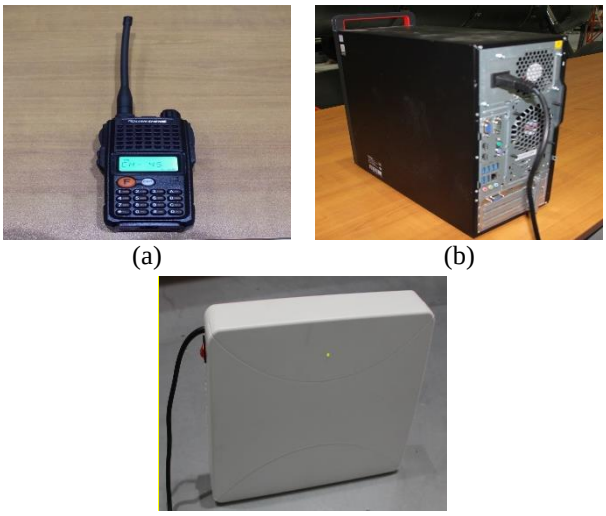

(a) (b)

(c)

Fig. 4. (a) The testing equipment of Intercom, (b) the testing equipment of Computer Host, and (c) the testing equipment of Shielding Device.

A. Single Type Signal Classification

The testing equipments in this research are shown in Fig. 4. Among them, the operation frequency of the intercom is 400MHz-470MHz. The shielding device mainly shields the signal of mobile phones, with the main frequency being 1GHz, 2GHz, 3GHz and 4GHz. The radiation emission of single type is shown in Fig. 5. Among them Figs. 5(a) and (b) are the emission data of a single intercom and two intercoms respectively. In the classification, both kinds data are used as training data of intercom.

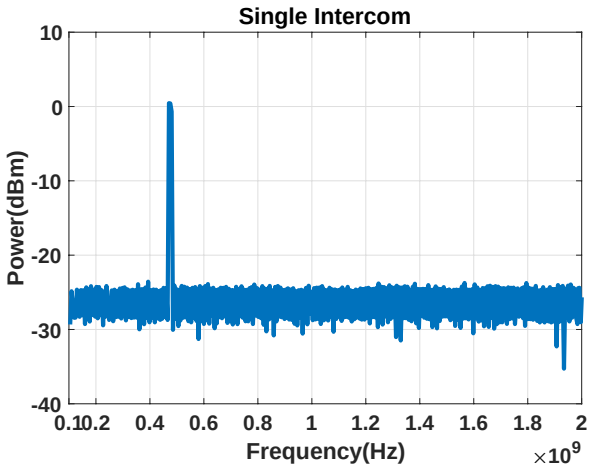

(a)

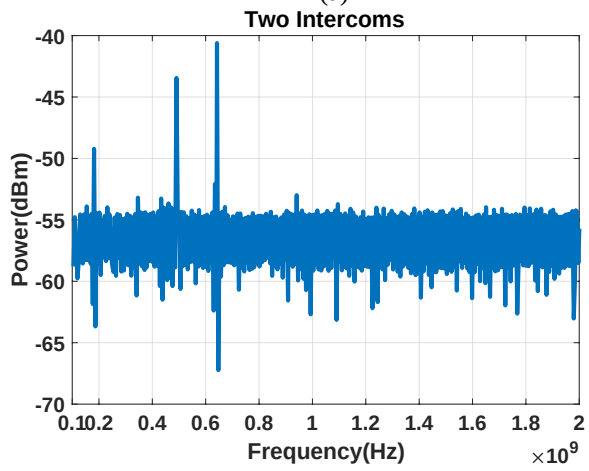

(b)

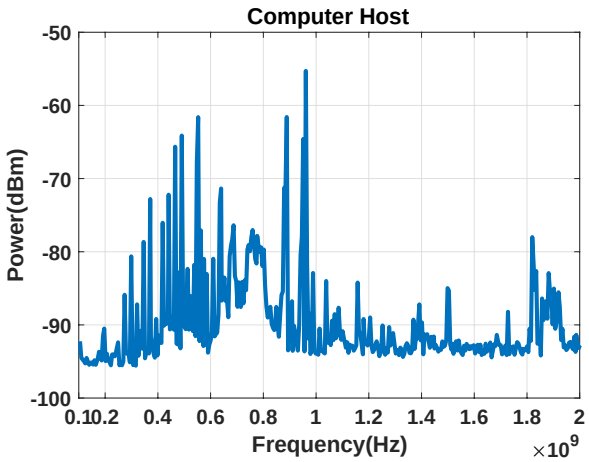

(c)

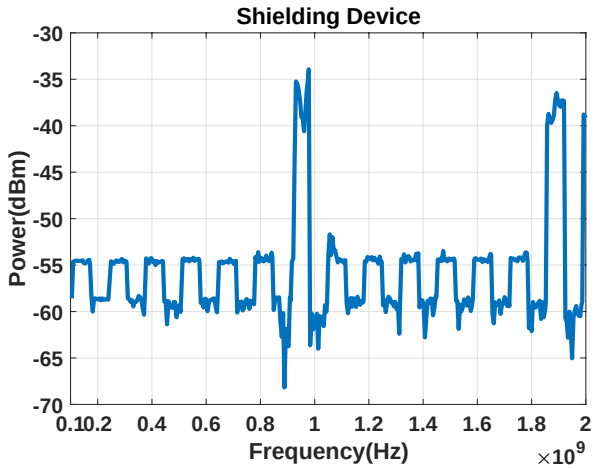

(d)

Fig. 5. (a), (b) The emission of a sigle intercom and two intercoms, (c) the emission of a sigle computer host, and (d) the emission of a sigle shielding device.

The frequency band of the emission is 100MHz-2GHz, and the data number of each type equipment is 90 groups. Therefore, the training data of three types for Adaboost algorithm is 270 groups, containing the emission data and their labels. Based on the training data, there are another 120 groups testing data. It's worth noting that whether the label of the testing data is known determine the classification accuracy of the algorithm. That means when use the label of testing data to predict the classification, the decision tree classifier only needs 1 to classify the 120 groups testing data completely, while the decision stump needs 3. However, when the label of testing data is unknown or we don't use the label while predicting, neither classifier could properly classify the 120 groups testing data. The classification accuracy on the testing data is shown in Table 2.

Table 2: Accuracy of different weak-classifiers

Adabost with Weak-Classifiers	The Label is Known (with only 1 classifier)	The Label is Unknown (with 3 Classifiers)
Decision Stump	0.68333	0.91675
Decision Tree	1	0.90005

Based on the analysis above, since the specific classification label of emission cannot be obtained usually in the actual complex electromagnetic environment, this paper prefers to use 3 decision stump weak-classifiers to predict the classification of the radiation emission data from the actual equipments without classification labels.

B. Mixed types signal classification

The three types of signals are combined in different forms, including pairwise combination and three types of mixing. The mixed types of testing data are 2,500 groups. At the same time, the training data and the corresponding label used in Adaboost algorithm are still the 90 groups data in part IV.A. The testing site is shown in Fig. 6.

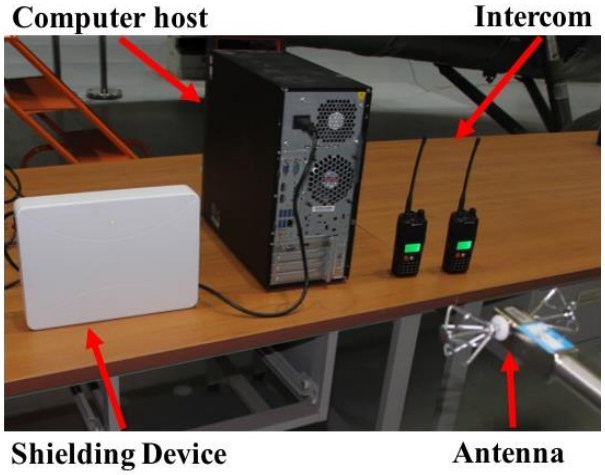

Fig. 6. The testing site.

1) Two Types Signal Mixed

In this part, each two types of radiation emission signals are mixed in proportion. At each proportion, there are 2,500 groups testing data of mixed types signals contain 50 groups for each type, so the classification probability is a statistical result. The quantitative relation curve of classification probability with the proportion of one type signal in the mixed environment is obtained by combining the three types signals from the equipments, i.e., the intercom, the computer host and the shielding device.

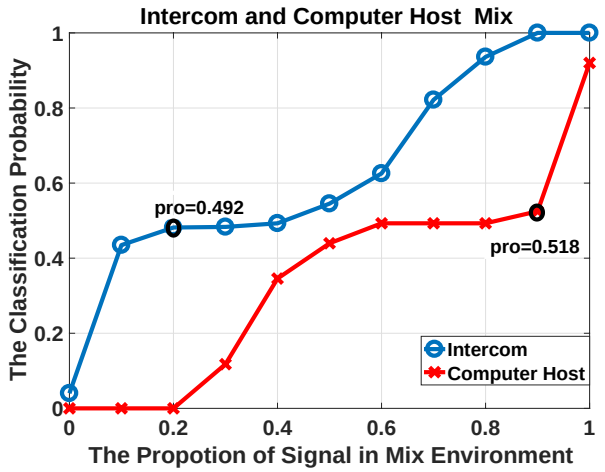

Fig. 7. The quantitative relation curve of classification probability with the proportion of intercom and computer host mixed environment.

By comparing above, it's shown that the Adaboost algorithm has different classification effect on the same type of signal in different combination situations. To be specific, Fig. 7 shows that when the intercome accounts for 20% in the mixed electromagnetic environment and the computer host accounts for 80%, the probability of the algorithm can classify intercom is 0.492. When computer host accounts for 90%, and intercom accounts for 10%, the probability classifying for computer host is only 0.518. It can be seen that the characteristics of the intercom are easier to classify when the two types signals are mixed.

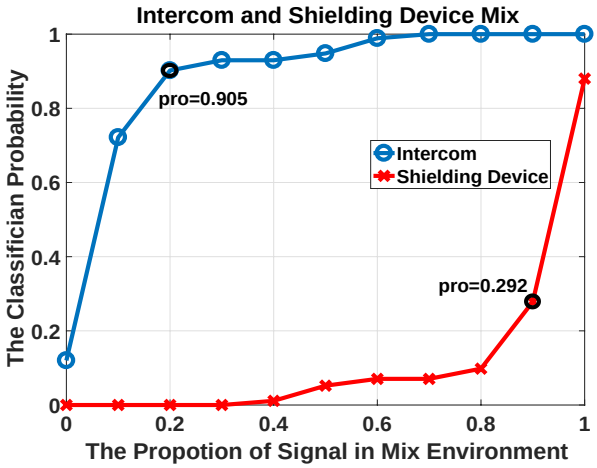

Fig. 8. The quantitative relation curve of classification probability with the proportion of intercom and shielding device mixed environment.

Figure 8 shows the combination of intercom and shielding device signals. When the intercome accounts for 20% in the mixed environment and the computer host accounts for 80%, the probability classifying for intercom is 0.905. When shielding device accounts for 90%, and intercom accounts for 10%, the classification probability of shielding device is 0.292. It can be seen that the characteristics of the intercom are easier to classify than shielding device.

Figure 9 shows the combination of computer host and shielding device signals. When the computer host accounts for 20% in the mixed environment and the shielding device accounts for 80%, the probability of computer host is 0.001. While, the probability of shielding device is 0.840, which shown that the characteristics of the computer host are easier to classify than shielding device.

2) Three Types Signal Mixed

When the three types of signals are mixed, the algorithm classification probability is shown in Fig. 10.

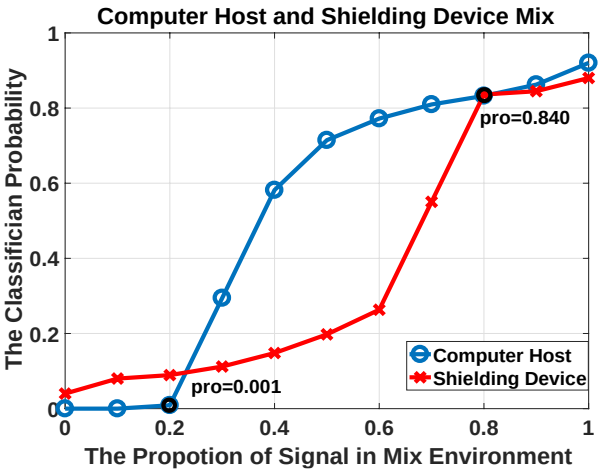

Fig. 9. The quantitative relation curve of classification probability with the proportion of computer host and shielding device mixed environment.

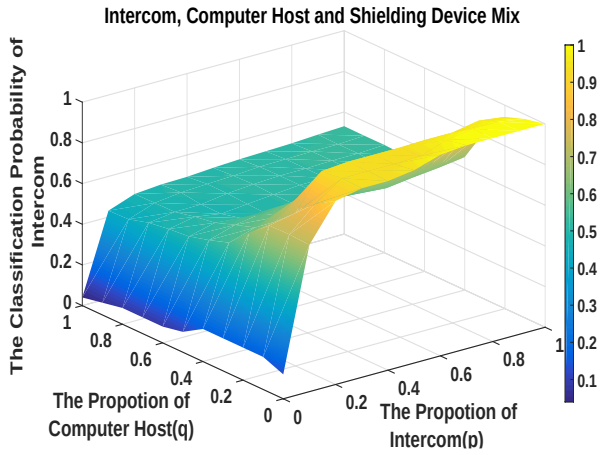

(a)

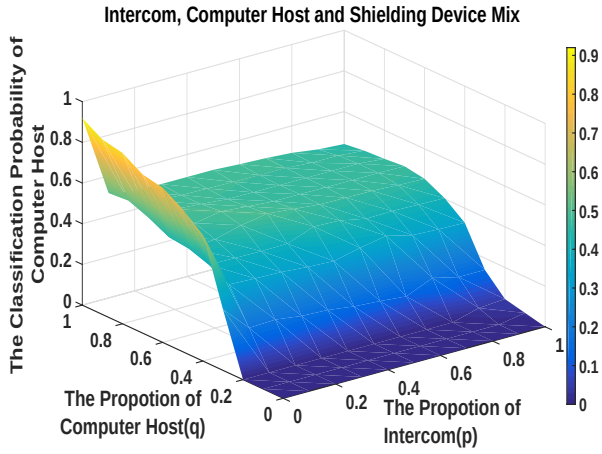

(b)

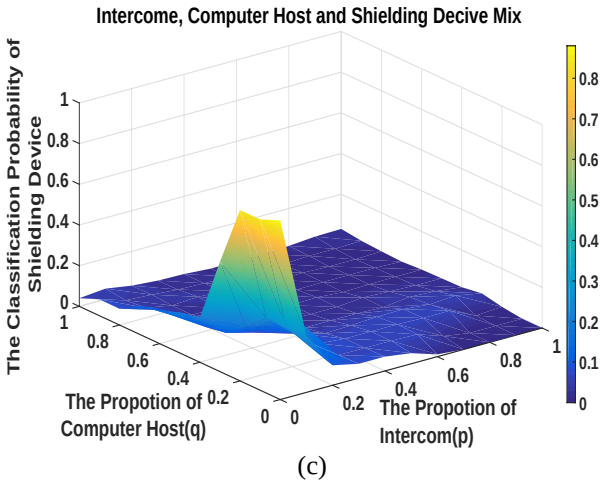

(c)

Fig. 10. The quantitative relation curve of classification probability with the proportion of three types mixed electromagnetic environment.

In our study, p is the proportion of intercom signals, q is the proportion of computer host signals, so the proportion of shielding devices is (1-p-q). Figure 10 (a) shows the statistical classification probability of intercom with the change of environment components. It can be seen that when the intercom accounts for about 20%, no matter how the components of computer host and shielding device change, the classification probability for intercom is always no less than 0.5. Figure 10 (b) shows the classification probability of computer host. When the computer host accounts for about 60%, no matter how the other two types signals change, the probability can be kept above 0.45. Figure 10 (c) is the classification probability of the shielding device. Only when the intercom signal accounts for less than 30% and the computer host signal is less than 60% could the probability of the shielding device be around 0.4.

V. CONCLUSION

Based on the "basic emission waveform theory", harmonic, narrowband and envelope are extracted as electromagnetic emission characteristics of different electromagnetic interference sources in the frequency domain. With carefully definition in Part III, the accuracy of Adaboost algorithm reaches 100% with 13 decision tree weak-classifiers. Our experiments shows that the number of weak-classifiers is fixed, the envelope characteristic is the first one to be classified, then followed by the harmonic and narrowband. In validation part, the electronic equipment intercom, computer host and shielding device are chosen to develop radiation emission test and emission data analysis. According to the basis analysis results of the single type signal classification, Adaboost algorithm with decision stump weak-classifier is selected to study on the classification in types mixed electromagnetic environment, the quantitative results of classification probability are obtained under different types signals components environment. It can be seen that the intercom is the closest to the narrowband signal of the basic emission characteristics and is also the most easily classified of the three types of signals.

That is to say, in the environment where multiple electronic devices work together, identification and classification of different devices and their components could be realized through our method. Only by accurate classification of electromagnetic emission and their characteristics can identification and positioning of electromagnetic interference sources be further realized.

ACKNOWLEDGMENT

This work was supported by the project 61427803 from the National Natural Science Foundation of China (NSFC).

REFERENCES

[1] D. L. Su, S. G. Xie, and F. Dai, *The Theory and Methods of Quantification Design on System-level Electromagnetic Compatibility*. National Defence Industry Press, pp. 53-58, 2015.

[2] D. L. Su, S. G. Xie, and A. X. Chen, "Basic emission waveform theory: A novel interpretation and source identification method for electro-magnetic emission of complex systems," *IEEE Transactions on Electromagnetic Compability*, vol. 99, pp. 1-10, 2017.

[3] D. Shi and Y. Gao, "Electromagnetic radiation source identification based on spatial character-istics by using support vector machines," *Appl. Comput. Electromagn. Soc. J.*, vol. 32, no. 2, pp. 120-127, 2017.

[4] J. Y. Wu, S Cui, and D. L. Su, "A support vector machine method based on spectrum data feature analysis," *Presented at Asia-Pacific Electromagnetic Week Conference on Electromagnetic Compatibility*, Xi'an, China, 2017.

[5] L. Breiman, "Random forests," *Mach. Learn.*, vol. 45, no. 1, pp. 5-32, 2001.

[6] Y. Freund, R. Schapire, and N. Abe, "A short introduction to boosting," *J. Jpn. Soc. Artif. Intell.*, vol. 14, no. 5, pp. 771-780, 1999.

[7] F. M. Takbir Hossain, Md. I. Hossain, and S. Nawshin, "Machine learning based class level prediction of restaurant reviews," *2017 IEEE Region 10 Humanitarian Technology Conference (R10-HTC)*, pp.420-423, 2017.

[8] S. Q. Wu and H. Nagahashi, "Parameterized AdaBoost: Introducing a parameter to speed up the training of real AdaBoost," *IEEE Signal Processing Letters*, vol. 21, no. 6, pp. 687-691, 2014.

[9] P. B. Zhang and Z. X. Yang, "A novel AdaBoost

framework with robust threshold and structural optimization," *IEEE Transactions on Cyberrnetics*, vol. 48, no. 1, pp. 64-76, 2018.

[10] C. Xiao and T. Zhao, "Identification method of EMI sources based on measured single-channel signal and its application in aviation secondary power source design," *IEEE Trans. Electromagn. Compat.*, vol. 59, no. 2, pp. 439-446, 2017.

[11] Y. X. Wang. "Research of Prediction Method of Sudden Cardiac Arrest Based on ECG Signals," Jilin University, June 2017.

[12] J. Zhu, S. Rosset, H. Zou, and T. Hastie, "Multi-class Adaboost," *Statistics and Its Interface*, vol. 2, no. 3, pp. 349-360, 2009.

Feasibility Analysis of the Installation of a Guided-Wave HEMP Simulator in an Electromagnetic Shielding Room

Yaoyao Li [1], Donglin Su [1*], Shuo Cui [1], and Weimin Li [2]

[1] School of Electronic and Information Engineering
Beihang University, Beijing, 100191, China
bravegoal@126.com, sdl@buaa.edu.cn, cuishuo@buaa.edu.cn

[2] China Academy of Launch Vehicle Technology, CALT
No. 1 Nan Da Hong Men Road, Fengtai District, Beijing, 100076, China
liweimin8103@163.com

Abstract ─ Field strength, waveform and uniformity are crucial to the validity of high-altitude electromagnetic pulse (HEMP) radiation sensitivity test (RS05/RS105) for large transient field facilities which are placed in expensive semi-anechoic chambers (SAC) usually. In this paper, we present a type of space requirements of those large transient field facilities installations in cheaper electromagnetic shielding room (ESR) by quantitative simulation analysis of the crucial factors. The field uniformity and the accuracy of guided-wave EMP simulator (GWES) in a SAC are verified by numerical cases and experiments. Time domain finite integral method (FIT) is employed to compute field data and singular value decomposition (SVD) technique has been used to extract the higher order modes (HOM). Based on the validated model, feasibility of GWES installation in an ESR was analyzed. The minimum space requirement of GWES installation has been obtained through optimization.

Index Terms ─ Field uniformity, HEMP, higher order modes, singular value decomposition, transient electromagnetic field.

I. INTRODUCTION

High-Altitude Electromagnetic Pulse (HEMP) is produced by nuclear explosion at high altitude and characterized by intense electric field strength, short duration, wide band in the frequency spectrum and large range coverage, which can damage electronic equipment of radar and communication systems, wires, crystal diodes, transistors, integrated circuits resistors, capacitors, filters, relays and other components [1, 2]. Therefore, the HEMP sensitivity test becomes critical for military and civil electronic systems. HEMP simulators are applied to generate pulse electric field which simulates the early nuclear explosion radiation. The waveforms are specified in MIL-STD-461G for operating RS105 test (transient electromagnetic field radiated susceptibility tests) [3, 4, 5]. In order to obtain good field distribution uniformity, guided-wave EMP simulators are widely used in electromagnetic compatibility (EMC) susceptibility tests of airplanes, vessels and other electronic devices and systems.

Several HEMP simulators satisfying the fast leading-edge requirement of IEC 61000-2-9 were designed and built worldwide, such as ALECS, ARES, EMPRESS II, and SIEM-2. These generators are generally built in open-area test site (OATS) or SAC to avoid affecting the test area. Depending on the size of the EUT, the size of these transient field facilities varies from several meters to several hundred meters. In indoor GWES sites, the low operating frequency (200 MHz) characteristics require ferrite absorbing materials, which is expensive both in space and money. However, if the EM field characteristics of the GWES in the room can be accurately predicted, the local laying of EM absorbing materials can be used and the cost can be significantly reduced. In [6], many HEMP simulator concepts evolved from design are described. In [7]-[9], a summary of developments in the HEMP research worldwide since 1975 was provided. In addition, the radiation patterns, higher order modes and some performance analysis research of HEMP simulators have been presented in [10]-[12]. A field uniformity analysis and calibrate method for eliminating the measurement error is presented in [13], [14]. Besides, in [15]-[16] the basic types or categories of EMP simulators were discussed. All of these works are about the standards, modeling, simulation and performance evaluation of HEMP simulator, without considering the performance changes after installation. No result of this type has been reported in the open literature.

In this paper, feasibility of a GWES placement in an ESR was analyzed. In Section II, we present the GWES computational model and simulation results by CST

Submitted On: October 14, 2018
Accepted On: March 21, 2019

[20]. The field uniformity and the accuracy of the experimental simulator are verified by numerical cases and experiments. We proved that the electric field in the working area of guided wave EMP simulator can be expressed as a linear combination of TEM, TM and TE modes, which is of great importance to the analysis of field uniformity, radiation leakage and fundamental mode damage. In Section III, FIT has been used to compute field data and SVD technique has been employed to extract the HOM on a grid of 7 x 5. In Section IV, we analyzed the influence of metal wall on GWES performance based on the validated model. Feasibility of GWES installation in an ESR was analyzed. The minimum space requirement of GWES installation has been obtained through optimization.

II. GWES MODELING AND VERIFICATION

A. GWES modeling

The modeling process is as follows. Firstly, the structure model and distributed load of HEMP generator were established. Secondly, the boundary condition and the reference point or reference plane were selected. Lastly, the structure and load value of the simulator are optimized to approximate the measured results. The simulation model is shown in Fig. 1. Virtual field probes are utilized in the test zone of the GWES model to perform a complete field mapping. Some parameters used in this study are as follows. The symmetric geometry is 1:1 according to [19] and the size is 5700 mm × 2500 mm ×1800mm. The corresponding rise time is 2.47 ns and 99% energy effective bandwidth is 95.2MHz. The maximum frequency of the simulation is set as 600 MHz, the metal wire grating and the plate are perfect electric conductors, and the single load is 138 ohms. The background environment is assigned to air.

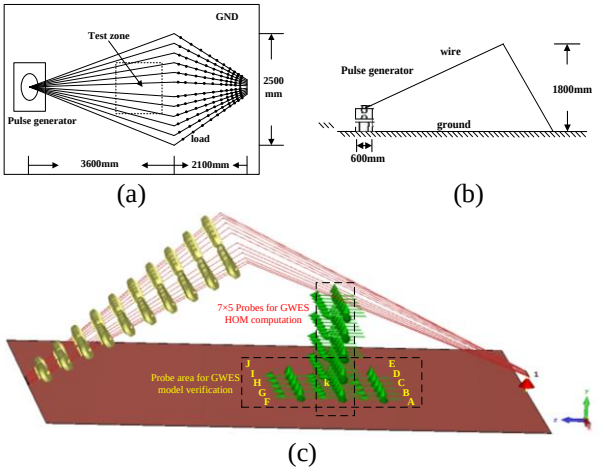

Fig. 1. Geometry of a GWES: (a) top view, (b) side view, and (c) 3-D structure and monitors placement.

The test zone is 1000 mm × 1000 mm. Eleven virtual field probes are placed on the ground plane of the test zone of the GWES model to perform field mapping. The positions of the probes are illustrated in Fig. 1 (c) marked as A to K. Also, there are 7 × 5 probes to monitor the EM field for HOM extracted by SVD.

B. Verification model

An ideal pulse generator voltage source U(t) is applied to produce the standard double exponential pulsed field E(t) [13], which are as follows:

$$U(t)=\begin{cases}0, & \text{when } t\le 0\\ U_0\cdot(e^{-\alpha t}-e^{-\beta t}), & \text{when } t>0\end{cases} \quad (1)$$

$$E(t)=\begin{cases}0, & \text{when } t\le 0\\ E_0\cdot k\cdot(e^{-\alpha t}-e^{-\beta t}), & \text{when } t>0\end{cases} \quad (2)$$

where $U_0=6.5\times10^4\,\mathrm{V}$, $E_0=5\times10^4\,\mathrm{V/m}$, $\alpha=4\times10^7\,\mathrm{s}^{-1}$, $\beta=6\times10^8\,\mathrm{s}^{-1}$, and $k=1.3$.

To verify the GWES model, field uniformity and waveform are compared by simulation and experiment. The measurement setup is shown in Fig. 2. A differential D-dot sensor is used as the ground plane sensor. Thus an integrator has to be used together with the D-dot. The correction factor of the D-dot sensor is 37.4 mV. The relationship between the correction factor C of the sensor, the oscilloscope reading U, and the peak electric field E is demonstrated in (3) [19]:

$$E(KV/m)=U(mV)/C[mV/(kV/m)]. \quad (3)$$

The measurement is as follows: Firstly, the electric field probe is calibrated and then configures the measurement as shown in Fig. 2. Secondly, the voltage is converted into the field strength of the observation point according to (3). Lastly, move the probe to the observation points shown in Fig. 1 in turn, and record readings to complete the measurement.

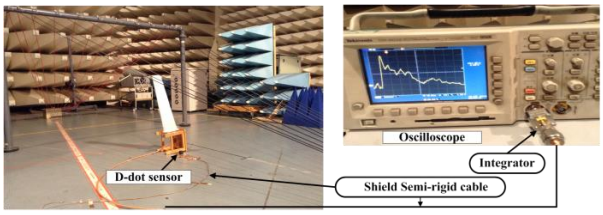

Fig. 2. Measurement setup of the GWES.

The field uniformity of the simulation model is verified as follows. The field uniformity will not change due to the output voltage of GWES. So we picked a median of 20.1 kV as the GWES output voltage to facilitate the test. A time domain FIT method has been employed to compute the time domain field results. We select CST as computational tool. In MWS, the virtual probes can monitor EM field components in the appointed

space position. And we selected peak field as the field uniformity inputs. According to the simulation and measurement position shown in Fig. 1 (c), numerical results and measurement results of the field in different positions are listed in Table 1.

Table 1: Comparison of simulation and measurement results of E-field uniformity

p	OR (mv)	OREY (KV/m)	ORLEY (dBV/m)	SEY (dBV/m)
A	48.0	1.28	62.17	111.236
B	52.4	1.40	62.93	111.326
C	54.8	1.47	63.32	111.481
D	54.4	1.45	63.25	111.394
E	50.2	1.34	62.56	111.053
F	35.6	0.95	59.57	109.876
G	36.4	0.97	59.76	109.938
H	38.4	1.03	60.23	108.442
I	35.0	0.94	59.42	108.386
J	34.8	0.93	59.37	108.205
K	42.8	1.14	61.17	109.82
Field uniformity(dB)		3.9		3.3

Where P represents the position of monitors, OR refers to oscilloscope reading voltage, OREY is the oscilloscope reading voltage transfer to linear field strength, ORLEY shows the oscilloscope reading voltage transfer to Logarithmic field strength, and SEY represents simulation field strength. It is shown that the deviation of the GWES model on field uniformity equals to 0.6dB.

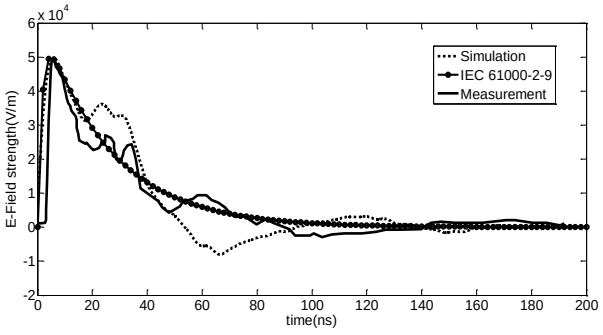

Fig. 3. Comparison of the electric field waveform between IEC 61000-2-9, simulation and measurement.

The field uniformity of eleven points from A to K is shown in Table 1. Without loss of generality, point C marked in Fig. 3 (c) is selected as the reference point for EM field waveform analysis. The numerical simulation result, standard curve and measurement result of point C are shown in Fig. 3. In the measurement, 1 to 3 nanoseconds propagation delay usually occurs when HEMP waveform propagates from MAX voltage source to point C, while there is no delay in the standard and simulation model. Therefore, the simulation result, standard curve and measurement cannot be overlapped in the time domain. In order to verify the accuracy, the rise time and maximum field strength are selected for comparison. The rise time is 2.47 ns and maximum field strength is 50000V/m. It shows good agreement with the HEMP standard of IEC 61000-2-9 [21], which an industry standards for HEMP waveform.

The electric field strength distributions through numerical simulation are shown in Fig. 4. The maximum field strength can reach 50000V/m. Those results show that the experimental GWES meets the standard requirements.

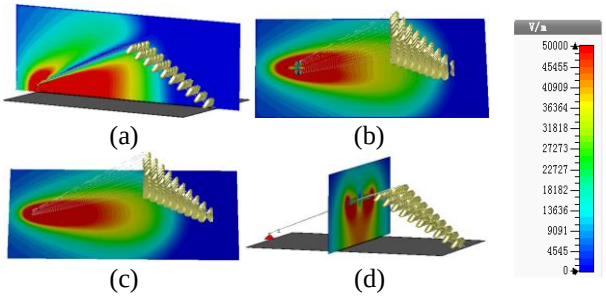

Fig. 4. GWES electric field strength distribution: (a) x=0 mm plane, (b) y=200 mm plane, (c) y= 500mm plane, and (d) Z=2820 mm plane.

The above work shows a good agreement to the EM field waveform, distribution and uniformity with the measured data, which proves that the GWES model is credible.

III. APPLICATION SVD FOR HOM ANALYSIS

A. Singular value decomposition (SVD)

In SVD, a matrix is decomposed into three matrices of same size. In this subsection, we present a brief description of the method and its application to the modal analysis of FIT simulation. The SVD of a matrix A is defined as follows [17, 18]:

If $A \in \Re^{m\times n}$, there would exist orthogonal matrices:

$$U = \left(u_1, u_2, \cdots u_m\right) \in \Re^{m\times m}, \tag{4}$$

$$V = \left(v_1, v_2, \cdots v_m\right) \in \Re^{n\times n}, \tag{5}$$

such that,

$$A = USV^T = \sum_{i=1}^{r} u_i \cdot \alpha_i \cdot v_i^T, \quad r = \min\left\{m, n\right\}, \tag{6}$$

where

$$S = diag\left(\alpha_1, \alpha_2, \cdots \alpha_r\right), \quad \alpha_1 \geq \cdots \geq \alpha_r \geq 0. \tag{7}$$

The vector u_i and v_i denote the *i*th left and right singular vectors, respectively, and the diagonal elements α_i of *S* are the singular values of matrix *A*. Considering a physical quantity simultaneously measured at *m*

different positions and sampled at *n* different times with a sampling interval t_s , the matrix representation of the above observation can be generally expressed by a rectangular array $x_{ij} = x_j\left[(i-1)t_s\right]$, where the row index *i* refers to time and the column index *j* refers to the channel. The SVD of the matrix x_{ij} is expressed as $X_{ij} = U_i^k s_k V_j^k$. The singular values *S* represent the amplitude of a mode, while *U* and *V* are the basis functions. In summary, the matrix X_{ij} has been decomposed into three parts - time (*U*), amplitude (*S*) and space (*V*).

B. SVD analysis on computed result

Based on the verified GWES model. FIT has been used to compute field data and SVD technique has been used to extract the higher order modes. SVD is performed on $E(x_{ij})$ measured at 35 positions (z=2320 mm plan) as shown in Fig. 1 (c). These field monitors locates in the y direction with an interval of 0.8 m. Each channel records 1000 points with a sampling interval of 200 ns.

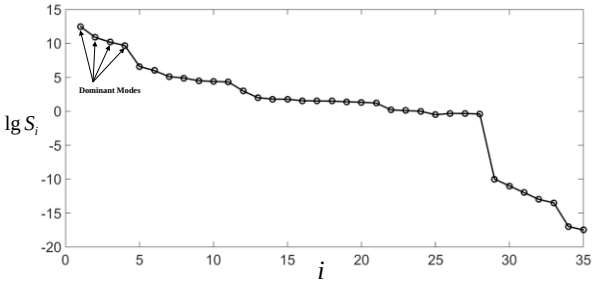

Fig. 5. Logarithms of the singular value S_i

The 35 singular values of the decomposed components are shown in Fig. 5. The x axis represents observation position indexes. Following the principle of [17], the word "dominant" is used in an approximate sense to describe modes whose singular values lie within three orders of magnitude of the strongest mode. It shows that there are four dominant modes (Eigen modes).

Figures 6 (a)-(d) exhibit the eigenvectors in the descending order. The eigen vector in Fig. 6 (a) is almost constant. Obviously, it corresponds to the TEM mode, which does not have any zero crossing. The eigen vectors illustrated in Figs. 6 (a), (b), (c) and (d) have one, two or three zero crossing, respectively, which represent the TM0 (TEM), TM1, TM2 and TM3 modes respectively.

The above HOM will cause the radiation leakage and destructive of the fundamental mode. In the following parts, we will analysis the radiation leakage in an ESR, and its impact to the test zone.

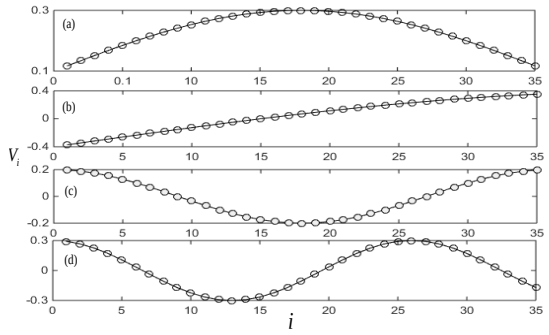

Fig. 6. Eigen vectors of the dominant modes.

IV. GWES PLACEMENT IN AN ESR

Limited by the funding, the indoor GWES test facility cannot have full coverage by absorbing materials. The size of a research institution ESR is shown in Fig. 7.

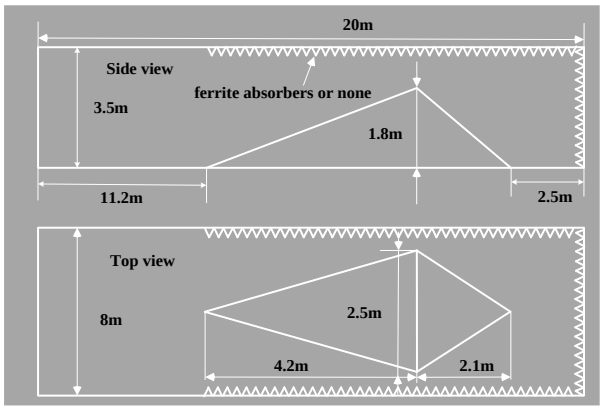

Fig. 7. An indoor GWES site.

If metallic walls (or electrical installations, barriers, etc.) are in the vicinity of the installation site, reflections of the wave can occur. The reflected waves will return to the test zone and added to the field below the antenna. Depending on the phase of the reflected wave, the distortion of the signal could be positive or negative. In order to analyze the feasibility, we carry out a simulation analysis based on the validated simulator above mentioned. It is assumed that absorbing materials forms a perfectly matched layer. The analysis procedure is shown in Fig. 8.

Step 1): Establish a model of shielding chamber loading GWES according to the actual size of ESR.

Step 2): The load surface wall, along with the front, rear and top walls are set as metal surfaces, while other walls are set as open. The distribution of the simulated field and the waveform characteristics of the uniform field in the test area are compared with those in the fully open condition, and the influential wall is obtained.

Step 3): If the influential wall exists, the part of the wall with larger influential surface is set as open, and the other area is metal wall. The minimum space requirement is obtained by the simulation method of step 2.

Step 4): The site size requirement of the test GWES is formed to provide technical support for MIL-STD-461G.

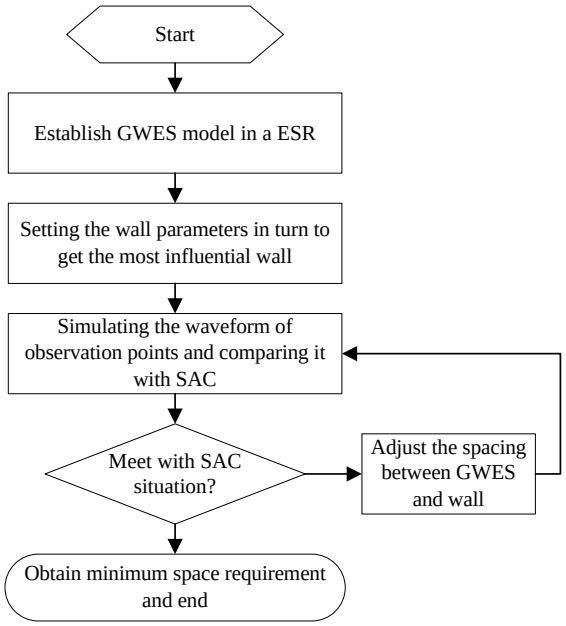

Fig. 8. Proposed installation feasibility analysis method operating flow chart.

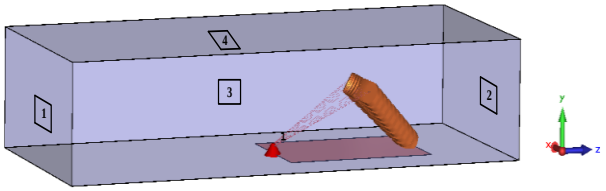

Fig. 9. GWES installation in an ESR model

The GWES-ESR model is shown in Fig. 9. The GWES model which is depicted in Fig. 9 is the same as we stated in part II. We choose the most important parameters of the E1 shape, i.e., the rise time $\tau_{10\%\sim90\%}$, the pulse width at half maximum t_f and the peak amplitude of the electric field E_0 [2] as the index of feasibility evaluation.

Comparing Fig. 10 (a) with Fig. 10 (b), it can be observed that field distributions produced by GWES installation in ESR and SAC situations are the same in the test zone which is 1000 mm × 1000 mm ×1000mm as shown in Fig. 1 (a). Shielding room slightly enhances the indoor field strength, compared to SAC. The field uniformity does not change according to the same calculation method in Table 1.

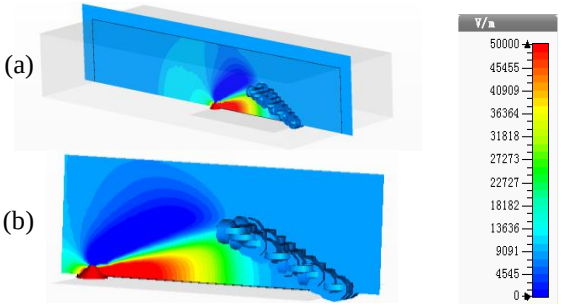

Fig. 10. Field distributions at x=0 mm plane and t=8.5ns produced by GWES installation in ESR and SAC situations.

In order to get the influence of shielding room on the test system, the waveform comparison between shielding room and semi-anechoic chambers at K point as illustrated in Fig. 1 (c) is carried out. The result is shown in Fig. 11.

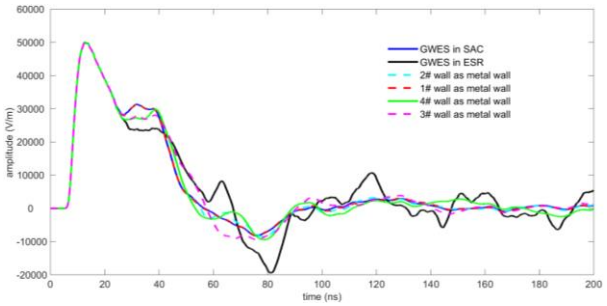

Fig. 11. Field waveforms produced by GWES installation in SAC and ESR situations

Considering Fig. 11 and the calculation results, it can be found that $\tau_{10\%\sim90\%}$, t_f and E_0 in ESR are almost the same with those from SAC condition. However, the electric field waveform in the back edge is distorted because of severe oscillatory effect from the reflection of the wall appears on the back edge of the pulse. To assess that impact, we select 5000 points to calculate the mean error between five curves and SAC curves. As shown in Table 2, installation in ESR and 4# wall has the greatest impact.

Table 2: Comparison of mean error on different simulation situation

Simulation Situation	Mean Error (V/m)
GWES in ESR	4276
2# wall as metal wall	285
1# wall as metal wall	182
4# wall as metal wall	1242
3# wall as metal wall	120

To eliminate the damped oscillation effect in the back edge caused by wall, we optimized the minimum distance between the facility and the wall. We define d1, d2, d3, whose shown on Fig. 12 are the variables to be optimized. We select the average deviation of E_z, E_x and E_y on pulse delay amplitude for SAC and ESR as the objective goal, so as to optimize d1, d2 and d3 respectively. When the average deviation of E_z is less than 10V/m, d1 is obtained. When the average deviation of E_x is less than 10V/m, d2 is obtained. When the average deviation of E_y is less than 10V/m, d3 is obtained. As shown on Fig. 11, the damped oscillation effect is minimum when d1 is equal to 3.2m, d2 is equal to 1.5m and d3 is equal to 1.8*H. It is feasible to install the GWES in ESR as long as the specified space requirements are followed.

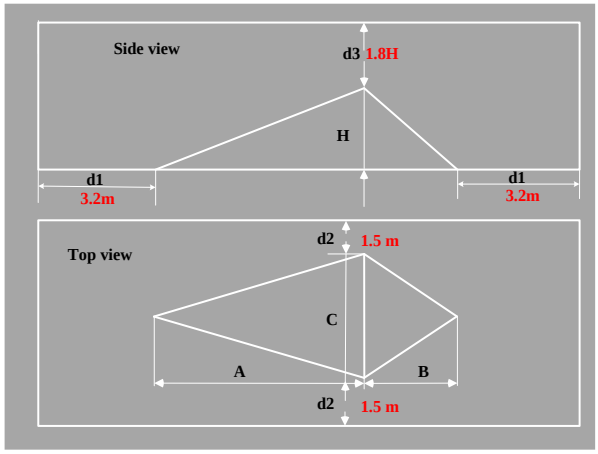

Fig. 12. The optimized minimum space requirements of GWES installation.

V. CONCLUSION

In this paper, feasibility of a popular guided-wave EMP simulator placement in an electromagnetic shielding room was analyzed by time domain finite integral method and singular value decomposition. A GWES model is built and validated by the good agreement on field strength, waveform and uniformity between simulations and measurements. Based on this GWES model, FIT has been used to compute field data and the SVD technique has been used to extract the higher order modes. Waveform distortion of GWES in ESR was simulated by FIT and the feasibility of GWES installation in an ESR was further analyzed. This proves that installation of the GWES in ESR as long as the specified space requirements is feasible and the minimal space requirement of GWES installation has been given by optimization method.

ACKNOWLEDGMENT

This work was supported by the project 61427803 and 61521019 from the National Natural Science Foundation of China (NSFC).

REFERENCES

[1] S. Song, H. Jiang, and Y.-L. Huang, "Simulation and analysis of HEMP coupling effect on a wire inside an apertured cylindrical shielding cavity," *Appl. Comput. Electromagn. Soc. J.*, vol. 27, no. 6, pp. 505-515, June 2012.

[2] F. Sabath and S. Potthast, "Tolerance values and the confidence level for high-altitude electromagnetic pulse (HEMP) field tests," *IEEE Trans. Electromagn. Compat.*, vol. 55, no. 3, pp. 518-525, June 2013.

[3] *Requirements for the control of electromagnetic interference characteristics of subsystems and equipment*, MIL-STD-461G, Dec. 2015.

[4] *Electromagnetic Compatibility (EMC) — Part 4-32: Testing and Measurement Techniques —High-Altitude Electromagnetic Pulse (HEMP) Simulator Compendium*, IEC 61000-4-32:2002, 2002.

[5] R. Hoad and W. A. Radasky, "Progress in high-altitude electromagnetic pulse (HEMP) standardization," *IEEE Trans. Electromagn. Compat.*, vol. 55, no. 3, pp. 532-538, June 2013.

[6] W. D. Prather and D. V. Giri, "Early developments in sensors and simulators at the air force weapons laboratory," *IEEE Trans. Electromagn. Compat.*, vol. 55, no. 3, pp. 431-439, June 2013.

[7] M. Ianoz, "A review of HEMP activities in Europe (1970 – 1995)," *IEEE Trans. Electromagn. Compat.*, vol. 55, no. 3, pp. 412-421, June 2013.

[8] J. C. Giles and W. D. Prather, "Worldwide high-altitude nuclear electromagnetic pulse simulators," *IEEE Trans. Electromagn. Compat.*, vol. 55, no. 3, pp. 475-483, June 2013.

[9] L. Shi, X. Zhang, Z. Sun, and R. Ma, "An overview of the HEMP research in China," *IEEE Trans. Electromagn. Compat.*, vol. 55, no. 3, pp. 422-430, June 2013.

[10] R. Kichouliya and M. J. Thomas, "Radiation pattern of a hybrid type high altitude electromagnetic pulse (HEMP) simulator," *IEEE International Symposium on Electromagnetic Compatibility*, Ottawa, pp. 530-535, July 2016.

[11] R. Kichouliya, S. M. Satav, and M. J. Thomas, "Experimental investigation on higher order modes in guided wave high altitude electromagnetic pulse (HEMP) simulator," *IEEE International Symposium on Electromagnetic Compatibility*, Ottawa, pp. 153-158, July 2016.

[12] J. J. A. Klaasen, "An efficient method for the

performance analysis of bounded-wave nuclear EMP simulators," *IEEE Trans. Electromagn. Compat.*, vol. 35, no. 3, pp. 329-338, Aug. 1993.

[13] L. Yao, T. Shen, N. Kang, J. Huang, D. Liu, F. Zhang, and H. Sun, "Use of a reference point method to calibrate the field uniformity when testing with transient electromagnetic fields," *IEEE Trans. Electromagn. Compat.*, vol. 59, no. 2, pp. 352-357, Apr. 2017.

[14] L. Yao, T. Shen, N. Kang, D. Liu, and J. Huang, "Time-domain simulation and measurement of a guided-eave EMP simulator's field uniformity," *IEEE Trans. Electromagn. Compat.*, vol. 55, no. 6, pp. 1187-1194, Dec. 2013.

[15] C. E. Baum, "EMP simulators for various types of nuclear EMP environments: An interim categorization," *IEEE Trans. Electromagn. Compat.*, vol. 20, no. 1, pp. 35-53, Dec. 1978.

[16] D. V. Giri, C. E. Baum, and W. D. Prather, "The relationship between NEMP standards and simulator performance specifications," *Sensor Simulation Note 538 Idus Martiae*, 2009.

[17] S. Ahmed and E. Li, "Application of singular value decomposition on FDTD simulation results – A novel approach for modal analysis of complex electromagnetic problems," *IEEE Microwave and Wireless Components Letters*, vol. 14, no. 11, pp. 519-521, Nov. 2004.

[18] S. Ahmed, D. Raju, S. Caturvedi, and R. Jha, "Modal analysis for a bounded wave simulator – Part I: Effect of test objects," *IEEE Trans. Electromagn. Compat.*, vol. 47, no. 1, pp. 171-182, Feb. 2005.

[19] *NEMP Transient Pulse Simulator Installation and User's Manual*, Montenaemc sa, Switzerland.

[20] CST STUDIO SUITE™ 2011, CST AG, Germany. www.cst.com

[21] Compatibility E. Part 2: Environment— Section: Description of HEMP Environment—Radiated Disturbance, *IEC 61000-2-9 Ed. 1.0*, Feb. 1996.

Yaoyao Li was born in Jingzhou, China, in 1986. He received the Ph.D. degree in Electromagnetic Compatibility and Electromagnetic Environment in 2017 from Beihang University, Beijing, China. His current research interests include System level electromagnetic compatibility and electromagnetic protection.

Donglin Su received the B.S., M.S., and Ph.D. degrees in Electrical Engineering from Beihang University, Beijing, China, in 1983, 1986, and 1999, respectively.

In 1986, she joined the Faculty of School of Electronics and Information Engineering, BUAA, where she was first an Assistant, then a Lecturer, later on an Associate Professor, and is currently a Full Professor. From 1996 to 1998, she was a Visiting Scholar with the Department of Electrical Engineering, University of California, Los Angeles (UCLA), Los Angeles, CA, USA, under the BUAA–UCLA Joint Ph.D. Program. She has authored more than 100 papers and coauthored several books. Her research interests include the numerical methods for microwave and millimeter-wave integrated circuits and systematic electromagnetic compatibility design of various aircrafts. Su is a Senior Member of the Chinese Institute of Electronics. She is the Chair of Beijing Chapter of the IEEE Antennas and Propagation Society and the Deputy Chair of the Antennas Society, Chinese Institute of Electronics. She was a recipient of two National Awards for Science and Technology Progress in 2007 and 2012, respectively

Shuo Cui was born in Qinhuangdao, China, in 1993. She received the B.E. degree in Applied Physics from Beihang University, Beijing, China, where she is currently working toward the Ph.D. degree in Electromagnetic Compatibility and Electromagnetic Environment. Her current research interests include electromagnetic emission and Electromagnetic calculation.

Weimin Li was born in Taiyuan, China, in 1981. She received the Ph.D. degree in Circuits and Systems in 2012 from Beihang University. He is currently a Senior Engineer with China Academy of Launch Vehicle Technology, Beijing, China. His research focuses on electromagnetic compatibility test.

Frequency Response of Electromagnetic Wave Propagation in Power Tracks

Cexing Wang and Tao Su

School of Electronics and Information Technology
Sun Yat-sen University, Guangzhou, Guangdong, China
wangcx3@mail2.sysu.edu.cn, sutao@mail.sysu.edu.cn

Abstract ― Previous investigations into the on-chip power distribution network (OCPDN) have focused on low frequency ranges. This study analyzes the high-frequency behavior of OCPDNs, where the wavelength approaches the dimension of the OCPDN and the track structure in the OCPDN. A theoretical model based on transmission line theory with common mode and differential mode analysis is established. The model shows that the power tracks can block the propagation of electromagnetic waves in certain frequency ranges and that wide stopbands exist. Full wave simulation based on (HFSS) is performed to verify the model. The simulation results match the theory, confirming the predicted behavior of the power tracks. Measurements are performed on prototype power tracks and the results are again consistent with the theory. The behavior of the power tracks shown here provides important information for the design of integrated circuits for millimeter-scale wave communications.

Index Terms ― Frequency response, on-chip power distribution network, pass-band, stop-band.

I. INTRODUCTION

Radio technologies in 5G communication employ millimeter-scale waves [1-3]. High-speed communication with large bandwidth is key to 5G communication. In addition, the stability of integrated circuits must be considered. Part of the on-chip power distribution network (OCPDN) for graphic memory is shown in Fig. 1. The structure consists of equidistant power tracks and shows periodicity in some parts.

The OCPDN may be exposed to signals with frequencies up to 100 GHz in the complex electromagnetic environment. Previous studies have analyzed the electromagnetic interference of power distribution network (PDN) below or close to 1 GHz [4]; however, its behavior in the millimeter-scale wave range is not well understood. Other studies into suppressing OCPDN noise [5-8] typically use extra structures instead of improving the power tracks. Many researchers have treated the problem of OCPDN analysis using numerical approaches with lumped elements. Therefore, a method of OCPDN analysis at such high frequencies is worth developing.

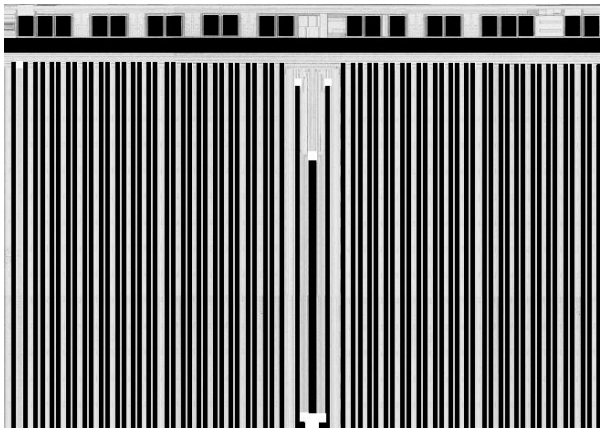

Fig. 1. Power tracks of the PDN in a memory integrated circuit.

According to [9], the shunt tracks of a periodic structure produce a stopband, which has a Bragg-like effect. In recent years, many studies have attempted to reduce the mutual coupling; for example, by using an electromagnetic band gap structure (EBG) [10, 11] or electromagnetic shielding mesh structure [12]. These periodic structures can block electromagnetic waves. Analyzing the behavior of the PDN by transmission line theory is possible because the space between the source and ground tracks is very small. In this study, we focus on the power tracks. As the wavelength approaches the feature size of the OCPDN, Bloch-like theory can be established to describe the behavior of the OCPDN. The following sections show the development of this theory.

II. THEORETICAL MODEL

A. System model

The power track structure is illustrated in Fig. 2, with some modifications. It consists of metal tracks distributed equidistantly on a ring. Consider the following scenario: a source is connected to the center of the left edge of the ring while a load is connected to the

Submitted On: September 22, 2018
Accepted On: March 21, 2019

center of the right edge of the ring. The characteristics of the power track structure for wave propagation can then be described using the ratio of outgoing power on the load to incoming power from the source; i.e., the S_{21} parameter. The objective is to solve the problem using the physical dimensions of wave propagation as well as process-related parameters.

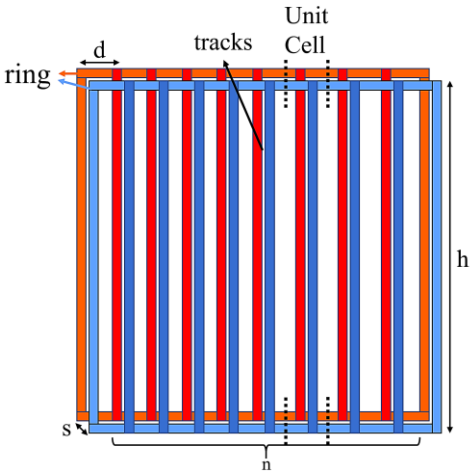

Fig. 2. A schematic model of power tracks.

The structure shows strong periodicity; it can be considered as a sequence of unit cells shown in Fig. 3 (a). As the wavelength of the electromagnetic wave is comparable to the cell dimension, the length of the track is half the wavelength and the interconnection between two tracks (one segment of the ring) is one eighth the wavelength in this paper. The tracks and the segments between two tracks should be considered as transmission lines. Their line impedances and propagation constants are Z_H, β_H and Z_W, k respectively.

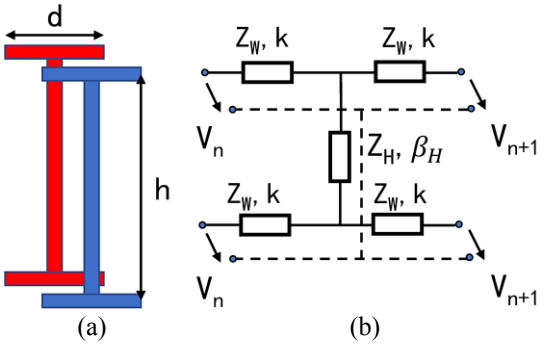

Fig. 3. (a) A unit cell of the power tracks. (b) Equivalent circuit of the unit cell.

The upper and lower parts of the power track are symmetrical. The source and the load are on the axis of symmetry. It is reasonable to consider wave propagation with the common mode method: the upper and lower edges of the ring have the same voltage distribution, as shown in Fig. 3 (b). Then, the unit cell can be split into two T cells, as shown in Fig. 4 (a), whose behavior is identical. Thus, only one T cell needs to be analyzed.

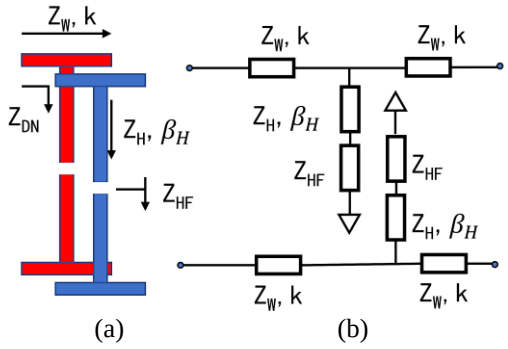

Fig. 4. (a) Two T cells of the unit cell. (b) The transmission line common mode model of the two T cells.

In Fig. 4, Z_{HF} denotes the load impedance viewed from the center of the track down or up. The equivalent impedance of a T cell will be discussed in the next section.

B. Common mode analysis

The behavior of the T cell can be described with an ABCD matrix. Given the cell size, the wave propagation constant and the line impedances, the ABCD matrix can be written into (2) in normalized form. Readers may refer to [13] for deduction details:

$$\begin{bmatrix} V_n \\ I_n \end{bmatrix} = \begin{bmatrix} A & B \\ C & D \end{bmatrix} \begin{bmatrix} V_{n+1} \\ I_{n+1} \end{bmatrix}, \tag{1}$$

$$\begin{bmatrix} A & B \\ C & D \end{bmatrix} = \begin{bmatrix} \cos\frac{kd}{2} & j\sin\frac{kd}{2} \\ j\sin\frac{kd}{2} & \cos\frac{kd}{2} \end{bmatrix} \begin{bmatrix} 1 & 0 \\ jZ_W Y_{DN} & 1 \end{bmatrix} \begin{bmatrix} \cos\frac{kd}{2} & j\sin\frac{kd}{2} \\ j\sin\frac{kd}{2} & \cos\frac{kd}{2} \end{bmatrix}. \tag{2}$$

The input impedance of the track, viewed from the ring edge into the track, is Z_{DN} (Fig. 4). For common mode operation, the middle point can be considered as an open, meaning that Z_{HF} equals ∞. Therefore, the input impedance of the track is given as:

$$\begin{aligned} Z_{DN} &= Z_H \frac{Z_{HF} + jZ_H \tan\beta_H \frac{h}{2}}{Z_H + jZ_{HF} \tan\beta_H \frac{h}{2}}, \\ &= Z_H \frac{\infty + jZ_H \tan\beta_H \frac{h}{2}}{Z_H + j\infty \tan\beta_H \frac{h}{2}}, \\ &= \frac{Z_H}{j\tan\beta_H \frac{h}{2}}. \end{aligned} \tag{3}$$

The values of k and β_H are equal in the model. Due to the periodicity of the tracks, the propagated wave on the power tracks can be defined as:

$$V_{n+1} = V_n e^{-j\beta d}. \tag{4}$$

Combining (2), (3), and (4) provides the dispersion relationship of the wave propagation in (5). For wave propagation without attenuation, in other words, the solution of $\cos \beta d$ exists in equation (5) and condition (6) should be satisfied. Frequency ranges violating condition (6) correspond to the stopbands:

$$\cos \beta d = \cos kd - \frac{1}{2}\frac{Z_W}{Z_H}\tan\frac{kh}{2}\sin kd, \tag{5}$$

$$f(k) = \left|\cos kd - \frac{1}{2}\frac{Z_W}{Z_H}\tan\frac{kh}{2}\sin kd\right| < 1. \tag{6}$$

Equation (6) is transformed into (7) and (8). The passband regions are shown in Fig. 5. In this figure, the horizontal axis is the propagation constant, k, and the vertical axis is the tangent function of k:

$$\frac{1}{2}\frac{Z_W}{Z_H}\tan\frac{kh}{2}\tan\frac{kd}{2} \le 1, \tag{7}$$

$$-1 \le \frac{1}{2}\frac{Z_W}{Z_H}\frac{tan\frac{kh}{2}}{tan\frac{kd}{2}}. \tag{8}$$

The method used for analyzing the power tracks is essentially the transmission line common model method. Further to the above equations, we can also build an equivalent circuit of the power tracks, as shown in Fig. 6, which gives the S_{21} parameter of every frequency.

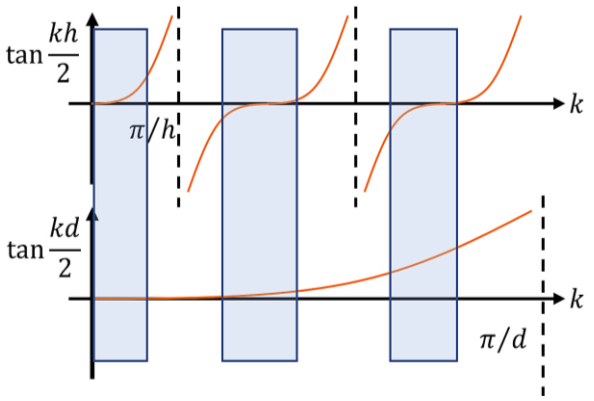

Fig. 5. Passband calculated with the common mode method.

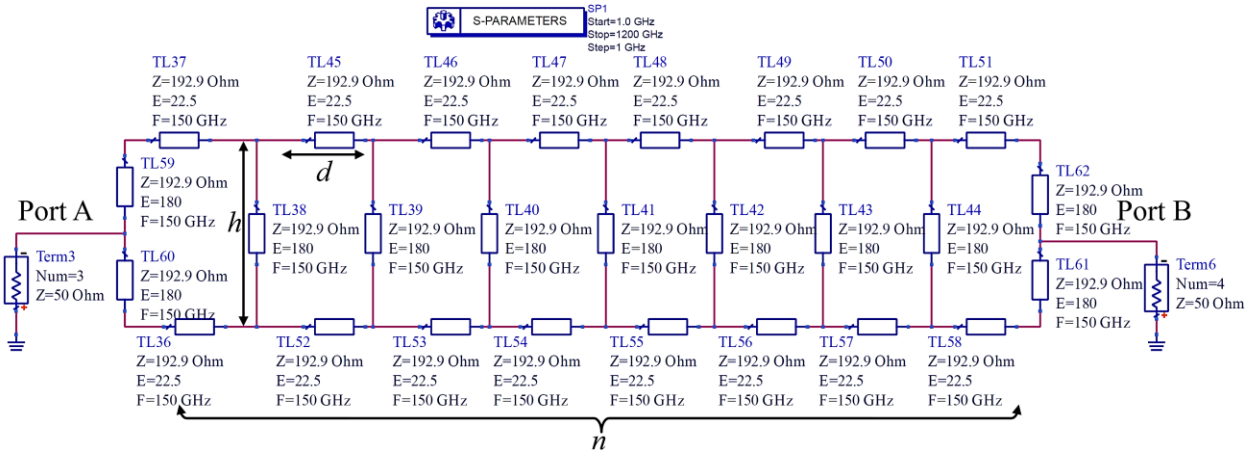

Fig. 6. Common mode model of ADS consisting of lossless transmission lines.

C. Differential mode analysis

Common mode wave propagation is an extreme situation with symmetrical ports. Moreover, the ports can be set anywhere on the power tracks, which makes the problem much more complex. Another extreme situation occurs whereby the wave phases in the upper and lower ends of the power tracks are opposite. Then, the two waves meet at the midpoint with a phase difference of 180°. This method is called differential mode, in which the middle point of the power tracks can be considered a short, meaning that Z_{HF} equals 0 as shown in Fig. 7.

For differential mode operation, the input impedance of the track is:

$$\begin{aligned} Z_{DN} &= Z_H \frac{Z_{HF} + jZ_H \tan\beta_H\frac{h}{2}}{Z_H + jZ_{HF}\tan\beta_H\frac{h}{2}}, \\ &= Z_H \frac{0 + jZ_H \tan\beta_H\frac{h}{2}}{Z_H + j0\tan\beta_H\frac{h}{2}}, \\ &= j\,Z_H \tan\beta_H\frac{h}{2}. \end{aligned} \tag{9}$$

Combining (2), (4), and (9), gives the dispersion relationship of the wave propagation in (10). For wave propagation without attenuation, condition (11) should be satisfied. Frequency ranges violating condition (11) correspond to the stopbands:

$$\cos \beta d = \cos kd + \frac{1}{2}\frac{Z_W}{Z_H}\frac{1}{\tan\frac{kh}{2}}\sin kd, \tag{10}$$

$$g(k) = \left|\cos kd + \frac{1}{2}\frac{Z_W}{Z_H}\frac{1}{\tan\frac{kh}{2}}\sin kd\right| < 1. \quad (11)$$

Equation (11) is transformed into (12) and (13). The passband regions are shown in Fig. 8:

$$\frac{1}{2}\frac{Z_W}{Z_H}\frac{1}{tan\frac{kh}{2}tan\frac{kd}{2}} \le 1, \quad (12)$$

$$-1 \le \frac{1}{2}\frac{Z_W}{Z_H}\frac{tan\frac{kd}{2}}{tan\frac{kh}{2}}. \quad (13)$$

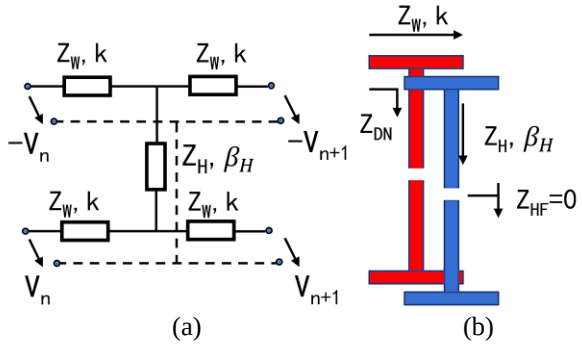

Fig. 7. (a) Voltage distribution, and (b) unit cell of the differential mode.

Through Advanced Design System (ADS) simulation, an ideal differential mode model is built to verify this method. There are two inputs at either end of the left edge, as shown in Fig. 9. The phase difference between the two input signals is 180°. At any location of the left edge, the source will produce two modes at the same time. According to our theory, the input impedance of the track and the general dispersion relationship is:

$$\Gamma = e^{-j\theta} = \frac{Z_L - Z_0}{Z_L + Z_0}, \quad (14)$$

$$Z_{DN} = Z_0\frac{Z_L + jZ_0\tan\beta_H\frac{h}{2}}{Z_0 + jZ_L\tan\beta_H\frac{h}{2}}, \quad (15)$$

$$\cos\beta d = \cos kd + \frac{1}{2}j\frac{1+jatan\frac{kh}{2}}{a+j\tan\frac{kh}{2}}\sin kd, \quad (16)$$

where θ is the voltage phase difference between both ends of the right edge and $a = \frac{1+e^{-j\theta}}{1-e^{-j\theta}}$.

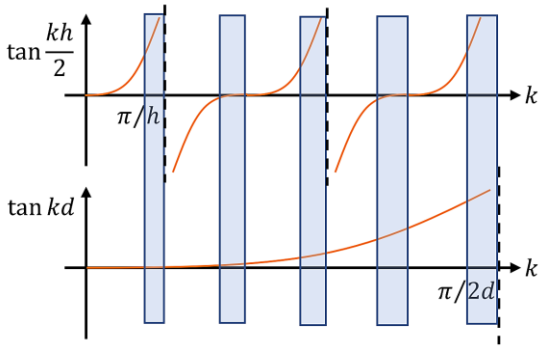

Fig. 8. Passband calculated with the differential mode method.

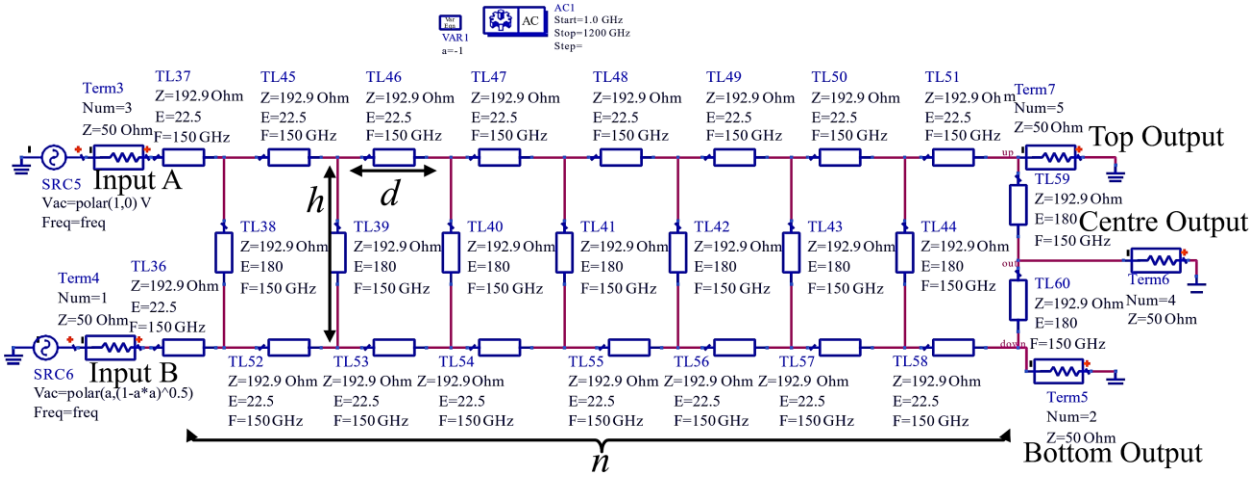

Fig. 9. Differential mode model of ADS consisting of lossless transmission lines.

III. VERIFICATION BY SIMULATION

In this section, we discuss the common-mode and differential-mode behavior and solve the problem of hybrid mode wave propagation. To illustrate this behavior, a simulation with the following parameters is used to verify our model: h represents the length of power tracks, d is the width of the unit cell, and n represents the number of unit cells. The cross-section of the ring and track are the same. The ring and track have the same line impedance, Z_0, which is equal to 192.924 Ω. Figure 10 compares $f(k)$ and 1 for h = 1 mm, d = 0.125 mm and n ranges from 7 to 21. According to the common mode

model and equation (6), the frequency ranges where $f(k)$ is above 1 correspond to the stopband, whereas other frequency ranges correspond to the passband. It is expected that the electromagnetic waves of the four bands will be blocked by the power tracks.

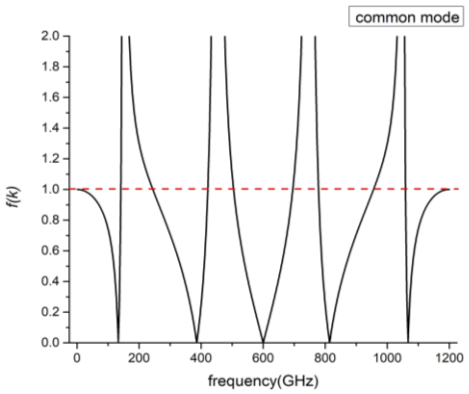

Fig. 10. Theoretical result of the common mode model.

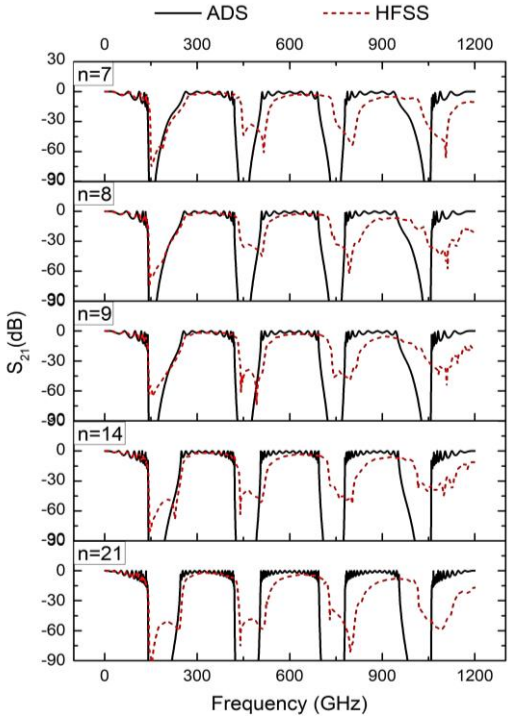

Fig. 11. Simulated S_{21} parameter with a variable number of tracks.

Figure 11 shows the simulation results of the common-mode equivalent circuit. It again predicts a stopband very close to the frequency range of the theoretical result. The three-dimensional structure of the power tracks is built using high-frequency structure simulator (HFSS) for full wave simulation. The results are also shown in Fig. 11. The HFSS simulation results match the ADS simulation results very well, and the two have very close stopbands. In the high-frequency range above 700 GHz, due to the skin effect, the HFSS simulation model impedance mismatch causes greater attenuation. The ranges of the stopband are weakly dependent on the number of unit cells if n is sufficiently large.

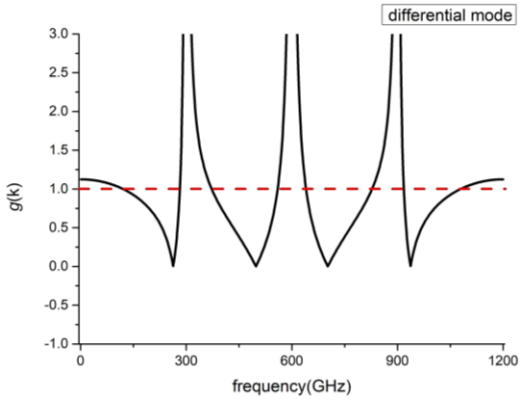

Fig. 12. Theoretical result of the differential mode model.

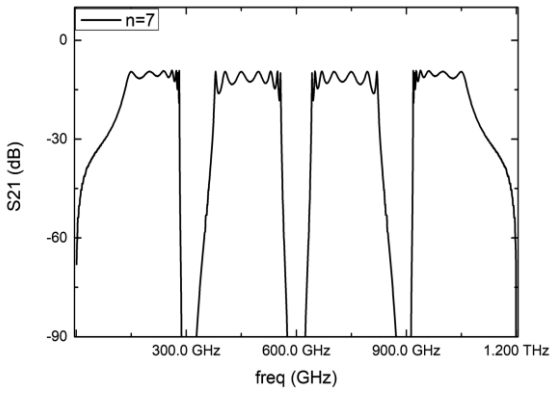

Fig. 13. S_{21} at the top output of the differential mode equivalent circuit in ADS.

Figure 12 compares $g(k)$ and 1. According to the differential mode model and (11), frequency ranges where $g(k)$ is above 1 also correspond to the stopband. In contrast to the common mode, the first stopband is near the DC area. The first passband area is located from approximately 121 GHz to 282 GHz. Figure 13 shows the simulation result of the ideal differential mode equivalent circuit in Fig. 9, which predicts the passbands close to the calculated frequency range. Meanwhile, electromagnetic wave near the DC area is blocked by the differential mode equivalent circuit. It should be noted that the frequency response of the differential mode is an ideal case. In fact, not only differential mode wave propagation but also common mode wave propagation

occurs at the same time. Figure 14 indicates that the differential mode is suppressed at the center output. In contrast to the midpoint, the output located in the rightmost track comprises two modes of guided waves. Therefore, we can predict differential mode behavior by subtracting the behavior at the midpoint.

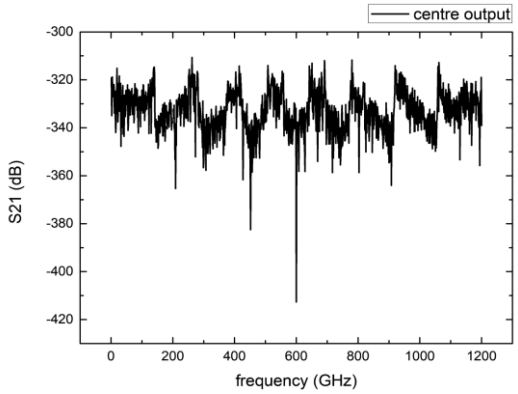

Fig. 14. S_{21} at the center output of the differential mode equivalent circuit in ADS.

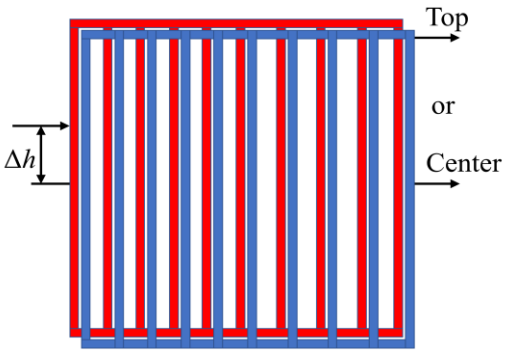

Fig. 15. Hybrid mode model.

Figure 15 shows the model used to verify the hybrid mode propagation. Δ*h* is the distance between the input location and the midpoint. The port at the top of the right edge collects the hybrid mode information but the midpoint can only collect common mode information. Only one output port is used at a time. The total length of the tracks is 1 mm. Five input locations are set to show the overlap of the hybrid mode. According to the differential mode method, there is no differential mode wave propagation while the input is at the midpoint.

As shown in the theoretical result and equivalent circuit simulation, the power of electromagnetic waves near 0 GHz, 300 GHz, 600 GHz, 900 GHz, or 1200 GHz are blocked by the differential mode method. Directly measuring the wave conduction of the differential mode is difficult; thus, equation (17) verifies the existence of the power of the differential mode:

$$\Delta|S_{21}|^2 = \left|S_{21hybrid}\right|^2 - |S_{21common}|^2. \quad (17)$$

The subtraction results from ADS and HFSS simulations are shown in Fig. 16. By subtracting the common mode EM wave, the results also show the stopbands near 0 GHz, 300 GHz, 600 GHz, 900 GHz, and 1200 GHz.

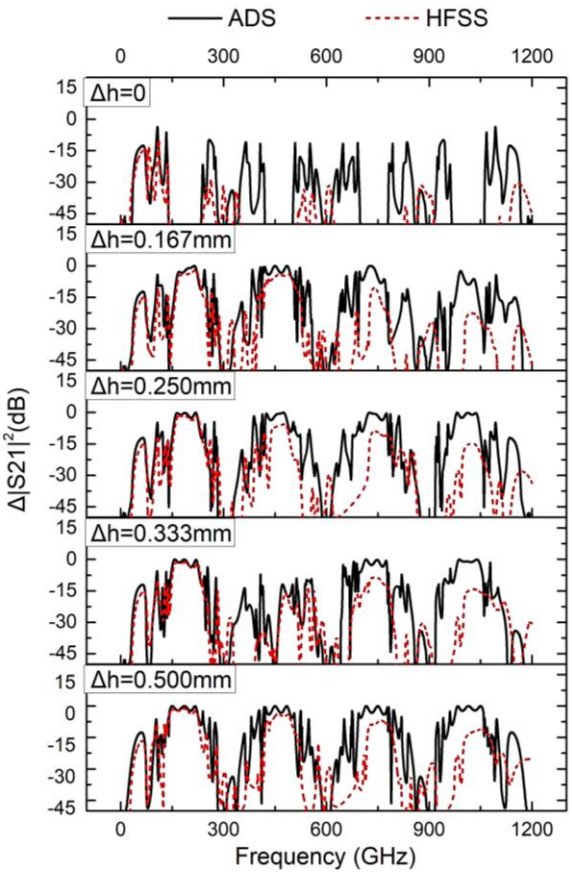

Fig. 16. $|S_{21top}|^2$ - $|S_{21center}|^2$ of simulations with a variable input distance.

IV. VERIFICATION BY MEASUREMENT

In this section, geometrical scale model measurements [14] based on a printed circuit board (PCB) shown in Fig. 17 are compared with the transmission line mode in ADS. The common mode test corresponds to port1 and port3, and the hybrid mode test corresponds to port2 and port4. With the following parameters: h = 100 mm, d= 12.5 mm, n = 7, and relative permittivity of the dielectric substrate is equal to 4.5, the first stopband of the common mode ranges from 0.8 to 1.3 GHz, according to the theory. By referring to [15], the attenuations can be calculated by the following equation:

$$\alpha\left[\frac{dB}{m}\right] = \frac{20\pi}{ln10}\frac{1}{Q_c\lambda_g}, \quad (18)$$

Q_c represents the quality factor at the resonant frequency and λ_g is the wavelength in the power tracks.

In the measurement, the effective permittivity is equal to 3.3, loss coefficient is equal to 3.66 dB/m, and dielectric loss angle tangent is equal to 0.05.

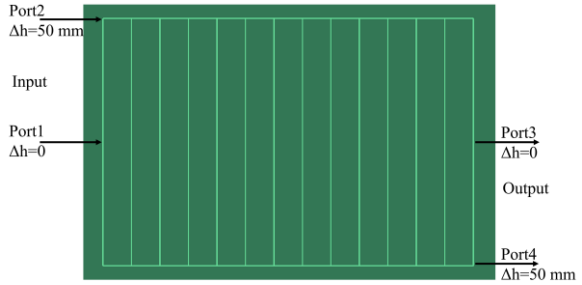

Fig. 17. Prototype of power tracks based on a printed circuit board.

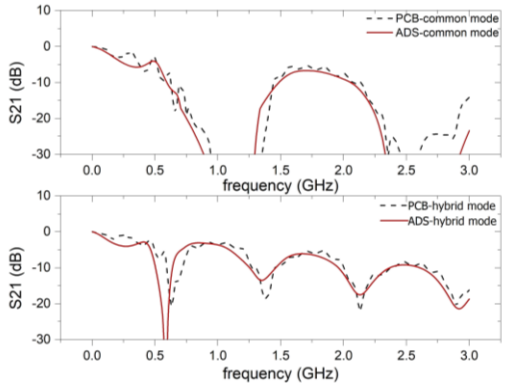

Fig. 18. Measurement and ADS results of common mode and hybrid mode methods.

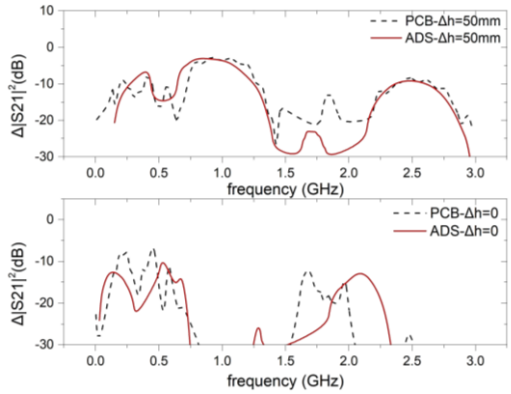

Fig. 19. Subtraction results of common mode and hybrid mode methods.

As shown in Fig. 18, the first stopband is very close to the frequency range and the second stopband also obeys the common mode theory. In Fig. 18, the hybrid mode measurement shows a different frequency response from the common mode and differential mode methods. To confirm the existence of the differential mode, this section calculates the power and squares S_{21} to obtain the result of the mixed-mode power minus the common-mode power in the simulation and experiment, respectively. Figure 19 shows the subtraction results from the measurement and transmission line model for $\varepsilon_{eff} = 3.3$, $\alpha = 3.66\,\mathrm{dB/m}$, and $\tan\delta = 0.05$. According to the differential mode theory, the above simulation shows the passband near 200 GHz, which corresponds to 1.2 GHz from the measurement. We verify that the power can split into two modes. If the input or output is set at the midpoint, no differential mode propagation occurs in the measurement either.

V. CONCLUSION

The propagation of electromagnetic waves in power tracks consists of two modes: common mode and differential mode. The first stopband of the common mode is where the wavelength is about twice the track length. The first stopband of the differential mode is where the wavelength is more than twice the track length. The widths of the stopband increase with the number of tracks and become saturated as the track number exceeds nine. Equations are presented for calculating the exact range of the stopbands. The frequency response of propagation in the power tracks in the general case is a combination of common-mode behavior and differential-mode behavior; it varies with the location of the source and observation points. If the source or observation point is located at the center of the power tracks, there will be no differential mode. However, because the stopbands of the two modes have an overlap, there is always a stopband for the propagation.

Employing equivalent circuits based on transmission line theory is an effective method for analyzing power tracks, as proved with field simulations and practical measurements. The frequency response of the power track reveals the millimeter-scale wave electromagnetic properties of on-chip power distribution networks. Our future study will work on more complex mesh structure. It also aids the development of new structures for millimeter-scale wave filter design.

ACKNOWLEDGMENT

Project 61471402 was supported by the National Science Foundation of China.

REFERENCES

[1] P. A. Dzagbletey and Y. Jung, “Stacked microstrip linear array for millimeter-wave 5G baseband communication,” *IEEE Antennas Wirel. Propag. Lett.*, vol. 17, no. 5, pp. 780-783, May 2018.

[2] S. Zhu, H. Liu, Z. Chen, and P. Wen, “A compact

gain-enhanced vivaldi antenna array with suppressed mutual coupling for 5G mm wave application," *IEEE Antennas Wirel. Propag. Lett.*, vol. 17, no. 5, pp. 776-779, May 2018.

[3] C. Choi, J. H. Son, O. Lee, and I. Nam, "A +12-dBm OIP3 60-GHz RF downconversion mixer with an output-matching, noise- and distortion-canceling active balun for 5G applications," *IEEE Microw. Wirel. Compon. Lett.*, vol. 27, no. 3, pp. 284-286, Mar. 2017.

[4] C. Yoon, et al., "A slope and amplitude controllable triangular-current generator for the injection of a broad-band PDN noise," *IEEE Electromagn. Compat. Mag.*, vol. 5, no. 4, pp. 112-116, Fourth Quarter 2016.

[5] J. Cho, Y. Kim, J. Kim, V. Sundaram, and R. Tummala, "Analysis of glass interposer PDN and proposal of PDN resonance suppression methods," *2013 IEEE International 3D Systems Integration Conference (3DIC)*, San Francisco, CA, pp. 1-5, 2013.

[6] K. Cho, et al., "Design and analysis of power distribution network (PDN) for high bandwidth memory (HBM) interposer in 2.5D terabyte/s bandwidth graphics module," *2016 IEEE 66th Electronic Components and Technology Conference (ECTC)*, Las Vegas, NV, pp. 407-412, 2016.

[7] S. Kim, Y. Kim, K. Cho, J. Song, and J. Kim, "Design and measurement of a novel on-interposer active power distribution network for efficient simultaneous switching noise suppression in 2.5-D/3-D IC," *IEEE Trans. Compon., Packag. Manuf. Technol.*, in press.

[8] H. Kim, S. Kim, J. Kim, C. Yoon, B. Achkir, and J. Fan, "On-chip linear voltage regulator module (VRM) effect on power distribution network (PDN) noise and jitter at high-speed output buffer," in *IEEE Electromagn. Compat. Mag.*, vol. 4, no. 2, pp. 108-113, Second Quarter 2015.

[9] C. Caloz and T. Itoh, *Electromagnetic Metamaterials: Transmission Line Theory and Microwave Applications*. Wiley-IEEE Press, 2006.

[10] I. Mazraeh-Fard, et al., "Design of a planar surface wave antenna with a bidirectional pattern based on periodic structures for telemetry applications," *Applied Computational Electromagnetics Society Journal*, vol. 31, no. 12, pp. 1431-1438, 2016.

[11] T. Jiang, T. Jiao, and Y. Li, "A low mutual coupling mimo antenna using periodic multi-layered electromagnetic band gap structures," *Applied Computational Electromagnetics Society Journal*, vol. 33, no. 3, pp. 305-311, 2018.

[12] H. M. El-Maghrabi, "Electromagnetic shielding effectiveness calculation for cascaded wire-mesh-screens with glass substrate," *Applied Computational Electromagnetics Society Journal*, vol. 33, no. 6, pp. 641-647, 2018.

[13] D. M. Pozar, *Microwave Engineering*. John Wiley & Sons, Inc., New York, 2012.

[14] C. A. Balanis, K. Zhang, and C. R. Birtcher, "Geometrical scale modeling of gain and echo area: simulations, measurements and comparisons," *Applied Computational Electromagnetics Society Journal*, vol. 33, no. 1, pp. 95-98, Jan. 2018.

[15] R. A. Pucel, "Design considerations for monolithic microwave circuits," in *IEEE Transactions on Microwave Theory and Techniques*, vol. 29, no. 6, pp. 513-534, June 1981.

Cexing Wang received the B.S. degree in Electrical Engineering from Sun Yat-sen University, Guangzhou, China, in 2017, where he is currently pursuing the M.S. degree.

His current research interests include the analysis of frequency response in OCPDN and filter design based on periodic structure.

Tao Su was born in Yiyang, China, in 1977. He received the B.Sc. degree in Physics from the University of Science and Technology of China, Hefei, China, in 2000, the M.Sc. degree in Microwave Engineering from the Munich University of Technology, Munich, Germany, in 2005, and the Doktor-Ingenieur degree in Electronic Engineering from the University of Erlangen-Nurnberg, Erlangen, Germany, in 2009.

He worked as a Doctor Student with Infineon Technologies AG, Munich, from 2006 to 2009. He is now an Associate Professor in the School of Electronics and Information Technology at Sun Yat-sen University, Guangzhou, China. His current research interest is the integrated circuits design.

A New Time-of-Flight Extraction Method for Narrowband Lamb Wave in Metallic Plate

Zhe Wang [1], Songling Huang [1], Qing Wang [2], Shen Wang [1], and Wei Zhao [1]

[1] State Key Laboratory of Power System, Department of Electrical Engineering
Tsinghua University, Beijing, 100084, China
huangsling@mail.tsinghua.edu.cn

[2] Department of Engineering, Durham University, Durham, DH1 3LE, United Kingdom

Abstract ─ Lamb wave is potential to evaluate the health state of plate-like structures in nondestructive testing. However, the dispersive and multimodal properties of Lamb wave bring negative effect on the extraction of time-of-flight (TOF) which is important information to map the structure. This paper proposes a new method based on the ridge analysis to accurately extract the TOF of narrowband Lamb wave. The method establishes the ridge curve in the time-frequency domain and then, the TOF of corresponding frequency can be obtained utilizing the time information in the ridge. An experiment system using the electromagnetic acoustic transducer is established on the steel plate to verify the performance of the proposed method. The results show that the ridge analysis method has higher accuracy than the traditional Hilbert Transform method. Furtherly, the sensitive analysis proves that the proposed method owns high stability and strong robustness.

Index Terms ─ Dispersion, Lamb wave, nondestructive testing, ridge analysis.

I. INTRODUCTION

The health monitoring of metallic plate is vital in the development of modern industry [1]. Lamb wave used in nondestructive testing provides an efficient method to inspect the defects in metallic plate [2]. Lamb wave propagating along the structure for a significant distance is sensitive to both surface and internal defects. By extracting the information in Lamb wave signal, the defect can be recognized and located, and the inspected structure can be mapped [3-5]. The commonly used features of the Lamb wave contain the time-of-flight (TOF), amplitude, frequency, phase and so on [6].

Lamb wave is a common mode propagating in plate-like structures. It can be easily generated by piezoelectric transducer or electromagnetic acoustic transducer (EMAT). Derived from medical X-ray tomography, Lamb wave tomography imaging (TI) has been developed for evaluating defects in metallic plates [7-8]. The technology of TI needs the accurate TOF of Lamb wave as the input information. TOF not only influences the locations of defects, but also affects the determination of defect depth. However, Lamb wave has the nature of dispersion which means the velocity of Lamb wave is dependent on the frequency. This phenomenon will bring dilation of Lamb wave packets in time domain after Lamb wave propagates a certain distance [9]. Thus the dispersion increases uncertainty in the determination of TOF. Lamb wave owns another characteristic of multimode, which means multiple modes coexist in structure although with one incitation frequency [10]. This phenomenon complicates the Lamb wave signals and makes it difficult to extract the TOF. Besides, noise which overwhelms the useful inspection signals cannot be ignored in actual inspection environment.

Several time-frequency analysis methods have been developed to extract the TOF of Lamb wave. The wavelet network trained to model the cross correlation was applied to measure the time between the ultrasonic pulse and reflected echo [11], but the construction of neural network needed enough training sets. The time-frequency energy density precipitation method established the time-domain energy density curve to calculate the TOF of narrowband Lamb wave inspection signal, which was feasible in dealing with the initial space-induced pulse from excitation signal [12]. The Hilbert Transform (HT) which detected the peak value of signal was applied to extract the characteristics of captured Lamb wave [13]. Ridge detection based on wavelet transform and Markov chain was proposed [14] and implemented in separation of multimodal guided wave signals in long bones [15]. Although the above methods provide effective measurement of TOF in specific situations, the time extraction is still limited by the dispersive nature of Lamb wave [16].

In the work to be described here, a new method based on short time Fourier transform (STFT) is proposed to extract the accurate TOF of narrowband Lamb wave. The theoretical foundations of the dispersive

Submitted On: September 18, 2018
Accepted On: January 26, 2019

Lamb wave are analyzed. Then basic procedures of the ridge analysis method are presented. The Lamb inspection experiment system is established to validate the effectiveness of the proposed method. For comparison, the traditional HT method is implemented. Besides, the sensitivity analysis for the proposed method is conducted.

II. TOF EXTRACTION METHOD BASED ON RIDGE ANALYSIS

The ridge analysis method utilizes the dispersive property of Lamb wave. It establishes the ridge curve in the time-frequency domain. Then the TOF information can be accessed through the ridge.

A. Theoretical analysis of the dispersive Lamb wave

Compared with ultrasonic bulk wave, it is advantageous that Lamb wave attenuates slowly along the structure and its wave field exists in the whole plate. However, the velocity of Lamb wave is not consistent. The Rayleigh-Lamb equation describes the essential feature of Lamb waves. Specifically, the symmetric and asymmetric modes can be separately expressed as [17]:

$$\frac{\tan(qh)}{\tan(ph)} = -\frac{4k^2pq}{(q^2-k^2)^2}, \tag{1}$$

$$\frac{\tan(qh)}{\tan(ph)} = -\frac{(q^2-k^2)^2}{4k^2pq}, \tag{2}$$

where $h = \frac{1}{2}d$, $p^2 = \frac{\omega^2}{c_L^2} - k^2$, $q^2 = \frac{\omega^2}{c_T^2} - k^2$, $k = \frac{\omega}{c_p}$, d is the plate thickness. c_L is the longitudinal wave velocity. c_T is the transverse wave velocity. c_P is the phase velocity. ω is the angular frequency and k is the wave number.

From equations (1) and (2), it is clear that the velocity of Lamb wave is dependent on the plate thickness and frequency. This phenomenon is called dispersion. Furtherly, the group velocity of Lamb wave is defined as $c_g = \frac{d\omega}{dk}$, which can be derived from the phase velocity. For a steel plate with Poisson's ratio of 0.28 and density of 7850 $k_g \cdot m^{-3}$, the Rayleigh-Lamb equation can be solved numerically and the phase velocity and group velocity dispersion curves can be obtained. The results are shown in Fig. 1. The symmetric and asymmetric modes of Lamb wave are marked as *S* mode and *A* mode, respectively.

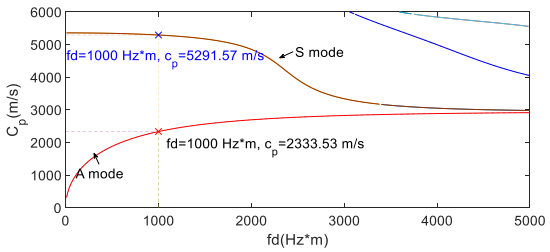

(a) Phase velocity dispersion curves

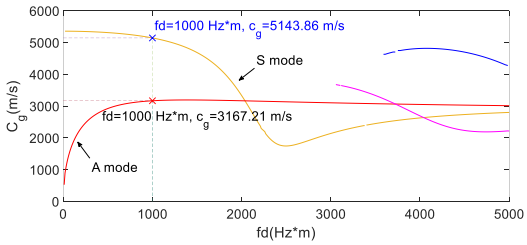

(b) Group velocity dispersion curves

Fig. 1. Dispersion curves of Lamb wave.

After Lamb waves of different frequencies propagate over a distance in plate, the time duration of wave packets would increase because of the dispersion. Then it will bring negative influence in the extraction of TOF. Therefore, to minimize the dispersion and control the mode of generated Lamb waves, the excitation signal should have narrow bandwidth. A windowed toneburst is usually adopted as the excitation signal. The Hanning window can be expressed as:

$$w(n) = \frac{1}{2}\left(1 - \cos\left(\frac{2\pi n}{N-1}\right)\right) R_N(n), \tag{3}$$

where N is the length of window and $R_N(n)$ is the rectangular window. The truncation effect of the window leads to spectrum leakage. The signal bandwidth could be in a region from f_{min} to f_{max} [9]:

$$f_{min} = f_0\left(1 - \frac{K}{n}\right), \tag{4}$$

$$f_{max} = f_0\left(1 + \frac{K}{n}\right), \tag{5}$$

where n is the cycle of the window and K is a constant. Figure 2 shows the signal and spectrum of a 5-cycle toneburst with the center frequency of 100 kHz.

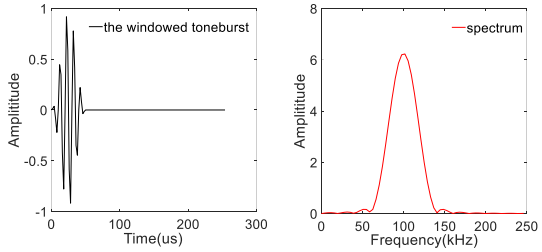

Fig. 2. 5-cycle toneburst and its spectrum.

B. Procedures of the ridge extraction method

The Lamb wave signal is typically non-stationary and its frequency varies over time. The Fourier Transform has the best frequency solution, but it lacks the time location of frequency. Therefore, it is not suitable to analyze Lamb wave signal. STFT, also called windowed Fourier transform, overcomes the shortcoming described as above. Giving signal $\boldsymbol{x(t)} \in \boldsymbol{L^2(R)}$, the definition of STFT is expressed as follows:

$$STFT(t,\omega) = \int x(\tau)g^*(\tau - t)e^{-j\omega\tau}d\tau, \quad (6)$$

where $g(t)$ is a window function. It satisfies $\|g(t)\| = 1$. The length of window function is an important parameter influencing the resolution of STFT. Subjected to the uncertainty principle, the shorter window length leads to better time resolution, but worse frequency resolution. The energy density spectrum called spectrogram is defined as:

$$S_x(t,\omega) = |STFT(t,\omega)|^2. \quad (7)$$

Due to the dispersive nature, Lamb waves of different frequencies arrive at the receiver at different times. Therefore, the spectrogram is like a mountain with inclined ridge in the time and frequency representation. To obtain the accurate TOF, the ridge analysis method is proposed and the theoretical procedures are listed as follows:

Step 1: Perform the discrete STFT on the preprocessed narrowband Lamb wave signal and calculate the spectrogram:

$$S_x(t_m,\omega_k) = |\sum_n x(n)g^*(n - t_m N)e^{-j\frac{2\pi}{M}nk}|^2. \quad (8)$$

Step 2: Locate the peak ridge point as the top of ridge. The peak ridge point lies in the maximum S_x in time-frequency region of wave packet:

$$(t_F,\omega_F) = \text{argmax}\, S_x(t,\omega). \quad (9)$$

Step 3: Search the other ridge points in an iterative process. The ridge is the route declined at the lowest pace in the spectrogram. After the locating of peak ridge point, the routes of the ridge in its bilateral sides are obtained by determining the ridge point one by one at discrete time.

For the right route, if (t_m,ω_m) is the former ridge point, then the frequency of next ridge point in time t_{m+1} can be expressed as in equation (10). Then the next obtained ridge point is (t_{m+1},ω_{m+1}):

$$\omega_{m+1} = \text{argmin}\left|\frac{S_x(t_{m+1},\omega_{m+1}) - S_x(t_m,\omega_m)}{\sqrt{(\omega_{m+1}-\omega_m)^2 + (t_{m+1}-t_m)^2}}\right|. \quad (10)$$

For the left route, if (t_m,ω_m) is the former ridge point, then the frequency of next ridge point in time t_{m-1} can be expressed as in equation (11). Then the next obtained ridge point is (t_{m-1},ω_{m-1}):

$$\omega_{m-1} = \text{argmin}\left|\frac{S_x(t_m,\omega_m) - S_x(t_{m-1},\omega_{m-1})}{\sqrt{(\omega_m-\omega_{m-1})^2 + (t_m-t_{m-1})^2}}\right|. \quad (11)$$

Step 4: Form the ridge curve in the time-frequency domain. After Step 3, the discrete ridge points (t_m,ω_m) are obtained. Then the least squares fitting method is used to establish the ridge curve:

$$\omega(t) = \text{argmin}\ \sum_{t_m}|\omega(t_m) - \omega_m(t_m)|^2, \quad (12)$$

where $\omega(t)$ is the fitted ridge.

Step 5: Determine the TOF. Assuming the excitation signal has the center frequency of f_c, the corresponding TOF in the fitted ridge curve can be calculated easily using the time information. For two wave packets, if the corresponding times of f_c in the obtained ridges are t_{c1} and t_{c2}, respectively, then:

$$\text{TOF} = t_{c2} - t_{c1}. \quad (13)$$

Figure 3 illustrates the procedures of the ridge analysis method.

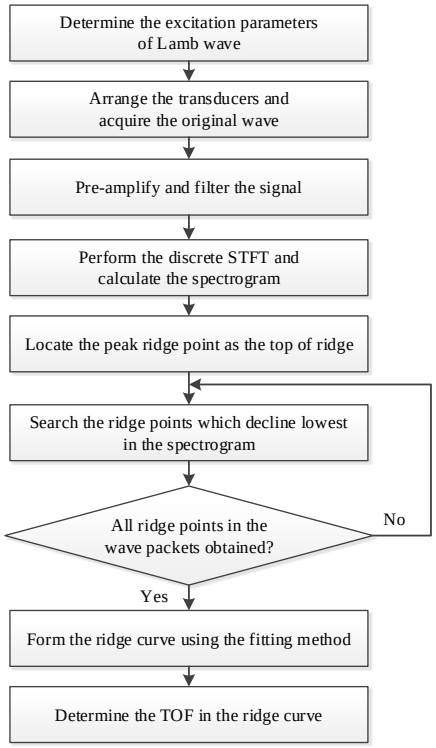

Fig. 3. The procedures of the ridge analysis method.

III. EXPERIMENTS AND RESULTS

A. Lamb inspection experiment system

To validate the effectiveness of the proposed ridge analysis method, Lamb inspection experiment system is established on the steel plate. Figure 4 (a) shows the schematic diagram of the experiment system. The inspected steel plate is 4 mm thick. The EMAT is used as the transmitter and receiver. And the EMAT is composed of meander coil and magnet, as Fig. 4 (b) shows. The coil is connected to the power amplifier and the magnet is used to supply the static offset magnetic field.

In the experiment system, the computer controls the power amplifier AG1024 to generate the high power excitation signal. The signal is Hanning windowed toneburst with the amplitude of 200 V. Its center frequency is 250 kHz and number of cycles is 5. The toneburst flows through the EAMT coil and generates the dynamic magnetic field. Based on the magnetostrictive effect and its inverse effect, the EMAT can generate and detect the Lamb waves. The received signal is amplified and filtered firstly by the signal conditioner. Then the signal is sampled by the data acquisition (DAQ) system and sent to the computer for further analysis.

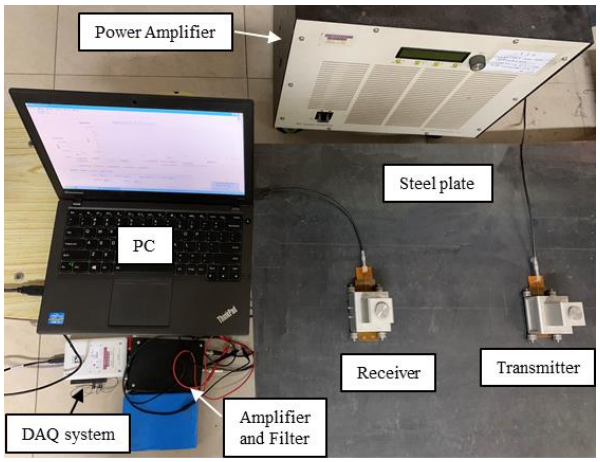

(a) The Lamb wave inspection system

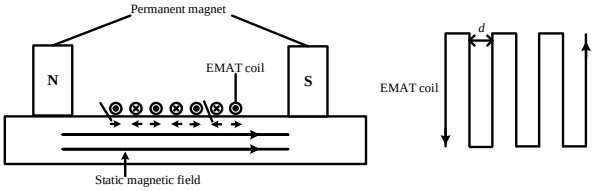

(b) Configuration of the transducer

Fig. 4. The setup of the experiment system.

S mode Lamb wave is sensitive to the defects and this mode is chosen to detect the plate. According to Fig. 1, under the parameters of corresponding excitation frequency and plate thickness, only the fundamental S mode and A mode Lamb wave exist. To generate pure A mode and avoid the modal interference, the transducer is configured deliberately. Specifically, the distance between the two adjacent coils is half of the wavelength, which can be expressed as:

$$d = \frac{1}{2}\lambda, \tag{14}$$

where λ is the wavelength of S_0 mode. And λ satisfies:

$$\lambda = \frac{c_p}{f}. \tag{15}$$

From Fig. 1, the phase velocity and group velocity of the generated S_0 mode are $5291.57\,m/s$ and $5143.86\,m/s$, respectively. Then λ can be calculated and $\lambda = 0.021\,m$.

B. TOF extracted by the ridge analysis method

In the experiment system described above, the distance between the transmitter and receiver is set as 800 mm initially and this distance can be changed by removing the receiver.

The signal waveform sent to the computer is shown in Fig. 5. During this time duration, the waves reflected from the boundary of plate have not reached the receiver and only two wave packets are collected. For clear analysis of the waveform, the two wave packets are marked as P_0 and P_1, respectively. The first wave packet P_0 is generated nearly simultaneously with the excitation toneburst signal. P_0 is the space-induced pulse which is induced by the receiver from the high power excitation signal in the transmitter. P_1 is the received signal of propagating Lamb wave. To recognize the mode of this signal, its TOF should be extracted.

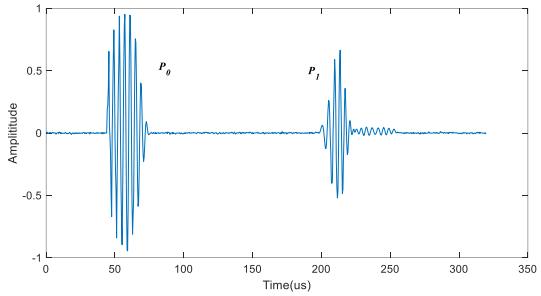

Fig. 5. The signal waveform of Lamb wave.

The signal is processed by implementing the ridge analysis method and the results are shown in Fig. 6. The Hamming function is selected as the window function of STFT. And the length of time window is 41, which is approximately one twentieth of the total sampling points. The chosen length gives a compromise of the time and frequency resolution. The fitting procedure in the proposed method weakens the influence of window length furtherly.

As Fig. 6 shows, the time-frequency distribution of the received wave packets P_1 is oblique corresponding to the axis. This phenomenon is the verification of the dispersion characteristic. The energy is concentrated along the center frequency 250 kHz, which is the same as the excitation frequency. The extracted TOF is 156.13 μs and the relative error between it and the theoretical TOF of S_0 mode is 3.27%. Therefore, the generated Lamb wave is the desired S_0 mode.

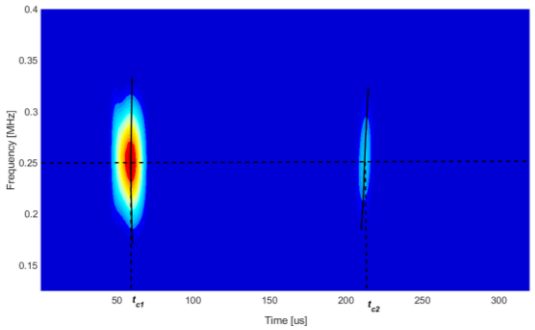

Fig. 6. The results by implementing the ridge analysis method.

To verify the accuracy of the ridge analysis method, the signal is also processed by the traditional HT method.

And then the results from the two methods are compared. Table 1 gives the calculated TOF and the relative error with the theoretical TOF. The relative error can be obtained by equation (16). The comparative results indicate that the TOF extracted by the ridge analysis method is more accurate than that extracted by the HT:

$$relative\ error = \frac{|calculated\ TOF - Theoretical\ TOF|}{Theoretical\ TOF}. \quad (16)$$

C. Sensitivity and robustness of ridge analysis method

The dispersion characteristic of Lamb wave brings the variation of velocities in difference frequency components. If Lamb wave propagates a longer distance, this dispersive phenomenon would become more remarkable, namely, the wave packet would become more dilated and the ridge curve would become more oblique.

Table 1: Comparison of TOF by ridge analysis and HT

Method	Calculated TOF (μs)	Theoretical TOF (μs)	Relative Error
Ridge Analysis	156.13	151.18	3.27%
HT	162.72	151.18	7.63%

In this part, the sensitivity and robustness of ridge analysis method are verified by re-implementing the algorithm in the Lamb wave after propagating different distance. The distances between the transmitter and receiver are changed and then the pre-amplified and filtered waveforms are acquired. For comparison, the ridge analysis method and HT are applied to extract the TOF, respectively. The results are shown in Fig. 7. Furtherly, the relative error between the theoretical TOF and calculated one is analyzed and plotted in Fig. 8.

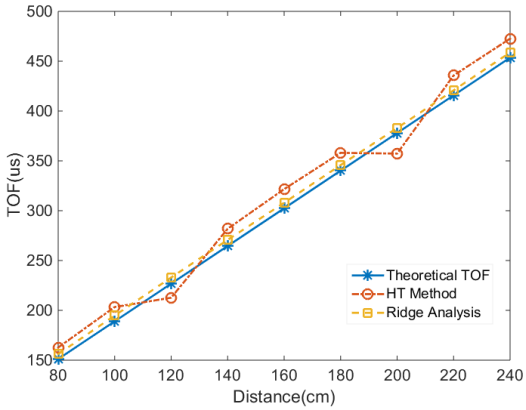

Fig. 7. The TOF extracted by HT method and the ridge analysis method.

From Fig. 7, it is clear that although the propagation distance increases, the TOF extracted by ridge analysis method is close to the theoretical TOF. While using the HT method, the difference of obtained TOF and theoretical TOF fluctuates over the distance. From Fig. 8, the presentation of relative error gives more evident comparison. The relative error from the proposed method becomes smaller when the Lamb wave propagates longer distance. This error is around 1.2% when the propagation distance is 0.24 m. Nevertheless, the relative error by HT method is much higher and this value varies considerably with different distance. The possible reason is that the HT method is influenced by the dispersive property of Lamb wave and the noise from the experiment environment.

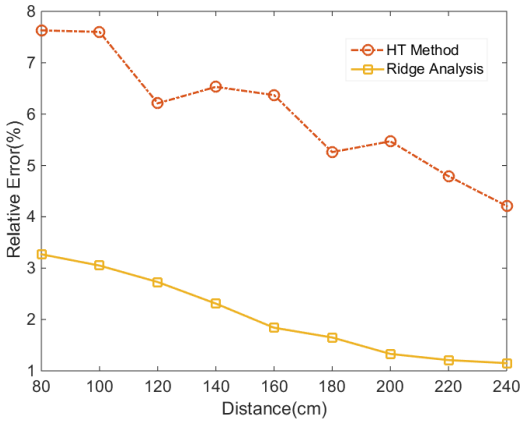

Fig. 8. The relative error of HT method and the ridge analysis method.

Due to the dispersive property, the wave packets of Lamb wave have larger duration in time than the initial excitation signal. However, the proposed method takes advantage of this property and extracts the time information steadily. What's more, the proposed method is insensitive to the experiment noise. Therefore, the ridge analysis method has better performance of accuracy and stability in terms of the extraction of TOF.

IV. CONCLUSION

In this paper, a new TOF extraction method based on the ridge analysis is proposed. This method utilizes the dispersive characteristic of Lamb wave to form the ridge curve in the time-frequency domain. The results of the experiments show that the TOF of Lamb wave inspection signal can be extracted effectively by applying the proposed method. Compared with the traditional HT method, the ridge analysis has higher accuracy. Specifically, the relative error between the TOF extracted by the proposed method and the theoretical TOF is around 1.2% when the propagation distance is 0.24 m, which is far less than the error brought by the HT method. Besides, the TOF extraction experiments in different propagation distances indicate that the proposed

method has good performance of stability and robustness. Therefore, the proposed ridge analysis method is suitable for application of high accuracy TOF extraction of dispersive Lamb wave.

ACKNOWLEDGMENT

This research was financially supported by the National Natural Science Foundation of China (Grant No. 51677093 and No. 51777100).

REFERENCES

[1] M. Mitra and S. Gopalakrishnan, "Guided wave based structural health monitoring: a review," *Smart Materials and Structures*, vol. 25, no. 5, p. 53001, 2016.

[2] J. L. Rose, "Guided wave nuances for ultrasonic nondestructive evaluation," *IEEE Transactions on Ultrasonics, Ferroelectrics and Frequency Control*, vol. 47, no. 3, pp. 575-583, 2000.

[3] F. Jenot, M. Ouaftouh, M. Duquennoy, and M. Ourak, "Corrosion thickness gauging in plates using lamb wave group velocity measurements," *Measurement Science and Technology*, vol. 12, no. 8, p. 1287, 2001.

[4] S. Legendre, D. Massicotte, J. Goyette, and T. K. Bose, "Wavelettransform-based method of analysis for lamb-wave ultrasonic NDE signals," *IEEE Transactions on Instrumentation and Measurement*, vol. 49, no. 3, pp. 524-530, 2000.

[5] D. Dai and Q. He, "Structure damage localization with ultrasonic guided waves based on a time-frequency method," *Signal Processing*, vol. 96, no. Part A, pp. 21-28, 2014.

[6] H. Z. Hosseinabadi, B. Nazari, R. Amirfattahi, H. R. Mirdamadi, and A. R. Sadri, "Wavelet network approach for structural damage identification using guided ultrasonic waves," *IEEE Transactions on Instrumentation and Measurement*, vol. 63, no. 7, pp. 1680-1692, 2014.

[7] S. Huang, Z. Wei, W. Zhao, and S. Wang, "A new omni-directional EMAT for ultrasonic lamb wave tomography imaging of metallic plate defects," *Sensors*, vol. 14, no. 2, p. 3458, 2014.

[8] Z. Wei, S. Huang, S. Wang, and W. Zhao, "Magnetostriction-based omni-directional guided wave transducer for high-accuracy tomography of steel plate defects," *IEEE Sensors Journal*, vol. 15, no. 11, pp. 6549-6558, 2015.

[9] P. D. Wilcox, M. Lowe, and P. Cawley, "Mode and transducer selection for long range lamb wave inspection," *Journal of Intelligent Material Systems and Structures*, vol. 12, no. 8, pp. 553-565, 2001.

[10] Y. Zhang, S. Huang, S. Wang, Z. Wei, and W. Zhao, "Recognition of overlapped lamb wave detecting signals in aluminum plate by EMD-based STFT flight time extraction method," *International Journal of Applied Electromagnetics and Mechanics*, vol. 52, no. 3-4, pp. 991-998, 2016.

[11] D. Grimaldi, "Time-of-flight measurement of ultrasonic pulse echoes using wavelet networks," *IEEE Transactions on Instrumentation and Measurement*, vol. 55, no. 1, pp. 5-13, 2006.

[12] Y. Zhang, S. L. Huang, S. Wang, and W. Zhao, "Time-frequency energy density precipitation method for time-of-flight extraction of narrowband lamb wave detection signals," *Review of Scientific Instruments*, vol. 87, no. 5, p. 054702, 2016.

[13] F. Li, H. Murayama, K. Kageyama, and I. Ohsawa, "Multiple damage assessment in composite laminates using a doppler-effect-based fiberoptic sensor," *Measurement Science and Technology*, vol. 20, no. 11, p. 115109, 2009.

[14] R. A. Carmona, W. L. Hwang, and B. Torrsani, "Multiridge detection and time-frequency reconstruction," *IEEE Transactions on Signal Processing*, vol. 47, no. 2, pp. 480-492, 1999.

[15] K. Xu, D. Ta, and W. Wang, "Multiridge-based analysis for separating individual modes from multimodal guided wave signals in long bones," *IEEE Transactions on Ultrasonics, Ferroelectrics, and Frequency Control*, vol. 57, no. 11, pp. 2480-2490, 2010.

[16] Z. Wang, S. Huang, Q. Wang, S. Wang, and W. Zhao, "Time of flight extraction of dispersive Lamb wave by ridge analysis," *Presented at the 2018 International Applied Computational Electromagnetics Society (ACES) Symposium*, Beijing, China, July 2018.

[17] J. L. Rose, *Ultrasonic Guided Waves in Solid Media*. Cambridge University Press, 2014.

Zhe Wang received his B.Sc. degree in 2016 from Chongqing University, now he is a Ph.D. candidate in the Department of Electrical Engineering, Tsinghua University. His main research interests include guided waves detection technology.

Songling Huang received his B.Sc. degree in 1991 from Southeast University, received his M.Sc. degree in 1998 from Tsinghua University, and received his Ph.D. degree in 2001 from Tsinghua University, now he is a Professor in Tsinghua University. His main research interests include Electromagnetic and Non-destructive testing.

Hybrid Plasmonic Waveguiding Model in a V-shaped Silicon Groove

Xiao-Jing Kuang [1,2], Zhi-Xiang Huang [1], Xin-Yuan Cao [2], Meng Kong [2], Jing Shen [2], and Xian-Liang Wu [1]

[1] Key Laboratory of Intelligent Computing & Signal Processing, Ministry of Education
Anhui University, Hefei, 230039, China
ziranisbest@163.com, zxhuang@ahu.edu.cn

[2] Key Laboratory of Simulation and Design for Electronic Information System
Hefei Normal University, Hefei, 230601, China
xycaobl@163.com

Abstract ─ A modified V-shaped silicon groove waveguide, embeded with metal nanowire,which is coated with a low refractive index layer was proposed. Finite element method (FEM) is used to numerically simulate the characteristics of the hybrid plasmonic mode at the wavelength of 1550nm. The simulation results show that the hybrid plasmonic mode can be confined to the dielectric layer on the surface of the metal nanowire. Meanwhile, factors on the modal properties are analyzed. Low loss and strong mode confinement can be realized by adjusting the size of the dielectric and metal nanowires as well as the angle of the V-shaped groove. The overall performance of the proposed model is superior to that of traditional hybrid plasmonic waveguides.

Index Terms ─ Finite element method, hybrid plasmonic waveguide, Modal analysis, V-shaped silicon groove.

I. INTRODUCTION

Surface plasmon polaritons (SPPs) have been widely used as information carriers for designing and preparing nano-waveguide structures. By the advantage of excellent conductivity and the breakthrough of diffraction barrier, surface plasmon waveguides (SPWs) has become one of the ideal design schemes for the new-generation optoelectronic integrated chips. A key issue in designing SPWs is how to get the balance between mode confinement and propagation length [1-2].

Up to present, researchers have made a variety of innovative improvements in the structure of optical waveguides, and have proposed a series of surface plasmonic waveguide structures, e.g., shapes, film, slit, cylinder, strip and V-shaped groove were designed; material patterns, dielectric-metal-dielectric (DMD), metal-dielectric-metal (MDM) and hybrid pattern were proposed [3-9].

Among the above plasmonic waveguide structures, the V-shaped groove structure has been shown that a strong lateral confinement on the SPP at the bottom of the groove resulted in low transmission loss in the optical communication bands [10-14]. In addition, the silicon waveguides are well compatible with complementary metal oxide semiconductors (CMOS), and it can be used as the basic module for the transmission, confinement and process of optical signals in photonic integrated circuits. The mode confinement ability of SPP structure can be further enhanced by combining metal waveguides with silicon devices [15-17]. However, SPPs mode transmits on the nanowire surface, the propagation constant is denoted as $\beta = 2\pi\, neff / \lambda$ [18], and the propagation length can be defined as $Lp = 1/2Im(\beta)$ [18]. Therefore, the propagation length of the metal-high refractive index dielectric was higher than that of the metal-low refractive index dielectric structure. In other words, the hybrid SPPs mode is confined to the low refractive index layer more efficiently. For the above reasons, based on the traditional structure [19-20], a modified waveguide model consisting of a metal nanowire covered with a dielectric film of low refractive index in a V-shaped silicon groove is proposed. FEM is used to numerically analysis the symmetrical hybrid SPP mode transmission due to its flexibility in geometrical modeling [6]. Furthermore, the factors on the modal properties are analyzed to facilitate the feasibility design of the waveguide structure, such as the size of the dielectric and metal nanowires, the angle of the V-shaped groove, et al.

II. GEOMETRY OF THE PROPOSED HYBRID V-GROOVE WAVEGUIDE AND THEORETICAL ANALYSIS

Based on the analysis above, the hybrid plasmonic waveguide model is proposed as shown in Fig. 1. In order to increase transmission distance, the V-shaped silicon groove waveguide was embedded with the metal

Submitted On: August 29, 2018
Accepted On: January 26, 2019

nanowire, which is coated with low refractive index dielectric layer.

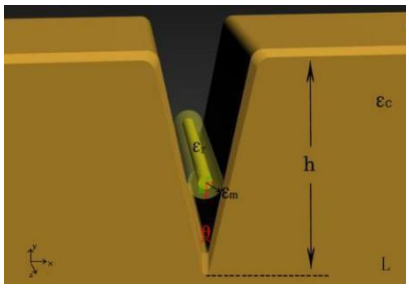

Fig. 1. Geometry of the proposed hybrid groove waveguide. The silicon slice (height h = 600 nm, width L = 800 nm, ε_c = 12.25) is used as the V-groove substrate with the angle (θ), and the silver nanowire (the radius is denoted by r, ε_m = -129+3.3i) [9] is coated with low-index dielectric SiO_2 (the radius is denoted by R), thus, the thickness of the SiO_2 (ε_r = 2.25) layer is denoted by $d = R - r$.

The surface plasmon mode transmits on the nanowire surface along z-axis. The vector field $\mathbf{\Phi}$ can be expressed as:

$$\mathbf{\Phi}(x,y,z)=\mathbf{\Phi}(x,y)e^{-j\beta z}=\left(\mathbf{\Phi}_t(x,y)+\mathbf{\Phi}_z(x,y)e^{-j\beta z}\right), \quad (1)$$

where, $\mathbf{\Phi}_t(x,y)$ and $\mathbf{\Phi}_z(x,y)$ are respectively represented by the horizontal and vertical field components. In this case, the wave equation is degenerated into two-dimensional cross section, which can be shown as:

$$\nabla^2\mathbf{\Phi}+\left(n^2-neff^2\right)(2\pi/\lambda)^2\mathbf{\Phi}=0, \quad (2)$$

where n and $neff$ denote the refractive index of material and the modal effective refractive index, respectively. The mode characteristics are analyzed by wave equation. The propagation length can be defined as:

$$L_p=1/2Im(\beta). \quad (3)$$

The modal properties also include the normalized mode area A_{eff}/A_0, which can be defined by the ratio of a mode's total energy density per unit length and its peak energy density. Here,

$$A_{eff}=\left[\int_{A\infty}W(r)\,dA\right]^2 \Big/ \int_{A\infty}W(r)^2\,dA; A_0=(\lambda/2)^2, \quad (4)$$

where $W(r)$ represents the effective energy density [18].

III. MODAL CHARACTERISTICS OF THE PROPOSED HYBRID V-GROOVE WAVEGUIDE

FEM method is carried out to simulate the plasmon characteristics with a wavelength at 1550 nm. The wave equation (2) is solved by combining the boundary condition of the above proposed model. Simulation results of the electric field energy flux density S_z for the fundamental hybrid plasmonic mode are shown in Fig. 2. Compared with different geometries, energy began to spread from the bottom of the groove to the surface of the metal nanowire, and was ultimately confined to the vicinity of the lower refractive index layer. Moreover, from Table 1, it is found that the proposed hybrid V-groove waveguide has the maximum value of the energy, which implies that the proposed waveguide structure has higher mode field confining ability for the strongest coupling between the channel plasmon polaritons (CPPs) mode and dielectric mode.

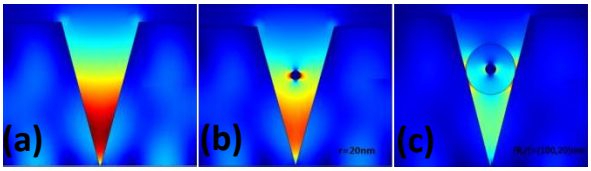

Fig. 2. S_z distributions of the fundamental mode of hybrid groove waveguide with different geometries: (a) conventional V-groove waveguide (θ = 30^0), (b) V-groove waveguide with metal nanowire (θ = 30^0, r = 20 nm), and (c) the proposed hybrid V-groove waveguide (θ= 30^0, [R, r] = [100, 20] nm).

Table 1: The maximum value of the electric field energy flux density S_z

Modal	(a)	(b)	(c)
S_z (V/m)	9.9814e7	1.4776e8	2.7261e8

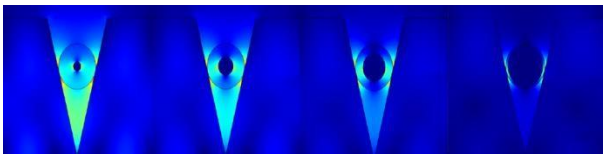

Fig. 3. S_z distributions of the fundamental mode with different r = 20, 40, 60, 90 at θ = 30^0 and R = 100 nm.

The influence of different thickness of the dielectric layer on the fundamental hybrid plasmonic mode is shown in Figs. 3 (a)-(b). For configurations with a relatively radius of the dielectric layer and nanowire (e.g., R = 100 nm), as the radius r of the nanowire increases, one can find that the distribution of energy gradually shifted from the entire groove area to the dielectric layer. Moreover, from Table 2, the maximum value of the electric field energy flux density S_z has increased with the decrease in the thickness of dielectric layer, which shows that the hybrid plasmonic mode can be confined to the thinner dielectric layer.

Table 2: The maximum value of the electric field energy flux density S_z

S_z (V/m)	r = 20 (nm)	r = 40 (nm)	r = 60 (nm)	r = 80 (nm)
R = 100 (nm)	2.7261e8	3.2873e8	4.3811e8	7.9982e8

It is of practical significance to investigate the influence of groove angle on the fundamental hybrid plasmonic mode. For configurations with [*R*, *r*] = [100, 60] nm, the electric field distribution of the fundamental plasmonic modes are shown in Fig. 4. While $\theta = 0^0$ (e.g., Fig. 4 (a)), the proposed structure is similar to a DMD hybrid plasmonic waveguide structure [9]. While $\theta = 180^0$ (Fig. 5 (c)), the proposed structure is similar to a hybrid waveguide structure consisting of a dielectric base and metal nanowire [18]. Through comparing the maximum energy electric field components (E_x and E_y) in Table 3, it can be seen that the hybrid mode appears as a symmetric quasi-TM mode with E_x as the dominant electric field components for $\theta < 90^0$. However, a further increase in the groove angle results in the confinement of symmetric quasi-TM mode. With more energy penetrating into the metal area, E_x decreases with the energy loss. When $|E_x|_{max}$ and $|E_y|_{max}$ are comparable for $\theta = 90^0$, both the symmetric quasi-TE and quasi-TM hybrid modes are supported. The value of $|E_x|_{max}$ continuously decreased along with the increased the groove angle from $\theta > 90^0$ to $\theta < 180^0$. It can be obtained that the hybrid mode appears as a symmetric quasi-TE mode with E_y as the dominant electric field components, indicating a transformation of the quasi-TE mode to quasi-TM mode, and polarization rotation can be realized by adjusting the groove angle.

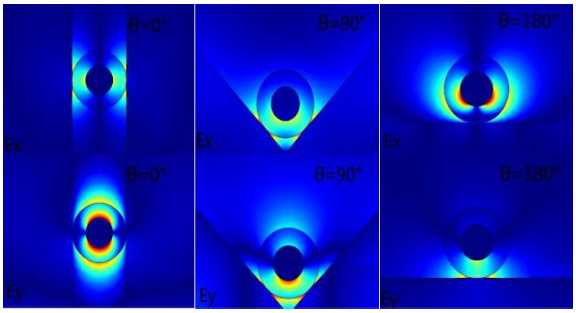

(a) (b) (c)

Fig. 4. Field distributions of the dominant electric component E_x and E_y on various angle.

Table 3: The maximum value of the electric field energy

	$\theta = 0^0$	$\theta = 90^0$	$\theta = 180^0$
$\|E_x\|_{max}$ (V/m)	4.0724e8	3.2086e8	1.6468e8
$\|E_y\|_{max}$ (V/m)	1.4162e8	3.2585e8	5.7815e8

Next, comparison is carried out between the proposed CPPs, V-groove waveguide with metal nanowire ($R = r$) and conventional V-groove waveguide ($R = r = 0$) [8-11]. Simulation results reveal that the proposed CPPs model has low effective refractive index (n_{eff}), long-distance transport (L_p) and strong mode confinement (A_{eff}/A_0) in Figs. 5 (a)-(c). One can further prove the strongest coupling between the plasmonic and dielectric mode.

Further, these factors of *R*, *r* and θ on the impact of the modal properties have been investigated. For configurations with θ (e.g., $\theta = 30^0$), Figs. 5 (a)-(c) illustrates that the value of n_{eff} increases monotonically; the value of L_p and A_{eff}/A_0 decreases when *r* gets bigger with the same *R*. Correspondingly; the value of n_{eff}, L_p and A_{eff}/A_0 have the same trend when *R* gets smaller with the same *r*. Meanwhile, compared with different angles, performance gets better in accordance with bigger θ. So the hybrid plasmonic waveguide model with low loss and strong mode confinement can be realized by adjusting the values of the *R*, *r* and θ.

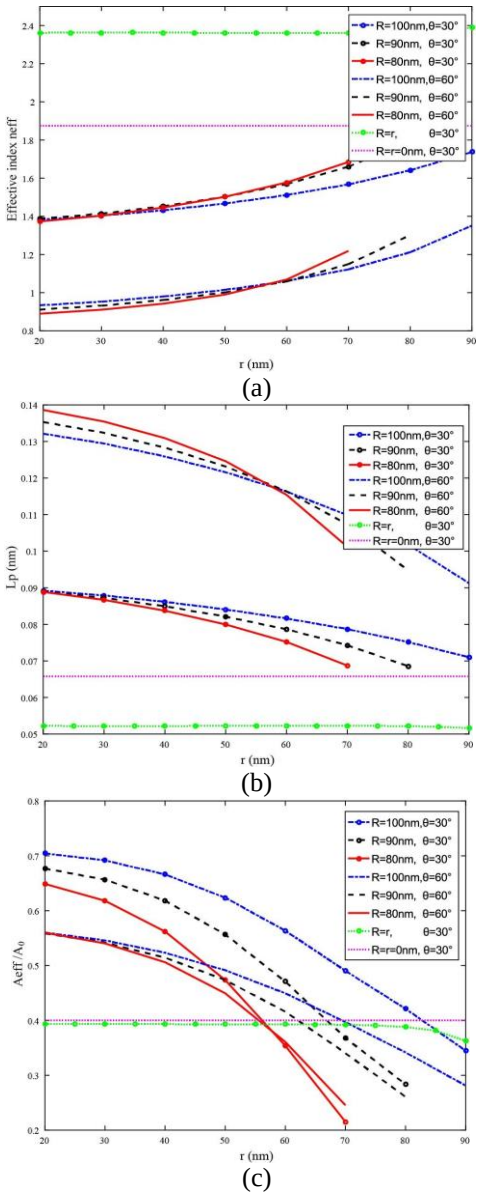

(a)

(b)

(c)

Fig. 5. Dependence of the modal properties of the fundamental hybrid mode with the different *R* and *r*; (a) the effective refractive index (n_{eff}), (b) the propagation length (L_p), and (c) normalized the effective area (A_{eff}/A_0).

IV. CONCLUSION

In this paper, a novel hybrid silicon groove waveguide model is proposed. FEM is used to numerically simulate the electric field energy for the fundamental hybrid plasmonic mode. Compared with conventional groove waveguide, more energy are confined on the low refractive index dielectric layer because of the strong coupling between plasma mode and dielectric mode. Meanwhile, these factors of R, r and θ on the impact of the modal properties have been investigated. The proposed model with low loss and strong mode confinement can be realized by adjusting the values of the R, r and θ, and polarization rotation of the hybrid mode can be achieved by changing the θ. Therefore, the proposed hybrid waveguide structure is compatible with traditional fabrication technologies, and has the potential to be used in highly integrated waveguide circuits.

ACKNOWLEDGMENT

This work was supported by the NSFC (Nos. 61601166, 61701001, 61701003, 61701163, 61801163), National Natural Science Fund for Excellent Young Scholars (No. 61722101), Universities Natural Science Foundation of Anhui Province (Nos. KJ2017ZD51, KJ2018ZD046, KJ2018A0488 and KJ2018A0489), Special Foundation for Young Scientists of Anhui Province (No. 2013SQRL065ZD), Anhui-Provincial Natural Science Foundation (No. 1808085MF167, 1808085QF204).

REFERENCES

[1] T. W. Ebbesen, C. Genet, and S. I. Bozhevolnyi, "Surface-plasmon circuitry," *Phys. Today*, vol. 61, no. 5, pp. 44-50, 2008.

[2] L. H. Wang, Z. X. Huang, and X. J. Kuang, "Designing and optimizing of surface plasmonic waveguide with nonlinear media," *Acta Photonica Sinica*, vol. 45, no. 2, pp. 0224002-0224005, 2016.

[3] K. C. Vernon, N. Tischler, and M. L. Kurth, "Coupling of energy from quantum emitters to the plasmonic mode of V groove waveguides: A numerical study," *Journal of Applied Physics*, vol. 11, no. 6, pp. 16-50, 2012.

[4] D. F. P. Pile and D. K. Gramotnev, "Channel plasmon-polariton in a triangular groove on a metal surface," *Opt. Lett.*, vol. 29, no. 10, pp. 1069-1071, 2004.

[5] E. Moreno, S. G. Rodrigo, and S. I. Bozhevolnyi, "Guiding and focusing of electromagnetic fields with wedge plasmon polaritons," *Phys. Rev. Lett.*, vol. 100, no. 2, p. 023901, 2008.

[6] A. V. Krasavin and A. V. Zayats, "Silicon-based plasmonic waveguides," *Opt. Exp.*, vol. 18, no. 65, pp. 11791-11799, 2010.

[7] D. X. Dai, Y. C. Shi, and S. L. He, "Gain enhancement in a hybrid plasmonic nano-waveguide with a low-index or high-index gain medium," *Opt. Exp.*, vol. 19, no. 14, pp. 12925-12936, 2011.

[8] R. F. Oulton, G. Barta, and D. F. P. Pile, "Confinement and propagation characteristics of subwavelength plasmonic modes," *New Journal of Physics*, vol. 10, no. 10, p. 105018, 2008.

[9] R. F. Oulton, V. J. Sorger, and D. A. Genov, "A hybrid plasmonic waveguide for subwavelength confinement and long-range propagation," *Nature Photonics*, vol. 2, no. 8, pp. 496-500, 2008.

[10] Y. S. Bian, Z. Zheng, and X. Zhao, "Highly confined hybrid plasmonic modes guided by for propagation nanowire embedded metal grooves low loss at 1550nm," *IEEE Journal of Selected Topics Quantum Electron*, vol. 19, no. 3, pp. 4800106, 2013.

[11] Y. S. Bian, Z. Zheng, and X. Zhao, "Hybrid plasmon polariton guiding with tight mode confinement in a V-shaped metal/dielectric groove," *J. Opt.*, vol. 15, no. 5, p. 055011, 2013.

[12] S. I. Bozhevolvui, V. S. Volkov, and E. Devaux, "Channel plasmon subwavelength waveguide components including interferometers and ring resonators," *Nature*, vol. 440, no. 7083, pp. 508-511, 2006.

[13] Y. Yue, L. Zhang, and J. Y. Yang, "Silicon-on-insulator polarization splitter using two horizontally slotted waveguides," *Opt. Lett.*, vol. 35, no. 9, pp. 1364-1366, 2010.

[14] R. Ding, T. Baehr-Jones, and W. J. Kim, "Low-loss strip-loaded slot waveguides in silicon-on-insulator," *Opt. Exp.*, vol. 18, no. 24, pp. 25061-25067, 2010.

[15] F. F. Lu, T. Li, and X. P. Hu, "Efficient second-harmonic generation in nonlinear plasmonic waveguide," *Opt. Lett.*, vol. 36, no. 17, pp. 3371-3373, 2011.

[16] X. L. He, L. Yang, and T. Yang, "Optical nano-focusing by tapering coupled photonic-plasmonic waveguides," *Opt. Exp.*, vol. 19, no. 14, pp. 12865-12872, 2011.

[17] J. Zhang, P. Zhao, E. Cassan, and X. Zhang, "Phase regeneration of phase-shift keying signals in highly nonlinear hybrid plasmonic waveguides," *Opt. Lett.*, vol. 38, no. 6, pp. 848-850, 2013.

[18] C. L. Zou, F. W. Sun, and Y. F. Xiao, "Plasmon modes of silver nanowire on a silica substrate," *Applied Physics Letters*, vol. 97, no. 18, p. 189, 2010.

[19] Y. S. Bian and Q. H. Gong, "Low-loss light transport at the subwavelength scale in silicon nano-slot based symmetric hybrid plasmonic waveguiding schemes," *Opt. Exp.*, vol. 21, no. 20, pp. 23907-23920, 2013.

[20] L. Chen, X. Li, and D. S. Gao, "An efficient

directional coupling from dielectric waveguide to hybrid long-range plasmonic waveguide on a silicon platform," *Appl. Phys. B*, vol. 111, no. 1, pp. 15-19, 2013.

Xiaojing Kuang was born in Anhui, China, in 1984. She received the B.S. and M.D. degrees from Anhui University, Hefei, China, in 2007 and 2010, She is a Ph.D. student in electromagnetic field and microwave technology at Anhui University. Her current research interests include time-domain numerical methods, micro and nano-scale technology.

Zhixiang Huang (M'16) was born in Anhui, China, in 1979. He received the B.S. and Ph.D. degrees from Anhui University, Hefei, China, in 2002 and 2007, respectively. He was a Visiting Scholar with Iowa State University, Ames, from 2010 to 2011. He is a member of OSA and IEEE. His current research interests include time-domain numerical methods, metamaterial and active meta-materials.

A Study on the Propagation Characteristics of AIS Signals in the Evaporation Duct Environment

Wenlong Tang [1], Hao Cha [1], Min Wei [2], Bin Tian [1*], and Yuefang Li [3]

[1] College of Electrical Engineering
Naval University of Engineering, Wuhan, 430033, China
wltang17@163.com, hydchj@sina.com, bintiannue123@163.com*

[2] The Unit 31003 of PLA, Beijing, 100191, China
13215608602@163.com

[3] Tianjin Navigation Instrument Research Institute, Tianjin, 300131, China
15556920497@163.com

Abstract ─ The propagation characteristics of signal of the Automatic Identification System (AIS) in the evaporation duct environment over the sea surface are investigated by using the parabolic equation method. The parabolic equation method has excellent stability and accuracy in solving the computational problem of electromagnetic wave propagation under different atmospheric conditions and it is probably the most suitable for the purpose of analyzing AIS signals. The propagation of AIS signals in air is determined by the variation of the refractivity with height. For AIS transmission, ducting propagation may be the most important propagation mechanism. The propagation loss of AIS signals in the evaporation duct is calculated and compared with that for the case of the standard atmosphere. In order to demonstrate the effect of evaporation duct on the propagation of AIS signals more intuitively, propagation loss versus range for three typical AIS links and the receiver height versus propagation loss under different atmospheric conditions are analyzed in details. The simulation results show that the evaporation duct has little influence on the AIS system.

Index Terms ─ AIS, evaporation duct, parabolic equation method, propagation loss.

I. INTRODUCTION

Automatic Identification System (AIS) is a new navigation aid that operates in the Very High Frequency (VHF) maritime mobile band, and its primary purpose is to facilitate the efficient exchange of navigation and voyage data between ships, and between ships and shore stations [1]. As a maritime navigation safety communication system, it can automatically provide vessel information, including the vessel's identity, type, position, course, speed, navigation status and other safety-related information to other ships and to shore stations in its surroundings. It also receives such information from similarly fitted ships and exchanges data with shore-based facilities automatically. When AIS signals propagate over the sea surface, it is easily affected by various atmospheric conditions. At the beginning of this research, only three papers were found to study the effects of atmospheric conditions on AIS signal propagation over the sea environment. A report by the International Telecommunications Union (ITU) examined some general propagation mechanisms that could enhance the shore-based AIS detection range, but ignores atmospheric conditions behind it [2]. Green et al. [3] analyzed phenomena that could theoretically affect the transmission of AIS signals. In their opinion, the parabolic equation method may be the most suitable for predicting the propagation characteristics of AIS signals in atmospheric duct conditions. Bruin [4] studied the impact of North Sea weather conditions on the performance of AIS, and the Advanced Refractive Effects Prediction System (AREPS) was used to calculate the propagation loss and predict AIS coverage.

Over the sea, evaporation duct is the most common type of anomalous propagation [5,6]. The height of the evaporation duct is usually between 6 m and 30 m, and generally no more than 40 m. When radio waves, especially microwaves, travel near the sea surface, they are easily affected by the evaporation duct. Part of energy is trapped in the duct and propagates beyond the line-of-sight, forming a very important evaporation duct propagation mechanism.

Because the evaporation duct has significant influence on the stability of the communication link and

Submitted On: September 20, 2018
Accepted On: December 21, 2018

the accurate estimation of the target position by radar, analysis of the effect of evaporation duct on radio waves has been the focus of attention. By studying the effects of the evaporation duct on the propagation of AIS signals, it is of profound significance to improve maritime situational awareness. At the same time, it also has important application value for the inversion research of atmospheric ducts.

The parabolic equation method is based on a reduction of the Helmholtz equation and it can be implemented to propagation over sea and land. It can accurately predict the propagation characteristics of electromagnetic waves in a complex environment and is commonly used in the study of wave propagation problems [7-9]. In addition, through the marching method, it can use the fast Fourier transforms technique to obtain solutions. For maritime propagation applications, the parabolic equation method can be solved by running on a laptop for a few seconds. To this end, the parabolic equation method is utilized to model the propagation of AIS signals under ducting conditions. The propagation loss of AIS signals in the standard atmosphere and the evaporation duct is calculated and compared.

II. AUTOMATIC IDENTIFICATION SYSTEM

In 2000, the AIS system was introduced by the International Maritime Organization (IMO) as a part of the Safety of Life at Sea (SOLAS) regulations, which require AIS to be fitted aboard all ships of 300 gross tonnage and upwards engaged on international voyages, cargo ships of 500 gross tonnage and upwards not engaged on international voyages and all passenger ships irrespective of size [10]. International regulations came into full force on December 31, 2004, and this system is known as Class A AIS system. After this date, all ships in service have installed an AIS system must operate it continuously except for international agreements, rules, or standards allow navigational information to be protected. In 2007, Class B AIS system was introduced for small vessels, including pleasure boats. Class A and Class B AIS systems are fully compatible and they can receive and decode each other's messages. Class A system's messages generally contain more information than Class B system's messages. However, they all provide essential safety information. In this paper, we only consider the Class A AIS system.

Two international channels have been allocated for AIS use and both frequencies are in the maritime VHF mobile band [11]. AIS 1 (161.975 MHz) and AIS 2 (162.025 MHz) are designated for long-range AIS systems. At all time, messages can be received on both channels, whilst messages should be transmitted alternately from AIS 1 and AIS 2 channels. Class A AIS system parameters are given in Table 1.

Table 1: AIS system parameters

Parameter	**Value**
Transmitter Power (W)	12.5
Frequency (MHz)	161.975/162.025
Antenna Gain (dBi)	2~5
Wavelength (m)	1.86
Receiver Sensitivity (dBW)	–137.0

III. AIS SIGNAL PROPAGATION MODELLING

A. Atmospheric refractivity model

Evaporation duct is a kind of duct with the highest frequency over the surface of the sea. It is formed by the evaporation of sea surface water vapour, which causes the atmospheric humidity to decrease sharply with height in a small height range. At a certain height, the modified atmospheric refractivity is minimized, which is defined as the evaporation duct height (Fig. 1).

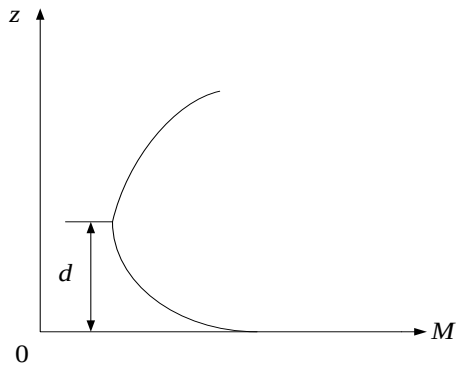

Fig. 1. Modified atmospheric refractivity profile for an evaporation duct.

The evaporation duct is usually described using a logarithmic model, which is defined as [12]:

$$M(z) = M(0) + 0.125z - 0.125d \ln\left(\frac{z + 0.00015}{0.00015}\right), \quad (1)$$

where $M(0) = 339$ is the modified atmospheric refractivity at the sea surface, z is the vertical height, and d is the evaporation duct height.

B. Parabolic equation method

The two-dimensional Helmholtz equation in Cartesian coordinates is given by [13]:

$$\frac{\partial^2 \phi}{\partial x^2} + \frac{\partial^2 \phi}{\partial z^2} + k_0^2 m^2 \phi = 0, \quad (2)$$

where ϕ is the electric or magnetic field in the horizontal or vertical polarization, respectively, x is the range and z is the height, $k_0 = 2\pi/\lambda$ is the free

space wave number, λ is the wavelength, and $m = 1 + M \times 10^{-6}$ is the height and range dependent modified refractive index.

A wave function is introduced to derive the parabolic equation:

$$\phi(\mathrm{x}, z) = u(\mathrm{x}, z) e^{ik_0 x}. \tag{3}$$

Substituting (3) into (2), yields:

$$\frac{\partial^2 u}{\partial x^2} + 2ik_0 \frac{\partial u}{\partial x} + \frac{\partial^2 u}{\partial z^2} + k_0^2 \left(m^2 - 1\right) u = 0. \tag{4}$$

Ignoring backward propagation waves, the standard narrow angle parabolic equation (SPE) can be written as:

$$\frac{\partial u(x,z)}{\partial x} = \frac{ik_0}{2}\left[\frac{1}{k_0^2}\frac{\partial^2}{\partial z^2} + m^2 - 1\right] u(x,z). \tag{5}$$

The split-step Fourier transform solution of the SPE is given by:

$$u(x_0 + \Delta x, z) = \exp\left(ik_0\left(m^2 - 1\right)\frac{\Delta x}{2}\right) \bullet \mathrm{F}^{-1}\left(\exp\left(-ip^2 \frac{\Delta x}{2k_0}\right)\mathrm{F}\left(u(x_0, z)\right)\right), \tag{6}$$

where F and F^{-1} represent the forward and inverse Fourier transforms respectively, $p = k_0 \sin\theta$ with θ being the propagation angle referenced from the paraxial direction, Δx is the range step, and $u(x_0, z)$ is the initial field distribution.

Split-step Fourier transform method is a stepping algorithm that calculates the field distribution of the next step based on the field distribution of the previous step. Given the initial field distribution $u(x_0, z)$, $u(x_0 + \Delta x, z)$ can be calculated using the split-step Fourier transform method. Thus, all numerical solutions can be determined by an iterative process.

It should be noted that in order to ensure accuracy of the SPE solution, propagation angles should be less than 15˚. For maritime evaporation duct propagation, the propagation elevation angle of electromagnetic waves is generally less than 1˚. Thus, the SPE is chosen to model the propagation characteristics of AIS signals in the atmospheric duct environment.

C. AIS signal model

Since AIS is a one-way communication system, according to the radio wave propagation theory, received AIS signal level is [4]:

$$P_r = \frac{P_t G_t G_r \lambda^2}{\left(4\pi R\right)^2} F^2, \tag{7}$$

where P_t is the transmitted power, G_t is the gain of the transmitter antenna, G_r is the gain of the receiver antenna, λ is the wavelength, R is the distance from the transmitter to the receiver, and $F = \sqrt{x}\left|u(x,z)\right|$ is the propagation factor.

The propagation loss PL of AIS signals is defined as [14]:

$$PL = 20\log\left(\frac{4\pi R}{\lambda}\right) - 20\log\left(F\right). \tag{8}$$

D. Rough sea surface effect

A flat sea surface is usually used in electromagnetic waves propagation modeling. However, in reality this is not the truth [15,16]. Since the wavelength of the AIS signal is 1.86 m, which is of the same order as the root mean square sea height variations under strong wind, the influence of sea surface roughness must be taken into account. Therefore, the effective reflection coefficient Γ_{eff} is introduced to account for the rough sea surface effect, which is defined as [17]:

$$\Gamma_{eff} = \rho \Gamma_e, \tag{9}$$

where Γ_e is the reflection coefficient of a flat sea surface, ρ is the roughness reduction factor, which is defined as:

$$\rho = \exp\left(-\frac{\gamma^2}{2}\right) I_0\left(\frac{\gamma^2}{2}\right), \tag{10}$$

where I_0 is the modified Bessel function of the first kind of order zero, γ is the Rayleigh roughness parameter, which is defined as:

$$\gamma = 4\pi\sigma \sin\alpha / \lambda, \tag{11}$$

where $\sigma = 0.0051\omega^2$ is the root mean square sea height, ω is the wind speed, α is the grazing incidence angle, and λ is the wavelength.

IV. NUMERICAL SIMULATION AND DISCUSSION

A. Comparison of propagation loss pattern

In this section, we present the simulation results of the propagation loss of AIS signals under different atmospheric conditions. The simulation parameters are: the AIS signal frequency is 162 MHz, the transmitter antenna is an omnidirectional antenna with a height of 10 m, the elevation angle is 0˚, and vertical polarization is adopted. Figure 2 contains the propagation loss for the standard atmosphere generated with the parabolic equation method. Figure 3 contains the propagation loss results for an ideal 30 m evaporation duct with the same simulation parameters.

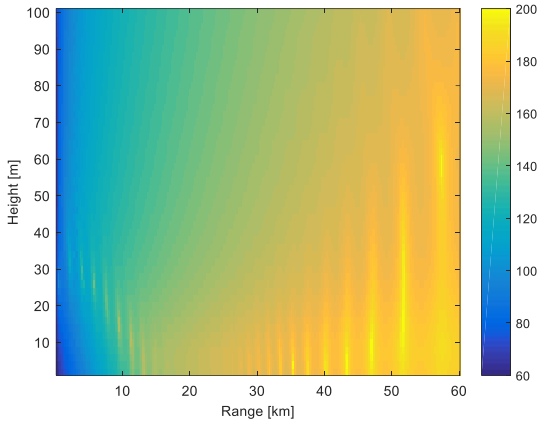

Fig. 2. Propagation loss for the standard atmosphere.

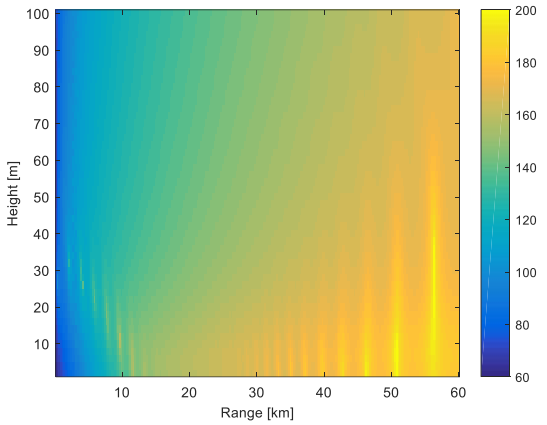

Fig. 3. Propagation loss for an ideal 30 m evaporation duct.

Comparing Fig. 2 with Fig. 3, we can see that the propagation loss pattern of the evaporation duct and the standard atmosphere are basically the same, indicating that the evaporation duct has almost no effect on the propagation of AIS signals.

B. Propagation loss versus range for three types of AIS links

In order to better reveal the influence of the evaporation duct on the propagation of the AIS signal, propagation loss at different duct height is given. Figure 4 shows propagation loss versus range for the AIS ship-to-ship link under the standard atmosphere and the 5 m, 15 m, 25 m, and 35 m height evaporation duct conditions. The receiver is located 10 m above mean sea level, which is a typical ship antenna height.

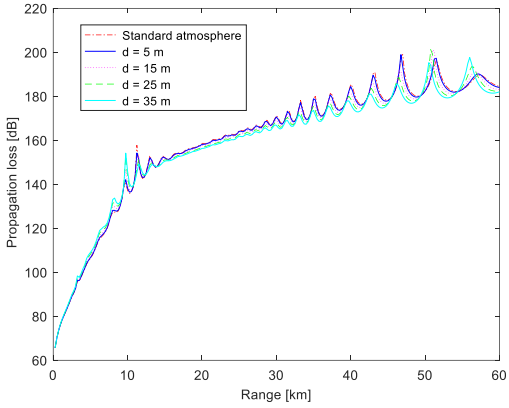

Fig. 4. Propagation loss under different evaporation duct height conditions at a receiver height of 10 m.

As can be seen from Fig. 4, as the distance increases, the propagation loss gradually increases. However, although the propagation loss generally decreases slightly as the height of the evaporation duct increases, the propagation loss curve is basically coincident with the propagation loss curve under standard atmospheric conditions, indicating that the evaporation duct has little effect on the propagation of the AIS signal.

For the AIS ship-to-shore link, the shore station usually has high antenna, typically 30 m. Figure 5 shows propagation loss versus range for the AIS ship-to-shore link under the standard atmosphere and different evaporation duct conditions.

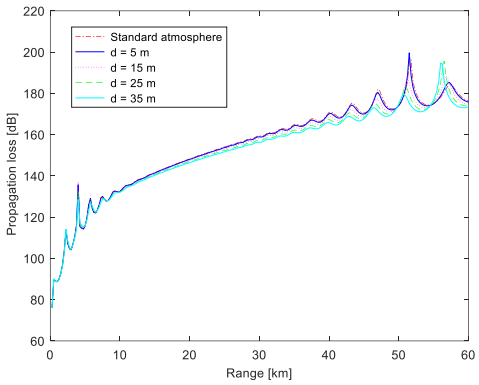

Fig. 5. Propagation loss under different evaporation duct height conditions at a receiver height of 30 m.

As noticed from Fig. 5, although the propagation loss is smaller than that of Fig. 4, the overall variation trend is consistent with Fig. 4, which indicates that the

evaporation duct has little effect on the AIS ship-to-shore link.

In addition to ship-to-ship link and ship-to-shore link, AIS receivers can also be installed on weather buoys throughout many coastal areas to form ship-to-weather buoy link. However, as the size of the weather buoy is much smaller, it can significantly limit the antenna height, which is typically 3 m. Propagation loss versus range for the AIS ship-to-weather buoy link under the standard atmosphere and different evaporation duct conditions is shown in Fig. 6.

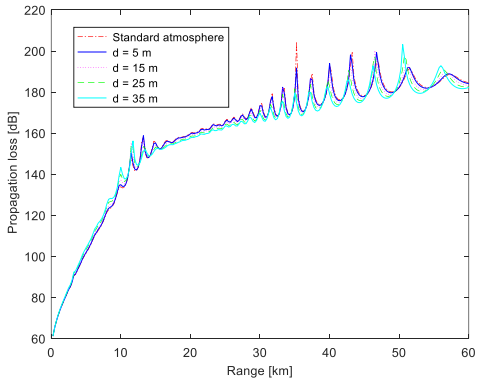

Fig. 6. Propagation loss under different evaporation duct height conditions at a receiver height of 3 m.

Compared with Fig. 4 and Fig. 5, since the receiving height is relatively low, the propagation loss is relatively large. Like the ship-to-ship link and the ship-to-shore link, the propagation loss curves in different atmospheric environments are basically coincident, indicating that the ship-to-weather buoy link is also less affected by the evaporation duct.

C. Receiver height versus propagation loss for AIS

Figure 7 shows the receiver height versus propagation loss at 20 km distance for a standard atmosphere and evaporation duct height of 5 m, 15 m, 25 m, and 35 m.

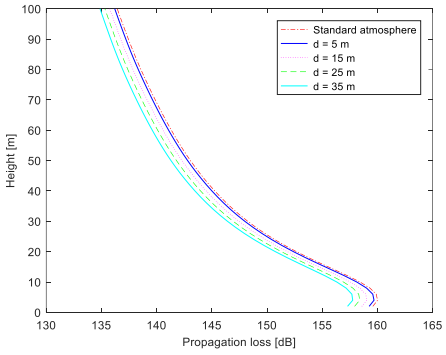

Fig. 7. Propagation loss under different evaporation duct height conditions at 20km distance.

It can be observed in Fig. 7 that as the height increases, the propagation loss first increases and then decreases, which is caused by diffraction mode propagation effect. In general, propagation loss under evaporation duct conditions is slightly reduced compared to the standard atmosphere, and the loss is also smaller as the duct height increases. However, the propagation loss of the standard atmosphere and the evaporation duct are almost the same, indicating that the evaporation duct has a certain influence on the propagation of the AIS signal, but it is very small.

V. CONCLUSION

In this work, the parabolic equation method is utilized to study the propagation characteristics of AIS signals in the evaporation duct environment over the sea surface. The propagation loss for the standard atmosphere and the evaporation duct is calculated and compared. The simulation results show that the propagation of AIS signals is hardly affected by the evaporation duct. It should be noted that this work mainly theoretically analyzes the problem of AIS signals propagation in the evaporation duct condition, and the simulation results need to be further verified by experiments, which will be investigated in the near future.

ACKNOWLEDGMENT

This work was supported by NSFC in China under Grant No. 41405009.

REFERENCES

[1] A. Goudossis and S. K. Katsikas, "Towards a secure automatic identification system (AIS)," *J. Mar. Sci. Technol.*, https://doi.org/10.1007/s00773-018-0561-3, 2018.

[2] "Long range detection of automatic identification system (AIS) messages under various tropospheric propagation conditions," *Tech. Rep. ITU-R M. 2123, International Telecommunications Union (ITU)*, 2007.

[3] D. Green, C. Fowler, D. Power, and J. Tunaley, "VHF propagation study," *Contractor report DRDC-ATLANTIC-CR-2011-152, Defense R&D Canada, London Research and Development Corp., C-Core*, 2012.

[4] E. R. Bruin, "On propagation effects in maritime situation awareness: Modelling the impact of North Sea weather conditions on the performance of AIS and coastal radar systems," *Master Thesis, Utrecht University*, 2016.

[5] H. Hitney and R. Vieth, "Statistical assessment of evaporation duct propagation," *IEEE Trans. Antennas Propagat.*, vol. 38, no. 6, pp. 794-799, 1990.

[6] S. D. Gunashekar, D. R. Siddle, and E. M.

Warrington, "Transhorizon radiowave propagation due to evaporation ducting," *Resonance*, vol. 11, no. 1, pp. 51-62, 2006.

[7] I. Sirkova, "Brief review on PE method application to propagation channel modeling in sea environment," *Cent. Eur. J. Eng*., vol. 2, no. 1, pp. 19-38, 2012.

[8] J. R. Kuttler and R. Janaswamy, "Improved Fourier transform methods for solving the parabolic wave equation," *Radio Science*, vol. 37, no. 2, pp. 5-11, 2002.

[9] Z. S. Wu, L. Li, L. K. Lin, and Z. W. Zhao, "Study on the maximum calculation height and the maximum propagation angle of the troposcatter wide-angle parabolic equation method," *IET Microwaves, Antennas & Propagation*, vol. 10, no. 6, pp. 686-691, 2016.

[10] Safety of life at sea (SOLAS) convention chapter V, regulation 19, 2000.

[11] "Recommendation, technical characteristics for an automatic identification system using time division multiple access in the VHF maritime mobile band," *Tech. Rep. Rec. ITU-R M.1371-5, International Telecommunications Union (ITU)*, 2014.

[12] R. A. Paulus, "Evaporation duct effects on sea clutter," *IEEE Trans. Antennas Propagat*., vol. 38, no. 11, pp. 1765-1771, 1990.

[13] M. Levy, *Parabolic Equation Methods for Electromagnetic Wave Propagation*, The Institution of Electrical Engineers, London, 2000.

[14] I. Sirkova, "Propagation factor and path loss simulation results for two rough surface reflection coefficients applied to the microwave ducting propagation over the sea," *Progress n Electromagnetics Research M*, vol. 17, pp. 151-166, 2011.

[15] D. E. Freud, N. E. Woods, H. C. Ku, and R. S. Awadallah, "Forward radar propagation over a rough sea surface: A numerical assessment of the Miller-Brown approximation using a horizontally polarized 3-GHz line source," *IEEE Trans. Antennas Propagat*., vol. 54, no. 4, pp. 1292-1304, 2006.

[16] M. D. Cui, H. Cha, and B. Tian, "A propagation model for rough sea surface conditions using the parabolic equation with the shadowing effect," *ACES Journal*, vol. 33, no. 6, pp. 683-689, 2018.

[17] P. E. Cadette, "Modeling tropospheric radiowave propagation over rough sea surfaces using the parabolic equation Fourier split-step method," *Master thesis, The George Washington University*, 2012.

Wenlong Tang received the B.S. degree in Radar Engineering and the M.S. degree in Signal and Information Processing from the Electronic Engineering Institute, Hefei, China, in 2014 and 2016, respectively. He is currently pursuing the Ph.D degree at the College of Electrical Engineering, Naval University of Engineering. His current research interests include radio wave propagation theory and atmospheric refractivity estimation techniques.

Hao Cha received the M.S. degree and the Ph.D. degree in Communication and Information System from the Nanjing University of Aeronautics and Astronautics, Nanjing, China, in 1990 and 1993, respectively. Now he is a Professor in Naval University of Engineering and majors in radar system. He is responsible for many scientific research projects, such as military scientific research projects, and his research achievements gained the army science-technology advance reward many times.